NONLINEAR INTERNAL WAVES, INTERNAL BORES, AND TURBULENT MIXING IN THE NEARSHORE COASTAL ENVIRONMENT

A DISSERTATION

SUBMITTED TO THE DEPARTMENT OF CIVIL AND ENVIRONMENTAL ENGINEERING

AND THE COMMITTEE ON GRADUATE STUDIES

OF STANFORD UNIVERSITY

IN PARTIAL FULFILLMENT OF THE REQUIREMENTS

FOR THE DEGREE OF

DOCTOR OF PHILOSOPHY

Ryan Kymn Walter

June 2014

This dissertation is online at: http://purl.stanford.edu/qr316zj4376

I certify that I have read this dissertation and that, in my opinion, it is fully adequate in scope and quality as a dissertation for the degree of Doctor of Philosophy.

Stephen Monismith, Primary Adviser

I certify that I have read this dissertation and that, in my opinion, it is fully adequate in scope and quality as a dissertation for the degree of Doctor of Philosophy.

Oliver Fringer

I certify that I have read this dissertation and that, in my opinion, it is fully adequate in scope and quality as a dissertation for the degree of Doctor of Philosophy.

Jeffrey Koseff

I certify that I have read this dissertation and that, in my opinion, it is fully adequate in scope and quality as a dissertation for the degree of Doctor of Philosophy.

Leif Thomas

I certify that I have read this dissertation and that, in my opinion, it is fully adequate in scope and quality as a dissertation for the degree of Doctor of Philosophy.

Brock Woodson

Approved for the Stanford University Committee on Graduate Studies.

Patricia J. Gumport, Vice Provost for Graduate Education

This signature page was generated electronically upon submission of this dissertation in electronic format. An original signed hard copy of the signature page is on file in University Archives.

Abstract

The nearshore coastal environment is generally taken to be one of the most productive and ecologically important parts of the ocean. The nearshore is also a complex environment from a physical standpoint, due in large part to the widespread and often irregular occurrence of nonlinear internal waves (NLIWs) that frequently appear more bore-like than wave-like. Indeed, this region of the ocean can be thought of as the “swash zone” for larger-scale internal wave fields on the continental shelf. These nearshore NLIWs and bores have considerable implications for the cross-shelf exchange and transport of nutrients, sediments, contaminants, larvae, and other scalars; turbulent dissipation and diapycnal mixing; and hypoxia development. Despite the ramifications and a growing body of literature on the subject, many questions still remain with respect to the evolution, fate, and impact of NLIWs and internal bores in the nearshore coastal environment. This dissertation addresses these issues in Monterey Bay, CA. Several observational field studies were conducted using a wide variety of instruments and measurement techniques, such as oceanographic mooring arrays and an underwater turbulence flux tower.

This work shows that nearshore internal bores produce transient stratification and mixing events, and represent the dominant source of variability, in the nearshore environment of southern Monterey Bay, CA. Specifically, these events control temperature and circulation dynamics, dominate turbulent mixing in the stratified interior, contribute to the majority of the variance in cross-shelf transport, and can create low dissolved oxygen (hypoxic) events. Individual bores also drive substantial changes to local mixing dynamics and the stratified turbulence field, with considerable

differences between the various phases of the bores. Furthermore, the strength and structure of the observed internal bores are dependent on a combination of low-frequency upwelling wind forcing, offshore stratification, and the local bathymetric slope.

Additionally, high resolution observations of rank-ordered packets of NLIWs in northern Monterey Bay, CA are presented. These NLIWs are some of the largest internal waves ever observed on the continental shelf. They are surmised to be generated at an upwelling front, modified by the presence of a strong background shear, and shown to be unstable to shear instabilities with large overturns and elevated turbulent mixing in the stratified interior. Finally, this dissertation examines the applicability of similarity scaling of turbulence spectra and cospectra in a shallow tidal flow in Elkhorn Slough, CA. Implications of the various findings, including biological processes, ecosystem health, numerical models, and nearshore hypoxia risk are discussed.

Acknowledgements

The path to the Ph.D. has been quite the journey down a very long and trying road. Yet, if I were to travel back in time and be presented with the choice of doing the Ph.D., or doing something else, I would pick doing the Ph.D. 100 times out of 100 times; that is a certainty. This incredible journey would not have been possible without a host of mentors, colleagues, friends, and family.

I would first like to thank my principal adviser, Stephen Monismith, who is without a doubt one of the smartest people I know. I remember my first day meeting with him when I arrived at Stanford: he handed me an external hard drive with about a hundred papers on turbulence, a dataset from Elkhorn Slough, and a few research questions to pursue. This is exactly the challenge that I sought. He challenged me in ways that I could have never imagined, and he allowed me the independence to pursue many of my own research questions. Moreover, he afforded me the opportunity to quite literally travel the world for various field expeditions and conferences. I am appreciative of these adventures, especially the underwater ones. I will never forget his unwavering support and loyalty in times of need, as well as all of those breakfasts at First Awakenings after a day of diving at Hopkins Marine Station.

I would also like to thank my unofficial co-adviser, Brock Woodson. He has been the guiding hand throughout my Ph.D., even after he left for Georgia, and has been such an incredible mentor and friend. Beyond teaching me how to successfully run a field campaign and dig deep into a dataset, he taught me other invaluable skills on how to conduct research, coordinate collaborative efforts, and optimize the field

research experience. I will never forget some of the adventures we had in Monterey Bay.

I would also like to thank the most cheerful person that I know at Stanford, Jeffrey Koseff. His exuberance and enthusiasm for science and fluid mechanics is contagious, and he is able to inject life into any topic, especially stratified turbulence. More than anything, I appreciate how much he cares about students; I aspire to emulate this. I will never forget his passion in life, especially when he was playing Ping-Pong against me and Robby Zeller at Ocean Sciences in Utah.

Oliver Fringer is definitely one of the most curious, and also humorous, people that I know at Stanford. Nobody else gets more excited about “cool” and interesting physics, especially internal waves, than him. I always look forward to chatting with him about fluid mechanics, or even life, because of his easygoing personality, sarcastic humor, and goofy laugh. I will never forget our time together in Italy, especially those long “discussions” with the Italians.

I would also like to thank Leif Thomas. He is one of the sharpest people that I know, and I am still in awe that he went through almost every GFD derivation by memory and without notes. I appreciate his laid-back personality and willingness to always chat physics with me in his office. He instilled in me a love of ocean physics, and I will never forget his courses and laboratory demonstrations.

Derek Fong is the heart of EFML and in many ways the glue that keeps it all together. Much of my educational experience has been in the classroom with him as a teacher; I aim to model my teaching style after him. More than being a tremendous teacher, he has been a great mentor and friend. I appreciate that his door is always

open for me to stop by and ask a question about ADCPs, or to chat about life. I will never forget one of the first discussions outside of the classroom that we had while on an early morning cruise through the Puget Sound on the way to the Snohomish River Estuary. Also, watch out for the Toce River sharks!

A special thanks goes out to my colleague, Marek Stastna. He has been incredibly supportive, full of ideas, and uplifting to work with. I have learned a tremendous amount about weakly and fully nonlinear wave theory through our collaborations. Even though we have never met in person, I do know that he is the type of professor that I want to be.

In my mind, EFML would not be EFML without the EFML Nerds. The Nerds have been such amazing labmates and friends, and most of my fieldwork would not have been possible without their help and dive support. I could write an entire chapter on the friendships I have made, advice I have received, and memories I have created with all of them. I am especially grateful for the opportunity to work with my best friend, Ryan Moniz, for 4.5 years of my Ph.D. It has been a fun ride, Ry-guy! I would also like to thank Jill Filice, Yusong Rogers, and Bill Sabala, all of whom made my life a whole lot easier.

Finally, I would like to thank my family and loved ones. I met some of my closest friends while a graduate student at Stanford. My parents and siblings have been incredibly supportive throughout this whole process, especially my older, and sometimes wiser, brother. We are the Brews. Last, and certainly not least, I would like to thank Allie “Otter.” She has supported me every step of the way over these past 2.5

years. I love you more than I love fluid mechanics and the ocean, and I cannot wait to explore the world with you.

Table of Contents

List of Tables

List of Figures

Chapter 1: Introduction

1.1: Background and Motivation

The nearshore coastal environment, defined here as the innermost portion of the continental shelf and extending from the shoreline to several kilometers offshore, is widely considered to be one of the most productive and ecologically important parts of the ocean [*Pauly and Christensen*, 1995; *Mann*, 2000]. The nearshore environment is home to a number of economically and ecologically important biota such as various shellfishes (lobsters, oysters, abalone, crabs, etc.), fishes (cod, rockfishes, etc.), and marine mammals such as harbor seals and the threatened California sea otter. The nearshore also supports some of the world's largest giant kelp forests, submerged sea grass patches, mangrove habitats, and coral reef communities, all of which are critical habitats and nurseries for nearshore ecological communities and fisheries worldwide, as well as of considerable economic value. Not surprisingly, the nearshore coastal environment encompasses many Marine Protected Areas (MPAs) and National Marine Sanctuaries, which are intended to promote ecosystem health and conservation efforts.

The nearshore is also a complex environment from a physical standpoint, due to the combined effects of and interaction between regional scale wind forcing and upwelling, local diurnal sea breezes, complex and highly variable topography, surface waves, spatiotemporally varying stratification and tidal currents, internal waves and bores, upwelling fronts, etc. [*Lentz et al.*, 2008; *Kirinich et al.*, 2009; *Lentz and Fewings*, 2012; *Woodson et al*., 2013]. In many nearshore locations, the physics are dominated by the often irregular occurrence of nonlinear internal waves (NLIWs) that

frequently appear more bore-like than wave-like [e.g., *Scotti and Pineda*, 2004; *Leichter et al.*, 1996; *Nam and Send*, 2011; *Davis and Monismith*, 2011; *Walter et al*., 2012]. These nearshore NLIWs have significant implications for the cross-shelf exchange and transport of scalars such as nutrients, contaminants, larvae, etc. [*Wolanski and Pickard*, 1983; *Leichter et al.*, 1996; *Boehm et al.*, 2002; *Pineda*, 1991, 1994, 1995, 1999]; turbulent dissipation and diapycnal mixing [*Venayagamoorthy and Fringer*, 2007; *Nam and Send*, 2011; *Davis and Monismith*, 2011; *Walter et al.*, 2012]; and the development of hypoxia [*Booth et al*., 2012]. Despite a growing body of literature on the subject [cf. *Leichter et al*., 1996; *Klymak and Moum*, 2003; *Scotti and Pineda*, 2004; *Shroyer et al*., 2008; *Nam and Send*, 2011; *Davis and Monismith*, 2011; *Woodson et al*., 2011; *Walter et al*., 2012; *Wong et al*., 2012; *Suanda*, 2014; *Suanda et al*., 2014], many open questions still remain with respect to the evolution, fate, and impact of NLIWs in the nearshore environment.

Internal gravity waves (i.e., internal and/or baroclinic tides) are generated in stably stratified waters when surface (barotropic) tides interact with variable bottom topography [e.g., *Garrett and Kunze*, 2007]. Energy is transferred from the barotropic tide into internal motions that propagate along density layers and away from local generation sites. Numerical studies of internal wave shoaling [e.g., *Venayagamoorthy and Fringer*, 2007] have identified the formation of upslope-surging internal bores (boluses) at shelf breaks that drive dense water masses across the adjacent shelf. As internal waves propagate into shallow water, they shoal and steepen, become highly nonlinear, and eventually break due to instabilities. This process is somewhat analogous to surface waves breaking on a beach; hence, the nearshore coastal ocean

can be thought of as the “swash zone,” or the “internal beach”, for larger-scale internal wave fields on the continental shelf.

More specifically, in shallow waters, nonlinear internal waves of depression shoal along a sloping bottom and morph into waves of elevation near the point where the pycnocline is located at the midpoint between the surface and the bottom [*Grimshaw et al.*, 1999; *Scotti and Pineda*, 2004; *Shroyer et al.*, 2009]. These bottom-trapped internal waves of elevation are characterized by upslope surging fronts, followed by dense, subpycnocline waters [cf. *Nam and Send*, 2011]. They have also been referred to as elevation-type solitary waves with trapped (cold) cores, in addition to solibores to emphasize the combination of wave-like and bore-like properties [e.g., *Klymak and Moum*, 2003; *Hosegood and van Haren*, 2004; *Scotti and Pineda*, 2004; *Nam and Send*, 2011]. In this work, the nonlinear cold water surges will be referred to as bores; this term emphasizes the shock-like nature of the change, and is used by analogy to describe discontinuous changes in depth in unsteady shallow water free surface flows [*Stoker*, 1948].

Internal waves and bores on the continental shelf are well-studied in theoretical, numerical, and experimental fluid mechanics (see *Lamb* [2013] and the sources therein). Yet, the majority of the aforementioned numerical and laboratory studies (see *Lamb* [2013]) have necessarily focused on isolated processes with simplified, idealized setups. Likewise, field studies have concentrated mainly on deeper shelf waters (50+ m depths; cf. Table 1 of *Alford et al*. [2012]), while the ultimate fate of NLIWs and bores in shallow regions (~20 m, i.e., the nearshore) has been mainly speculative. Internal bores and/or bore-like features (i.e., NLIWs in

shallow water) are common along continental margins: the Florida Strait [*Leichter et al*., 1996], New England shelf [*Colosi et al*., 2001], California Bight [*Pineda*, 1991, 1994, 1995; *Nam and Send*, 2011], Monterey Submarine Canyon [*Shea and Broenkow*, 1982; *Breaker and Broenkow*, 1994; *Storlazzi et al*., 2003], etc. Yet, detailed observations of NLIWs and internal bores in shallow waters are rare, partly due to the lack of measurements with sufficiently high temporal and spatial resolution to accurately resolve the dynamics. Here, we take advantage of detailed measurements of NLIWs and bores to better understand how these features affect nearshore dynamics and the consequent impacts on nearshore coastal ecosystems.

1.2: Research Topics

The primary objective of this dissertation is to better understand the evolution, fate, and impact of NLIWs and internal bores in the nearshore coastal environment.

This dissertation aims to identify the general characteristics of these features and their effect on nearshore circulation, temperature structure, and mixing dynamics. Biological and ecological implications are also considered and discussed. Several observational field studies were conducted in Monterey Bay, CA using a wide variety of instruments and measurement techniques, such as oceanographic mooring arrays and an underwater turbulence flux tower. Experimental setups are described in each respective chapter.

Monterey Bay, CA is located along the eastern Pacific Ocean and central California coast, and is part of the highly productive California Current Large Marine Ecosystem (CCLME) (Figure 1.1). Monterey Bay is characterized by a semi-enclosed

embayment, covering an area of approximately 550 km^2, and features one of the largest submarine canyons on the west coast of the United States (Figure 1.1). Large amplitude internal waves are a common feature in and around the canyon, where isopycnal displacements often reach hundreds of meters [e.g., *Breaker and Broenkow*, 1994; *Petruncio et al.*, 1998; *Kunze et al.*, 2002], as well as on the shelf and in the nearshore environment [*Storlazzi et al.*, 2003; *Woodson et al*., 2011; *Walter et al*., 2012]. Additionally, numerical models have documented both the local generation of internal tides, as well as the interaction of locally and remotely generated internal tides, at the M_2 tidal period near the shelf edge and inside the canyon [*Carter*, 2010; *Kang and Fringer*, 2012]. Monterey Bay also harbors an extremely large ecological diversity including some of the west coast's largest kelp (*Macrocystis pyrifera*) forests, MPAs, sizeable commercial fisheries, and large eco-tourism industries [*Kildow and Colgan*, 2005; *Raheem et al.*, 2011]. Furthermore, the protected coastline of southern Monterey Bay, and the location of Hopkins Marine Station (Figure 1.1), is historically one of the most ecologically studied shorelines on the west coast of the United States. These facets make Monterey Bay an ideal location to study the evolution, fate, and impact of NLIWs and internal bores in the nearshore coastal environment. Other topics addressed in this work are highlighted below.

Turbulent mixing by NLIWs and nearshore internal bores, and stratified turbulence dynamics.

Continental shelves are thought to be an important, and highly variable, contributor to the dissipation of turbulent kinetic energy in the ocean [*Munk and*

Wusch, 1998; *Carter et al.*, 2005]. Likewise, the irreversible mixing of mass and momentum is often linked to the cascade of energy at large-scales through an internal wave continuum to small-scale turbulence [*Kunze et al.*, 2002; *Klymak and Moum*, 2007a, 2007b]. Estimates of turbulent mixing in coastal areas are important for quantifying the vertical mixing of tracers, with significant biological and ecological ramifications [e.g., *Boehm et al.*, 2002; *Leichter et al.*, 1996; *Pineda*, 1994]. Specifically, diapycnal mixing affects many ecologically important processes such as nutrient cycling, primary production, hypoxia development, and the mixing of tracers such as pollutants from sewage outfalls [e.g., *Wolanski and Pickard*, 1983; *Leichter et al.*, 1996; *Boehm et al.*, 2002; *Chan et al.*, 2008]. This work aims to better understand the evolution of turbulence in the presence of NLIWs and nearshore internal bores. The ability to measure, and potentially parameterize, turbulent dissipation and mixing by these features would prove to be extremely helpful in coastal ecosystem management.

While the dynamics of stratified turbulence have been investigated widely in both the laboratory [cf. *Itsweire et al.*, 1986; *Ivey and Imberger*, 1991; etc.] and numerical simulations [cf. *Holt et al.*, 1992; *Shih et al.*, 2005; etc.], comprehensive field measurements of stratified turbulence on the shelf are limited (see *Davis and Monismith* [2011] and the references therein). This work seeks to characterize the fundamental dynamics of stratified turbulence in the nearshore coastal environment using high-frequency turbulence measurements collected with an underwater turbulence flux tower.

Prediction of nearshore internal bores: the effect of wind-driven upwelling cycles, offshore stratification, and bottom bathymetry.

The lifecycle and ultimate fate of internal waves propagating from the shelf to the nearshore environment is highly variable due to a dynamic environment with changing bathymetry, spatially and temporally evolving stratification, tidal and wind forcing, and coastal upwelling/downwelling influences [*Pineda and Lopez*, 2002; *Davis and Monismith*, 2011; *Lamb*, 2013 and the references therein]. Further field observations are needed to assess the influence of changing environmental conditions on the offshore to onshore (shelf to nearshore) translation of internal wave/tide fields in the coastal environment. For instance, in the Southern California Bight, *Pineda and Lopez* [2002] hypothesized that the observed nearshore internal bores were dependent on low-frequency wind forcing (e.g., upwelling/relaxation time scales) through the modification of the offshore stratification and thermocline depth. Furthermore, *Boegman et al*. [2005] found that breaking internal waves were strongly dependent on the ratio of the local boundary slope to the internal wave slope (i.e., internal Iribarren number). This dissertation seeks to address how wind forcing, offshore stratification, and bottom bathymetry influence the strength and structure of nearshore internal bores.

Cross-shelf exchange and oxygen variability due to NLIWs and nearshore internal bores.

NLIWs have been linked to the cross-shelf exchange and transport of nutrients [*Leichter et al.*, 1996; *Boehm et al.*, 2002; *Wong et al*., 2012], larvae [*Pineda*, 1991,

1994, 1995, 1999], and low dissolved oxygen (DO)/pH waters [*Booth et al*., 2012]. Indeed, NLIWs and bores may be an important mechanism whereby deeper offshore waters, which are typically low in DO and pH [e.g., *Checkley and Barth*, 2009], are supplied to the nearshore environment [cf. *Booth et al*., 2012]. While it is well established that seasonal upwelling cycles contribute to oxygen variability and hypoxic events in nearshore waters, the role of other physical processes, such as NLIWs and internal bores, is less understood [*Chan et al*., 2008]. In particular, *Booth et al*. [2012] recorded regular intrusions of hypoxic water in the nearshore of Monterey Bay, CA, and linked the intrusions to internal bores. This dissertation seeks to understand how NLIWs and internal bores affect cross-shelf exchange, as well as nearshore DO variability and low DO events.

1.3: Dissertation Outline

This dissertation is organized into six chapters and a supplementary Appendix. Chapter 1 provides a background and motivation for the research, and outlines the major research objectives. Chapters 2 – 5 are presented as early and/or completed drafts for peer-reviewed journals. Accordingly, each of these chapters contains a separate introduction and review of the relevant literature, experimental setup and methods, results, discussion, and conclusion section. Chapter 2 examines the general characteristics of nearshore internal bores in southern Monterey Bay. This chapter was published in the *Journal of Geophysical Research – Oceans* [*Walter et al*., 2012]. Chapter 3 investigates how regional scale upwelling wind cycles and changing offshore stratification influence nearshore internal bores and oxygen variability. This

chapter was recently published in the *Journal of Geophysical Research – Oceans* [*Walter et al*., 2014]. Chapter 4 explores the evolution of turbulence in the presence of internal bores and characterizes the dynamics of stratified turbulence in the nearshore coastal environment. This chapter is prepared as a draft for future journal submission. Chapter 5 presents detailed observations of highly nonlinear internal waves at a coastal upwelling front and examines their potential for turbulent mixing. This chapter is prepared as draft for future journal submission. Chapter 6 highlights the findings and discusses avenues for future research. Appendix A considers the applicability of similarity scaling of turbulence spectra and cospectra in a shallow tidal flow in Elkhorn Slough, CA. This research was published in the *Journal of Geophysical Research – Oceans* [*Walter et al*., 2011]. Appendix B contains additional details about the Monterey Tower Node (MOTOWN) experiments.

1.4: Figures

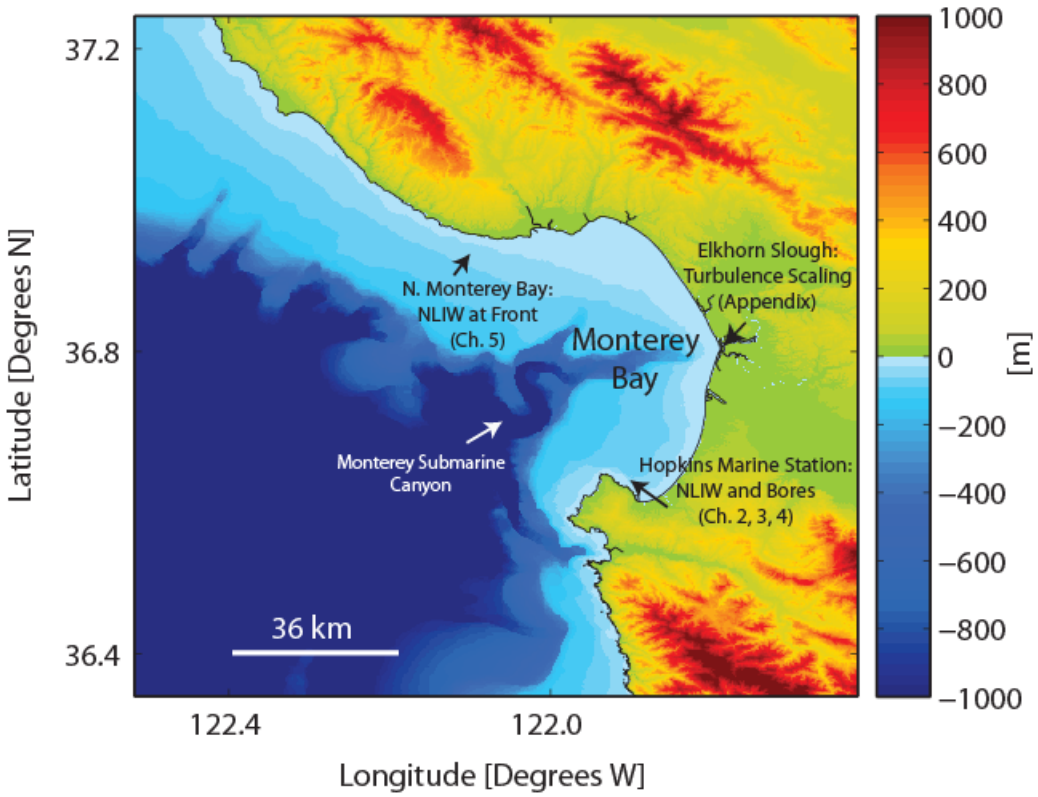

Figure 1.1: Bathymetry and topography of the Monterey Bay, CA region. Also highlighted are the specific study sites and topics covered in this dissertation.

Chapter 2: Nearshore internal bores and turbulent mixing in southern Monterey Bay

This chapter is a reproduction of the work published in the *Journal of Geophysical Research – Oceans*. As the main author of the work, I made the major contributions to the research and writing. Co-authors include C. Brock Woodson[1], Robert S. Arthur[1], Oliver B. Fringer[1], and Stephen G. Monismith[1].

DOI: 10.1029/2012JC008115

[1]Environmental Fluid Mechanics Laboratory, Stanford University, Stanford, CA, USA

2.1: Abstract

We observed transient stratification and mixing events associated with nearshore internal bores in southern Monterey Bay using an array of instruments with high spatial and temporal resolution. The arrival of the bores is characterized by surging masses of dense (cold) water that tend to stratify the water column. The bore is followed by a gradual drop in the temperature throughout the water column over several hours (defined here as the bore period) until a sharp warm-front relaxation, followed by high frequency temperature fluctuations, returns the column back to nearly its original state (defined here as the mixing period). Mixing periods revealed increased temperature variance at high frequencies ($\omega > \overline{N}$), as well as a greater percentage of events where dynamic instabilities may be present ($Ri < 0.25$), suggesting active mixing of the stratified water column. Turbulent dissipation rates in the stratified interior during the mixing period, estimated using the technique of isopycnal slope spectra, revealed mean values the same order of magnitude as near-bed bottom-generated turbulence. Observations indicate that local shear-produced turbulent kinetic energy by the warm front relaxations dominates mixing in the stratified interior. The non-canonical nature of these bore and relaxation events is also investigated with a numerical model, and the dynamics are shown to depend on the internal Iribarren number. Our results suggest that nearshore internal bores interacting with local bathymetry dramatically alter local dynamics and mixing in the nearshore with important ecological implications.

2.2: Introduction

Energetic nonlinear internal waves are ubiquitous features in the nearshore coastal ocean, defined here as the innermost portion of the continental shelf extending from the shoreline to about 2 km offshore, where internal waves often appear bore-like rather than wave-like [e.g., *Pineda*, 1994; *Leichter et al.*, 1996; *Storlazzi et al.*, 2003; *Scotti and Pineda*, 2004; *Nam and Send*, 2011; *Davis and Monismith*, 2011; *Wong et al.*, 2012]. Numerical studies of internal wave shoaling [e.g., *Venayagamoorthy and Fringer*, 2007] have identified the formation of internal bores (boluses) that act to drive dense water across the adjacent shelf where they can impact coastal ecosystems. In effect, the nearshore coastal ocean can be thought of as the "swash zone" for larger-scale internal wave fields on the continental shelf. From a practical standpoint, these flows are observed to be important for cross-shelf transport and exchange of nutrients, sediments, and contaminants [*Wolanski and Pickard*, 1983; *Leichter et al.*, 1996; *Boehm et al.*, 2002]; larval transport [*Pineda*, 1991, 1994, 1995, 1999]; and turbulent mixing and dissipation [*Venayagamoorthy and Fringer*, 2007; *Nam and Send*, 2011].

In shallow waters, as nonlinear waves of depression shoal along a sloping bottom, they morph into waves of elevation near the point where the pycnocline is located at the midpoint between the surface and the bottom [*Grimshaw et al.*, 1999; *Scotti and Pineda*, 2004; *Shroyer et al.*, 2009]. These bottom-trapped internal waves of elevation are characterized by upslope surging fronts, followed by dense (cold) waters [cf. *Nam and Send*, 2011]. They have also been referred to as elevation-type solitary waves with trapped (cold) cores, as well as solibores to emphasize the combination of wave-like and bore-like properties [e.g., *Klymak and Moum*, 2003;

Hosegood and van Haren, 2004; *Scotti and Pineda*, 2004; *Nam and Send*, 2011]. Here, we will refer to nonlinear cold water surges as bores. This term emphasizes the shock-like nature of the change, and is used by analogy to describe discontinuous changes in depth in unsteady shallow water free surface flows [*Stoker*, 1948].

The typical (referred to here as canonical) bore on a sloping shelf has an initial steep face (often called a front) that is responsible for the bulk of the temperature drop associated with the bore event. This front is followed by a gradual tapered warming where the temperature returns to roughly its original state slowly over several hours [e.g., *Leichter et al.*, 1996; *Hosegood and van Haren*, 2004]. In this case, instabilities and mixing associated with the bore event are often confined to the initial propagation of the core and trailing internal waves. For the canonical case, no strong warm front is observed.

The bore events observed in this study do not follow the canonical description and are defined here as non-canonical. While the initial bore still provides a sharp drop in temperature, the temperature continues to decrease slowly over several hours. This cooling is followed by an abrupt warm front and high frequency fluctuations that return the water column to roughly its original temperature. The warm front can be viewed as the relaxation of the bores downslope [e.g., *Pineda*, 1994]. As the cold bores propagate onshore into warmer water, a front is formed between the cold bore water and the displaced warm water. Eventually the bore, like swash on a beach, comes to rest, and the currents reverse, as the cold waters (followed by displaced warm waters) rush back offshore near the bottom [*Pineda*, 1994]. As we will show,

the canonical versus non-canonical nature of these bores is dependent on local bathymetry and internal wave properties.

The first objective of this study is to understand the general characteristics and fate of bores in the nearshore environment of southern Monterey Bay. Internal bores are common along many continental margins [*Shea and Broenkow*, 1982; *Pineda*, 1991, 1994, 1995, 1999; *Leichter et al.*, 1996; *Colosi et al.*, 2001; *Klymak and Moum, 2003; Storlazzi et al.*, 2003; *Hosegood and van Haren*, 2004; *Nam and Send*, 2011]. Yet, detailed observations of internal bores in the nearshore are rare, mainly due to the lack of measurements with sufficiently high temporal and spatial resolution to adequately resolve the dynamics [cf., *Scotti and Pineda*, 2004; *Nam and Send*, 2011]. Here, we take advantage of detailed measurements of cold bores in southern Monterey Bay in order to better understand their dynamics and effect on the nearshore coastal environment.

The second objective is to quantify local turbulent dissipation and mixing by internal bores in the nearshore environment of southern Monterey Bay. Continental shelves and the nearshore environment are thought to be an important, but highly variable, contributor to the dissipation of turbulent kinetic energy (TKE) in the ocean [*Carter et al.*, 2005]. Likewise, the irreversible mixing of momentum is often linked to the cascade of energy at large-scales through an internal wave continuum to small-scale turbulence [*Kunze et al.*, 2002; *Klymak and Moum*, 2007a, 2007b]. Consequently, shoaling internal waves provide a significant energy transfer pathway, where instabilities and breaking are directly linked to turbulent dissipation. Recent studies have estimated turbulent dissipation rates in stratified flows with success using

horizontal gradients of vertical isotherm displacements, or isopycnal slopes [*Klymak and Moum*, 2007a, 2007b; *Woodson et al.*, 2011]. Here, we use the isopycnal slope spectra method to assess turbulent dissipation and mixing due to localized shear-induced turbulence generated by the observed bore events.

The overall goal of this study is to examine how internal bores affect nearshore circulation dynamics, local turbulent mixing, and the consequent impacts on nearshore coastal ecosystems. Here, we focus on local water column dynamics and mixing in the nearshore environment of southern Monterey Bay. Regional forcing and generation mechanisms, as well as energetics, will be investigated in future studies. In section 2.3, we introduce the field site, sampling strategy, and data processing methods. Section 2.4 describes the general features of the bores and warm front relaxations including propagation characteristics, effects on the density field, and detailed structure. This is followed by a quantitative comparison of the temperature variance and the potential for turbulent mixing between the bore and relaxation events. Finally, we employ the technique of isopycnal slope spectra to estimate turbulent dissipation rates associated with the relaxation events. Section 2.5 provides a discussion of the results including an examination of the non-canonical nature of the bores using a numerical model, as well as an examination of turbulence in the stratified interior and nearshore environment. Section 2.6 summarizes the findings and highlights potential implications.

2.3: Site Description and Methods

2.3.1: Experimental Setup

Monterey Bay, located along the central coast of California, is a semi-enclosed embayment and features one of the largest submarine canyons on the west coast of the United States (Figure 2.1a) [*Carter et al.*, 2005]. Large amplitude internal waves are a common feature in and around the canyon, with isopycnal displacements reaching hundreds of meters [e.g., *Breaker and Broenkow*, 1994; *Petruncio et al.*, 1998; *Kunze et al.*, 2002]. Currents are dominated by the M_2 (~12.42 h period) tidal component with barotropic velocities reaching up to 0.2 m/s on the shelf [*Breaker and Broenkow*, 1994], although baroclinic tidal velocities are important near the head of the Monterey Canyon [*Carter,* 2010]. The southern portion of the bay, which is the location of this study, is protected from dominant swell and not significantly influenced by diurnal winds so that the currents are not strongly correlated with surface wave and wind forcing [*Woodson*, 2013].

Moored instrument arrays were deployed from 1 to 16 May 2010 in southern Monterey Bay in order to capture internal bore activity. Moorings were arranged in approximately a right triangle offshore of Hopkins Marine Station (HMS – Stanford University, Pacific Grove, CA) located in the southern end of the bay and just inside of the Monterey Peninsula (Figure 2.1b). The main/center (MN) and along-shore (AS) moorings were deployed on the 15 m isobath about 100 m apart, while the cross-shore (XS) mooring was placed approximately 100 m offshore of MN near the 20 m isobath (Figure 1b). Each mooring was equipped with a dense vertical arrangement of SBE39 and SBE56 temperature loggers ($n \geq 6$ at each mooring) throughout the water column.

MN and XS each had a bottom-mounted SBE 37 conductivity-temperature-depth (CTD) logger. An RDI 1200 kHz Workhorse acoustic Doppler current profiler (ADCP) was deployed at the MN mooring sampling in fast-ping Mode 12 with 0.25 m vertical bin spacing. The ADCP was leveled by divers in order to minimize instrument tilt errors.

In order to capture the high temporal variability associated with the bores and estimate dissipation rates using isopycnal slope spectra, the temperature loggers and ADCP at the MN mooring were programmed to maximize the sampling frequency while maintaining enough battery life to capture a sufficient number of bore and relaxation events (10 to 16 May 2010, n = 7 events). Details of mooring configurations, sampling rates, and periods of deployment are given in Table 2.1. In what follows, detailed analyses of individual bore events (n = 7) presented will be during the one-week sampling period when all three moorings collected data (10 to 16 May 2010), while general characteristics of the bore arrival will include results over the entire study period (1 to 16 May 2010). Longer time series collected in this region as part of PISCO (Partnership for Interdisciplinary Studies of Coastal Oceans), albeit with less temporal and spatial resolution than the current study, indicate that these results are representative of longer time scales [*Woodson*, 2013].

2.3.2: Data Analysis

2.3.2.1: Data Processing

Velocity measurements from the ADCP were rotated into cross-shore (u), along-shore (v), and vertical (w) velocity components using principal axes obtained from an ADCP associated with a long term PISCO mooring at the site (Figure 2.1b).

Here, *u* velocities are defined as positive onshore, *v* velocities positive along-shore headed into the bay (~southeastward), and *w* velocities positive upward (Figure 2.1b). During the summer upwelling season, salinity variations in Monterey Bay are minimal so that density is largely controlled by temperature [e.g., *Woodson et al.*, 2009, 2011]. Analysis of the bottom-mounted CTD data showed that small changes in salinity varied linearly with temperature (R^2 = 0.93). Therefore, densities at all depths were calculated using the observed temperature and the derived linear relationship from the CTD measurements for salinity as a function of temperature.

Spectral calculations are performed using the fast Fourier transform (FFT). For the time series of interest, the time-mean was removed and the series was linearly detrended. Next, the data were split into smaller segments, which were then zero padded to achieve the next power of two for the FFT and to increase frequency resolution. The choice of window length signified a compromise between the increased number of degrees of freedom (DOF) for each spectral estimate, decreased frequency resolution, and length of the original record. Each segment was multiplied by a Hamming window with 50% overlap to decrease spectral leakage. Spectral densities were computed using the FFT, and segments were block averaged. Confidence intervals (95%) were calculated using a chi-square variable analysis and the "equivalent" number of DOF [*Emery and Thompson*, 2004].

2.3.2.2: General Characteristics and Propagation

The triangular configuration of the moorings was utilized to calculate the speed (c) and direction of propagation (Θ) of the bore features following the analysis of *Pineda* [1999] and *Woodson et al.* [2011]. Phase speeds and directions were

determined with errors less than 1%, based on the spatial design and the sampling frequency of the instruments [e.g., *Lee*, 1961; *Woodson et al.*, 2011]. Estimates of the bore and warm front relaxation speeds were determined using the 4 meter above bottom (mab) temperature logger at all moorings. Similar phase speeds were found using loggers at other heights. Bores were defined as large, step-like drops in the temperature field (ΔT ~ -0.5° C, cooling in ~ 1 min), throughout the lower portion (0 to 10 mab) of the water column. Likewise, relaxations of the bores were classified as even larger step-like increases in the temperature field ($\Delta T \geq 1°$ C, warming in ~ 5 min) throughout the water column (0 to 12 mab). Ambient currents were taken into account by removing the depth-averaged (barotropic) current in the direction of the bore/relaxation (U_{depth}) for an hour prior to the arrival of the bore/front. Thus, the actual propagation speed of the bore, $c = c_{obs} - U_{depth}$, was found using the observed propagation speed (c_{obs}) in the presence of a barotropic current (U_{depth}).

2.3.2.3: Isopycnal Slope Spectra and Turbulent Dissipation

Isopycnal slope spectra were utilized to predict dissipation of TKE (ε). Isotherm displacements (ζ) were calculated for several hours following the passage of the bore relaxations (warm fronts) as,

$$\zeta = z - Z_o(\rho), \tag{2.1}$$

where z is the thermistor depth and $Z_o(\rho)$ is the depth at which the observed density (ρ) is equal to the reference density profile [*Klymak and Moum*, 2007a, 2007b]. Reference density profiles were taken near the arrival of the warm fronts where the density field did not change significantly in time and spatial resolution was increased

by linearly interpolating between adjacent loggers. A Taylor-advection scheme was employed to convert time measurements of ζ into the spatial domain using,

$$x = c_{obs} t \,. \tag{2.2}$$

Horizontal gradients of ζ were computed to yield the isopycnal slope (ζ_x). Time series of ζ_x were then FFTed as outlined above to produce isopycnal slope spectra (ϕ_{ζ_x}). These spectra were lightly smoothed using a 9-point geometric mean filter, which had no significant effect on dissipation estimates.

The turbulence subrange consists of both the inertial-convective and inertial-diffusive subranges,

$$\phi_{\zeta_x}^{Turb} = 4\pi \frac{\Gamma < \varepsilon >}{< N^2 >} \left[C_T < \varepsilon >^{-1/3} (2\pi k_x)^{1/3} + q\nu^{1/2} < \varepsilon >^{-1/2} (2\pi k_x) \right], \tag{2.3}$$

where $C_T \approx 0.44$ and $q \approx 2.3$ are constants, $<N^2>$ is the time-mean of the average vertical buoyancy frequency squared over the relaxation event with $N^2 = -\frac{g}{\rho_o}\frac{\partial \rho}{\partial z}$, k_x is the horizontal wavenumber, $\Gamma = 0.2$ is the assumed mixing efficiency, $<\varepsilon>$ is the average dissipation following the passage of the warm front, and ν is the kinematic viscosity of seawater [*Klymak and Moum*, 2007a, 2007b; *Woodson et al.*, 2011]. It is important to note here that $\Gamma = 0.2$ was taken to be a constant based on the turbulence activity numbers ($\varepsilon/\nu N^2$, Section 4.2) found in this study [*Shih et al.*, 2005]. $<\varepsilon>$ was estimated by fitting the observed ϕ_{ζ_x} to Equation (2.3) in the turbulence subrange ($0.04 < k_x < 0.3$ cpm) and using a non-linear least squares regression to find $<\varepsilon>$ [*Woodson et al.*, 2011]. Confidence limits (95%) for $<\varepsilon>$ were found by fitting the upper and lower 95% confidence intervals of ϕ_{ζ_x} to Equation (2.3). Sensitivity of the

above procedure to c_{obs}, $\langle N^2 \rangle$, and Γ was estimated by varying the three parameters and looking at the ratio of $\langle \varepsilon \rangle / \langle \varepsilon_o \rangle$ for each parameter, where $\langle \varepsilon_o \rangle$ is the average dissipation calculated from the originally observed parameters.

2.4: Results

2.4.1: General Characteristics and Propagation

A time series of density measured at the MN mooring during the week-long period (10 to 16 May 2010; Figure 2.2) clearly shows repeated episodes of energetic cold (bores) and warm (relaxations) water intrusions propagating through the array. The observed bores are non-canonical. The cold water events (bores) take the form of sudden changes in the density field, especially in the bottom portion of the water column, where the waters change quickly from nearly homogeneous to stratified ($\Delta T \sim$ -0.5° C, cooling, ~ 1 min for ΔT). Following the arrival of the initial bore, a series of small amplitude internal waves (10 - 20 min period) are observed, as the temperature gradually decreases over several hours (from hereafter referred to as the bore period). The water column structure again changes dramatically at the end of the bore period when the waters suddenly warm ($\Delta T \geq 1°$ C, warming, ~ 5 min for ΔT), a process we refer to as the warm front relaxation since it returns the water column to nearly its original state. Following the sharp front, high-frequency fluctuations (<1 min period) are sustained over several hours and erode the stratification until the water column returns to being well mixed (from hereafter referred to as the mixing period).

The propagation speed of the bores (c) is compared to the theoretical propagation speed of a linear, hydrostatic, first-mode internal wave [e.g., *Venayagamoorthy and Fringer*, 2007],

$$c_1 = \frac{ND}{\pi}, \tag{2.4}$$

where D is the water depth and N is the maximum of the ten-minute averaged buoyancy frequency following the bore arrival (Figure 2.2c). Observations deviated slightly from linear theory, likely due to the nonlinear signature of the bores (Fr ~ 0.7). Phase speeds estimated using both normal mode analysis and solutions to the Taylor-Goldstein equations [*Smyth et al.*, 2010] were extremely erratic due to the rapidly varying density field. The observed median propagation speed of the bores and relaxations (not shown) was 0.12 and 0.l6 m/s, respectively. Directionality of the bores as they passed through the moorings indicates a median heading of 195.4° (range of 176.2° to 201.76°) from true north, which is inside the bay and appearing to come from near the canyon mouth (Figure 2.1a). Conversely, the relaxations were modulated by the local along-shore barotropic currents and had a median heading of 153.8° (range of 136.0° to 154.3°; Figure 2.1a), which is roughly along-shelf headed into the bay.

Analysis of the longer time record (1 to 16 May 2010) of densities from the XS mooring was performed to elucidate the timing and arrival of the bores and relaxations with respect to the local tidal phase. Tides in the bay are mixed semi-diurnal and dominated by the M_2 tidal component [e.g., *Breaker and Broenkow*, 1994; Figure 2a]. Tidal phasing was referenced with respect to the lowest lows on 1 May and 10 May

2010 with a diurnal period (~24.82 h period). Two reference dates were used because the interaction of the mixed tidal frequencies (M_2 and K_1) in the transition from neap to spring tide causes a slight phase shift so that the lowest low changes. The time between the bore and relaxation (Δt ~ bore period) arrival was also calculated. The phasing with respect to tidal height of the bore and relaxation, respectively, as a function of Δt shows no apparent pattern between the timing of arrival with respect to the local tidal phase, as the data is scattered about all phases (Figure 2.2d). Likewise, there is a broad range of times between the bore and the relaxation (Δt ~ 6 – 20 h), again with no clear link to the phase of the local tides. Further examination of the record indicates no clear pattern in the arrival of the bores and/or relaxations, or Δt, with respect to spring-neap variability of the tide (not shown). These results are expected given that the observed propagation speeds may have been comparable to spatially and temporally ambient currents throughout the bay. Two additional processes may potentially modulate both the timing and duration of the bore-relaxation events. First, regional scale upwelling acts to uplift the thermocline to depths that may allow for observation of these events in the nearshore. Secondly, internal seiching within Monterey Bay may also contribute to variability of bore-relaxation events on time scales of 5-10 days.

The importance of the bore and relaxation events to the overall local velocity field is shown in Figure 2.3. While depth-averaged currents are structured in a way that resembles a boundary layer profile, empirical orthogonal function (EOF) analysis (not shown) suggests that this flow is much more sheared than would be predicted given the local sandy bottom, even accounting for the effects of surface waves. The

along-shore flow is consistently directed out of the bay and to the northwest with the arrival of the cold bores, switching to positive and into the bay with the arrival of the warm front. Cross-shore velocities, which reach more than 0.1 m/s in some places, are much more irregular. However, the arrival of the bores tends to coincide with positive onshore velocities, especially near the bottom of the water column, while the fronts correspond to offshore velocities near the bottom. As with the temperature field, the dominant variability of the velocity field is largely due to the repeated sequence of bores and fronts.

The detailed velocity and density structure for an example bore and relaxation is shown in Figure 2.4. Waters are well mixed and quiescent until the arrival of the bore, which is marked by a sharp front of dense water in the form of a gravity current with cross-shelf velocities increasing rapidly to nearly 0.1 m/s onshore. The bore is highly nonlinear ($Fr \sim 0.7$) and unstable at the nose with O(1 m) density overturns present. The warm front relaxation takes the form of a surface gravity current with stronger local shear.

2.4.2: Bore vs. Mixing Period

In order to compare energetics and dynamics between the bores and warm front relaxations, composite (n = 7 events) bore and mixing periods (defined in 2.4.1) were calculated. Composite temperature spectra were computed by taking each bore or mixing period event, respectively, linearly detrending, removing the mean, windowing, calculating the spectra, and then averaging all respective events (n = 7) in frequency space. The composite mixing period dominated temperature variance at high frequencies by nearly a decade compared to the bore period and the entire record

(Figure 2.5). Likewise, significant energy in the temperature fluctuations during the mixing period was sustained at frequencies higher than the average buoyancy frequency ($\omega > \overline{N}$), indicating that the variability is not due to internal waves, and is likely due to turbulent fluctuations.

To evaluate the potential for mixing due to shear instabilities, gradient Richardson numbers were calculated as, $Ri = \frac{N^2}{S^2}$, where $S^2 = \left(\frac{\partial U}{\partial z}\right)^2 + \left(\frac{\partial V}{\partial z}\right)^2$ is the vertical shear in the horizontal direction squared and (U, V) are ten-minute averaged velocity profiles. While the bores tend to stably stratify the water column ($Ri > 0.25$), the relaxation events have a much greater percentage of periods where dynamic instabilities ($Ri < 0.25$) may be present (Figure 2.6). Thus, local shear-generated turbulence during the warm front relaxations (mixing period) contributes significantly to the local temperature variance and provides a mechanism for active mixing of the stratified water column.

2.4.3: Turbulent Dissipation and Mixing

The importance of relaxation events to local mixing was examined by estimating the dissipation rate of TKE using isopycnal slope spectra over the mixing period. Estimates were made near the thermocline (~6 mab), although other locations in the stratified interior provided similar results. An example of this result is shown in Figure 2.7. The low wavenumber portion of the spectrum ($k_x \leq 10^{-2}$ cpm) represents the internal wave subrange and depends highly on the stratification and frequency content of the internal wave field [*Klymak and Moum*, 2007a, 2007b]. As the spectrum moves towards higher wavenumbers, the spectrum turns blue, with increasing energy

at higher frequencies. In the turbulence subrange ($0.04 < k_x < 0.3$ cpm), the dissipation fit to Equation (2.3) follows the calculated spectrum. At the highest wavenumbers, the spectrum begins to turn red, with decreasing energy at higher frequencies. The reddening of the spectra typically occurred near one standard deviation less than the mean buoyancy wavenumber,

$$k_N = \frac{2\pi < N >}{c_{obs}}, \tag{2.5}$$

likely due to the fact that sharper density gradients and overturns are not resolved by the average buoyancy frequency. For the example shown (Figure 2.7), the average dissipation over the mixing period ($<\varepsilon>$) was estimated to be 1.41 x 10^{-8} m^2/s^3 with upper and lower error bounds (95% confidence intervals) of 2.58 x 10^{-8} and 8.55 x 10^{-9} m^2/s^3, respectively. The range of $<\varepsilon>$ values observed over all mixing periods associated with the relaxation of the bores (n = 7) was 2.91 x 10^{-9} to 2.06 x 10^{-8} m^2/s^3, with a mean value of 1.00 x 10^{-8} m^2/s^3. Error bounds for each individual event had similar upper and lower percentage errors as the example given above. A robust feature of the spectra is that for increasing turbulent dissipation, there is an increase in the variance at higher wavenumbers, which is consistent with previous studies [*Klymak and Moum*, 2007a, 2007b].

A common measure for characterizing turbulence in stratified environments is the turbulence activity parameter, $\varepsilon/\nu N^2$ [e.g., *Shih* et al., 2005]. In order to evaluate the potential for turbulent mixing due to shear instabilities by relaxation events, the turbulence activity parameter for each mixing period (e.g., $<\varepsilon>/\nu<N^2>$) was plotted as a function of the local median gradient *Ri* following the warm fronts (Figure 2.8). An

inverse relationship exists between the turbulence activity parameter and local median *Ri* such that at the highest activity numbers, the local median *Ri* nears the critical value (0.25). Furthermore, plotting the turbulence activity against the number of individual points that had $Ri < 0.25$ following the relaxations revealed the general trend that as the turbulence activity increased, so did the number of potentially dynamically unstable events (i.e., $Ri < 0.25$, figure not shown). This again points to local shear-produced turbulence as the dominant mixing mechanism in the stratified interior at this site.

Uncertainty of the dissipation estimates was evaluated by performing a sensitivity analysis with three input parameters to the isopycnal slope spectra model: c_{obs}, $\langle N^2 \rangle$, and Γ. The observed propagation speed (c_{obs}) and averaged buoyancy frequency ($\langle N^2 \rangle$) were varied from 75 to 125% of the originally calculated value, while the mixing efficiency (Γ) was varied between 0.1 and 0.29 based on direct numerical simulations (DNS) and turbulence activity numbers observed since Γ itself is a function of the turbulence activity number [*Shih et al.*, 2005]. Figure 2.9 displays the effect of the three inputs to the calculated dissipation along with standard deviations across all relaxation events (n = 7) at each point. Dissipation estimates were not sensitive to the calculated values of c_{obs} and $\langle N^2 \rangle$, as these parameters never changed the calculated dissipation by more than a factor of two, which is within the 95% confidence range. Likewise, dissipation was weakly dependent on the choice of mixing efficiency near 0.2, but did change by a factor of three at the smallest value of $\Gamma = 0.1$; however, given the observed turbulence activity numbers, Γ is not likely to be this low [*Shih et al.*, 2005] and hence not as influential in the dissipation estimate.

The only parameter that showed significant variability across different relaxation events, as highlighted by the standard deviations shown in Figure 2.9, was c_{obs}. These results highlight the robustness of the isopycnal slope spectra model for estimating dissipation.

2.5: Discussion

2.5.1: Non-canonical nature

Using a numerical model, we examined the non-canonical nature of the observed bores, in which the initial bore is followed by gradual cooling of the water column until an abrupt warm front relaxation and high frequency oscillations quickly erode the stratification. This structure appears to be dependent on the bathymetric slope, which can be measured relative to the internal wave slope using the internal Iribarren number,

$$\xi = \frac{s}{\left(\frac{a}{\lambda}\right)^{1/2}}, \tag{2.6}$$

where s is the bathymetric slope, and a and λ are the offshore amplitude and wavelength of the incoming internal wave, respectively [e.g., *Boegman et al.*, 2005]. To examine this dependence, we employed the fully nonlinear, nonhydrostatic model SUNTANS [*Fringer et al.*, 2006] in a two-dimensional domain that represents a vertical transect along the median observed propagation path of the bores (195.4°, Figure 2.1a and Figure 2.1c). The model domain was 20 km long and 80 m deep, with a horizontal grid spacing (Δx) of 5 m and a vertical grid spacing (Δz) of 1 m. A time step size (Δt) of 1 s was chosen in order to satisfy the stability constraint associated

with the calculation of the internal waves. The turbulence model assumed a constant eddy viscosity of 10^{-4} m^2/s in both the horizontal and vertical directions and no scalar diffusivity. The model was initialized with realistic stratification measured from CTD casts in southern Monterey Bay near the time of the field observations (courtesy of Monterey Bay Research Aquarium Institute), and was forced at the offshore boundary by the mode-1 internal wave field associated with this stratification and the M_2 tidal frequency. The model was run for six tidal periods (~ 2.7 x 10^5 time steps). With these parameters, two scenarios were considered: a canonical case with a gentler slope ($\xi \sim 0.2$) and a non-canonical case with a steep slope taken from actual bathymetry ($\xi \sim 2$, Figure 2.1c). Since the slope (s) and wavelength (λ) are set by the bathymetry and forcing, respectively, the modeled Iribarren number (ξ) is set by the initial amplitude (a) of the wave, which was chosen to match the observed change in temperature due to the bores in the realistic case.

The model results show a clear distinction in the nature of the bores for different Iribarren numbers. Figure 2.10 shows, for both cases, a snapshot of the bore at several times, along with the temperature signal observed at the 15 m isobath (the location of field observations at MN). The lower Iribarren number (gentler slope) case results in a canonical bore structure. In this case, the incoming wave has time to shoal, steepen, and break, sending a bore (bolus) up the slope. This leads to a more canonical temperature signal at the 15 m isobath with an abrupt cold front followed by gradual warming [e.g., *Leichter et al.*, 1996; *Hosegood and van Haren*, 2004]. Conversely, the higher Iribarren number (steeper slope) case results in a non-canonical bore structure that is qualitatively similar to our observations. In this case, the incoming wave does

not have time to shoal or break. Rather, the wave essentially sloshes up and down the steep slope in a similar manner to a standing wave at a vertical wall. As the wave sloshes up, it sends gradually cooler water past the 15 m isobath. After reaching its peak position on the slope, it quickly recedes back down the slope, resulting in an abrupt warm front at the 15 m isobath. The corresponding temperature signal (Figure 2.10) is qualitatively similar to that shown in Figure 2.2b. Although the model greatly simplifies the real system, it captures and reproduces the basic dynamics of the observed non-canonical bores, and demonstrates the importance of the Iribarren number on internal wave shoaling dynamics in southern Monterey Bay and potentially other nearshore regions.

2.5.2: Turbulent Dissipation and Mixing

Estimates of turbulent dissipation rates in coastal zones are important in determining vertical mixing of tracers. Variability in turbulent mixing on the shelf has been attributed to various physical phenomena and often spans several orders of magnitude [*Carter et al.*, 2005]. Conventional estimates of turbulent dissipation with moored instruments have significant issues in coastal zones due to small velocities with a high noise floor and wave contamination. Likewise, wave-turbulence separation methods for estimating turbulent stresses and shear production (and ultimately dissipation assuming equilibrium turbulence) from ADCPs are also affected by waves [e.g., *Rosman et al.*, 2008; *Kirincich et al.*, 2010], with wave-turbulence separation methods often not appropriate in certain environments [*Walter et al.*, 2011]. However, the technique of using isopycnal slope spectra to estimate dissipation rates does not

suffer significantly from surface wave contamination and may be appropriate for use in coastal waters with strong wave signatures [e.g., *Woodson et al.*, 2011].

Turbulent dissipation rates of the warm front relaxations in this study were on average an order of magnitude larger than the average dissipation rates found by *Carter et al.* [2005] on the southern shelf of Monterey Bay using microstructure measurements. Likewise, *Carter et al.* [2005] observed the passing of high acoustic backscatter events with elevated dissipation rates the same order of magnitude as the events in this study, which they attribute to non-linear internal waves. However, they lacked the spatial and temporal resolution to fully resolve these events that are likely similar to the bores observed in this study. Given that their average dissipation rates included these elevated dissipation events, it is not a leap to say that the bore events in this study might be associated with dissipation rates two orders of magnitude larger than the background level (i.e., excluding bore events) previously observed on the southern shelf of Monterey Bay.

Dissipation estimates can be compared to the near-bed, bottom-generated turbulence by considering the law of the wall scaling for dissipation,

$$\varepsilon \sim \frac{u_*^3}{\kappa z}, \tag{2.7}$$

where $\kappa = 0.41$ is the Von Kármán constant, z is the height above the bed, and u_* is the friction velocity [*Pope*, 2000]. The friction velocity squared is estimated using a drag-law near the bed,

$$u_*^2 = C_d u_b^2, \tag{2.8}$$

where C_d = 2.5 x 10^{-3} is the drag coefficient for a sandy bottom [*Gross and Nowell*, 1983], and $u_b = \sqrt{u^2 + v^2}$ is the near-bed velocity taken to be at the first ADCP bin height of z = 0.935 m. Thus, the bottom-generated turbulence can be approximated by,

$$\varepsilon \sim \frac{\left(C_d\right)^{3/2} u_b{}^3}{\kappa z}. \tag{2.9}$$

The mean near-bed dissipation was 2.90 x 10^{-8} m^2/s^3, which is comparable to the mean dissipation value near the thermocline of 1.00 x 10^{-8} m^2/s^3 found using isopycnal slope spectra. Turbulence in the stratified interior during the relaxation events is the same order of magnitude as the near-bed, bottom-generated turbulence. Moreover, the stratification present throughout the bore/relaxation event should limit bottom-generated TKE to the region near the bed where it is unable to penetrate vertically [cf. *Monismith and Fong*, 1996]. Consequently, the local shear-produced TKE in the stratified interior by the warm front relaxations, rather than the bottom-generated TKE, dominates mixing in the middle of the water column. It appears that the turbulence structure in the presence of nearshore bores is substantially different than would be expected from the standard conceptual model of a bottom mixed layer under a stratified interior (Figure 2.11).

Vertical turbulent diffusivities were quantified during the relaxation events following the *Osborn* [1980] formulation:

$$\kappa_\rho = \Gamma \frac{< \varepsilon >}{< N^2 >}. \tag{2.10}$$

where Γ = 0.2 was taken to be a constant based on the turbulence activity numbers found in this study and the DNS simulations of *Shih et al.* [2005]. Diffusivities ranged

from 1.84 x 10^{-6} to 2.31 x 10^{-5} m^2/s with a mean value of 1.00 x 10^{-5} m^2/s, indicating the importance of the bore relaxation events to diapycnal mixing in the interior.

2.6: Summary and Implications

We observed transient stratification and mixing events associated with nearshore internal bores in southern Monterey Bay using an array of instruments with high spatial and temporal resolution. Velocity and density data show repeated episodes of cold and warm water intrusions propagating through the array. The arrival of the bores is characterized by surging masses of dense (cold) water near the bottom that tend to stratify the water column. The bore is followed by a gradual decline in temperature throughout the water column (bore period) until a sharp warm-front relaxation and high frequency fluctuations return the column back to roughly its original state (mixing period). The structure of the bores did not follow the canonical shape of shoaling internal waves on a gentle, linear slope. The non-canonical nature of these bores and relaxations was examined with a numerical model and explained by a dependence on the internal Iribarren number.

Composite bore and mixing periods (n = 7 events) revealed increased temperature variance at high frequencies during the mixing period ($\omega > \overline{N}$), as well as a greater percentage of events where dynamic instabilities may be present ($Ri < 0.25$). Estimates of turbulent dissipation rates in the stratified interior during the mixing period were found using isopycnal slope spectra and revealed average values the same order of magnitude as near-bed bottom-generated turbulence. Observations indicate

that local shear-produced TKE by the warm front relaxations in the stratified interior dominates mixing in the middle of the water column.

The transient stratification and mixing events generated by these bores dramatically alter the physical environment found in the nearshore and represent the dominant source of variability in this ecologically important region of the inner shelf. The bores and fronts are an important mechanism by which deeper offshore waters are supplied to the nearshore. These waters are also a significant source of nutrients to support macrophyte and phytoplankton growth [*Leichter et al.*, 1996; *McPhee-Shaw et al.*, 2007; *Lucas et al.*, 2011], and can significantly affect other organisms because of the low dissolved oxygen (DO) concentration and pH that is found at depth in the eastern Pacific [e.g., *Checkley and Barth*, 2009]. The low DO waters can also lead to the development of hypoxic events [*Chan et al.*, 2008], if the relaxation events do not provide enough mixing to reoxygenate the water column. Likewise, the bores and relaxations are thought to promote the exchange of organisms and larvae between the nearshore and regions of the inner shelf further offshore [e.g., *Pineda*, 1991, 1994, 1995, 1999]. While large-scale models like the Central California Coast Regional Ocean Modeling System (ROMS) have significantly improved our understanding of how mesoscale transport might affect connectivity of different habitats, they cannot yet be used with much confidence to assess connectivity with nearshore environments like kelp forests because these current models simply do not resolve important physics such as internal bores. Finally, the turbulence in the presence of nearshore internal bores is substantially different than would be expected from the standard conceptual model of a bottom mixed layer under stratified interior. This ultimately affects the

diapycnal mixing that is critical for many ecological processes including benthic grazing, primary production, nutrient cycling, hypoxia development, and the mixing of tracers such as pollutants from sewage outfalls [e.g., *Wolanski and Pickard*, 1983; *Leichter et al.*, 1996; *Boehm et al.*, 2002; *Chan et al.*, 2008]. As the results of this study show, internal bores dramatically alter the physics of coastal environments and need to be considered when assessing nearshore water column dynamics and local mixing.

2.7: Acknowledgements

R. Walter was supported by the Department of Defense (DoD) through the National Defense Science & Engineering Graduate Fellowship (NDSEG) Program. Additional support to R. Walter and R. Arthur was provided by the Stanford Graduate Fellowship (SGF). Support to C. Woodson was provided by the Center for Ocean Solutions. R. Arthur and O. Fringer gratefully acknowledge ONR grant N00014-08-1-0904 (scientific officers Dr. C. Linwood Vincent, Dr. Terri Paluszkiewicz and Dr. Scott Harper). The helpful comments of two anonymous reviewers contributed significantly to this manuscript. Special thanks to the students of the Spring 2010 course taught at Stanford University, CEE 363G Field Techniques in Coastal Oceanography, who helped with the deployment and recovery of the instruments. We acknowledge Bill Smyth for providing code for solving the Taylor-Goldstein equations. Bathymetry data used in this study were acquired, processed, archived, and distributed by the Seafloor Mapping Lab of California State University Monterey Bay.

2.8: Figures and Tables

Table 2.1: Mooring configurations, instrument details, and sampling specifics.

Mooring ID	Location		Water Depth (m)	Instrument Depth (mab)	Sampling Interval (s)	Sampling Period
	Latitude (°N)	Longitude (°W)				
Thermistors (SBE39 and SBE56*)						
XS	36.6219	121.8997	20	2, 4, 6, 8, 10, 12, 14	6	1 to 16 May 2010
AS	36.622	121.9008	15	4, 6, 8, 10, 12	6	1 to 16 May 2010
MN	36.6212	121.9005	15	2, 3*, 4, 6, 10, 12	1*, 3	10 to 16 May 2010
CTDs (SBE37)						
XS	36.6219	121.8997	20	0	30	1 to 16 May 2010
MN	36.6212	121.9005	15	0	30	10 to 16 May 2010
ADCP (RDI 1200 kHz)						
MN	36.6212	121.9005	15	0, 0.25 m bins	1 (mode 12)	10 to 16 May 2010

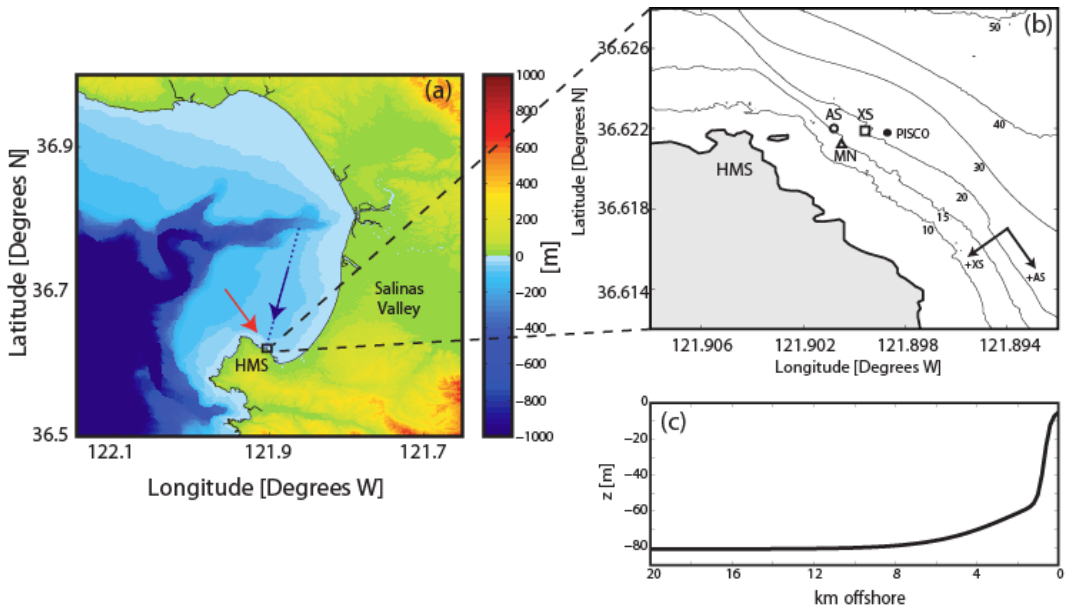

Figure 2.1: (a) Bathymetry and topography of the Monterey Bay region with the study site indicated by a black box and median bore (blue) and relaxation (red) headings shown. (b) Nearshore study site with mooring locations (MN – triangle, AS – circle, XS – square). Bathymetry (10, 15, 20, 30, 40, 50 m isobaths) shown along with the location of Hopkins Marine Station (HMS – Stanford University). The filled circle is the long-term PISCO HMS mooring. (c) Section along the median observed propagation path of the bores (dotted blue line, a) showing the bathymetry used in the numerical model for the non-canonical case (Section 2.5.1).

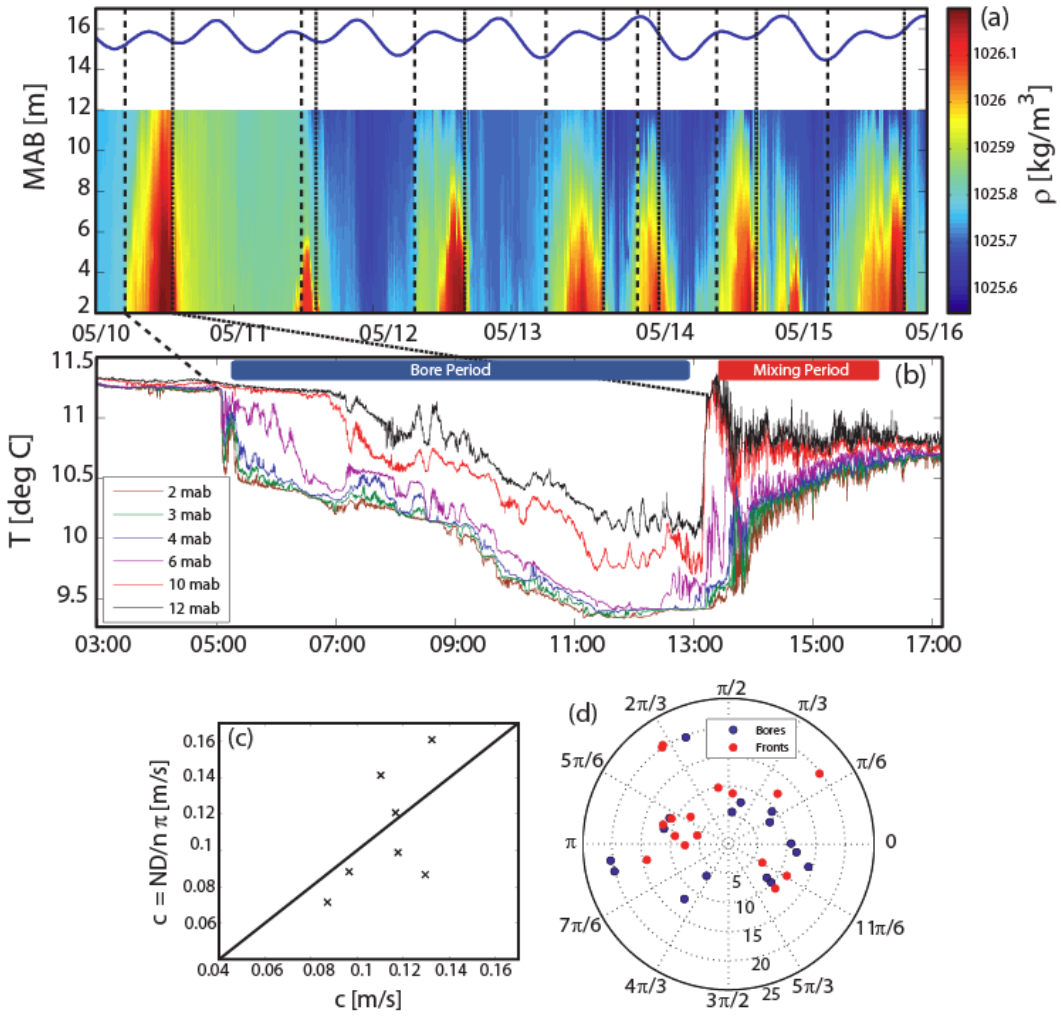

Figure 2.2: (a) Density contour plot from MN highlighting the arrival of bores and relaxations with dashed black lines and dotted black lines, respectively, along with the location of the free surface. (b) Time series of temperature at various heights throughout the water column for the 10 May 2010 bore and relaxation event. The bore (blue) and mixing (red) periods for this particular event are identified with boxes. (c) The calculated bore propagation speed against the theoretical phase speed of a mode-one internal wave. (d) Phasing with respect to the lowest low tidal height (see text for details) for the bores (blue) and relaxations (red), respectively, as a function of the time in hours between the initial bore and relaxation (Δt).

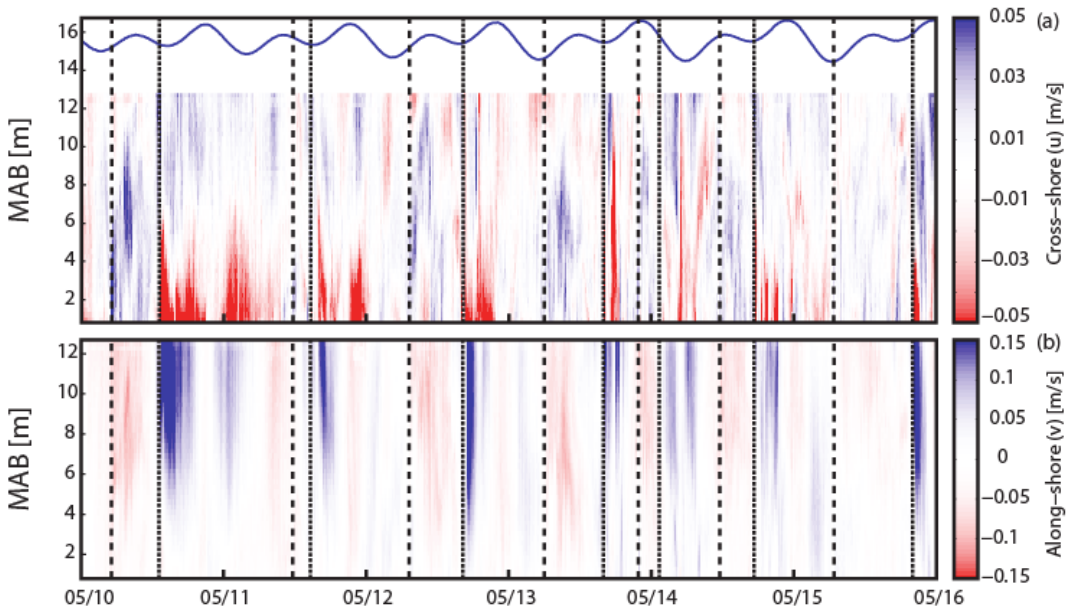

Figure 2.3: Velocity contour plots from MN for (a) cross-shore and (b) along-shore velocities, highlighting the arrival of bores and relaxations with dashed black lines and dotted black lines, respectively, along with the location of the free surface. Velocities shown are ten-minute averages.

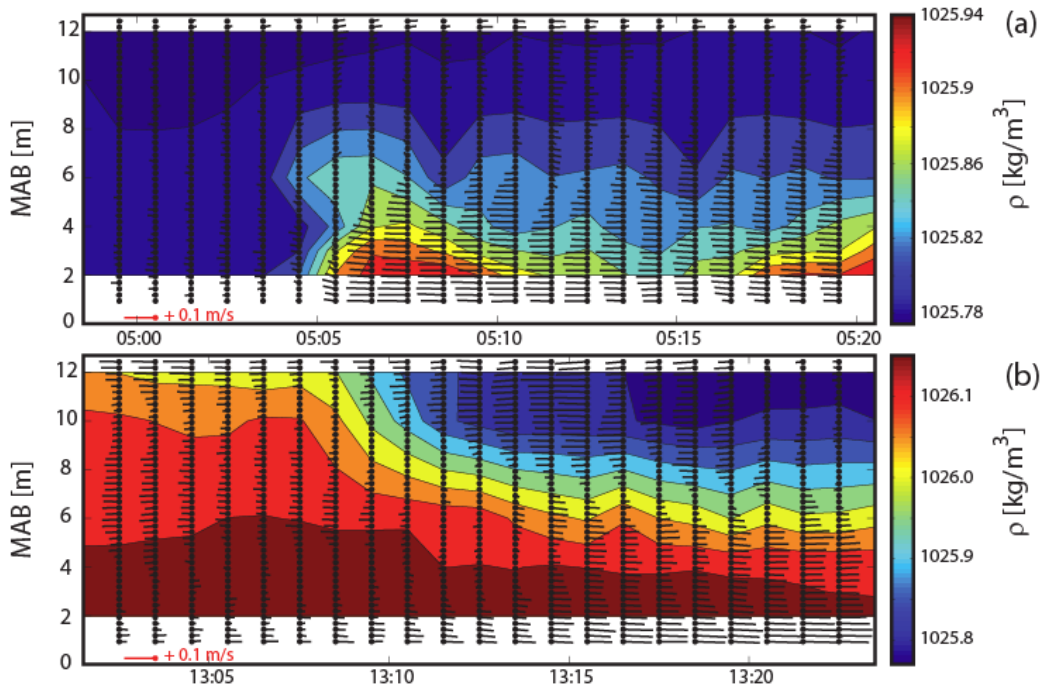

Figure 2.4: Cross-shore/vertical plane showing velocity vectors superimposed on a contour plot of density at MN on 10 May 2010, illustrating the detailed structure of an individual (a) bore and (b) relaxation event. Densities and velocities shown are one-minute averages, and velocities are depicted in 0.25 m bins with the tail of the velocity vector denoted by a black circle. The red velocity vector in the bottom left corner is shown for scale and represents a positive cross-shore velocity of 0.1 m/s.

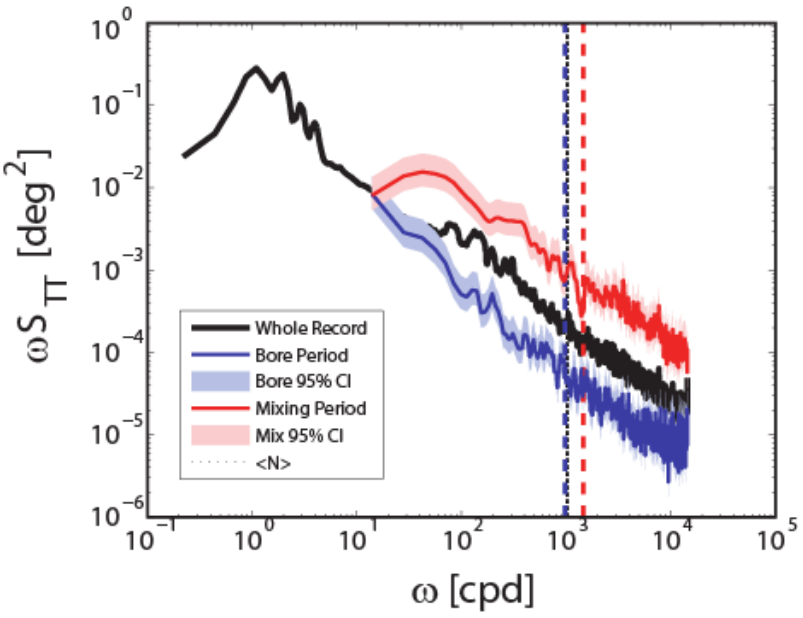

Figure 2.5: Variance preserving temperature spectra at 2 mab for the entire record (black), as well as composite bore (blue) and mixing (red) periods (n = 7 events). Also shown is the average buoyancy frequency over each respective period.

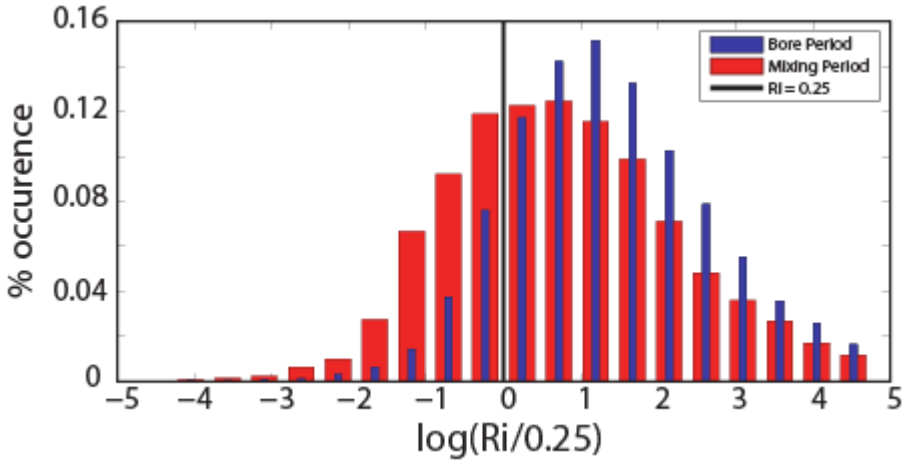

Figure 2.6: Histograms of normalized, logarithmic gradient Richardson number [log(*Ri*/0.25) < 0 is equivalent to *Ri* < 0.25] for composite bore (blue) and mixing (red) periods (n = 7 events), respectively. The solid black line indicates the critical *Ri* = 0.25.

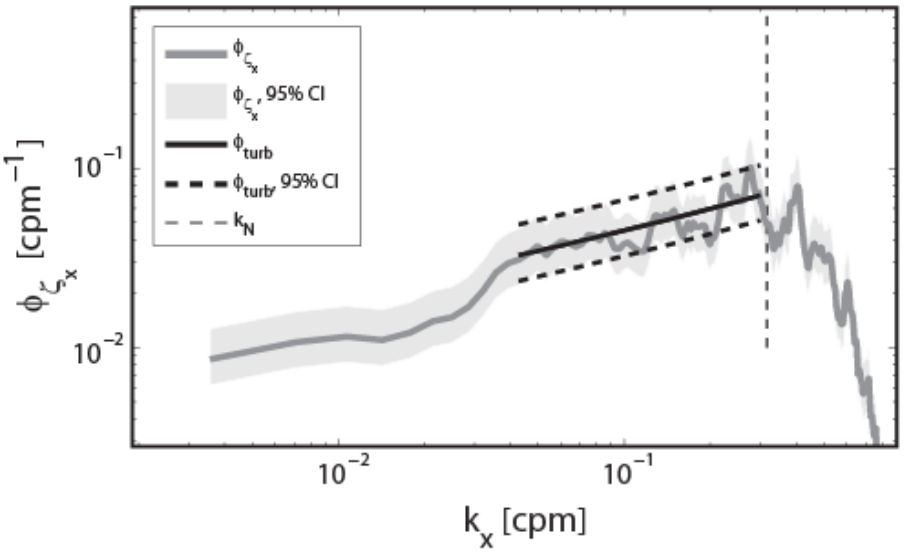

Figure 2.7: Example isopycnal slope spectrum (dark grey line) for several hours following the relaxation event on 15 May 2010. Confidence intervals (95%) for the spectrum are denoted by light grey shading, a solid black line indicates the non-linear least squares regression fit to Equation (2.5) in the turbulence subrange for estimating turbulent dissipation along with upper and lower bounds for dissipation (thick dashed black lines), and the thin dashed black line highlights one standard deviation below the mean buoyancy frequency wavenumber where the spectrum begins to roll-off.

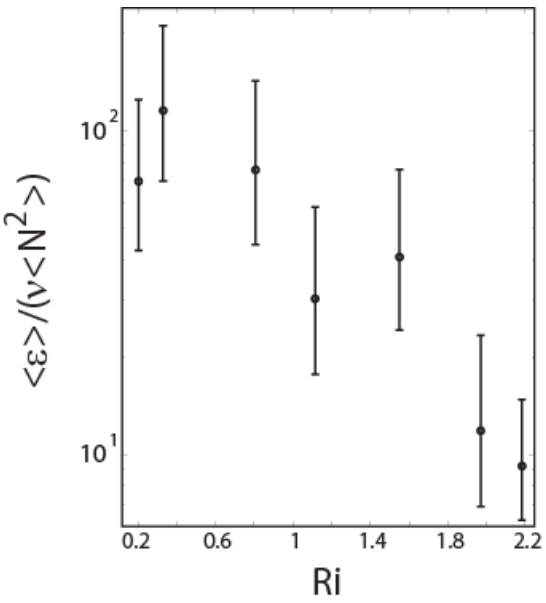

Figure 2.8: Turbulence activity number ($<\varepsilon>/\nu<N^2>$) as a function of the local gradient Richardson number (*Ri*) for the relaxation events. Richardson numbers presented are the median of the ten-minute averaged values for thirty minutes following the arrival of the warm-front relaxation.

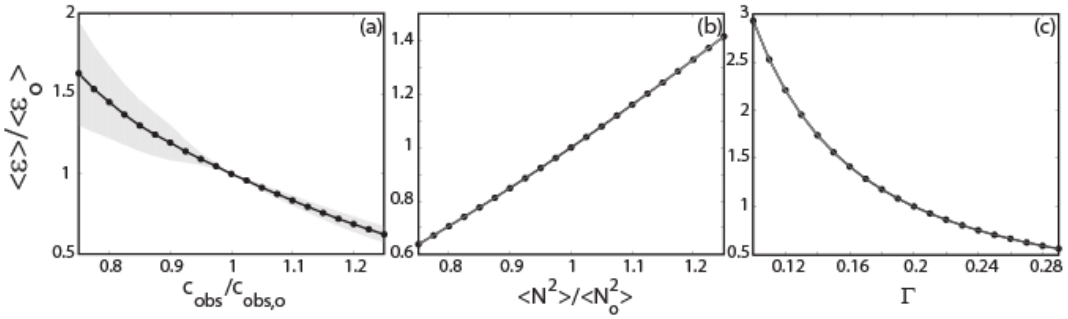

Figure 2.9: Sensitivity of the calculated dissipation rates to three input parameters to the isopycnal slope spectra model: (a) the observed relaxation propagation speed (c_{obs}), (b) the calculated average stratification over the mixing period ($\langle N^2 \rangle$), and (c) the mixing efficiency (Γ). A subscript "*o*" denotes the originally calculated and/or observed value. Black dots represent the mean value taken across all (n = 7) relaxation events, while grey shading indicates one standard deviation from the mean. Note that for (b) and (c) the standard deviation is very small so that shading is difficult to distinguish.

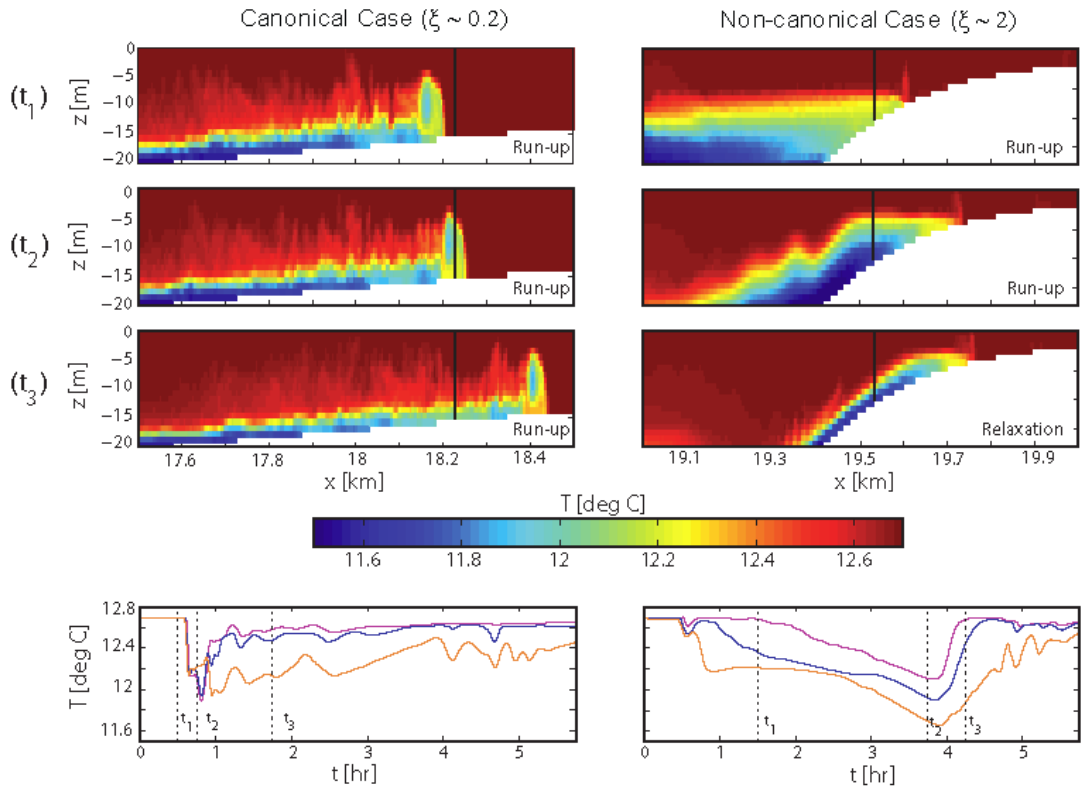

Figure 2.10: Numerical model results for the (a) canonical (gentle slope, $\xi \sim 0.2$) and (b) non-canonical (actual slope, $\xi \sim 2$) cases. Shown in the top three rows are cross-shelf/vertical snapshots of the bores at different representative times (t_1, t_2, and t_3). The 15 m isobath is labeled with a vertical black line. The bottom row shows the vertical temperature structure at the 15 m isobath, including the 2 mab (brown), 4 mab (blue), and 6 mab (magenta), virtual thermistors, similar to Figure 2.2b. Also shown on the bottom row with dotted black lines are the corresponding snapshot times (t_1, t_2, and t_3) from the top three rows. Time in the bottom row is referenced to the beginning of representative bore events in each simulation.

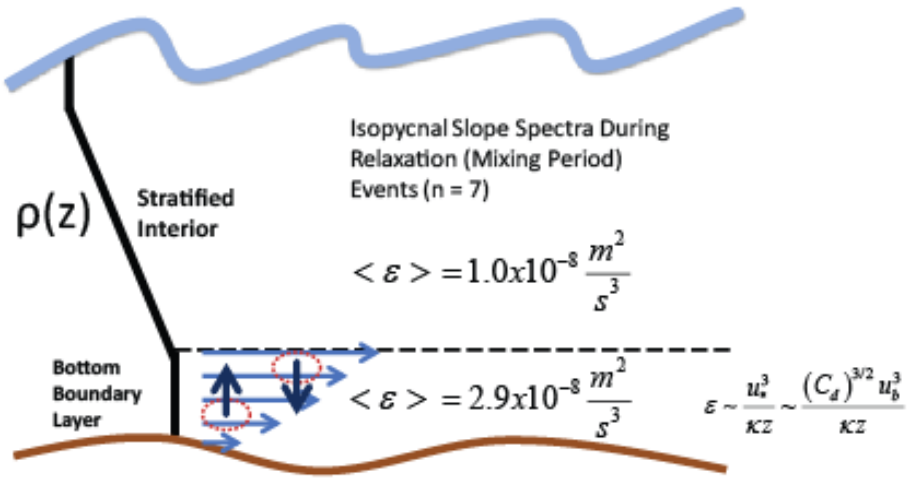

Figure 2.11: Turbulence conceptual model for the stratified interior during bore events in southern Monterey Bay. Local shear-produced TKE in the stratified interior by the warm front relaxations, rather than the bottom-generated TKE, dominates mixing in the middle of the water column. Dissipation in the stratified interior calculated using isopycnal slope spectra and bottom-generated turbulence estimated using the law of the wall and a drag law near the bed.

Chapter 3: Connecting wind-driven upwelling and offshore stratification to nearshore internal bores and oxygen variability

This chapter is a reproduction of the work recently published in the *Journal of Geophysical Research – Oceans*. As the main author of the work, I made the major contributions to the research and writing. Co-authors include C. Brock Woodson[1], Paul R. Leary[2], and Stephen G. Monismith[3].

DOI: 10.1002/2014JC009998

[1]COBIA Lab, College of Engineering, University of Georgia, Athens, GA, USA

[2]Hopkins Marine Station of Stanford University, Pacific Grove, CA USA

[3]Environmental Fluid Mechanics Laboratory, Stanford University, Stanford, CA, USA

3.1: Abstract

This study utilizes field observations in southern Monterey Bay, CA to examine how regional scale upwelling and changing offshore (shelf) conditions influence nearshore internal bores. We show that the low-frequency wind forcing (e.g., upwelling/relaxation time scales) modifies the offshore stratification and thermocline depth. This in turn alters the strength and structure of observed internal bores in the nearshore. An internal bore strength index is defined using the high-pass filtered potential energy density anomaly in the nearshore. During weak upwelling favorable conditions and wind relaxations, the offshore thermocline deepens. In this case, both the amplitude of the offshore internal tide and the strength of the nearshore internal bores increase. In contrast, during strong upwelling conditions, the offshore thermocline shoals towards the surface, resulting in a decrease in the offshore internal tide amplitude. As a result, cold water accumulates in the nearshore (nearshore pooling), and the internal bore strength index decreases. Empirical orthogonal functions are utilized to support the claim that the bore events contribute to the majority of the variance in cross-shelf exchange and transport in the nearshore. Observed individual bores can drive shock-like drops in dissolved oxygen (DO) with rapid onset times, while extended upwelling periods with reduced bore activity produce longer duration, low DO events.

3.2: Introduction

The nearshore coastal ocean, defined here as the innermost portion of the continental shelf and extending from the shoreline up to several kilometers offshore, is generally taken to be one of the most productive and ecologically important parts of the ocean [*Pauly and Christensen,* 1995; *Mann*, 2000]. The nearshore is also a complex environment from a physical standpoint, due in large part to the widespread and often irregular occurrence of nonlinear internal waves (NLIWs) that frequently appear more bore-like than wave-like [e.g., *Scotti and Pineda,* 2004; *Leichter et al*., 1996; *Nam and Send,* 2011; *Davis and Monismith,* 2011; *Walter et al*., 2012]. Indeed, this region of the ocean can be thought of as the "swash zone" for larger-scale internal wave fields on the continental shelf. These nearshore NLIWs have considerable implications for the cross-shelf exchange and transport of nutrients, sediments, contaminants, larvae, and other scalars [*Wolanski and Pickard*, 1983; *Pineda*, 1991, 1994, 1995, 1999; *Leichter et al*., 1996; *Boehm et al*., 2002; *Noble et al*., 2009]; turbulent mixing and dissipation [*Sandstrom and Elliot,* 1984; *Venayagamoorthy and Fringer,* 2007; *Nam and Send,* 2011; *Davis and Monismith,* 2011; *Walter et al*., 2012]; and hypoxia development [*Booth et al*., 2012]. Despite a growing body of literature on the subject [cf. *Leichter et al*., 1996; *Klymak and Moum*, 2003; *Lerczak et al*., 2003; *Scotti and Pineda,* 2004; *Shroyer et al*., 2008; *Nam and Send,* 2011; *Davis and Monismith,* 2011; *Woodson et al*., 2011; *Walter et al*., 2012; *Wong et al*., 2012], many questions still remain with respect to the evolution, fate, and impact of NLIWs in the nearshore environment and their connection to the larger-scale internal wave/tide field on the shelf.

Internal waves on the continental shelf are well-studied in numerical, experimental, and theoretical fluid mechanics (see *Lamb* [2013] and the sources therein for a comprehensive review). Yet, the majority of the aforementioned numerical and laboratory studies (see *Lamb* [2013]) have necessarily focused on simplified, idealized setups and isolated processes. Likewise, field studies have concentrated mainly on deeper shelf waters (50+ m depths; cf. Table 1 of *Alford et al*. [2012]), while the ultimate fate of NLIWs in the shallower, nearshore regions (~20 m) has been mainly speculative. The lifecycle and ultimate fate of internal waves propagating from the shelf to the nearshore environment is highly variable due to a dynamic environment with changing bathymetry, spatially and temporally evolving stratification, tidal and wind forcing, and coastal upwelling/downwelling influences [*Pineda and Lopez*, 2002; *Davis and Monismith*, 2011; *Lamb*, 2013]. Thus, further field observations are needed to assess the influence of changing environmental conditions on the offshore to onshore (shelf to nearshore) translation of internal wave/tide fields in the coastal environment.

Nearshore internal bores are a common feature that produce transient stratification and mixing events, and represent the dominant source of variability, in the ecologically-important region of southern Monterey Bay, CA [*Walter et al*., 2012]. Internal bores in this region are characterized by an upslope surging flow of dense water that tends to stratify the water column ("bore period" from *Walter et al*. [2012]). The bore period is followed by a strongly sheared downslope flow in the form of a warm-front, and high frequency temperature oscillations, as the bore feature relaxes back downslope and returns the water column back to nearly its original state ("mixing

period" from *Walter et al*. [2012]). During the mixing period, shear instabilities result in elevated levels of turbulent dissipation and diapycnal mixing in the stratified interior, consequently affecting local mixing dynamics that are critical for many ecologically important processes. Furthermore, the structure of the bores and relaxations in this region (see *Walter et al*. [2012]) was examined with a numerical model and explained by the steep bathymetric slope in the region and dependence on the internal Iribarren number,

$$\xi = \frac{s}{\left(\frac{a}{\lambda}\right)^{1/2}}, \tag{3.1}$$

where s is the bathymetric slope, and a and λ are the offshore amplitude and wavelength of the incoming internal wave, respectively [e.g., *Boegman et al*., 2005]. While the bore characteristics were hypothesized to be dependent on regional scale upwelling/downwelling and offshore conditions, that study focused on local dynamics of the observed internal bores in the nearshore [*Walter et al*., 2012].

The main objective of this study is to assess how wind forcing and offshore stratification influence nearshore internal bores, which are a common feature along many continental margins [*Shea and Broenkow*, 1982; *Holloway*, 1987; *Pineda*, 1991, 1994, 1995, 1999; *Pineda and Lopez*, 2002; *Leichter et al*., 1996; *Colosi et al*., 2001; *Klymak and Moum*, 2003; *Hosegood and van Haren*, 2004; *Nam and Send*, 2011]. For instance, in the Southern California Bight, *Pineda and Lopez* [2002] hypothesized that the observed nearshore internal bores were dependent on low-frequency wind forcing (e.g., upwelling/relaxation time scales) through the modification of the offshore

stratification and thermocline depth. We test this hypothesis in southern Monterey Bay, a region strongly influenced by regional scale upwelling/downwelling [e.g., *Rosenfeld et al*., 1994].

Additionally, we examine how offshore conditions and nearshore internal bores affect nearshore dissolved oxygen (DO) variability and the potential development of hypoxia, which has drawn significant attention in recent years [*Chan et. al*., 2008; *Hofmann et. al*., 2011]. While oxygen minimum zones (OMZs) occur naturally [*Wyrtki*, 1962; *Kamykowski and Zentara*, 1990; *Helly and Levin*, 2004], climatic changes appear to have driven OMZ expansions [*Keeling and Garcia*, 2002; *Stramma et. al*, 2008, 2010] and brought OMZs into shallower shelf margins [*Bakun*, 1990; *Grantham et al*., 2004; *Helly and Levin*, 2004; *Bograd et al*., 2008]. The increased prevalence of inner shelf hypoxic intrusions has caused massive mortalities, and other deleterious impacts, to fish and invertebrates [*Grantham et. al*., 2004; *Ekau et. al*., 2010; *McClatchie et. al*., 2010]. Upwelling-driven hypoxic events occur primarily via direct advection of low DO, subthermocline waters [*Grantham et. al*., 2004; *Bograd et. al*., 2008; *Chan et. al*. 2008]. Internal bores are another DO transport mechanism and act to drive intrusions of hypoxic water at higher frequencies than low-frequency upwelling/relaxation cycles [*Booth et. al*., 2012]. We show that these two DO transport processes, upwelling/relaxation cycles and internal bores, are not independent. Furthermore, we expand on the *Booth et al*. [2012] study and link regional upwelling dynamics and nearshore internal bore activity to the strength and frequency of low DO events, and DO variability, in the nearshore.

In Section 3.3, we introduce the field site, the experimental setup, and data processing methods. Section 3.4 describes the high resolution observations made over a 3 week study period and connects the regional scale upwelling/relaxation trends with the offshore conditions and stratification. This is followed by results that link the offshore characteristics with the nearshore internal bores. Section 3.5 qualifies the findings over the 3 week study period using lower resolution measurements made over an approximately 2.5 month time period. Section 3.5 also discusses biological and ecological implications of the results and highlights the interconnectedness of the shelf and the nearshore. Specifically, the potential for cross-shelf transport, as well as oxygen variability and low oxygen events, are discussed since internal bores are an important mechanism by which deeper offshore waters are transported to the nearshore. Finally, we summarize the findings in Section 3.6.

3.3: Site Description and Methods

3.3.1: Study Site

Monterey Bay, located along the eastern Pacific Ocean and central California coast, is a semi-enclosed embayment that contains one of the largest submarine canyons in the United States (Figure 3.1a). Covering an area of approximately 550 km^2, the bay features a narrow shelf (i.e., shelf break of ~100 m within a few km from the coast at some locations) with about 80% of the bay shallower than 100 m [*Breaker and Broenkow,* 1994]. Monterey Bay harbors an extremely large ecological diversity including some of the west coast's largest kelp (*Macrocystis pyrifera*) forests, marine

reserve systems, large commercial fisheries, and eco-tourism industries [*Kildow and Colgan*, 2005; *Raheem et al*., 2011].

General physical conditions in Monterey Bay include tides that are mixed semi-diurnal, with currents dominated by the M_2 (~12.42 hr period) tidal component (M_2 tidal amplitude of ~0.5 m; see *Rosenfeld et al*. [2009] and *Carter* [2010]). Currents on the shelf tend to be 180° out of phase relative to the canyon (i.e., directed out of the bay on the flood tide due to inflow through the canyon) [*Petruncio et al.*, 1998; *Carter*, 2010]. Large amplitude internal waves are a ubiquitous and well-documented phenomenon along the continental margin in and around the Monterey Submarine Canyon, where isopycnal displacements often reach hundreds of meters [e.g., *Breaker and Broenkow*, 1994; *Petruncio et al.*, 1998; *Kunze et al.*, 2002]. Additionally, numerical models have confirmed both the local generation of internal tides, as well as the interaction of locally and remotely generated internal tides, at the M_2 tidal period inside the canyon and near the shelf edge [*Carter*, 2010; *Kang and Fringer*, 2012]. Finally, as mentioned earlier, internal motions in the form of bores are a common feature in the nearshore regions of southern Monterey Bay, and based on their observed propagation direction, seem to originate near the canyon mouth (Figure 3.1a; *Walter et al*. [2012]).

During the upwelling season in Monterey Bay (~April to September), regional upwelling favorable winds (northwesterly) create a strong upwelling jet at Point Año Nuevo that flows southward across the mouth of the bay [*Rosenfeld et al*., 1994]. During periods of strong upwelling favorable winds (typically lasting 5 - 14 days), dense upwelled waters inundate the shelf and begin to accumulate, as the main

offshore thermocline rises towards the surface. This process is interrupted during regional wind relaxation events lasting several days, whereby upwelling favorable winds weaken [cf. *Beardsley et al*., 1987].

3.3.2: Experimental Setup

The current study was part of a larger project (Monterey Tower Node - MOTOWN) aimed at understanding how nearshore internal bores affect circulation dynamics and turbulent mixing in the nearshore coastal environment. Here, we focus on connecting regional scale dynamics and upwelling to observed nearshore internal bores. Turbulent mixing by the nearshore bores, as well as various budgets (e.g., energy, momentum, etc.), will be investigated in future contributions. As such, only the moored instrument arrays and data used in this study will be described here.

Several densely instrumented moorings were deployed from 3 to 24 August 2012 (3 weeks) in southern Monterey Bay, CA. The nearshore mooring (NS; Figure 3.1b) was deployed on the ~15 m isobath just offshore of Hopkins Marine Station (HMS – Stanford University, Pacific Grove, CA). This is the location of previous observations of nearshore internal bores [*Walter et al*., 2012], as well as regular intrusions of low DO water by internal motions [*Booth et al*., 2012]. In order to capture the vertical structure and high frequency motions of the bores, this mooring was equipped with 22 SBE56 temperature loggers throughout the water column [0 to 9 meters above the bed (mab) in 0.5 m increments, 10, 11, 12 mab], all of which were sampling at 0.5 s periods. NS also contained a SBE39 temperature logger at the surface, which sampled at 10 s intervals. Additionally, the mooring included SBE37 conductivity-temperature-depth (CTD) loggers at 0 (24 s), 2 (6 s), 4 (6 s), 6 (6 s), and

8 (24 s) mab, where the sampling interval is given in parentheses for each instrument. The NS site also had a SeapHOx at 1 mab measuring DO concentrations [e.g., *Frieder et al.*, 2012]. An RDI 1200 kHz Workhorse acoustic Doppler current profiler (ADCP) was deployed at the NS site sampling in fast-ping Mode 12 (6 subpings per 1 s ensemble) with 0.5 m vertical bin spacing. This sampling scheme results in a small error standard deviation of 0.12 cm/s for ten-minute averages, which is the averaging interval used in further analysis. The ADCP was also leveled by divers to within 1 degree of the horizontal using a bubble level in order to minimize instrument tilt errors.

In addition to the high resolution measurements over the 3 week study period described above, long-term measurements from the same location over an approximately 2.5 month study period (13 June to 31 August) were analyzed. Long-term measurements were from a near-bottom (1 mab) SBE56 temperature logger (2 s sampling period) and a SeapHOx measuring DO concentrations (10 min sampling period).

In order to capture regional scale stratification and the upwelling induced effect on the shelf, observations from an offshore mooring (OS; Figure 3.1a) on the shelf near the ~85 m isobath were used. The OS mooring location also lines up with the previously observed propagation pathway (i.e., from near the canyon mouth to the NS site) of the nearshore internal bores (Figure 3.1b; *Walter et al*. [2012]). This mooring was equipped with a vertical collection [1.75, 10, 20, 30, 40, 50, 60, 70 mab, and surface] of RBR TR-1040 temperature loggers sampling at 30 s intervals. During the experiment, the near surface thermistor malfunctioned and so the surface

temperature was obtained at thirty-minute intervals using the nearby National Data Buoy Center (NDBC) buoy 46092 (M1; Figure 3.1a). The offshore mooring also had CTDs located at 3 and 70 mab, sampling at 30 s and 3 min intervals, respectively. The OS mooring collected data over the approximately 2.5 month period (13 June to 31 August). Results from the 3 week period (3 to 24 August) are presented in conjunction with the high resolution NS measurements in Section 3.4, while the long-term results (2.5 month period) are discussed in Section 3.5.

Regional, offshore winds were collected at ten-minute intervals from the NDBC buoy 46042 (36.785 N, 122.469 W). All times referenced in the text and figures are in local time, Pacific Daylight Time, unless otherwise noted.

3.3.3: Analyses

Velocity measurements from the NS ADCP were rotated into cross-shore, along-shore, and vertical velocity components using the principal axes obtained from a long-term ADCP near the site (Figure 3.1b; PISCO – Partnership for Interdisciplinary Studies of Coastal Oceans). The principal axes of the long-term record were within 2 degrees of those calculated in the current study. Regional, upwelling favorable winds were calculated using the mean along-coast direction across Monterey Bay [north-northwesterly winds from 330°; e.g., *Woodson et al.*, 2009].

During the summer upwelling season, salinity variations in Monterey Bay are sufficiently small so that density is largely controlled by temperature [e.g., *Woodson et al.*, 2009, 2011; *Walter et al.*, 2012]. Analysis of the nearshore CTD data showed that small changes in salinity varied linearly with temperature throughout the water column (e.g., $R^2 = 0.91$, p-value < 0.001 for the 2 mab CTD) with nearly identical linear

regression coefficients between different depths. Therefore, densities at all nearshore thermistor locations were calculated using the observed temperature and derived linear relationship from the CTD measurements for salinity as a function of temperature. Density profiles at the offshore site were calculated using the same method described above with the offshore CTD data ($R^2 = 0.58$, p-value < 0.001 for the temperature-salinity regression using ten-minute averages of both the 3 and 70 mab CTDs). The lower coefficient of determination in the OS regression versus the NS regression is likely the result of large regional relaxations that act to advect open ocean water masses with marginally lower salinities into the Bay. These water masses deviate slightly from the general temperature-salinity relationship; however, the salinity deviations are small and do not contribute significantly to the density calculation.

Spectral and coherence calculations were performed using the fast Fourier transform (FFT), following standard methods [e.g., *Walter et al*., 2011]. Hamming windows with 50% overlap between adjacent segments were used with the choice of window length in the calculations representing a compromise between the number of degrees of freedom (DOF) for confidence intervals, frequency resolution, and length of the original record. Confidence intervals for the spectra were calculated using a chi-squared variable analysis and the equivalent number of DOF (EDOF). For the coherence analysis, confidence limits were quantified using the EDOF [*Emery and Thompson*, 2004].

A dynamical analysis of the bores requires an index that can accurately quantify their strength and intensity. This index also needs to be robust enough to capture the non-canonical and shock-like nature of the bores. Whereas conventional

internal wave analysis considers perturbations to a well-defined and quasi-steady background density field, often defined as the low-pass filtered density field [e.g., *Nash et al.*, 2005], the bore features observed at this site do not follow this convention. Specifically, the bores often propagate into a well-mixed (i.e., unstratified) water column in the nearshore, making the conventional internal wave approach invalid since there is no well-defined "background state," and the highly nonlinear, asymmetric bores do not behave in a wave-like manner. Rather, the bores are characterized by nonlinear pulses of dense fluid in and out of the nearshore, similar to an estuarine flow where dense water from the ocean advects up and down the estuary during the tidal cycle. The conventional approach in the current study leads to a bore hysteresis effect, whereby the background state is contaminated by the previous bore events. This illustrates the need for a more robust proxy for the observed features that accounts for their bore-like properties (i.e., nonlinear, asymmetric, and transient) and the observed background conditions.

Based on the above considerations, we define a bore strength proxy using the potential energy density anomaly often used in estuarine flows [*Simpson et al.*, 1978],

$$\phi = -\frac{g}{H}\int_0^H (\rho - \rho_m) z dz \,, \tag{3.2}$$

where g is the gravitational acceleration, H is the water column depth, z is the height above the bottom, and $\rho_m = \frac{1}{H}\int_0^H \rho dz$ is the depth mean density. The potential energy density anomaly represents the amount of energy required to mix the water column completely, and hence is an index of stratification. Since the instantaneous vertical distribution over depth is used, the proxy accurately captures the transient

stratification and mixing events associated with the bores. In order to delineate bores during the nearshore periods when stratification is present, as well as the periods when the bores propagate into a well-mixed environment, the bore strength index is defined as the high-pass filtered (33 h half-amplitude period) potential energy density anomaly. Results were not sensitive to the filter period used.

The effect of the temporally varying, regional stratification on the offshore internal wave/tide field is examined using a linear, normal mode analysis. This theory considers normal mode perturbations to a stratified fluid, and in the longwave limit, leads to the following linear eigenvalue problem:

$$\begin{aligned} \frac{d^2\hat{\psi}}{dz^2} + \frac{N^2}{c^2}\hat{\psi} = 0, \\ \hat{\psi}(0) = 0,, \\ \hat{\psi}(\mathrm{H}) = 0, \end{aligned} \tag{3.3}$$

where $N^2(z) = -\frac{g}{\rho_o}\frac{\partial\overline{\rho}}{\partial z}$ is the buoyancy frequency squared, $\overline{\rho}$ is a time-averaged density profile, and $\hat{\psi}$ and c are eigenfunction and eigenvalue pairs corresponding to the vertical structure function and phase speed of a linear disturbance, respectively. The largest eigenvalue, and the focus of this study, corresponds to the linear, long-wave speed (c_{lw}). We use the phase speed as a proxy for the strength of the offshore stratification, and consequently the offshore internal wave/tide field. Thus, changes in the offshore (regional) internal wave/tide field will be examined using the time variability of c_{lw}.

3.4: Results

3.4.1: General Observations

The time series of regional upwelling favorable winds measured during the study clearly shows multiple periods (~ 7-10 days) of prolonged upwelling winds interspersed with relaxation events (~ 2-3 days) where the winds diminish (Figure 3.2a). During upwelling episodes, the offshore temperature structure is highlighted by cooling throughout the water column, especially near the bottom (Figure 3.2b). This facet is consistent with advection of cooler waters from the deep, offshore environment. Correspondingly, the offshore thermocline shoals towards the surface, while the near-surface stratification decreases, as evident in the expansion of the highlighted isotherms (Figure 3.2b). In contrast, during weak upwelling favorable conditions or regional relaxation occurrences, the offshore temperature field warms, and the thermocline deepens (Figure 3.2b). During these periods, near-surface stratification also increases, as seen in the compression of the isotherms and increase in the vertical temperature gradient (Figure 3.2b). Likewise, vertical fluctuations in the thermocline increase in magnitude during the relaxations, in comparison to the upwelling periods (Figure 3.2b). From henceforth, the offshore thermocline depth will refer to the distance from the sea surface to the vertical location of the 11.2° isotherm. Besides capturing the vertical gradients in the offshore stratification and the offshore internal wave activity well, this particular isotherm was chosen to delineate the thermocline since it is an isotherm that regularly appears with internal bores in the nearshore. However, all statistics and conclusions presented hereafter are valid for other isotherms within the thermocline region (e.g., 12.4°, 12.15°, 11.5°, 11.2°, etc.).

The nearshore site is marked by repeated pulses of cold water intrusions (i.e., nearshore internal bores) that advect in and out of the nearshore environment (Figure 3.2c). During weak upwelling favorable conditions and/or relaxations when the offshore thermocline is deep, the internal bore features propagate along the bed into well-mixed waters in the nearshore. These bores are characterized by transient stratification (upslope flow) and mixing (downslope flow) events, whereby the water column nearly returns to its original, well-mixed state following the downslope flow. In many cases, the bore events perturb and stratify the entire water column. The structure of the bore events during weak upwelling/relaxation conditions is consistent with previous observations made during the early upwelling season by *Walter et al.* [2012]. During extended periods of upwelling favorable conditions when the offshore thermocline becomes shallower, the structure is quite different. Rather than propagating into well-mixed waters near the bottom of the water column, the bores perturb a pre-existing stratification along the nearshore thermocline (Figure 3.2c). This pre-existing stratification is the result of the extended upwelling conditions, whereby cool, offshore waters inundate the nearshore and begin to accumulate, or "pool" (Figure 3.2c). From hereafter, we will refer to this process as nearshore pooling.

The arrival of an internal bore is characterized by a strong near-bottom onshore (upslope) flow in the cross-shore and an along-shore flow out of the bay (Figure 3.2e and Figure 3.2f). During the relaxation of the bore (i.e., advecting out of the nearshore), the cross-shore velocity is highlighted by strong offshore (downslope) flow, while the along-shore velocity is directed back into the bay (Figure 3.2d and Figure 3.2f; see *Walter et al*. [2012]).

Examination of the NS potential energy density anomaly over the record reveals large fluctuations during weak upwelling conditions and relatively weaker fluctuations during the upwelling periods and nearshore pooling (Figure 3.3a). These fluctuations are superposed on a low-frequency trend, whereby during active upwelling the low-pass signal increases due to the increased stratification (i.e., nearshore pooling, Figure 3.3a). Removing this low-frequency trend yields the high-passed anomaly, or the bore strength proxy. The bore strength proxy characterizes the magnitude of the nearshore internal bores and closely follows the scale of the perturbation to the nearshore temperature field (Figure 3.3b and Figure 3.2c, respectively). During weaker upwelling conditions, the bore index has the greatest magnitude (Figure 3.3b), and these large fluctuations align with the large amplitude bores that perturb nearly the entire water column. In contrast, during strong upwelling, the bore strength proxy is weak (Figure 3.3b). This aspect coincides with periods of nearshore pooling, during which the bores generate small-amplitude perturbations to the pre-existing thermocline.

A time series of near-bed (1 mab) DO and temperature is shown in Figure 3.2d. Also highlighted is the DO concentration identified by *Vaquer-Sunyer and Duarte* [2008] as the threshold necessary to maintain 90% biodiversity (i.e., below 4.6 mg/L DO, 60% air saturation, hypoxic). Figure 3.2d highlights the strong covariation between DO concentration and water temperature (a linear regression between the two variables yields $R^2 = 0.77$, p-value < 0.001). During weak upwelling conditions and/or relaxations there are large fluctuations in DO and temperature, consistent with the large amplitude internal bores observed (e.g., Figure 3.3b). Likewise, the DO

concentrations stay above the critical biological threshold, and low DO levels observed in individual bore events do not persist. This is likely due to a combination of both the advection of the low DO water back offshore, and the stronger vertical mixing observed during the warm-front relaxations of the bores that acts to reoxygenate the water column ("mixing period" from *Walter et al*. [2012]). In contrast, during upwelling favorable conditions, low DO levels persist for extended periods of time and the intense fluctuations of DO and temperature are not observed (Figure 3.2d). During the nearshore pooling period, the low DO levels persist below the 4.6 mg/L hypoxic level [*Vaquer-Sunyer and Duarte*, 2008] for nearly three days (9 to 12 August; Figure 3.2d) and reach as low as 2.66 mg/L. It is important to note that the DO measurements presented in Figure 3.2d are near-bed (1 mab) measurements, while the bores observed during upwelling conditions typically perturb the mid-water thermocline region in the nearshore. Nonetheless, the decrease in DO fluctuations is consistent with the reduction in the bore strength index (Figure 3.3b).

Spectral analysis of the bore strength proxy reveals a dominant peak at the semi-diurnal frequency (M_2 tidal component, Figure 3.4c). The offshore thermocline depth also shows a dominant peak near the M_2 tidal component; however, there is also significant energy at low frequencies (< 0.3 cpd, Figure 3.4b). This low-frequency energy is consistent with the ~7-10 d period of the offshore thermocline depth (Figure 3.2b). Regional upwelling favorable winds are dominated by lower frequencies (< 0.3 cpd), while the semi-diurnal variability is largely absent (Figure 3.4a).

3.4.2: Connecting Offshore and Nearshore Dynamics

Regional upwelling favorable winds are significantly coherent with the offshore thermocline depth at low frequencies (e.g., < 0.4 cpd, Figure 3.5a). Analysis of the phase lag reveals that the thermocline height lags the winds at low frequencies of ~0.3 cpd and 0.1 cpd by ~0.67 d to 1.1 d, respectively (Figure 3.5b). The low-frequency coherence suggests that, as expected, the offshore stratification is largely governed by wind-driven upwelling/relaxation cycles during this 3 week period.

In order to examine how the temporally varying, offshore stratification affects the offshore internal wave/tide field, linear long-wave speeds were calculated using a normal mode analysis (see Section 3.3.3). The phase speed can be used as an index for the strength of the offshore stratification and internal waves. Figure 3.6 highlights how the phase speed changes over time due to the evolving offshore stratification. In particular, during periods of active upwelling when the offshore thermocline shoals towards the surface, phase speeds are lowest (i.e., wave amplitudes are the smallest). In contrast, during relaxation events, where surface waters are warmer and the thermocline is deeper, increased stratification leads to larger phase speeds. Active upwelling causes the thermocline to shoal towards the surface and decreases internal wave amplitudes, while relaxations deepen the thermocline and allow for increased wave phase speeds and amplitudes. Correspondingly, when the offshore wave field is weakest during upwelling periods, the nearshore bore index (high-pass filtered potential energy density anomaly) also displays the smallest magnitudes (Figure 3.6 and Figure 3.3b, respectively). Likewise, weak upwelling events/relaxations are

highlighted by a stronger offshore internal wave field that coincides with a larger nearshore bore index.

Coherence between the nearshore bore index and the offshore thermocline depth further supports the connection between offshore and nearshore internal dynamics. The two parameters are significantly coherent at the semi-diurnal frequency (~M_2 tidal component, Figure 3.7a). Analysis of the phase lag indicates that the nearshore index lags the offshore thermocline height by ~2.0 h at this frequency (Figure 3.7b). Given that there are only two moorings in the current study, it is impossible to assess accurately the propagation speed and direction of the internal wave field. Moreover, estimating internal wave transit times from the coherence analysis assumes that the internal wave field is propagating on a direct line from the OS to the NS mooring, an assumption that cannot be validated in the current study.

3.5: Discussion

3.5.1: Long-term Record and Offshore to Nearshore Connection

It is important to qualify the results presented above over the 3 week time period, especially since this short record only captured a few upwelling/relaxation cycles. To address this issue, we analyzed the OS data and low resolution NS data (i.e., temperature and DO at 1 mab) that are available over an approximately 2.5 month period (see Section 3.3.2 for details). Figure 3.8a highlights that over the longer record the upwelling favorable winds are characterized by the same periodic upwelling/relaxation cycles at low frequencies (~ 7-10 days) seen during the 3 week record [cf. *Beardsley et al.*, 1987]. This periodicity is confirmed by the upwelling

wind spectrum (Figure 3.9a), which also reveals the diurnal variability of the winds caused by diurnal sea breezes [e.g., *Woodson et al*., 2009]. Similar to the 3 week period, these upwelling (relaxation) cycles drive offshore cooling (warming) of the water column (Figure 3.8b). These cycles also generally result in shoaling (deepening) of the offshore thermocline and a decrease (increase) in the offshore internal wave activity, as seen in the phase speeds obtained from the normal mode analysis (Figure 3.8b and Figure 3.8d, respectively). Furthermore, Figure 3.8c highlights the nearshore response of temperature and DO to the low-frequency winds and offshore stratification. That is, a general decrease (increase) in DO and temperature during upwelling (relaxation) periods. Moreover, there are numerous low oxygen (i.e., below 4.6 mg/L; hypoxic) events observed during upwelling periods over the 2.5 month record (Figure 3.8c).

A coherence analysis was performed on the upwelling favorable winds and the offshore thermocline depth over the ~2.5 month record. The significant coherence at low frequencies (Figure 3.10) corroborates the fact that the offshore temperature structure is largely governed by wind-driven upwelling/relaxation cycles. Also evident in the coherence is a significant peak at the diurnal frequency, suggesting that the diurnal sea breeze also modulates the thermocline. While this diurnal frequency component was largely absent from the thermocline depth spectrum during the 3 week period, wavelet analysis (not shown) supports the fact that there is significant temporal variability in the diurnal frequency component of the offshore thermocline depth that is linked to periods of increased wind forcing.

Figure 3.11 confirms that changes in the offshore stratification result in modification of the offshore internal wave field. Specifically, increases (decreases) in the offshore thermocline depth generally result in increases (decreases) in the offshore normal mode phase speed, and therefore the strength of the offshore internal waves. In order to connect the offshore internal wave activity to nearshore internal bore activity, it is necessary to derive a new nearshore bore index over the 2.5 month record using the near-bottom temperature since the previously defined bore index (i.e., high-pass potential energy density anomaly) requires high resolution vertical density measurements that are only available during the 3 week period. Figure 3.12a shows a scatter plot over the 3 week period of the windowed-standard deviation (1 day windows with 50% overlap; results not sensitive to choice of window used) of the near-bottom temperature versus the potential energy density anomaly bore strength index. The two quantities are highly correlated (R^2 = 0.98 for the bin-averaged values, p-value < 0.001), indicating that the standard deviation of the near-bottom temperature can be used as a proxy for nearshore internal bore activity. Figure 3.12b shows a scatter plot over the 2.5 month period of this nearshore bore proxy (standard deviation of the near-bottom temperature) versus the offshore internal wave activity (normal mode phase speeds), and highlights how increases (decreases) in the offshore internal wave field translate into increases (decreases) in the nearshore bore field.

The results presented above offer insight into the connection between offshore and nearshore internal dynamics. We surmise that the internal bores observed in the nearshore are related to the onshore translation and propagation of the offshore internal tidal field (M_2 tidal component). However, it is important to note that there are

other factors that complicate the dynamics and predictability of not only the nearshore internal bores, but also the transformation and propagation of the offshore internal wave field to the nearshore [cf., *Nash et al*., 2012]. The recent review by *Lamb* [2013], and the references therein [e.g., *Nash et al*., 2012], provides a comprehensive overview of factors affecting the propagation and transformation of internal waves over the continental shelf. This includes, but is not limited to, strong barotropic tidal forcing, baroclinic effects and strong background shear, mesoscale and submesoscale variability, and complicated bathymetry including submarine canyons, all of which are found in the Monterey Bay region [*Breaker and Broenkow*, 1994].

There has also been considerable research into factors affecting the M_2 internal tide field in the Monterey Bay region, including the effects of the Monterey Submarine Canyon and Big Sur Ridge [e.g., *Carter*, 2010; *Kang and Fringer*, 2012]. However, the aforementioned studies are large-scale modeling efforts that do not account for upwelling/relaxation cycles or variable environmental conditions (i.e., stratification) on the shelf, and do not accurately capture internal dynamics on the shelf and in the nearshore. It is also possible that the internal wave field represents energy from multiple source locations (both locally and remotely generated internal tides), further complicating the predictability of the internal tide [cf., *Kelly and Nash*, 2010; *Nash et al*., 2012]. These factors make the predictability of the bores in the nearshore (and offshore) difficult, and might also explain why *Walter et al*. [2012] found no relationship between the arrival times of the nearshore bores and the phase of the local tides over a two-week period. Future field and modeling studies are needed to

assess the spatiotemporal variability of the internal tide field in Monterey Bay and elsewhere.

3.5.2: Oxygen Variability and Low Oxygen Events in the Nearshore

While it is well established that seasonal upwelling cycles contribute to oxygen variability and low oxygen events in the shallow waters along the eastern Pacific, the role of other physical processes is poorly understood [*Chan et al*., 2008]. In particular, previous observations near the study site clearly show regular intrusions of low DO water that are attributed to internal motions [*Booth et al*., 2012]. We expand on this work below and examine how nearshore internal bores in different upwelling regimes can lead to drastically different durations and onset rates of hypoxia in the nearshore.

Figure 3.13a and Figure 3.13b show scatter plots over the approximately 2.5 month study period of the windowed-standard deviation (1 day windows with 50% overlap; results not sensitive to choice of window used) of the near-bottom DO concentration versus the near-bottom temperature (i.e., long-term nearshore bore proxy). The important point is that there is extensive DO variability that is tightly linked to nearshore temperature variability (i.e., internal bore activity). Interestingly, the windowed-mean DO concentrations, seen as colored and scaled circles in Figure 3.13a, demonstrate that the lowest mean concentrations are observed during periods of reduced bore activity and oxygen variability. This coincides with periods of prolonged upwelling and nearshore pooling, whereby low oxygen waters (i.e., below 4.6 mg/L; hypoxic) are able to persist for several days. In contrast, Figure 3.13b shows the windowed-minimum DO concentrations and highlights that strong bore variability produces transient pulses of low oxygen (i.e., below 4.6 mg/L; hypoxic). This

indicates that while extended upwelling periods with reduced bore activity are important for the duration of low DO events, individual bores can drive shock-like drops in DO with rapid onset times. Indeed, both onset time and duration of the low DO events are important for assessing potential impacts of hypoxia, each with likely different implications for nearshore ecological communities.

Monterey Bay, as part of the California Current Large Marine Ecosystem (CCLME), is listed as a "hotspot" for ecological risk from upwelled hypoxia [*Hofmann et. al.*, 2011]. While the hypoxic durations presented here are relatively short (longest event lasts ~3 days from 9 to 12 August), the high frequency nature of individual bore events represent shock-like drops in oxygen which may amplify ecological impacts [*Burton et. al.*, 1980]. Additionally, rockfish (*Sebastes spp.*), which are abundant at the study site, have shown profound response to DO concentrations slightly below the concentrations reported here [*Grantham et al.*, 2004]. Avoidance, which often occurs in reported ranges of 2 - 4 mg/L [*Wannamaker and Rice*, 2000; *Brady and Targett*, 2010], can drive much greater indirect impacts, through density-dependent factors, than direct lethal effects [*Eby and Crowder*, 2002; *Breitburg et al.*, 2009; *Craig*, 2012]. Furthermore, measurements reported here cover habitat for ecologically and commercially important species. Dungeness crabs (*Cancer magister*) and market squid (*Loligo opalescens)*, two of California's most valuable commercial species, have shown major sensitivity to hypoxia [*Vojkovich,*1998; *Grantham et. al.*, 2004; *Zeidberg et al.*, 2006], and are particularly relevant here due to their dependence on habitat within this study site and their likely sensitivity to nearshore pooling [*Young et al.*, 2011; *Zeidberg et al.*, 2012].

3.5.3: Bores as a Mechanism for Cross-shelf Exchange

Figure 3.14 shows vertical profiles of temperature and cross-shore velocity for a representative bore event on 16 August. The arrival of the bore and the dense, offshore waters are characterized by a strongly sheared baroclinic flow with onshore flow near the bed and offshore flow in the upper portion of the water column (Figure 3.14b). Eventually, the bore reverses direction and propagates back downslope with offshore flow near the bed and onshore flow near the surface. During this phase, the strongest cross-shelf velocities are observed, and the vertical profiles are bottom intensified (i.e., strongest near the bed). The flow reversal, or the relaxation of the bore back downslope, has been implicated in the onshore transport of larvae in the warm-water front that appears in Figure 3.14a (~8:30 – 9:00) [e.g., *Pineda*, 1994; "mixing period" in *Walter et al.*, 2012]. We note that the Monterey Bay study site contains steeper bathymetric slopes and a more complex shoreline compared to the gradually sloping bathymetry typically found in Southern California [e.g., *Pineda*, 1994; *Wong et al*., 2012] resulting in slightly different bore dynamics (see *Walter et al*. [2012]). Nonetheless, this period of the bore event consistently has the strongest cross-shelf velocities, and previous observations indicate that elevated levels of diapycnal mixing in the stratified interior are observed during the warm-water relaxations [*Walter et al*., 2012]. Thus, not only are scalars exchanged in the cross-shelf direction during these flows, but they are also likely mixed vertically.

We employed an empirical orthogonal function (EOF) analysis on the cross-shelf velocity field over the 3 week period to decompose the signal into its principal components, or dominant statistical modes. The EOF analysis provides a description

of the spatial variability of the velocity field through the modal shapes (eigenfunctions), as well as the temporally variability through the modal amplitude time series [*Emery and Thompson*, 2004]. Figure 3.15 highlights the vertical structure of the first three principal components (EOF modal shapes) of the cross-shore velocity field, along with the percent contribution of each mode to the total variance. The first mode, which describes 52.5% of the total variance, follows the vertical structure of the cross-shore velocity observed during the bore events (Figure 3.15 and Figure 3.14b, respectively). Particularly, the profile represents a sheared baroclinic structure that is bottom intensified (i.e., non-zero depth average and largest magnitude near the bottom of the water column), similar to the bore events observed. Spectral analysis of the first mode amplitude time series reveals a dominant peak at the semidiurnal frequency (~M_2 tidal component, Figure 3.4d). Furthermore, the coherence between the bore strength index and the first mode amplitude time series is significant at the semidiurnal frequency (~M_2 tidal component, significant squared coherence of 0.52, not shown). This finding further supports the claim that the bores dominate cross-shelf exchange and transport in the nearshore, and that these bores likely contribute to the majority of the cross-shelf velocity variance observed. While velocity measurements were only available over the 3 week study period, long-term measurements in the region demonstrate that wind- and wave-driven cross-shelf exchange is small compared to exchange by internal bores [*Woodson,* 2013].

3.6: Summary

The ultimate fate of NLIWs and bores in shallow, nearshore regions (~20 m) has been mainly speculative [cf. *Lamb* 2013], despite their biological and ecological implications [*Wolanski and Pickard*, 1983; *Leichter et al.*, 1996; *Boehm et al.*, 2002; *Pineda*, 1991, 1994, 1995, 1999; *Booth et al*., 2012; *Walter et al*., 2012; *Wong et al*., 2012]. *Pineda and Lopez* [2002] first hypothesized that low-frequency phenomena modulate the offshore stratification, and in turn affect nearshore internal bores in Southern California. We expand on this early work and present observations suggesting that low-frequency upwelling wind patterns modulate the offshore stratification and thermocline depth in southern Monterey Bay, CA, which in turn alters the strength and structure of the bores in the shallow, nearshore region (Figure 3.16).

The internal bore events are shown to contribute to the majority of the variance in cross-shelf exchange and transport in the nearshore. Furthermore, we link the nearshore oxygen variability to the nearshore bore activity. We show that individual bores can create short-lived low DO (hypoxic) events with shock-like onset times, but that extended upwelling periods are important for the duration of low DO episodes. Further assessment of how the strong DO variability and low DO (hypoxic) events affect nearshore communities is the subject of ongoing research. Likewise, future studies are needed to further assess the spatiotemporal variability of the internal wave/tide field in Monterey Bay [e.g., *Nash et al*., 2012], including further assessment of its formation and energetics [*Carter*, 2010; *Kang and Fringer*, 2012]. We recognize that the detailed measurements throughout the water column at the nearshore site were

only available over a 3 week study period, and that inferences were made about the nearshore internal bore field over the 2.5 month period using the near-bottom temperature (see Section 3.5.1, Figure 3.12a). Given this, we stress that care should be taken in drawing generalized conclusions about the processes described, especially over longer time periods. Finally, the observations were collected during the late upwelling season in Monterey Bay; further observations are needed to assess the influence of the seasonal variability in the upwelling winds [cf., *García-Reyes and Largier*, 2012], and the oceanic response, as well as the extension of the results to other upwelling systems and sites.

3.7: Acknowledgements

This work was funded by the National Science Foundation through grants OCE-1235552 and DEB-1212124, and by the Singapore Stanford Program. R. Walter was supported by the Stanford Graduate Fellowship. This manuscript greatly benefited from the helpful comments of three anonymous reviewers. We acknowledge helpful discussions with Jeff Koseff, Derek Fong, Oliver Fringer, Kurt Rosenberger, Curt Storlazzi, and Olivia Cheriton. Data used in this study are available by contacting R. Walter. Offshore data used in this study were provided to R. Walter by the United States Geological Survey's Pacific Coastal and Marine Science Center. Bathymetry data used in this study were acquired, processed, archived, and distributed by the Seafloor Mapping Lab of California State University Monterey Bay.

3.8: Figures

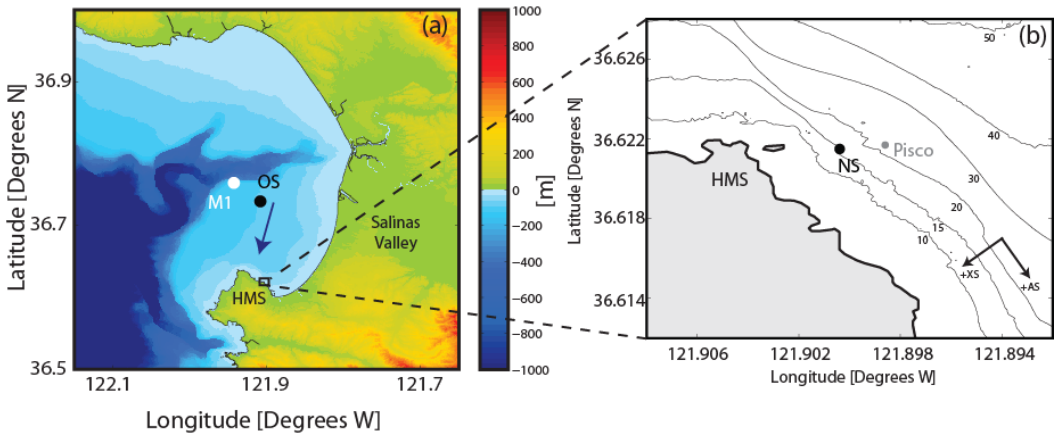

Figure 3.1: (a) Bathymetry and topography of the Monterey Bay, CA region with the study site indicated by a black box. The filled circles represent the offshore mooring (OS, black) and M1 buoy (white). Also shown is the median bore propagation heading from *Walter et al*. [2012] (blue arrow). (b) Study site with the nearshore mooring (NS) shown as a filled black circle. Also Bathymetry contours (10, 15, 20, 30, 40, 50 m isobaths) shown along with the location of Hopkins Marine Station (HMS – Stanford University).

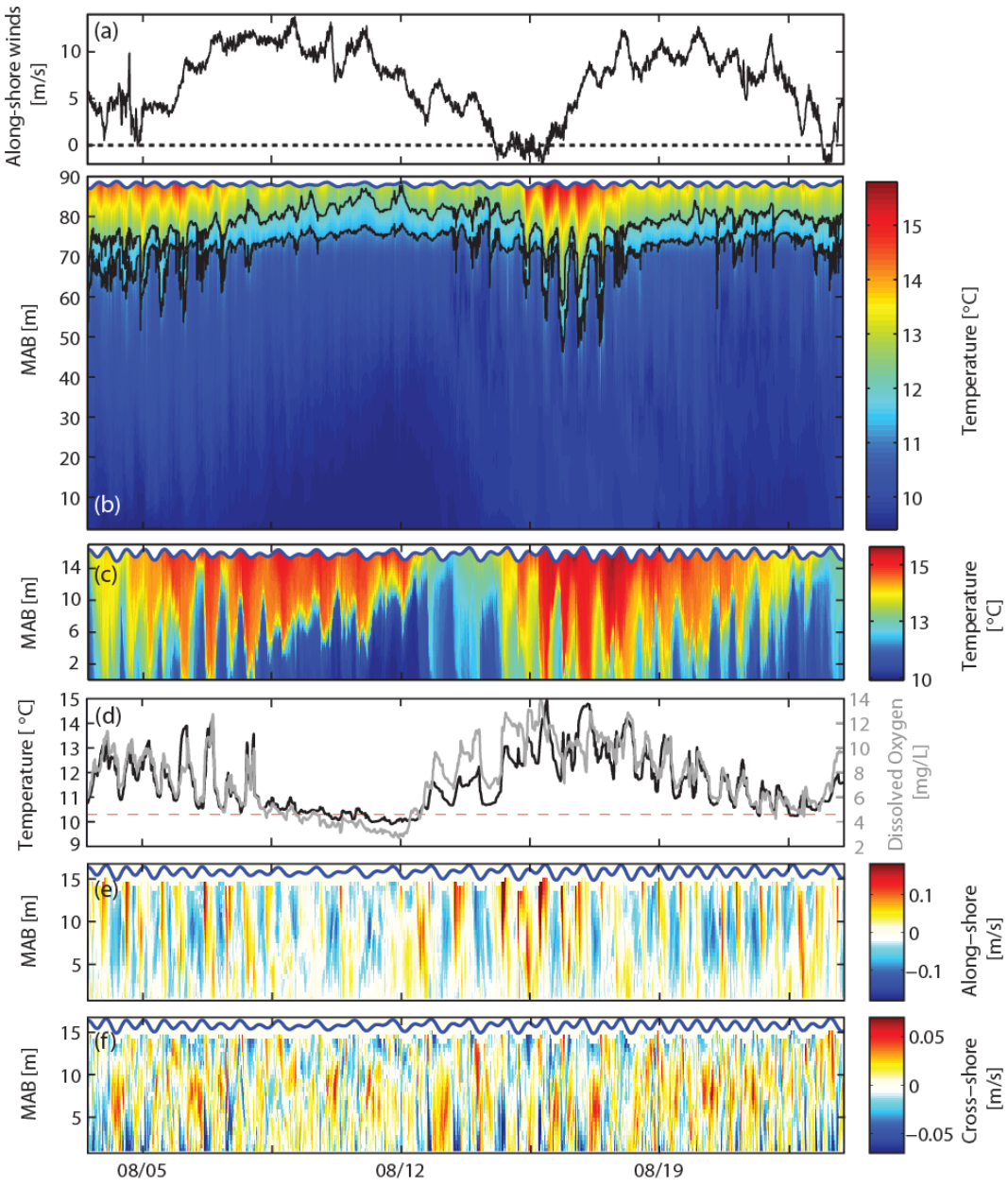

Figure 3.2: Time series over the 3 week study period of the (a) regional upwelling favorable winds (positive), (b) vertical temperature structure at the offshore (OS) mooring (11.2° and 12.15° isotherms shown as solid black lines highlight the thermocline structure), (c) vertical temperature structure at the nearshore (NS) mooring, (d) near-bottom temperature (left axis, black) and dissolved oxygen (right axis, grey) at the NS mooring, and the vertical velocity structure (ten-minute averages) at the NS mooring for the (e) along-shore (positive into the bay) and (f) cross-shore (positive onshore) velocity components, respectively. The location of the sea surface (blue line) is shown in panels (b-c) and (e-f). The dashed red line in panel (d) denotes the DO concentration identified by *Vaquer-Sunyer and Duarte* [2008] as a critical biological threshold (i.e., below 4.6 mg/L; hypoxic).

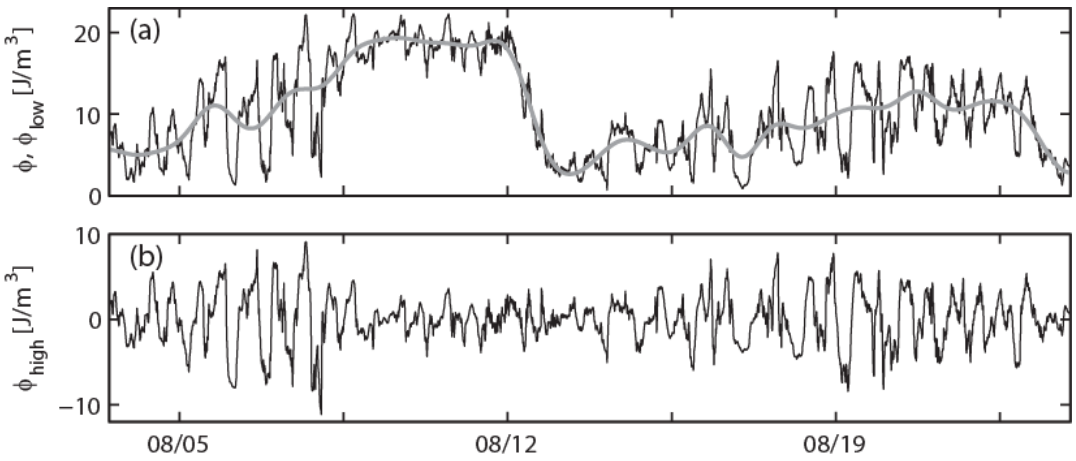

Figure 3.3: Time series over the 3 week study period of the (a) potential energy density anomaly (low-pass filtered time series shown in grey) and (b) high-pass filtered anomaly (bore strength proxy) at the nearshore (NS) study site.

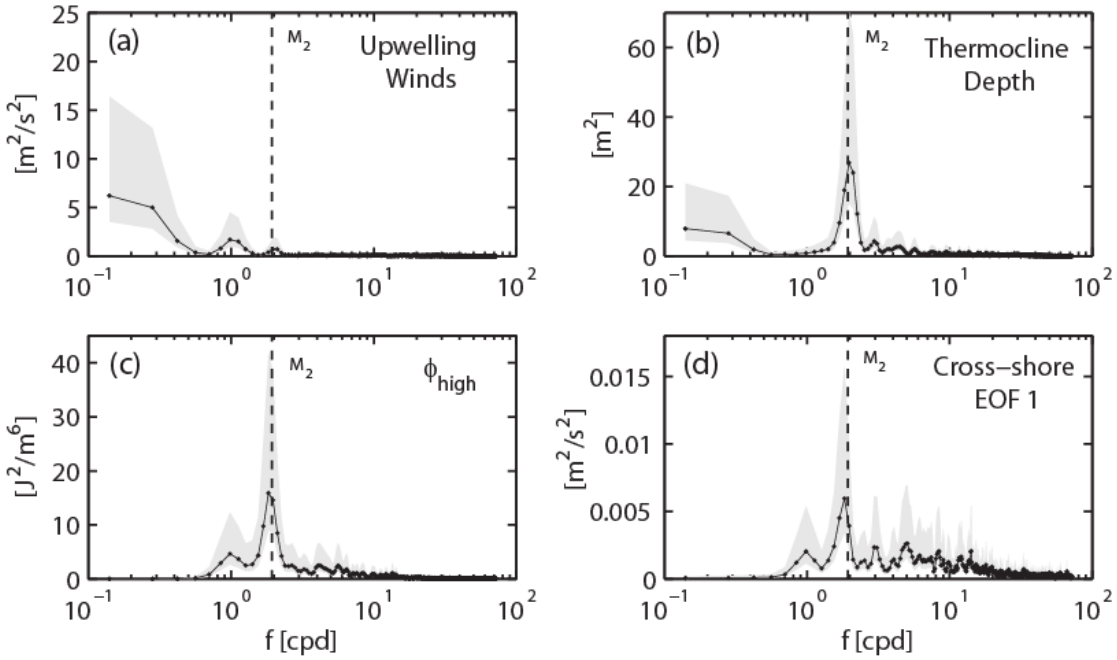

Figure 3.4: Variance-preserving power spectra over the 3 week study period of the (a) regional upwelling winds, (b) offshore thermocline depth (11.2° isotherm), (c) high-pass filtered potential energy density anomaly (bore strength proxy), and (d) 1st mode, EOF amplitude time series of the cross-shore velocity field. 80% confidence intervals are denoted by grey shading and the location of the M_2 tidal component by a dashed black line.

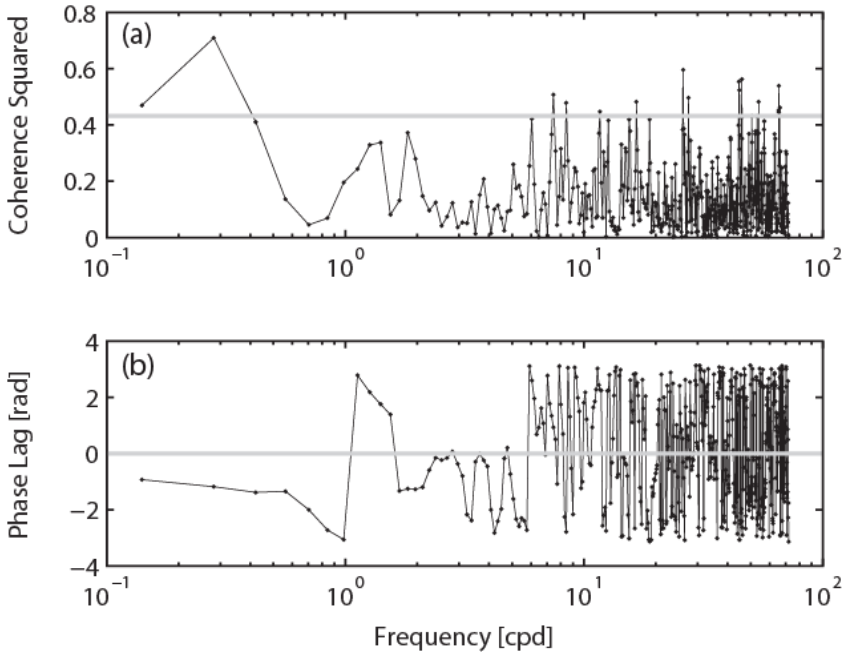

Figure 3.5: Coherence squared (a) and phase lag (b) between the regional upwelling favorable winds and the offshore thermocline depth (11.2° isotherm) over the 3 week study period. The 95% confidence level is shown as a grey line in panel (a). A negative phase lag at a given frequency indicates that the upwelling winds lead the offshore thermocline depth.

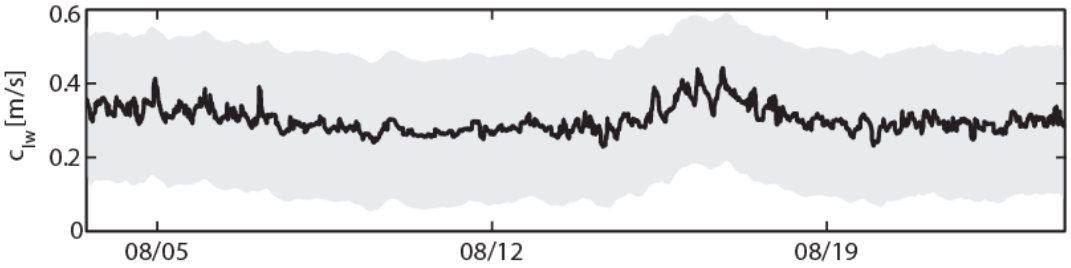

Figure 3.6: Linear, long-wave phase speeds from the offshore mooring (black line) over the 3 week study period. Internal wave phase speeds were calculated using the offshore stratification (ten-minute averages) and a normal mode analysis (Section 3.3.3). The grey shading denotes the phase speed in the presence of a typical barotropic current on the shelf of +/- 0.2 m/s [e.g., *Breaker and Broenkow*, 1994].

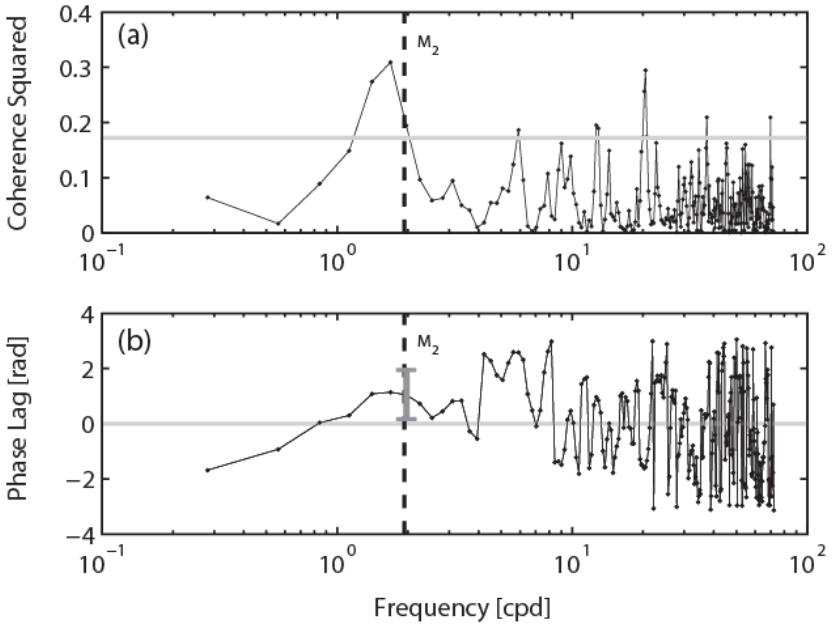

Figure 3.7: Coherence squared (a) and phase lag (b) between the high-pass filtered potential energy density anomaly (bore strength proxy) and the offshore thermocline depth (11.2° isotherm) over the 3 week study period. The 90% confidence level is shown as a grey line in panel (a). The location of the M_2 tidal component is denoted by a dashed black line in (a) and (b). Confidence levels for the phase lag at the semi-diurnal frequency (~M_2 tidal component) is shown in (b) as a grey error bar. A positive phase lag at a given frequency indicates that the bore strength proxy lags the offshore thermocline depth.

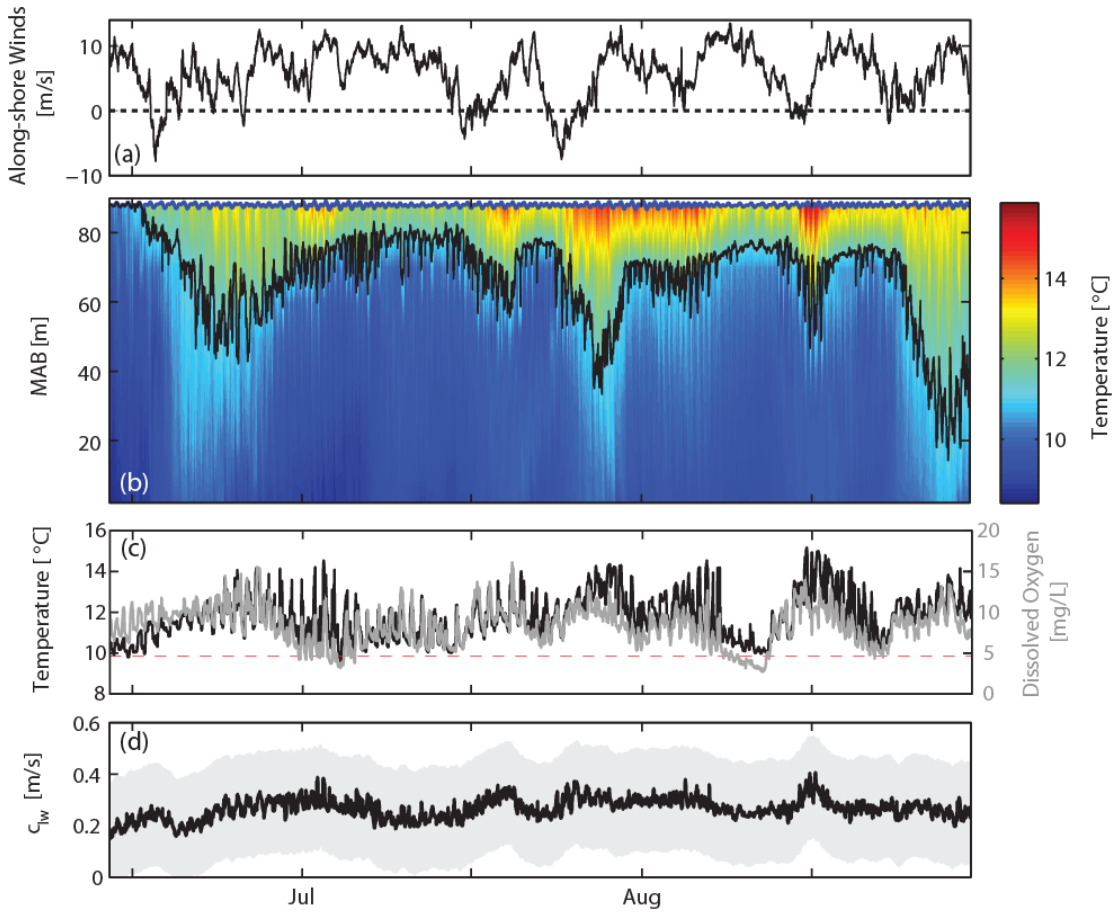

Figure 3.8: Time series over the approximately 2.5 month study period of the (a) regional upwelling favorable winds (positive), (b) vertical temperature structure at the offshore (OS) mooring (11.2° isotherm shown as a solid black line to highlight the thermocline structure), (c) near-bottom temperature (left axis, black) and dissolved oxygen (right axis, grey) at the NS mooring, and (d) linear, long wave speeds from the OS mooring (black line) calculated using the OS stratification (ten-minute averages) and a normal mode analysis (Section 3.3.3). The location of the sea surface (blue line) is shown in panel (b). The dashed red line in panel (c) denotes the DO concentration identified by *Vaquer-Sunyer and Duarte* [2008] as a critical biological threshold (i.e., below 4.6 mg/L; hypoxic). The grey shading in panel (d) denotes the phase speed in the presence of a typical barotropic current on the shelf of +/- 0.2 m/s [e.g., *Breaker and Broenkow*, 1994].

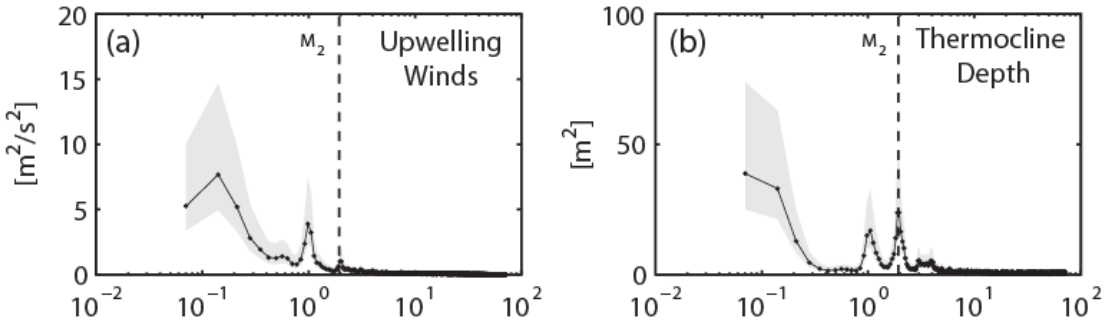

Figure 3.9: Variance-preserving power spectra over the approximately 2.5 month study period of the (a) regional upwelling winds and the (b) offshore thermocline depth (11.2° isotherm). 80% confidence intervals are denoted by grey shading and the location of the M_2 tidal component by a dashed black line.

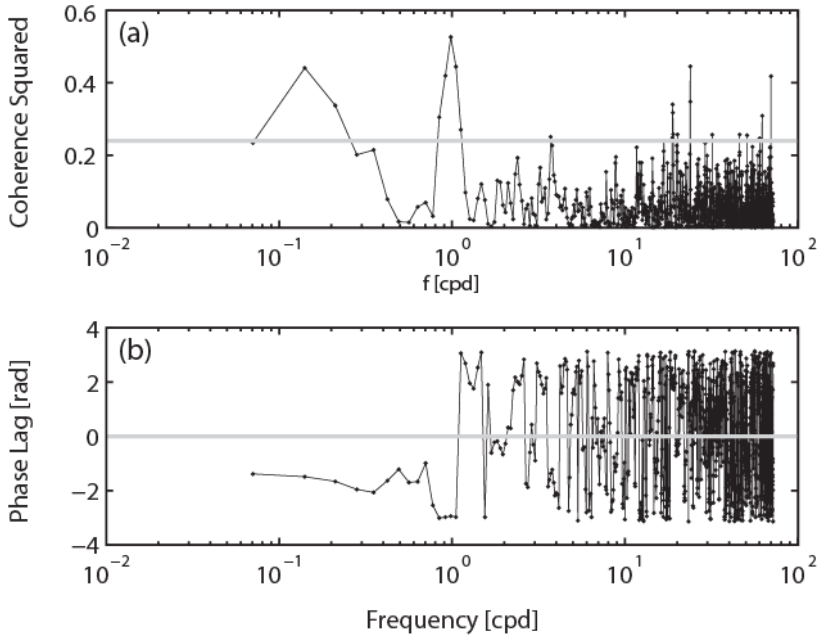

Figure 3.10: Coherence squared (a) and phase lag (b) between the regional upwelling favorable winds and the offshore thermocline depth (11.2° isotherm) over the approximately 2.5 month study period. The 95% confidence level is shown as a grey line in panel (a). A negative phase lag at a given frequency indicates that the upwelling winds lead the offshore thermocline depth.

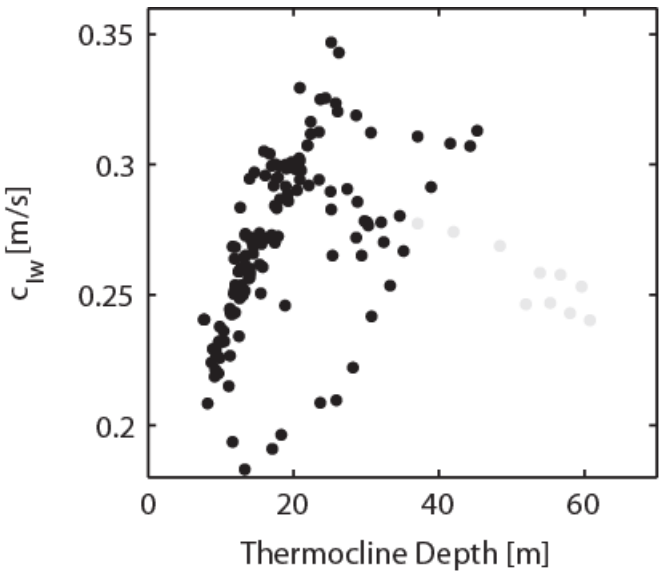

Figure 3.11: Scatter plot over the approximately 2.5 month study period of the windowed-mean linear, long wave speeds from the offshore (OS) mooring calculated using the OS stratification (ten-minute averages) and a normal mode analysis (Section 3.3.3; proxy for the strength of the offshore internal wave/tide field) and the windowed-mean of the OS thermocline depth (11.2° isotherm). Mean values were calculated using 1 day windows with 50% overlap, and results were not sensitive to the choice of window used. The grey dots denote the period from 26 August to 30 August, during which an extended relaxation event resulted in anomalously large thermocline depths.

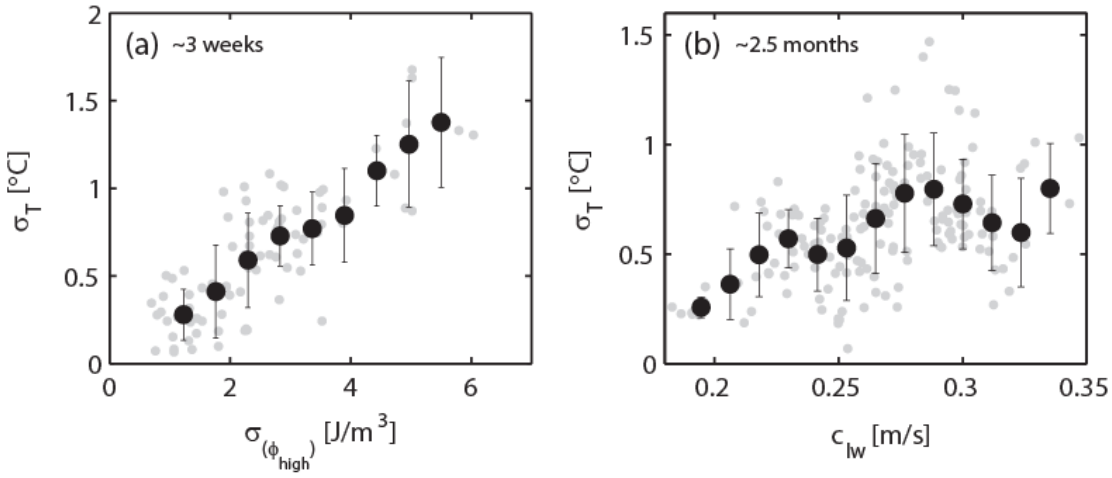

Figure 3.12: (a) Scatter plot over the 3 week study period of the windowed-standard deviation of the near-bottom temperature (long-term bore strength proxy) and the windowed-standard deviation of the high-pass filtered potential energy density anomaly (short-term bore strength proxy), both from the nearshore (NS) mooring. (b) Scatter plot over the approximately 2.5 month study period of the windowed-standard deviation of the near-bottom temperature (long-term bore strength proxy) at the NS mooring and the linear, long wave speeds from the offshore (OS) mooring calculated using the OS stratification (ten-minute averages) and a normal mode analysis (Section 3.3.3; proxy for the strength of the offshore internal wave/tide field). Windowed-standard deviation values were calculated using 1 day windows with 50% overlap, and results were not sensitive to the choice of window used. The grey dots denote the windowed values, while the black dots represent bin-averaged values. The black error bars on the bin-averaged values signify the standard deviation of the binned results.

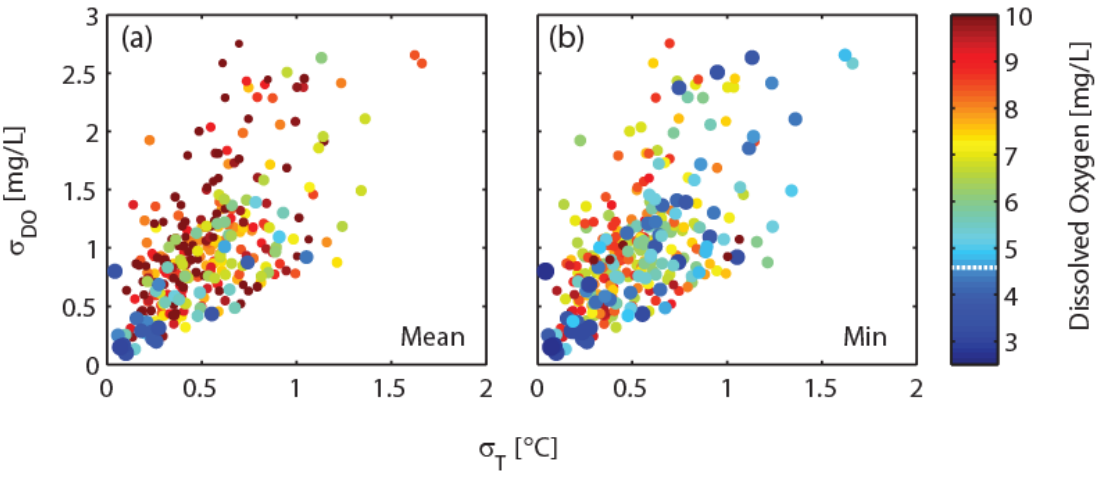

Figure 3.13: Scatter plot over the approximately 2.5 month study period of the windowed-standard deviation of the near-bottom dissolved oxygen (DO) concentration and the windowed-standard deviation of the near-bottom temperature (long-term bore strength proxy), both from the nearshore (NS) mooring. Windowed-standard deviation values were calculated using 1 day windows with 50% overlap, and results were not sensitive to the choice of window used. The colored circles in panels (a) and (b) denote the windowed-mean and windowed-minimum dissolved oxygen concentrations, respectively, as indicated in the colorbar. The size of the circles has also been scaled to highlight the low DO values (i.e., larger circles indicate lower DO concentrations). The dashed white line on the colorbar signifies the DO concentration identified by *Vaquer-Sunyer and Duarte* [2008] as a critical biological threshold (i.e., below 4.6 mg/L; hypoxic).

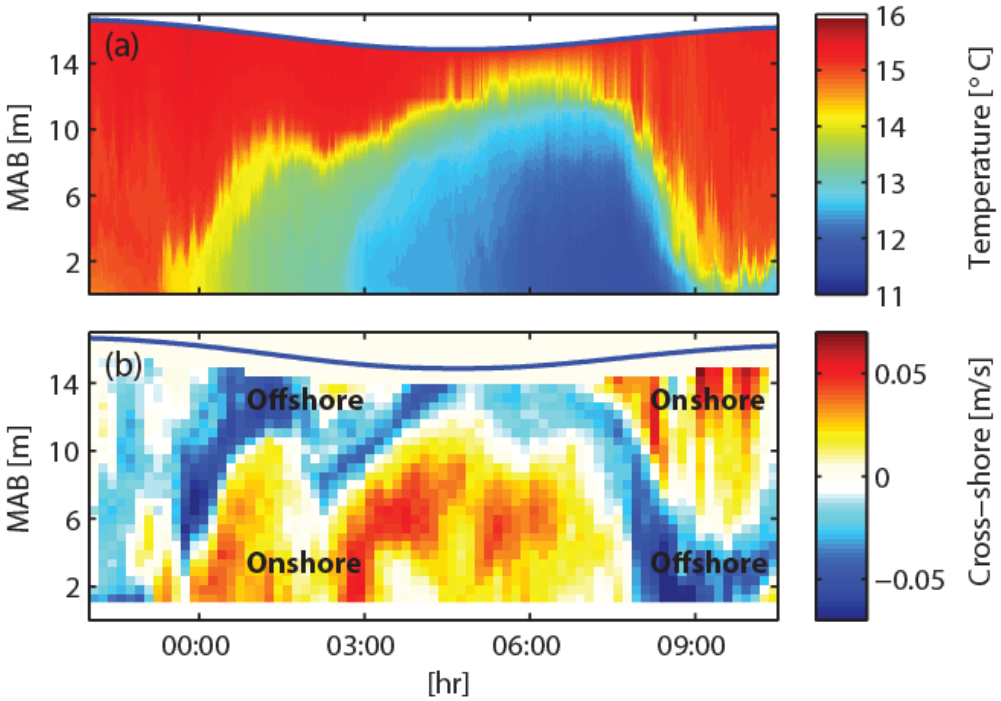

Figure 3.14: Example nearshore internal bore event from 16 August 2012. (a) Vertical temperature structure. (b) Cross-shore velocity structure (positive onshore, ten-minute averages). The location of the free surface (blue line) is shown in panels (a) and (b).

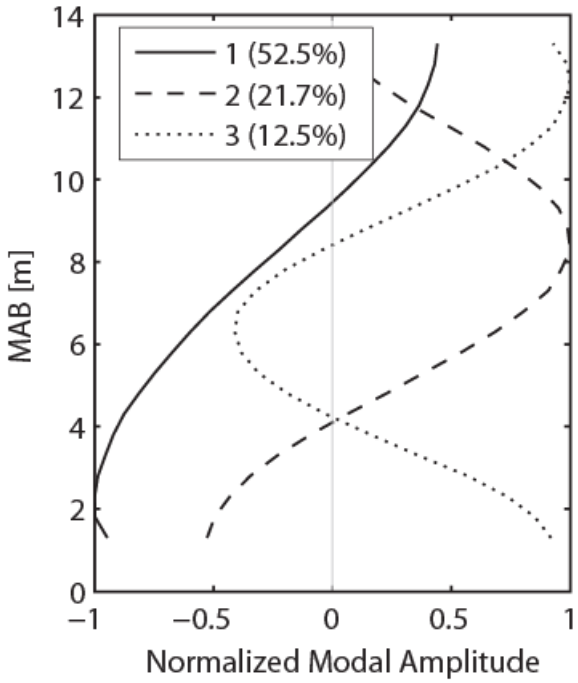

Figure 3.15: Vertical profiles for the first three statistical modes obtained from the EOF analysis for the cross-shore velocities over the 3 week study period. The first, second, and third modes are represented by solid, dashed, and dotted black lines, respectively, and the percent contribution to the total variance of each mode is also shown in the legend. The modal amplitude is normalized by the maximum vertical value for each component.

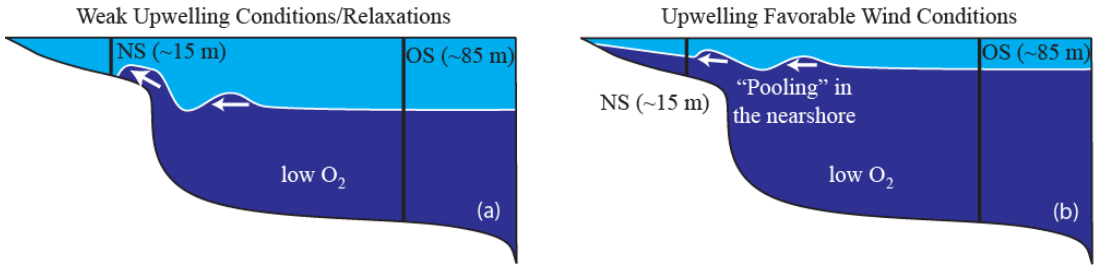

Figure 3.16: Schematic cartoon highlighting how wind-driven upwelling and offshore stratification influence nearshore internal bores. (a) During weak upwelling conditions/relaxations, the offshore thermocline is deeper, internal wave activity increases in the offshore, nearshore bore activity increases, and the bores propagate into well-mixed waters in the nearshore. (b) During upwelling favorable conditions, the offshore thermocline shoals towards the surface, offshore internal wave and nearshore bore activity both decrease, "pooling" develops in the nearshore, and the nearshore bores perturb a pre-existing stratification.

Chapter 4: Stratified turbulence in the nearshore coastal ocean: dynamics and evolution in the presence of internal bores

This chapter is prepared as a manuscript for future submittal. As the main author of the work, I made the major contributions to the research and writing. Co-authors include Michael Squibb[1], C. Brock Woodson[2], Jeffrey R. Koseff[1], and Stephen G. Monismith[1].

[1]Environmental Fluid Mechanics Laboratory, Stanford University, Stanford, CA, USA

[2]COBIA Lab, College of Engineering, University of Georgia, Athens, GA, USA

4.1: Abstract

High-frequency measurements of stratified turbulence throughout the water column were collected over a two-week period in the nearshore environment of southern Monterey Bay, CA using a cabled observatory system and an underwater turbulence flux tower. The tower contained a vertical array of acoustic Doppler velocimeters and fast-response conductivity-temperature sensors, providing a nearly continuous data set of turbulent velocity and density fluctuations and a unique look into the stratified turbulence field. The evolution of various turbulence quantities and direct measurements of the vertical turbulent diffusivity are examined in the presence of nearshore internal bores, both in the near-bed region and in the stratified interior. We show that individual bores can drive substantial changes to local turbulence and mixing dynamics, with considerable differences between the leading and trailing edges of the bores. Using direct observations of the flux Richardson number, our measurements confirm previous observations that show the highest mixing efficiencies (Γ) occurring in regions of buoyancy-controlled turbulence. Parameterizations of the flux Richardson number as a function of the turbulence activity number are also presented. Finally, we demonstrate that the commonly used assumption of a constant mixing efficiency ($\Gamma = 0.2$) for calculating turbulent diffusivities leads to significant overestimates compared to diffusivity values calculated using the directly measured mixing efficiency. Implications of the results are discussed.

4.2: Introduction

Continental shelves are thought to be an important, yet highly variable, contributor to mixing and the dissipation of turbulent kinetic energy in the oceans [*Munk and Wusch*, 1998; *Carter et al.*, 2005]. Furthermore, estimates of turbulent mixing in coastal zones are important for understanding the vertical mixing of tracers, with significant biological and ecological implications [e.g., *Boehm et al.*, 2002; *Leichter et al.*, 1996; *Pineda*, 1994]. Specifically, diapycnal mixing affects many ecologically important processes such as nutrient cycling, primary production, hypoxia development, and the mixing of tracers such as pollutants from sewage outfalls [e.g., *Wolanski and Pickard*, 1983; *Leichter et al.*, 1996; *Boehm et al.*, 2002; *Chan et al.*, 2008]. The dynamics of stratified turbulence have been investigated widely in both the laboratory [cf. *Itsweire et al.*, 1986; *Ivey and Imberger*, 1991; etc.] and numerical simulations [cf. *Holt et al.*, 1992; *Shih et al.*, 2005; etc.]; however, extensive field measurements of stratified turbulence on the shelf are somewhat limited (see *Davis and Monismith* [2011] and the references therein). While microstructure profiler measurements have revealed much insight into oceanic turbulence, turbulence on the shelf is highly intermittent in time and extremely patchy in space [e.g., *Moum and Rippeth*, 2009]. Indeed, the combined effects of boundary layers (bottom and surface), variable stratification, vertical velocity shear, internal waves, and a host of other physical processes in the coastal environment contribute to the complex spatiotemporal variability of turbulence, making it difficult to obtain comprehensive measurements using discrete profiles. Turbulence measurements have expanded to moored platforms in recent years in order to capture extended time series of high

frequency events and provide a closer examination of turbulence in highly dynamic systems [cf. *Shaw et al.*, 2001; *Davis and Monismith*, 2011].

In order to represent the energetics of turbulent velocity fluctuations, and also provide a means for evaluating and understanding turbulence measurements, the turbulent kinetic energy (TKE) equation is employed [e.g., *Tennekes and Lumley*, 1972]:

$$-\frac{\partial}{\partial t}\left(\frac{\overline{u_i' u_i'}}{2}\right) - U_j \frac{\partial}{\partial x_j}\left(\frac{\overline{u_i' u_i'}}{2}\right) - \frac{\partial}{\partial x_j}\left(\frac{1}{\rho_o}\overline{p' u_j'} + \frac{1}{2}\overline{u_i' u_i' u_j'} - 2\nu \overline{u_i' e_{ij}}\right) - \overline{u_i' u_j'}\frac{\partial U_i}{\partial x_j} = \frac{g}{\rho_o}\overline{\rho' u_3'} + \varepsilon . \tag{4.1}$$

Here $x_j = [x, y, z]$ is the spatial coordinate with z positive upwards, $u_i = [u, v, w]$ represents the velocity vector, $U_i = [U, V, W]$ is the time-averaged velocity vector, $u_i' = [u', v', w']$ is the turbulent velocity vector, $\rho = \rho_o + \rho'$ is the density field with contributions from time-averaged and fluctuating components, p is the pressure, ν is the kinematic viscosity, $e_{ij} = \frac{1}{2}\left(\frac{\partial u_i'}{\partial x_j} + \frac{\partial u_j'}{\partial x_i}\right)$ is the fluctuating strain rate tensor, ε is the TKE dissipation rate, and an overbar represents an appropriate Reynolds average. The first two terms on the left hand side (LHS) represent the time rate of change of TKE and rate of change of TKE due to advection by the mean flow, respectively. The next term on the LHS represents energy flux divergences, and specifically spatial transport due to pressure fluctuations, the turbulence itself, and viscous stresses, respectively. The final term on the LHS is the shear production (P) of TKE from the mean flow through the interaction of the Reynolds stress with the mean velocity shear field. The first term on the right hand side (RHS) denotes the buoyancy flux (B). A positive B

signifies a loss of TKE to potential energy in a stably stratified fluid, while a negative *B* implies buoyant production of TKE (i.e., counter-gradient flux) and typically occurs in an unstably stratified fluid. The last term on the RHS represents the loss, or dissipation (ε), of TKE to internal energy by viscosity and small-scale strains. Note that wave-turbulence interaction terms that arise from the decomposition of the velocity vector into time-averaged, periodic, and fluctuating components and the triple decomposition of the TKE equation are not included, as they require a closure model and cannot be estimated accurately in the field [*Reynolds and Hussain*, 1972; *Davis and Monismith*, 2011].

Despite its importance for understanding turbulence measurements, there exists a paucity of literature examining the TKE budget in marine bottom boundary layers. The assumption of equilibrium turbulence, whereby the shear production of TKE balances the dissipation of TKE ($P = \varepsilon$), has been tested in several strong tidal flows. *Gross and Nowell* [1985], *Trowbridge et al.* [1999], and *Sanford and Lien* [1999] all found that close to the bed, there was a local balance of production and dissipation. However, *Sanford and Lien* [1999] found that away from the bed, dissipation exceeded production. Likewise, *Walter et al.* [2011] surmised that the advection of non-local TKE was likely responsible for dissipation exceeding production near the bed in a shallow tidal flow, possibly due to inhomogeneous bathymetry and bottom roughness (i.e., vegetation). While valuable, the above studies were limited to measurements near the bed in strong tidal flows with little, or no, density stratification present.

Shaw et al. [2001] examined the TKE budget on the continental shelf in a stratified environment and found that near the bed buoyancy fluxes were negligible so that there was a local balance between production and dissipation. Further up in the water column (4.35 m above the bottom in ~70 m of water), stratification and buoyancy fluxes were important; however, the local TKE budget (i.e., $P = B + \varepsilon$) did not close. *Feddersen et al.* [2007] collected nearshore measurements close to the surf zone (~3.2 m depth) and found that shear production was much less than dissipation, concluding that non-local transport of turbulence was important. *Reidenbach et al.* [2006] found a local balance of production and dissipation over a coral reef and sandy bottoms near the bed (1 m above the bottom); however, these measurements were limited to the bottom mixed layer and were likely not influenced by stratification and other processes further up in the water column (water depths of 8 – 24 m at different sites). Most recently, *Davis and Monismith* [2011] studied internal waves shoaling on the inner shelf (19 m depth) using high frequency turbulence measurements near the bed (3 m above the bed maximum instrument height). TKE balances in this complex stratified shear-flow environment revealed that dissipation greatly exceeded production by nearly an order of magnitude, while buoyancy fluxes were generally negligible. The authors suggested that the horizontal transport of non-local TKE by internal wave driven flows was responsible for the imbalance.

The aforementioned studies offer a glimpse into the knowledge gap that exists in analyzing and understanding the TKE budget in the stratified coastal environment. In particular, previous studies have been limited to near-bed measurements. Indeed, the standard conceptual model of a bottom mixed layer under a stratified interior is

that the presence of stratification acts to dampen vertical velocity fluctuations and confines the bottom-generated TKE to the region near the bed where it is unable to penetrate vertically. However, recent observations of nearshore internal bores reveal that the dissipation of turbulent kinetic energy in the stratified interior, estimated using isopycnal slope spectra, is comparable, and in some cases, greater than the dissipation of TKE associated with bottom-generated turbulence [*Walter et al.*, 2012]. Additionally, there have been an increased number of observations documenting the generation of TKE by nonlinear internal waves in the stratified interior [e.g., *Moum et al.*, 2003; *Woodson et al.*, 2011]. It is clear that the turbulence structure in the presence of nonlinear internal waves and bores may be substantially different than that expected from the standard model of a bottom mixed layer under a stratified interior. Questions arise as to how the TKE budget will evolve throughout the water column in the presence of stratified shear flows such as those seen with nonlinear internal waves and bores, with important implications for vertical mixing processes.

This study looks at high-frequency turbulence measurements throughout the water column in the nearshore coastal environment, both in the stratified interior and near the bed. We take advantage of a cabled observatory system at Hopkins Marine Station of Stanford University in southern Monterey Bay, CA, which allows for nearly continuous measurements in time. Nearshore internal bores are a common feature that produce transient stratification and mixing events, and represent the dominant source of variability, in this ecologically important region [*Walter et al*., 2012; see *Walter et al*. [2014] for a description of how regional scale upwelling and changing offshore (shelf) conditions influence the observed bores]. Internal bores at this site are marked

by an upslope surging flow of subthermocline water that tends to stratify the water column (leading edge of the bore, or the "bore period" from *Walter et al*. [2012]). This period is followed by a strongly sheared downslope flow in the form of a warm-front, high frequency temperature oscillations, and elevated levels of turbulent dissipation, as the bore features relax back downslope (trailing edge of the bore, or the "mixing period" from *Walter et al*. [2012]). However, it is important to note that the isopycnal slope spectra method used to calculate turbulent dissipation was only appropriate during the "mixing period," and the TKE dissipation represented a time-averaged value over the mixing period (~several hours; see *Walter et al*. [2012]). A more detailed examination of how the nearshore internal bores affect TKE dissipation, as well as other turbulence quantities, across the various periods, or phases, of the bores is warranted.

The main objective of this work is to better characterize the dynamics of stratified turbulence in the nearshore coastal environment. We also seek to better understand the evolution of turbulence in the presence of nearshore internal bores. Not only do these measurements provide a better understanding of the modification to the turbulence dynamics by internal bores, but they also comprise one of the most comprehensive sets of stratified turbulence data collected in the coastal environment. In Section 4.3, we introduce the field site, the experimental setup and underwater turbulence flux tower, and data processing methods. Section 4.4 describes the evolution of the turbulence dynamics at various heights throughout the water column, including the strongly stratified interior, during various conditions and in the presence of nonlinear internal bores. Section 4.5 highlights and describes the various stratified

turbulence regimes observed, as well as turbulent mixing dynamics. Finally, we summarize the findings and discuss implications in Section 4.6.

4.3: Site Description, Experimental Setup, and Methods

4.3.1: Site Description and Experimental Setup

Monterey Bay is located along the central coast of California within the highly productive California Current Large Marine Ecosystem (CCLME) (Figure 4.1a). It is a semi-enclosed embayment that features one of the largest submarine canyons on the west coast of the United States. Monterey Bay also contains a narrow continental shelf with about 80% of the bay shallower than 100 m [*Breaker and Broenkow*, 1994]. Additionally, it is home to large commercial fisheries, as well as some of the west coast's largest kelp (*Macrocystis pyrifera*) forests, the latter of which are a critical habitat and nursery for nearshore biological communities.

Tides in Monterey Bay are mixed semi-diurnal, with currents dominated by the M_2 (~12.42 hr period) tidal component [cf. *Rosenfeld et al*., 2009; *Carter*, 2010]. Moreover, large amplitude internal waves are a well-documented feature along the continental margin in and around Monterey Submarine Canyon, where isopycnal displacments can reach hundreds of meters [e.g., *Breaker and Broenkow*, 1994; *Petruncio et al.*, 1998; *Kunze et al.*, 2002]. The current study was conducted in southern Monterey Bay at Hopkins Marine Station of Stanford University (HMS – Figure 4.1), the location of previous observations of nearshore internal bores [*Walter et al*., 2012; *Walter et al*., 2014]. This study utilizes a cabled observatory system at HMS, the Kelp Forest Array (KFA, Appendix B, Figure B.1). The KFA is comprised

of a cable from shore that contains fiber optic cables for Ethernet and copper wires carrying 300 VDC. This cable connects to an underwater “node” located several hundred meters offshore near the 15 m isobath (Figure 4.1b). This underwater “node” distributes 24/48 VDC and Ethernet to various “subnodes,” which are used to interface with oceanographic instruments. The subnodes also power the instruments and convert data streams from serial to Ethernet. Data is then acquired using virtual serial ports on a remote computer on shore.

The current study was part of a larger project (Monterey Tower Node - MOTOWN) aimed at understanding how nearshore internal bores affect circulation dynamics and turbulent mixing in the nearshore coastal environment. Here, we focus on the stratified turbulence dynamics, as well as the evolution of the turbulence in the presence of nearshore internal bores. Various budgets (e.g., energy, momentum, etc.), will be investigated in future contributions. As such, only the relevant instrumentation and data used in this study will be described in detail (see Appendix B).

The centerpiece of this experiment was an 8 m tall underwater turbulence flux tower that was deployed near the 15 m isobath next to the underwater subnodes (Figure 4.1b-e, Appendix B, Figure B.2). On the submerged tower, we attached 6 Nortek acoustic Doppler velocimeters (ADVS) at 0.3, 1, 2, 4, 6, and 8 meters above the bed (mab) fixed to arms that protruded several meters away from the tower (Figure 4.1c-e). The ADVs were leveled by divers to within 1° using a bubble level, and the arms were positioned so that they were extending out from the tower (60° from true north). Each of the ADVs was equipped and synched with a Precision Measurement Engineering, Inc. (PME) fast-response thermistor (FP07) and conductivity (ceramic

plate) sensor (fast CT). The fast CTs were positioned to sample approximately 1 cm away from the ADV sampling volume so that collocated measurements of velocity (ADVs) and density (fast CTs) were obtained. All of the ADV/fast CT combos were synched together to ensure a common time base and then connected to the KFA cabled observatory system. This allowed continuous, collocated measurements of turbulent velocity and density fluctuations at 64 Hz for nearly two weeks (14:00 on 8 August 2012 to 08:00 on 21 August 2012). This configuration also enabled us to measure turbulent fluxes of momentum and density.

Surrounding the tower, we deployed an array of densely instrumented moorings that collected velocity and temperature (density) measurements throughout the water column (Figure 4.1b). Findings from these surrounding moorings will be discussed in a future contribution, and hence the detailed mooring configurations are not included here. In addition to the ADV/fast CT vertical array, the tower was also equipped with 22 SBE56 temperature loggers throughout the water column [0 to 9 meters above the bed (mab) in 0.5 m increments, 10, 11, 12 mab], all of which sampled at 0.5 s periods [see *Walter et al.*, 2014]. There was also a SBE39 temperature logger at the surface location, sampling at 10 s intervals. In addition, the tower included SBE37 conductivity-temperature-depth (CTD) loggers at 0 (24 s), 2 (6 s), 4 (6 s), 6 (6 s), and 8 (24 s) mab, where the sampling period is denoted in parentheses for each vertical location. In order to measure vertical profiles of velocity throughout the water column, a RDI 1200 kHz Workhorse acoustic Doppler current profiler (ADCP) was deployed at the tower location. The ADCP sampled in fast-ping Mode 12 (6 subpings per 1 s ensemble) with 0.5 m vertical bin spacing. This sampling

scheme results in a small error standard deviation of 0.12 cm/s for ten-minute averages. The ADCP was also leveled by divers to within 1 degree of the horizontal using a bubble level in order to minimize instrument tilt errors.

4.3.2: Methods

4.3.2.1: Data Processing

Velocity measurements from the ADCP and ADVs were rotated into cross-shore (u), along-shore (v), and vertical velocity (w) components using the principal axes obtained from a long-term ADCP near the site (Figure 4.1b). The principal axes of the long-term record were within 2 degrees of those calculated from the ADCP in the current study. During the summer upwelling season in Monterey Bay, salinity variations are sufficiently small such that density is mainly controlled by temperature [e.g., *Woodson et al*., 2009, 2011; *Walter et al*., 2012; *Walter et al*., 2014]. Analysis of the tower CTD data showed that small changes in salinity varied linearly with temperature throughout the water column (e.g., $R^2 = 0.91$, p-value < 0.001 for the 2 mab CTD) with nearly identical linear regression coefficients between different depths. Consequently, densities were calculated at all tower thermistor locations using the observed temperature and derived linear relationship from the CTD measurements for salinity as a function of temperature. All times referenced in the text and figures are in local time, Pacific Daylight Time, unless otherwise noted.

Spectral and coherence calculations were performed using the fast Fourier transform (FFT), using standard methods [e.g., *Walter et al*., 2011]. Hamming windows with 50% overlap between adjacent segments were used. The window length, and hence the number of windows in each ten-minute segment, was chosen by

taking into account the number of degrees of freedom (DOF) for confidence intervals, frequency resolution, and length of the original record. A chi-squared variable analysis and the equivalent number of DOF (EDOF) were used to calculate confidence intervals for the spectra. For the coherence analysis, confidence limits were quantified using the EDOF [*Emery and Thompson*, 2004].

4.3.2.2: Turbulence Analysis and Quantities

For the turbulence analysis, ADV and fast CT data were processed using ten-minute intervals with 50% overlap. This standard averaging interval represents a trade-off between capturing an appropriate number of realizations of the desired turbulent length scales and maintaining quasi-stationary statistics [e.g., *Soulsby*, 1980; *Davis and Monismith*, 2011; *Walter et al*., 2011]. Quality control of the ADV and fast CT data was performed by removing ADV data points with correlations less than 70% and temporal derivatives (i.e., accelerations) greater than the acceleration due to gravity. Following this, the phase-space threshold filtering method of *Goring and Nikora* [2002], which utilizes first- and second-order differencing and a Universal criterion, was used to identify data spikes. When ADV velocity data points were removed based on the above criterion, the corresponding fast CT data points were also removed so that buoyancy flux calculations would not be biased. Following removal, individual erroneous data spikes were replaced using a linear interpolation between neighboring points. Longer sections of bad data were replaced with white noise scaled by the velocity variance in the particular ten-minute segment. The scaled white noise contained a flat spectral signature and did not affect statistics and turbulence

quantities. Ten-minute segments with more than 15% removed data were not used for further analysis.

Another important consideration for the data quality control is wake effects from the tower and supporting legs. Analysis of velocity spectrograms (Appendix B, Figure B.3) reveals varying degrees of wake interference for velocities with mean horizontal directions oriented such that the velocity vector passes through the tower and legs (i.e., 30° to 90° from true north). Hence, ten-minute segments with this mean directionality were removed from further analysis.

In order to accurately calculate various turbulence statistics and quantities, such as momentum/buoyancy fluxes and dissipation, it is necessary to account for the effects of surface waves (i.e., wave-turbulence decomposition). Previous studies [e.g., *Shaw et al*., 2001; *Davis and Monismith*, 2011; see reference below] have successfully removed surface wave contamination of the turbulence signal by using a differencing method between vertically separated sensors, which was originally developed by *Trowbridge* [1998], and later updated by *Shaw and Trowbridge* [2001] and *Feddersen and Williams* [2007] to include adaptive filtering. Briefly, this method assumes that turbulence is uncorrelated between adjacent sensors, or that the vertical separation between sensors is greater than the largest turbulent length scale, so that motions that are correlated between the sensors are due to waves. Thus, by differencing the two velocity signals, only the turbulence component remains. Unfortunately, the adaptive filtering method was not successful in separating waves and turbulence in the current data set based on inspection of the velocity spectra and cospectra in the waveband frequencies (not shown). This technique also proved unsuccessful in the surface layer

observations of *Gerbi et al*. [2008], and the near-bed observations of *MacVean and Lacy* [2014]; the authors attributed the failure of the differencing method to multidirectional waves and decorrelated motions at higher frequencies, respectively. Analysis of velocity spectrograms (Appendix B, Figure B.3) in the current study reveals that sensors at different heights measured wave energy at different frequencies. For instance, while increased energy was often seen in the lower frequencies associated with longer period surface waves (~ 10 s periods) at most vertical locations, the shorter period waves were mainly seen in the spectra of the upper tower instruments. Various differencing combinations of the vertical locations were explored unsuccessfully.

Thus, to separate waves and turbulence, we employ the spectral "phase" decomposition method of *Bricker and Monismith* [2007]. This method has been successfully used in previous field studies in a variety of coastal and estuarine locations [e.g., *Hansen and Reidenbach*, 2012; *Wilson et al*., 2013; *MacVean and Lacy*, 2014]. Briefly, this method utilizes the phase lag between the velocity components (e.g., u and w) of surface waves to interpolate the magnitude of the turbulence under the wave peak. When considering the two-sided cross-spectral density (CSD) of u and w, the turbulence spectrum can be expressed as the difference between the spectrum of raw velocities and that of the wave-induced velocities. Integrating under the spectrum of each component, leads to an expression for the turbulent Reynolds stress,

$$\overline{u'w'} = \overline{uw} - \overline{\tilde{u}\tilde{w}}, \tag{4.2}$$

where primes and tildes denote fluctuating and wave components, respectively.

By writing the Fourier coefficients (U_j, W_j) in phasor notation (e.g., $U_j = |U_j| e^{i\angle U_j}$, where $\angle U_j$ is the phase) and utilizing the Euler relation, the wave stress [i.e., last term in Equation (4.2)] can be determined from the data series by summing over the two-sided spectral domain, where the odd (imaginary) component gives no contribution:

$$\overline{\tilde{u}\tilde{w}} = \sum_{j=wave-peak} |\tilde{U}_j||\tilde{W}_j| \cos(\angle W_j - \angle U_j). \tag{4.3}$$

Here, the magnitude of $\tilde{U}_j$ ($\tilde{W}_j$) is the difference between the raw U_j (W_j) and the turbulence $U_j^{'}$ ($W_j^{'}$), which is found by interpolating the auto-spectral density (PSD) of *u* (*w*) below the wave peak using a least squares fit to the data to the left and right of the identified waveband (e.g., Figure 4.2b). The turbulent Reynolds stress is then found by subtracting the wave stress, which is found by integrating the wave component of the CSD over the wave peak [Equation (4.3)], from the integral of the total stress over the full frequency domain using Equation (4.2). We refer the reader to *Bricker and Monismith* [2007] for further details.

The aforementioned approach relies on an accurate delineation of the frequency range of the waves for interpolation of the PSD. For each ten-minute segment, we calculated the coherence between the vertical velocity component and the ADV pressure signal and identified the waveband by those frequency components that showed a statistically significant coherence within the frequency range 0.05 to 0.4 Hz, which encompasses the range of wave frequencies observed in the spectra over the experiment (e.g., Figure 4.2a). Upon inspection of the velocity spectra and cospectra, this method proved robust in accurately capturing the waveband (e.g., Figure 2b).

Moreover, the cumulative integral of the wave-filtered cospectra (Ogive curves) resembled the expected forms, at least to the degree generally reported in the literature [cf. *Kaimal et al.*, 1972; *Walter et al.*, 2011; Appendix B, Figure B.4]. The same methodology was employed to calculate the along-shore component of the Reynolds stress ($\overline{\mathrm{v}'w'}$), turbulent density fluxes ($\overline{\rho' w'}$), and each TKE component [$k = \frac{1}{2}\left(\overline{\mathrm{u}'\mathrm{u}'} + \overline{\mathrm{v}'\mathrm{v}'} + \overline{\mathrm{w}'\mathrm{w}'}\right)$].

Using a dataset from a similar turbulence tower setup at the Kilo Nalu Observatory in Mamala Bay, HI, where the *Feddersen and Williams* [2007] differencing method proved successful, the *Bricker and Monismith* [2007] performed equally well in the wave-turbulence decomposition and calculation of momentum and density fluxes [*Squibb et al.*, personal communication, unpublished data]. Finally, in order to limit the effects of unsteady advection of turbulence by the waves, we restricted further analysis to periods when $\sigma_{U_h} / U_h < 2$; σ_{U_h} is an estimate of the surface-wave orbital velocities, and is calculated as the standard deviation of the horizontal velocity components in each ten-minute window (i.e., $u_h = \sqrt{u^2 + v^2}$), while U_h is the mean horizontal flow speed. This limitation is comparable to that used in similar studies of turbulence estimates in the presence of surface wave forcing [e.g., *Gerbi et al.*, 2008; *Davis and Monismith*, 2011].

Using the wave-removed momentum fluxes, the shear production (P) of TKE was calculated from Equation (4.1) as,

$$P = -\overline{u'w'}\frac{\partial U}{\partial z} - \overline{\mathrm{v}'w'}\frac{\partial V}{\partial z}, \qquad (4.4)$$

where the vertical gradients of the mean horizontal velocities (*U* and *V*) were calculated from the ADVs. Similar production results were achieved using the velocity gradients estimated from the ADCP at the tower, as well as various spline fits to the ADV velocity data. The buoyancy flux (*B*) term in the TKE equation [Equation (4.1)], was calculated using the wave-removed density flux,

$$B = \frac{g}{\rho_o}\overline{\rho' w'}. \tag{4.5}$$

Dissipation of TKE was estimated using Kolmogorov's -5/3 law and an inertial subrange fit following the method outlined in *Feddersen et al*. [2007]. This method uses the high-frequency portion of the vertical velocity spectrum together with the *Lumley and Terray* [1983] model for the effect of the waves on the turbulent wavenumber spectrum to calculate dissipation, since waves act to advect turbulent eddies past the instrument sensor and alias wave energy into higher frequencies than the waveband frequencies. Dissipation was calculated at various radian frequencies (ω),

$$\varepsilon(\omega) = \left[\frac{S_{w'w'}(\omega) 2(2\pi)^{3/2}}{\alpha M_{w'w'}(\omega)} \right]^{3/2}, \tag{4.6}$$

where α = 1.5 is Kolmogorov's constant, $S_{w'w'}$ is the vertical velocity spectrum, and $M_{w'w'}$ is an integral over three-dimensional wavenumber space that depends on the wave-orbital velocities and mean flow [*Lumley and Terray*, 1983; *Feddersen et al*., 2007]. The spectrum of vertical velocities was used since this velocity component is the least noisy [e.g., *Voulgaris and Trowbridge*, 1998].

Dissipation was calculated at various cyclic frequencies (0.8, 1.0, 1.2, 1.4, 1.6 Hz) within the inertial subrange. This particular range of frequencies encompasses a region that is higher than the dominant waveband, lower than the noise floor, and consistently produced a -5/3 power law fit (e.g., Figure 4.2). Dissipation estimates at the various cyclic frequencies produced consistent results, indicating that the *Lumley and Terray* [1983] model for the wave advection of frozen turbulence is reasonable [cf. *Feddersen et al.*, 2007]. Following *Feddersen et al.* [2007], a frequency-averaged dissipation value (hereafter referred to as ε) is obtained for every ten-minute segment using a log-mean of the dissipation values at the various cyclic frequencies.

Furthermore, we restricted the dissipation estimates to ten-minute segments that satisfied the condition, $\frac{u'_{h,rms}}{U_h} < 0.3$, where $u'_{h,rms}$ is the root-mean-square of the turbulent velocity fluctuations along the mean horizontal flow direction. This criterion ensures that Taylor's frozen turbulence hypothesis, which is used to convert measurements from frequency to wavenumber space, is valid (see *Bluteau et al.* [2011] and the references therein). Additionally, dissipation estimates that did not yield a -5/3 power law fit in the inertial subrange were rejected. This was implemented by computing the least squares power law fit to the spectra in the inertial subrange and discarding estimates in each ten-minute window where the coefficient of regression (R^2) between the power law fit and the *Feddersen et al.* [2007] fit (i.e., -5/3 power law) was less than 0.7 [cf. *Bluteau et al.*, 2011]. This particular cutoff effectively eliminated periods where a -5/3 fit was not achieved, ensuring the existence of an inertial subrange. As discussed later in the manuscript, turbulence activity numbers,

$\varepsilon/\nu N^2$, where $N^2 = -\frac{g}{\rho_o}\frac{\partial \overline{\rho}}{\partial z}$ is the buoyancy frequency squared and is a measure of the strength of stratification, were generally well above 100, further ensuring a well-defined inertial subrange with minimal anisotropic effects (see *Gargett et al*. [1984], and *Bluteau et al*. [2011] and the references therein). Uncertainty in the dissipation estimates were quantified by calculating dissipation with Equation (4.6) using the upper and lower confidence intervals (90%) of the vertical velocity spectra, and the method outlined above. The minimum (maximum) uncertainty bound on the dissipation estimates was a decrease (increase) by a factor of 0.49 (1.49), which does not significantly alter any of the results or conclusions.

The traditional approach of estimating the vertical turbulent diffusivity of density (κ_ρ) is to utilize the *Osborn* [1980] steady-state formulation,

$$\kappa_\rho = \Gamma \frac{\varepsilon}{N^2}, \tag{4.7}$$

where Γ is the mixing coefficient. The mixing coefficient (Γ) is related to the flux Richardson number (R_f) [e.g., *Ivey and Imberger*, 1991],

$$R_f = \frac{B}{B+\varepsilon}, \tag{4.8}$$

by the following relation,

$$\Gamma = \frac{R_f}{1-R_f}. \tag{4.9}$$

In Equation (4.1), the RHS represents TKE sink terms; TKE is transferred to internal energy through viscous dissipation at a rate ε, and in a stably stratified fluid, to potential energy through the buoyancy flux. Thus, the flux Richardson number, which is related to the mixing coefficient by Equation (4.9), represents the ratio of the

amount of TKE lost to potential energy for a stably stratified fluid to the net mechanical energy available to sustain turbulent motions [i.e., LHS of Equation (4.1), which is equal to $B + \varepsilon$; cf. *Ivey and Imberger*, 1991; *Davis and Monismith*, 2011; *Dunckley et al*., 2012]. Whereas the conventional approach is to estimate κ_ρ using a constant mixing coefficient, $\Gamma = 0.2$ ($R_f = 0.17$), in Equation (4.7), here we are able to directly calculate the mixing coefficient using Equations (4.8) and (4.9), and hence the vertical diffusivity,

$$\kappa_\rho = \frac{R_f}{1 - R_f} \frac{\varepsilon}{N^2}. \tag{4.10}$$

We note that Equation (4.10) for calculating κ_ρ is identical to, $\kappa_\rho = \frac{B}{N^2}$, obtained from the eddy diffusivity model formulation,

$$-\overline{\rho' w'} = \kappa_\rho \frac{\partial \overline{\rho}}{\partial z}. \tag{4.11}$$

4.4: Results

4.4.1: General Observations

Examination of the detailed temperature structure over the entire study period reveals episodic cold water intrusions that propagate in (onshore/upslope flow) and out (offshore/downslope flow) of the nearshore (Figure 4.3). These intrusions are typical of nearshore internal bores that act to drive transient stratification and mixing events [e.g., *Walter et al*., 2012]. The record is also characterized by several distinct regimes that change the nearshore temperature structure and stratification. From approximately 7 to 14 August and starting again on about 21 August, the nearshore is marked by a

low-frequency “pooling” of cold water throughout the bottom portions of the water column (Figure 4.3a). This increases the stratification in the nearshore, causing the bores to perturb the pre-existing thermocline. This is in contrast to periods where the nearshore is well-mixed (i.e., uniform temperature throughout the water column). In this case, the bores propagate into the well-mixed waters and act to stratify the water column.

Walter et al. [2014] show that the two nearshore regimes are related to the regional wind-driven upwelling cycles and offshore stratification. During weak upwelling conditions, the offshore thermocline is deeper, and the nearshore internal bores propagate into well-mixed waters. During upwelling favorable conditions, the offshore thermocline shoals towards the surface, nearshore “pooling” develops as subthermocline waters inundate the nearshore, and nearshore internal bores perturb the pre-existing stratification. Noteworthy is the fact that the bores stratify the water column at higher frequencies (~semidiurnal period) than the upwelling cycles (~7-10 day period) that drive the nearshore pooling, and they also drive the major perturbations to the pre-existing stratification.

Examination of the velocity structure reveals that the bore events contribute to the majority of the variance in the cross-shelf velocity field. This is confirmed using an empirical orthogonal function (EOF) analysis (see *Walter et al*. [2014]). We refer the reader to *Walter et al*. [2012] and *Walter et al*. [2014] for a more detailed examination of the cross-shore and along-shore velocity and shear fields in the presence of the nearshore internal bores.

4.4.2: TKE Budget

The TKE budget was analyzed over the entire turbulence record to first test the often used equilibrium turbulence assumption, whereby shear production of TKE is locally balanced by the dissipation of TKE (i.e., $P = \varepsilon$). Figure 4.4 shows a scatterplot of ε versus P at the various instrument heights. Near the bed (0.3 mab), the production balances dissipation and the assumption of equilibrium turbulence appears valid. This is consistent with previous observations of near-bed turbulence in strong tidal flows and coastal environments [*Gross and* Nowell, 1985; *Trowbridge et al.*, 1999; *Sanford and Lien*, 1999; *Shaw et al*., 2001; *Reidenbach et al.*, 2006]. However, Figure 4.4 also reveals that further away from the bed, the local balance begins to break down.

Specifically, the dissipation of TKE is much greater than the local production of TKE, by roughly an order of magnitude. Including the buoyancy flux term (B), as well as the TKE vertical transport term [i.e., $\frac{\partial}{\partial z}\left(\overline{kw'}\right)$] from Equation (4.1), does not improve the balance. These terms are typically several orders or magnitude smaller than the production and dissipation term, a facet consistent with previous studies [e.g., *Shaw et al*. 2001; *Davis and Monismith*, 2011]. Even when calculating the production using the total stress values (e.g., no wave removal, or $\overline{uw}$ and $\overline{vw}$), dissipation is still greater than production. We note that the comparison of production versus dissipation appears to be independent of the strength of surface wave forcing (i.e., σ_{U_h}/U_h). Also, TKE dissipation values calculated with the *Feddersen et al*. [2007] method during periods of low wave forcing ($\sigma_{U_h}/U_h \ll 1$) were similar to those obtained using an inertial subrange method that does not take into account the effect of the

waves on the high frequency portion of the spectrum (e.g., Equation 7 in *Shaw et al.* [2001]; Equation A1 in *Davis and Monismith* [2011]) for dissipation values above $10^{-6.5}$ m^2/s^3. Non-equilibrium turbulence ($P \neq \varepsilon$), especially away from the bed, has been previously observed in strong tidal flows [*Sanford and Lien*, 1999; *Walter et al.*, 2011], as well as coastal environments [*Shaw et al.*, 2001; *Feddersen et al.*, 2007; *Davis and Monismith*, 2011; *Squibb et al.*, unpublished results and personal communication].

We surmise that the elevated levels of dissipation are due to the horizontal transport of TKE, whereby turbulence is generated and advected to the measurement site where it is locally dissipated. This hypothesis seems likely at the current study site given the energetic nonlinear internal waves that may be breaking and advecting remotely generated turbulence to the tower location [cf. *Davis and Monismith*, 2011; *Arthur and Fringer*, personal communication]. While we are not able to test this hypothesis with the available data, the examination of local turbulent dissipation by breaking internal waves (bores) at various locations along a sloping shelf is the subject of ongoing numerical work [*Arthur and Fringer*, unpublished results and personal communication]. Indeed, the assumption of equilibrium turbulence, especially away from the bed, in the presence of nonlinear internal waves may not be appropriate in all environments.

We also test the applicability of the classic law of the wall scaling for dissipation,

$$\varepsilon = \frac{u_*^3}{\kappa z}, \tag{4.12}$$

where κ = 0.41 is the Von Kármán constant, z is the height above the bed, and u_* is the friction velocity [*Pope*, 2000]. The friction velocity is estimated using the magnitude of the near-bed Reynolds stresses,

$$u_*^2 = \sqrt{\left(-\overline{u'w'}\right)^2 + \left(-\overline{v'w'}\right)^2} \,. \tag{4.13}$$

Figure 4.5 highlights the boundary layer scaling for dissipation at the various instrument heights. Closer to the bed (0.3, 1, 2 mab), the law of the wall scaling for dissipation typically matches the order of magnitude of the observed dissipation values. Further up in the water column, however, the scaling begins to break down with the law of the wall scaling underpredicting the observed dissipation values. This result is expected and is likely due to the presence of stratification that acts to modify the logarithmic region and the applicable turbulent length scales (i.e., the turbulent eddies outside of the constant-stress wall region no longer scale as the distance from the wall) [e.g., *Perlin et al.*, 2005].

4.4.3: Evolution of Turbulence and Mixing in the Presence of Bores

Figure 4.6 highlights the density and velocity structure, turbulence production and dissipation, and measured vertical diffusivity over the entire record during which the turbulence tower collected measurements. Also shown is the vertical structure of the time derivative of density (Figure 4.6b), which is meant to highlight the leading (positive derivative; "bore period' from *Walter et al*. [2012]) and trailing (negative derivative; "mixing period" from *Walter et al*. [2012]) edges of the bores. The derivative was low-pass filtered (3 h half-amplitude period) in order to better delineate the bore interface and reduce some of the higher frequency variability. Examination of

the turbulence production and dissipation (Figure 4.6e and Figure 4.6f) reveals large fluctuations (changes of several orders of magnitude) that appear to be coherent with the bore events. The measured vertical diffusivity also shows large variations that are seemingly linked to the bore events, with many of the values well above the canonical value of ~10^{-5} m^2/s for the ocean interior [*Gregg*, 1989]. We examine these trends in further detail below by first examining individual bore events in each of the two previously mentioned nearshore regimes: a well-mixed nearshore, and a stratified nearshore (nearshore "pooling").

Figure 4.7 highlights nearshore internal bores propagating into well-mixed waters. The arrival of the initial bore (~00:00, leading edge) is characterized by a dense mass of water that tends to stratify the water column, as well as a strong onshore (upslope) flow near the bottom in the cross-shore direction. There is a corresponding increase in the density time gradient along the bore interface, highlighted by the isopycnals in Figure 4.7a-d. The arrival of the bore is also marked by a decrease in the dissipation throughout the water column, except for the near-bottom sensors (0.3 mab and 1 mab), which display an order of magnitude larger dissipation values compared to the stratified interior. Examination of the turbulence production reveals slightly smaller values during the bore arrival, except for several small peaks (e.g., ~02:30) that correspond to times of elevated velocity shear. The vertical diffusivities demonstrate slightly lower values further up in the water column during the arrival of the bore.

During the relaxation of the bore in Figure 4.7 (~08:00, trailing edge), the water column structure quickly changes as the bore advects back offshore

(downslope). There is a corresponding sharp decrease and change in sign of the density time derivative. We note that the sharper gradient on the trailing edge, compared to the leading edge, and the general "non-canonical" structure of the bore was examined by *Walter et al*. [2012] with a numerical model and explained by the steep bathymetric slope in the region and dependence on the internal Iribarren number,

$$\xi = \frac{s}{\left(\frac{a}{\lambda}\right)^{1/2}}, \tag{4.14}$$

where s is the bathymetric slope, and a and λ are the offshore amplitude and wavelength of the incoming internal wave, respectively [e.g., Boegman et al., 2005]. Turbulence dissipation in the stratified interior peaks by nearly two orders of magnitude during the trailing edge of the bore, and is comparable to the near-bed dissipation values seen during the bore. This facet is consistent with the observations of *Walter et al*. [2012] (i.e., dissipation in the stratified interior comparable to near-bed dissipation during the "mixing period"), but the current data set provides a more complete description of the temporal and spatial evolution. There is also a sharp increase in the turbulence production, which is due to the large increase in shear. Careful examination reveals that the vertical diffusivity peaks slightly further up in the water column following the trailing edge of the bore. The second bore event shown in Figure 4.7 (~12:00 to 18:00) more clearly shows the peaks in dissipation, production, and vertical diffusivity during the trailing edge of the bore in comparison to the leading edge.

We also examine the detailed structure of an individual bore propagating into a pre-existing stratification in Figure 4.8. In this case, the bore perturbs the nearshore pycnocline region, as seen in the density time gradient and cross-shelf velocity fields. While there is a large gap of discarded turbulence data from the quantity control restrictions, the turbulence structure seems to follow the same trends observed earlier. That is, the arrival of the bore coincides with decreases in the turbulence dissipation, production, and vertical diffusivity, while there appears to be increases in these parameters during the trailing edge.

We expand on the individual bore event findings and consider the evolution of various turbulence terms averaged across all bore events. Here, we focus on the bore interface and assess how the various phases of the bore (e.g., leading versus trailing edge) affect the stratified turbulence dynamics. The bore interface can be thought of as the nearshore pycnocline since it coincides with the region of the strongest stratification in the nearshore and separates the nearshore waters from the denser offshore waters. Figure 4.9 shows how various turbulence quantities, bin-averaged across all measurements at all instrument heights, vary as a function of the low-pass filtered time derivative of density. The density time derivative captures the phases of the bore (e.g., positive values, leading edge; negative values, trailing edge). Calculations were also restricted to regions of strong density stratification where $N^2 > 10^{-3.5}\ 1/s^2$, which effectively isolates the bore interface.

Figure 4.9a reveals that the density stratification peaks slightly in the leading and trailing edges of the bore. Furthermore, in accord with the individual bore observations presented above, the dissipation (Figure 4.9b) and production (Figure

4.9c) of TKE increase in the trailing edge of the bore by almost an order of magnitude compared to the other phases. In order to assess the evolution of the stratified turbulence and turbulent mixing, the buoyancy flux (Figure 4.9d) and the flux Richardson number (Figure 4.9e) were computed. As expected based on the density stratification, the buoyancy flux shows maximum values in the leading and trailing edges of the bore. On the other hand, the flux Richardson number, which is related to the mixing efficiency by Equation (4.9), illustrates a minimum in the trailing edge of the bore, whereas the leading edge of the bore shows much larger values. Also shown is the often assumed constant value of $R_f = 0.17$, which corresponds to a constant mixing efficiency of $\Gamma = 0.2$. It is clear that the mixing efficiencies calculated along the bore interface are much smaller than this constant value, with significant variation with respect to the bore phase. While the trailing edge of the bore is more turbulent than other phases, the efficiency of mixing is smaller. This leads to measured turbulent diffusivities (Figure 4.9f) that are not as large as expected under the assumption of a constant mixing efficiency, but that are still slightly higher than the other phases of the bore. Indeed, employing the traditional approach of estimating turbulent diffusivity by assuming a constant mixing efficiency leads to large overestimates of the diffusivity (shown in grey in Figure 4.9f), particularly in the trailing edge.

4.5: Discussion

4.5.1: Stratified Turbulence Regimes and Mixing Efficiency

The nature of stratified turbulence, and the influence of buoyancy, is often evaluated in a turbulent Reynolds number (Re_t) and turbulent Froude number (Fr_t)

parameter space [e.g., *Ivey and Imberger*, 1991; *Davis and Monismith*, 2011; *Dunckley et al*., 2012]. Before defining these quantities, several important length scales are first introduced [cf. *Itswiere et al*., 1986; *Shih et al*., 2005]. In the absence of buoyancy effects, the Prandtl mixing-length scale characterizes the size of the energy-containing turbulent eddies,

$$l_m = \left\{ \frac{\left[\left(-\overline{u'w'} \right)^2 + \left(-\overline{v'w'} \right)^2 \right]^{1/2}}{S^2} \right\}^{1/2} , \tag{4.15}$$

where $S^2 = \left(\frac{\partial U}{\partial z} \right)^2 + \left(\frac{\partial V}{\partial z} \right)^2$. However, the presence of density stratification and buoyancy limits the size of the largest turbulent eddies. The Ozmidov scale represents the length scale at which buoyancy forces are equal to inertial forces, and is the largest turbulent scale allowed by buoyancy forces,

$$l_o = \left(\frac{\varepsilon}{N^3} \right)^{1/2} . \tag{4.16}$$

The turbulent eddies at the largest scales transfer energy through the inertial subrange to smaller and smaller scales until molecular viscosity acts to dissipate TKE into internal energy. The scale at which turbulent motions are damped by viscous forces, or the scale at which TKE is dissipated by viscosity and small-scale strains, is defined as the Kolmogorov length scale,

$$l_k = \left(\frac{\nu^3}{\varepsilon} \right)^{1/4} . \tag{4.17}$$

In a density stratified medium, the range of possible turbulent length scales is bounded by the Kolmogorov scale at the smallest end and the Ozmidov scale at the largest end.

The turbulent overturning length scale, and the largest turbulent length scale in a statistical sense [cf. *Itswiere et al*., 1986], is defined using the Ellison length scale,

$$l_e = \frac{\rho'}{\partial\overline{\rho}/\partial z}. \tag{4.18}$$

However, the Ellison length scale is difficult to measure in the field and is affected by internal waves [*Itswiere et al*., 1986; *Davis and Monismith*, 2011]. DNS simulations of a stratified shear flow indicate that in the energetic regime (i.e., $\varepsilon/\nu N^2 > 100$), which is the case for nearly all measurements here, a constant relationship between the Ellison and Prandtl mixing-length scale exists [$l_e \approx 2.5 l_m$; *Shih et al*., 2005]. This relationship will be used for calculations of the Ellison length scale in what follows [cf. *Davis and Monismith*, 2011].

Using these length scale definitions, the turbulent Reynolds number, which is the ratio of the inertial to viscous forces in the energy-bearing eddies, is defined as follows,

$$\mathrm{Re}_t = \left(\frac{l_e}{l_k}\right)^{4/3}. \tag{4.19}$$

The turbulent Froude number represents the ratio of the inertial forces to the buoyant forces in the energy-bearing eddies,

$$Fr_t = \left(\frac{l_o}{l_e}\right)^{2/3}. \tag{4.20}$$

Figure 4.10 shows all of the measurements at each vertical location in the Re_t-Fr_t parameter space. The parameter space has been divided into three regions that classify the nature of the stratified turbulence: the buoyancy-affected region (Region 1), the

buoyancy-controlled region (Region 2), and a region where the combination of buoyancy and viscosity completely suppress turbulent motions (Region 3) [e.g., *Luketina and Imberger*, 1989; *Ivey and Imberger*, 1991]. Measurements at the current study site are confined to Regions 1 and 2, with most of the observations occurring in the buoyancy-controlled region (Region 2, Figure 4.10a). Figure 4.10b displays the percentage of points at each vertical location in each of the three regions. The near-bed measurements (0.3 mab) are predominately in Region 1, while further up in the water column, the majority of the points lie in Region 2.

Figure 4.11 highlights the distribution of several parameters in the Re_t-Fr_t space. The turbulence activity number, which can also be recast in terms of the Ozmidov and Kolmogorov length scales, $\frac{\varepsilon}{\nu N^2} = \left(\frac{l_o}{l_k}\right)^{4/3}$, is shown in Figure 4.11a. Nearly all of the measurements fall into the energetic regime [i.e., $\varepsilon/\nu N^2 > 100$, *Shih et al*., 2005], with values as large as 10^6. Examination of the flux Richardson number (Figure 4.11b) reveals that the largest values occur in the buoyancy-controlled region, with the majority of the observations falling below the "critical," or commonly used, value of 0.17. These results seem to suggest that the largest values of R_f do not occur near $Fr_t = 1$ [see *Ivey and Imberger*, 1991], but that the most efficient mixing occurs when the eddy overturning scale (l_e) is greater than the Ozmidov scale (l_o). *Davis and Monismith* [2011] (direct estimates of Γ, field measurements) and *Dunckley et al*. [2012] (parameterized estimates of Γ, field measurements) find a similar trend (i.e., maximum efficiency in Region 2), with the former noting that it is likely due to internal wave forcing and the nonlocal advection of TKE. Furthermore, the finding

that the most efficient mixing occurs near $Fr_t = 1$ was based on parameterizations from laboratory results with an average Re_t of approximately 40, which is several orders of magnitude smaller than the observations here (e.g., Figure 4.10a and Figure 4.11).

In many oceanic applications, the mixing efficiency is often taken to be a constant, $\Gamma = 0.2$; however, as discussed in recent review by *Ivey et al*. [2008], a host of laboratory experiments and DNS simulations over the last two decades suggest that the mixing efficiency is not a universal constant. Indeed, there is a clear consensus that the mixing efficiency is highly variable (i.e., not constant) and depends of various parameters including the age of the turbulent patch, the origin of the turbulence, the strength of the stratification, the turbulence activity number, the location in the domain, etc. [e.g., *Rohr et al*., 1984; *Itsweire et al*., 1986*; Ivey and Imberger*, 1991 and the references therein; *Barry et al*., 2001; *Smyth et al*., 2001; *Peltier and Caulfield*, 2003; *Rehmann*, 2004; *Rehmann and Koseff*, 2004; *Shih et al*., 2005; *Ivey et al*., 2008 and the references therein, *Stretch et al*., 2010; *Hult et al*., 2011a, 2011b; *Dunckley et al*., 2012; *Bouffard and Boegman*, 2013, etc.]. More recently, field measurements of the flux Richardson number confirm a strong dependence on the turbulence activity number [*Davis and Monismith*, 2011; *Bouffard and Boegman*, 2013], in accordance with previous DNS results [e.g., *Shih et al*., 2005]. Indeed, estimates of turbulent diffusivities are extremely sensitive to the choice of mixing efficiency used [cf. *Dunckley et al*., 2012]. Figure 4.11c highlights the turbulent diffusivity calculated using the measured mixing efficiency [Equation (4.10)]. This is contrasted with Figure 4.11d, where the diffusivity is calculated from an assumed $\Gamma = 0.2$. There are substantial differences in the estimated diffusivities. Notably, the

constant mixing efficiency formulation leads to overestimates of several orders of magnitude compared to the values calculated using the directly measured mixing efficiency.

The turbulence activity number is a common measure for characterizing turbulence in stratified environments, and several studies have noted the dependence of the flux Richardson number on the activity number [e.g., *Shih et al*., 2005 and the references therein; *Davis and Monismith*, 2011]. The DNS simulations of *Shih et al*. [2005] show that in the intermediate range ($7 < \varepsilon/\nu N^2 < 100$), the constant flux Richardson number formulation ($R_f = 0.17$) is valid; however, as the turbulence transitions into the energetic regime ($\varepsilon/\nu N^2 > 100$), the flux Richardson number displays a power-law dependence on the activity number, $R_f \sim (\varepsilon/\nu N^2)^{-1/2}$. A similar power-law dependence was found in the field observations of *Davis and Monismith* [2011].

Figure 4.12 displays the flux Richardson number as a function of the turbulence activity number for the current data set, as well as the least squares power law fit to the data [i.e., $R_f \sim (\varepsilon/\nu N^2)^{-1/2}$]. The power law fit is much closer to the DNS measurements of *Shih et al*. [2005], compared to the field measurements of *Davis and Monismith* [2011]. This may be due to the fact that *Davis and Monismith* [2011] were inferring density fluxes from heat fluxes. Nonetheless, the observations from this experiment (MOTOWN) confirm the general trend that for increasing turbulence activity numbers, the flux Richardson number decreases and approaches values much less than the constant value of 0.17. We note that the current observations reach turbulence activity numbers several orders of magnitude larger than previous

observations [*Shih et al*., 2005; *Davis and Monismith*, 2011], which is of particular importance for field observations in energetic and highly turbulent environments. This particular parameterization is attractive for field-based observations since the turbulence activity number is composed of variables readily measured using vertical profiling instruments.

Several studies have examined the dependence of the flux Richardson number on other parameters such as the gradient Richardson number, $Ri = N^2/S^2$ [*Rohr et al*., 1984; *Holt*, 1992; *Rehmann and Koseff*, 2004; *Stretch et al*., 2010; *Davis and Monismith*, 2011], with mixed results. The current data set indicates that R_f increases for increasing *Ri*, but with considerable scatter (Appendix B, Figure B.5). Moreover, the turbulence activity number can also be cast in terms of other non-dimensional parameters, $\varepsilon/\nu N^2 \sim Re_t/Ri \sim Re_t Fr_t^2$, making other parameterizations of R_f possible (see discussion in *Shih et al*. [2005]). This is the subject on ongoing work and will be reported elsewhere.

4.6: Summary and Implications

We collected high-frequency measurements of stratified turbulence throughout the water column in the nearshore environment of Monterey Bay, CA using a cabled observatory system and an underwater turbulence flux tower. The measurements collected offer a unique look into the dynamics of stratified turbulence in the coastal environment for several reasons: 1) nearly two weeks of continuous measurements of collocated velocity and density fluctuations at 64 Hz were collected allowing direct estimates of momentum and density fluxes, as well as mixing efficiencies; 2) the

observations are not confined to the near-bed region, similar to previous studies, but they extend into the stratified interior providing insight into the vertical evolution of the stratified turbulence and mixing dynamics in various stratified turbulence regimes; and 3) the measurements captured transient stratification and mixing events associated with nearshore internal bores, thus providing a unique look into the evolution of stratified turbulence in the presence of nearshore internal bores with high spatial and temporal coverage.

Examination of various terms in the TKE budget reveals that the dynamical balance of production of TKE equaling the dissipation of TKE (i.e., equilibrium turbulence) is only valid in a small near-bed region; this is also the case for the law of the wall scaling for dissipation. Further up in the water column, this dynamical balance breaks down, with dissipation exceeding production. Including the vertical TKE transport and buoyancy flux terms does not improve the balance; we surmise that the non-local advection of TKE, possibly due to the shoaling internal waves and bores, is responsible for this imbalance [cf. *Davis and Monismith*, 2011; *R. Arthur and O. Fringer*, unpublished results and personal communication]. These results suggest that the commonly used assumption of equilibrium turbulence, as well as the law of the wall scaling for dissipation, should be carefully employed.

Measurements at the tower location confirm previous observations of nonlinear internal bores that drive intrusions of dense, offshore waters [e.g., *Walter et al*., 2012; *Walter et al*., 2014]. We considered the evolution of the different turbulence terms averaged across all bore events to examine how the various phases (e.g., leading versus trailing edge) of the bore affect local mixing dynamics. The trailing edge of the

bore is characterized by elevated TKE dissipation and production values by almost an order of magnitude compared to the leading edge; however, lower mixing efficiencies lead to measured turbulent diffusivities that are not as large as expected under the assumption of a constant mixing efficiency, but that are still higher than the leading edge. These aspects are likely due to a combination of the "non-canonical" structure of the bore and the local internal Iribarren number [cf. *Walter et al*., 2012], as well as the mixing efficiency dependence on various parameters such as the turbulence activity number.

It is clear that the turbulence structure in the presence of nearshore internal bores is substantially different than that expected from the traditional model of a bottom mixed layer under a stratified interior. The elevated levels of turbulent mixing within the stratified interior are an important source of mixing that affect many physical and biological processes. Currently, large scale models, such as the Regional Ocean Modeling System (ROMS), along the CCLME do not accurately capture the physics of nearshore internal bores. It is critical that fine-scale mixing and transport due to shoaling internal waves and bores in the nearshore coastal environment be better resolved (with careful consideration of the non-hydrostatic nature of these features), or accurately parameterized, to avoid errors in assessing nearshore dynamics, such as larval connectivity. Furthermore, the internal bores are a mechanism by which deeper, offshore Pacific waters with low dissolved oxygen (DO) and pH levels [e.g., *Checkley and Barth*, 2009] are supplied to the nearshore [*Walter et al*., 2012; *Walter et al*., 2014]. Understanding how the mixing evolves throughout the stratified interior is crucial to assessing nearshore DO/pH variability, the potential

development of hypoxia, and ocean acidification in this region [e.g., *Booth et al*., 2012]. Indeed, we surmise that the strength and intensity of nearshore bores, and in particular the trailing edge of the bore, may be important factors governing water column DO and pH levels in this region.

Finally, we present direct measurements of the flux Richardson number, and hence the mixing efficiency, over a variety of forcing regimes. Our results suggest that the most efficient mixing occurs in regions of buoyancy-controlled turbulence (Fr_t < 1), consistent with previous field observations [*Davis and Monismith*, 2011; *Dunckley et al*., 2012]. The findings also confirm, and extend, previous DNS [*Shih et al*., 2005] and field [*Davis and Monismith*, 2011] parameterizations of the flux Richardson number, and hence the mixing efficiency, as a function of the turbulence activity number. Particularly, the findings suggest that the widely used assumption of a constant mixing efficiency, $\Gamma = 0.2$, leads to significant overestimates of the vertical turbulent diffusivity, with important implications for both regional and local mixing processes such as heat and energy budgets, larval connectivity, nutrient cycling, hypoxia development, and primary production [e.g., *Wolanski and Pickard*, 1983 *Leichter et al*., 1996; *Chan et al*., 2008; etc.].

4.7: Acknowledgements

This work was funded by the National Science Foundation through grant OCE-1235552. Ryan Walter was supported by the Stanford Graduate Fellowship. We thank the members of the Environmental Fluid Mechanics Laboratory and Paul Leary for dive support and help in the field. We acknowledge helpful discussions with Robert

Arthur, Jamie Dunckley, and Oliver Fringer. Bathymetry data used in this study were acquired, processed, archived, and distributed by the Seafloor Mapping Lab of California State University Monterey Bay.

4.8: Figures

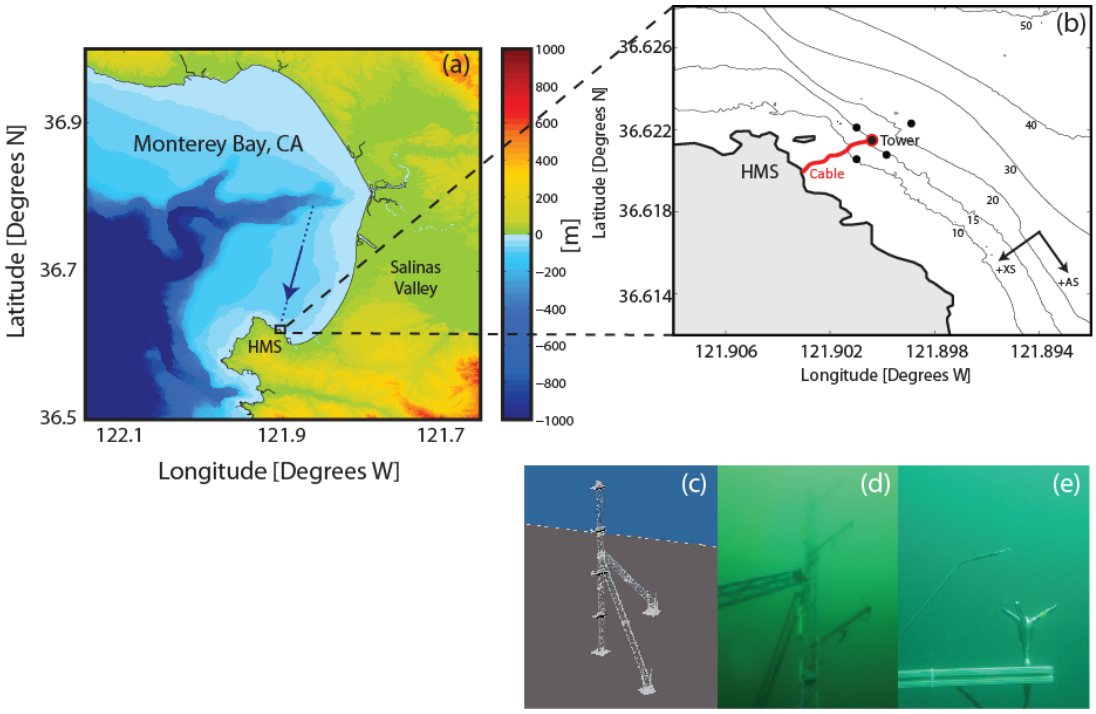

Figure 4.1: (a) Bathymetry and topography of the Monterey Bay, CA region with the study site indicated by a black box. Also shown is the median bore propagation heading from *Walter et al.* [2012] (blue arrow). (b) Study site with the moorings shown as filled black circles, as well as the location of the turbulence flux tower (black circle with red outline) and the approximate location of the cabled observatory system (cable – red line). Bathymetry contours (10, 15, 20, 30, 40, 50 m isobaths) are also shown along with the location of Hopkins Marine Station (HMS – Stanford University). (c) Computer animated drawing of the turbulence flux tower (M. Squibb). (d) Turbulence flux tower deployed in the field, showing the arms with ADV/fast CT combos (shown are the 4, 6, and 8 mab arms). (e) Example ADV and co-located fast CT deployed in the field.

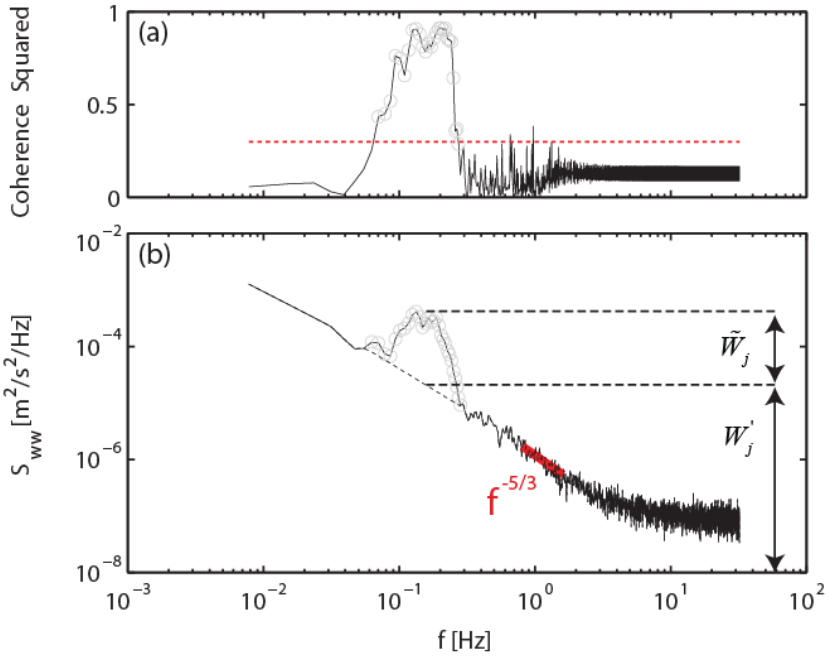

Figure 4.2: Example wave-turbulence decomposition for a representative ten-minute data series at the 4 mab ADV. (a) Coherence squared between the vertical velocity component and the pressure signal (solid black line). Grey dots denote the identified waveband, or the frequency components that are significantly coherent (i.e., above the 95% confidence level denoted by the dashed red line) in the waveband. (b) Power spectral density (PSD) of the vertical velocity component (S_{ww} – solid black line). Grey dots denote the data points within the waveband, and the dashed black line is a least squares fit to the data to the left and right of the waveband (see Section 4.3). The wave component ($\tilde{W}_j$) is found by subtracting the PSD above the dashed black line in the waveband region. Also shown is -5/3 power law fit in the inertial subrange (solid red line).

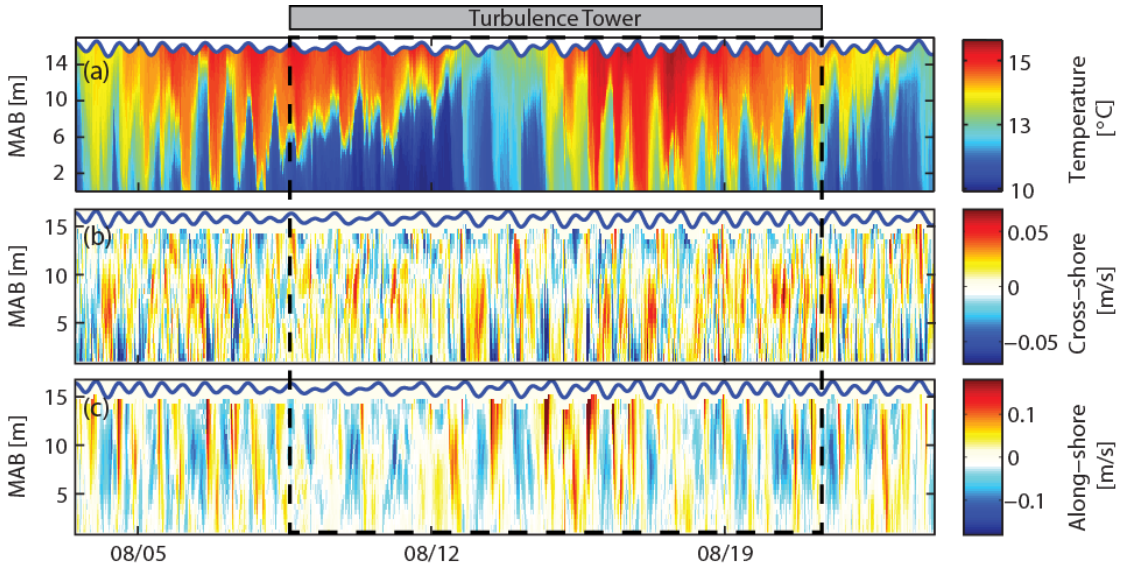

Figure 4.3: Time series over the entire study period at the tower location of the (a) vertical temperature structure, (b) vertical structure of the cross-shore velocity field (ten-minute averages, positive onshore), and (c) vertical structure of the along-shore velocity field (ten-minute averages, positive into the bay). The location of the sea surface (blue line) is also shown in panels (a-c). The dashed black box indicates the time period during which the underwater turbulence tower collected measurements.

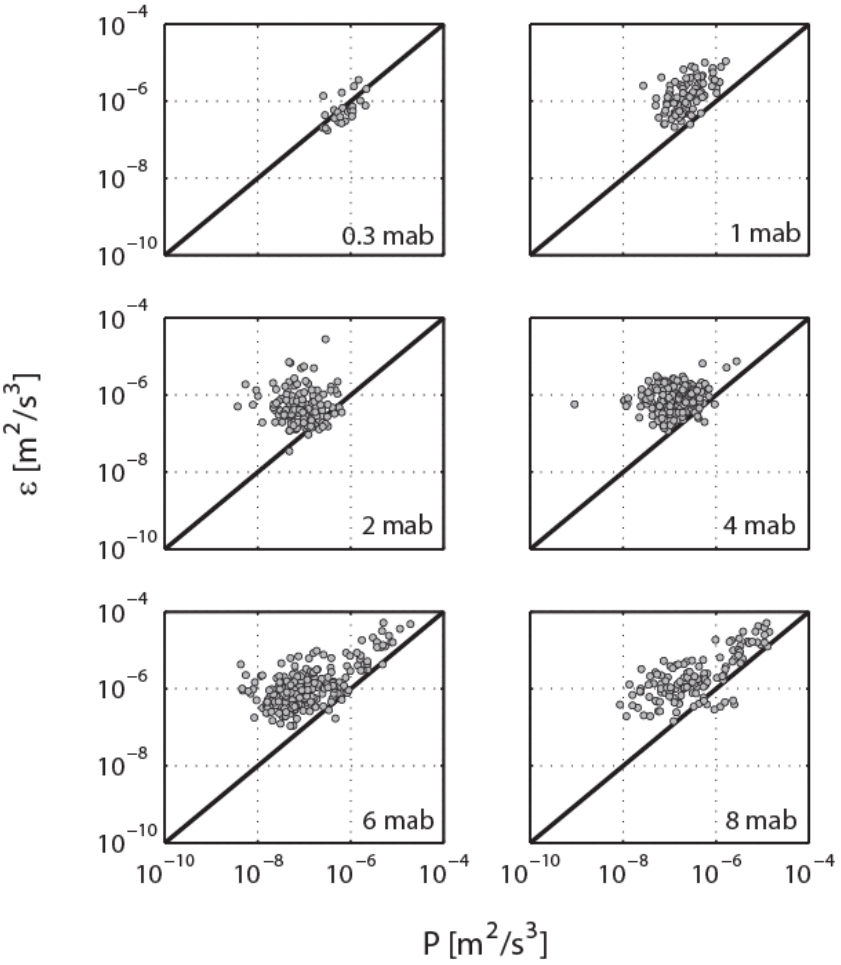

Figure 4.4: Dissipation (ε) versus production (*P*) of TKE at various heights above the bed. Individual events are indicated with gray circles, while the solid black line represents equilibrium turbulence ($P = \varepsilon$).

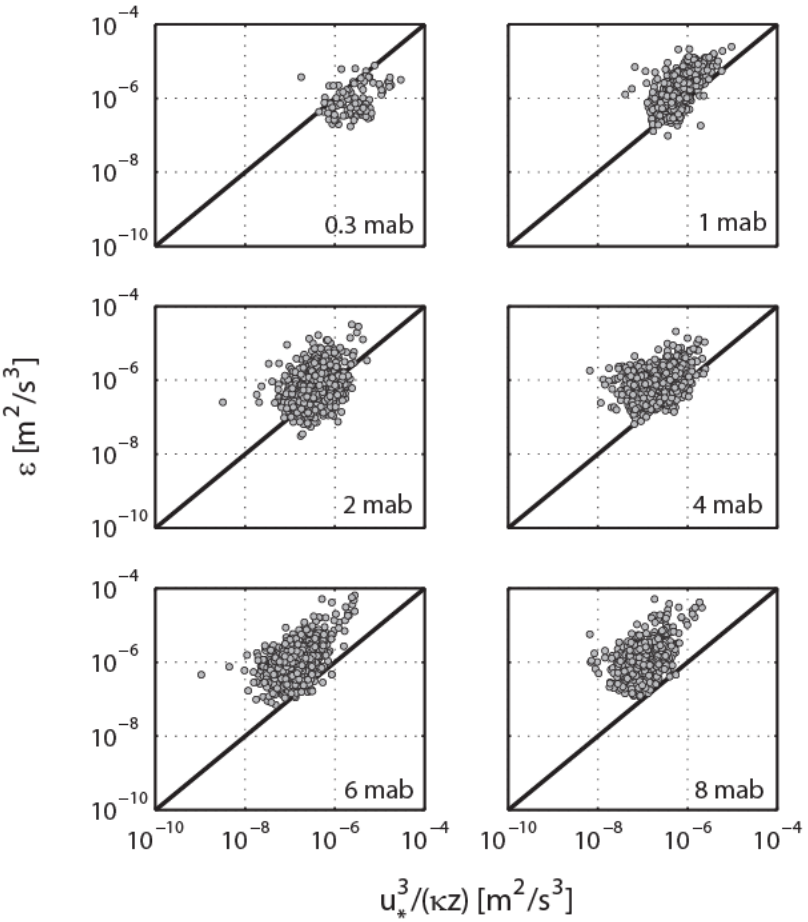

Figure 4.5: Observed dissipation of TKE (ε) versus the bottom boundary layer scaling (i.e., law of the wall) for dissipation, $u_*^3 / \kappa z$ at various heights above the bed. The friction velocity, u_*, was estimated using the magnitude of the near-bed, horizontal Reynolds stresses at the 1 mab ADV, while the height above the bed, z, varied. Individual events are indicated with gray circles, while the solid black line represents the one-to-one relationship expected in a canonical boundary layer shear flow.

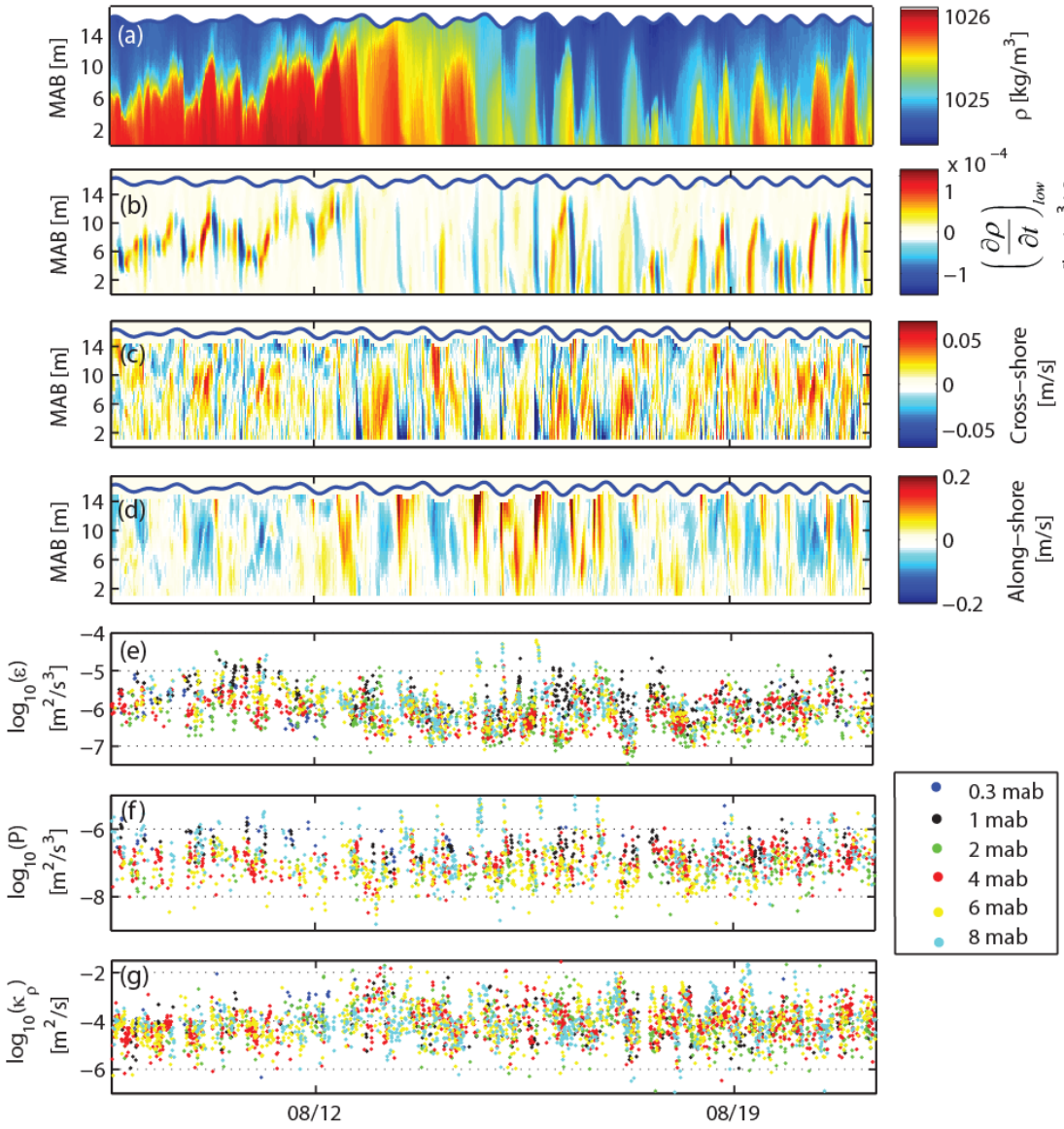

Figure 4.6: Time series over the entire study period at the tower location of the (a) vertical density structure, (b) low-pass filtered, time derivative of density, (c) vertical structure of the cross-shore velocity field (ten-minute averages, positive onshore), (d) vertical structure of the along-shore velocity field (ten-minute averages, positive into the bay), (e) dissipation (ε) of TKE at various heights above the bed, (f) production (*P*) of TKE at various heights above the bed, and (g) vertical turbulent diffusivity, $\kappa_\rho = \frac{B}{N^2} = \frac{R_f}{1-R_f}\frac{\varepsilon}{N^2}$, at various heights above the bed. The location of the sea surface (blue line) is also shown in panels (a - d). Missing values in panels (e - g) correspond to periods that did not fit the quality control criteria for each respective variable (see Section 4.3).

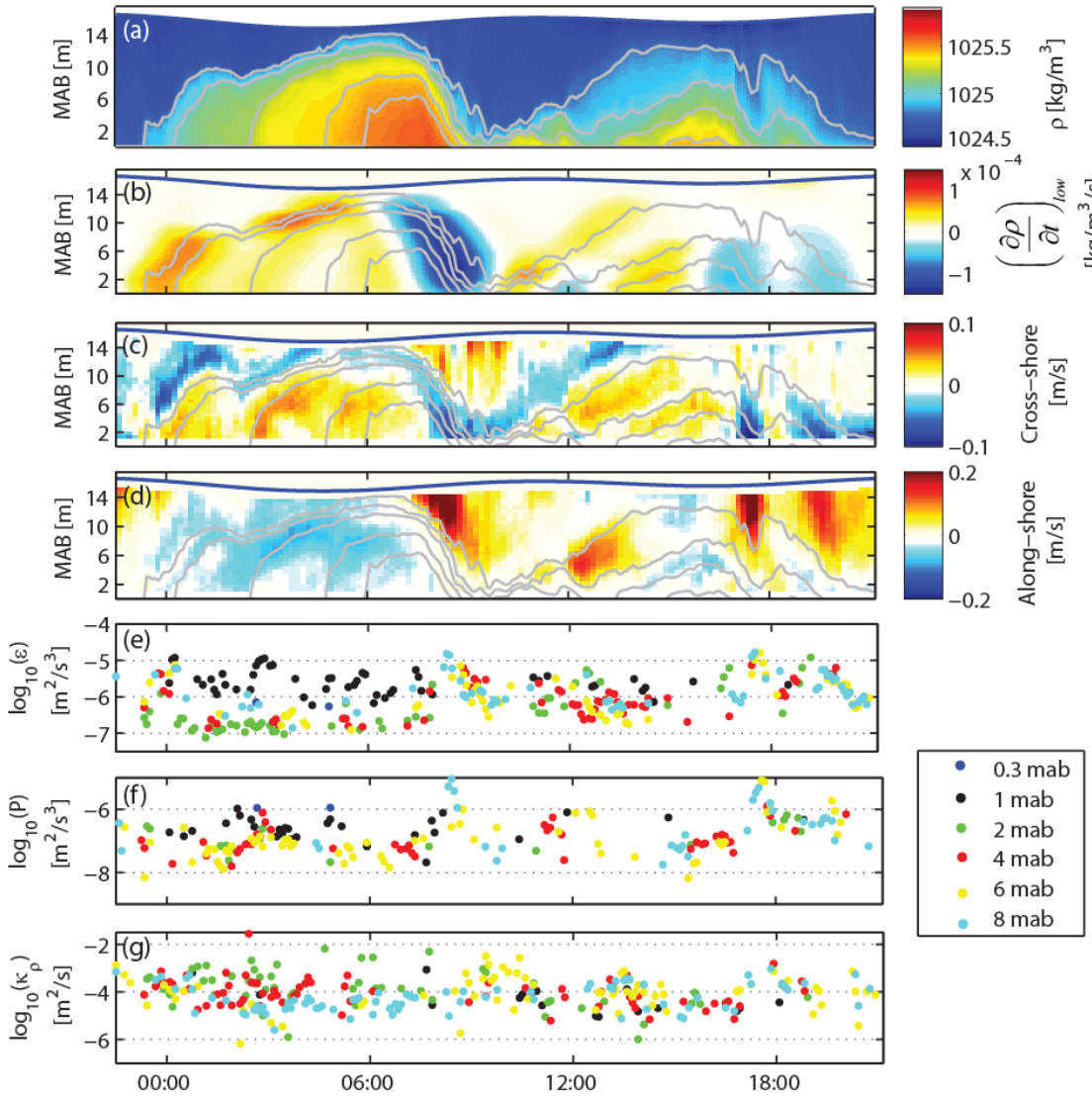

Figure 4.7: Example nearshore internal bore event (16 August 2012) propagating into well-mixed waters at the tower location. (a) Vertical density structure, (b) low-pass filtered, time derivative of density, (c) vertical structure of the cross-shore velocity field (ten-minute averages, positive onshore), (d) vertical structure of the along-shore velocity field (ten-minute averages, positive into the bay), (e) dissipation (ε) of TKE at various heights above the bed, (f) production (*P*) of TKE at various heights above the bed, and (g) vertical turbulent diffusivity, $\kappa_\rho = \frac{B}{N^2} = \frac{R_f}{1-R_f}\frac{\varepsilon}{N^2}$, at various heights above the bed. Isopycnals (grey lines: 1025.5, 1025.4, 1025.2, 1025.0, and 1024.8 *kg/m*^{3}), as well as the location of the sea surface (blue line), are also shown in panels (a - d). Missing values in panels (e - g) correspond to periods that did not fit the quality control criteria for each respective variable (see Section 4.3).

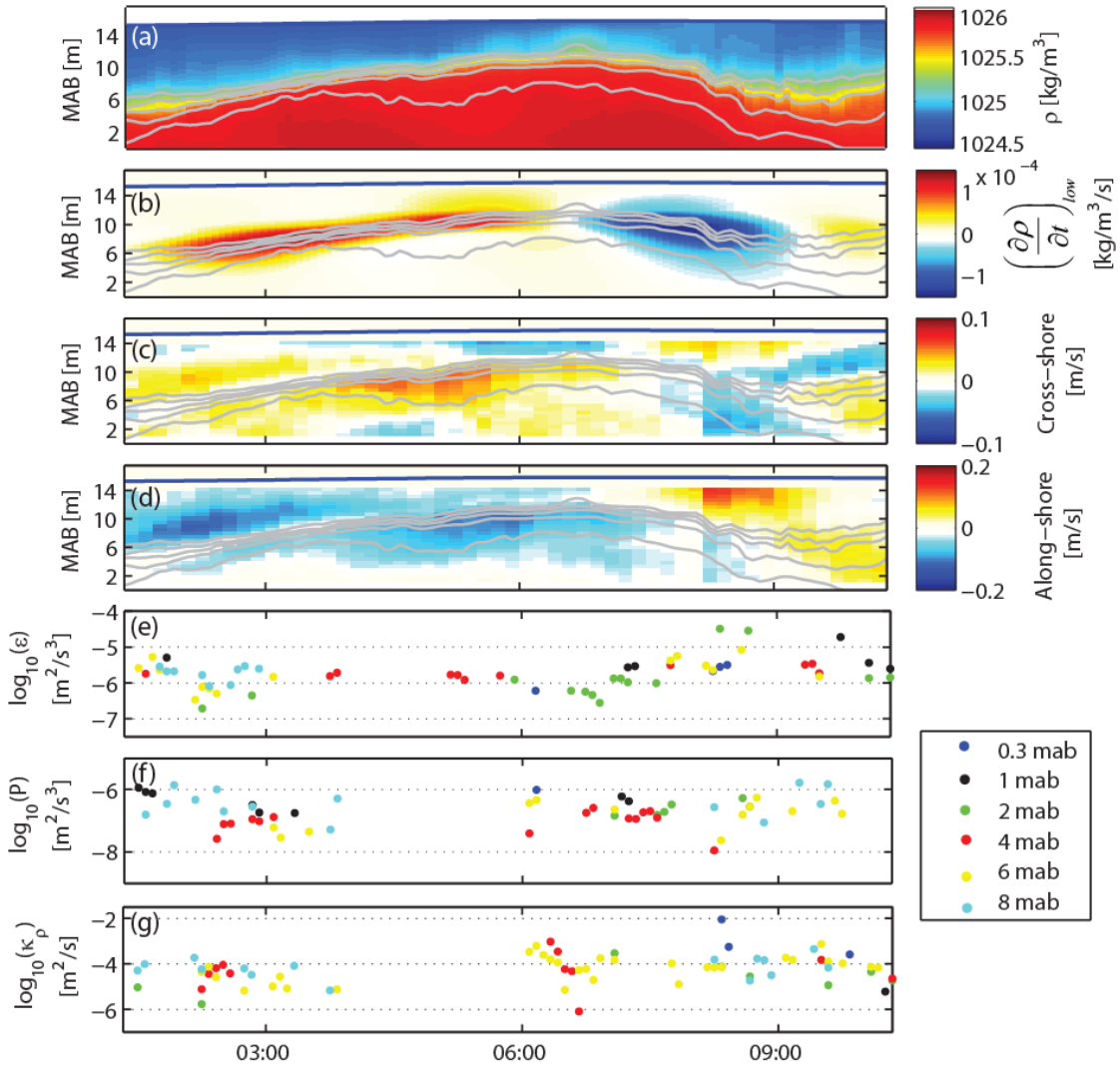

Figure 4.8: Example nearshore internal bore event (10 August 2012) propagating into stratified waters at the tower location. (a) Vertical density structure, (b) low-pass filtered, time derivative of density, (c) vertical structure of the cross-shore velocity field (ten-minute averages, positive onshore), (d) vertical structure of the along-shore velocity field (ten-minute averages, positive into the bay), (e) dissipation (ε) of TKE at various heights above the bed, (f) production (*P*) of TKE at various heights above the bed, and (g) vertical turbulent diffusivity, $\kappa_\rho = \frac{B}{N^2} = \frac{R_f}{1-R_f}\frac{\varepsilon}{N^2}$, at various heights above the bed. Isopycnals (grey lines: 1025.9, 1025.8, 1025.6, 1025.4, and 1025.2 *kg/m*^{3}), as well as the location of the sea surface (blue line), are also shown in panels (a - d). Missing values in panels (e - g) correspond to periods that did not fit the quality control criteria for each respective variable (see Section 4.3).

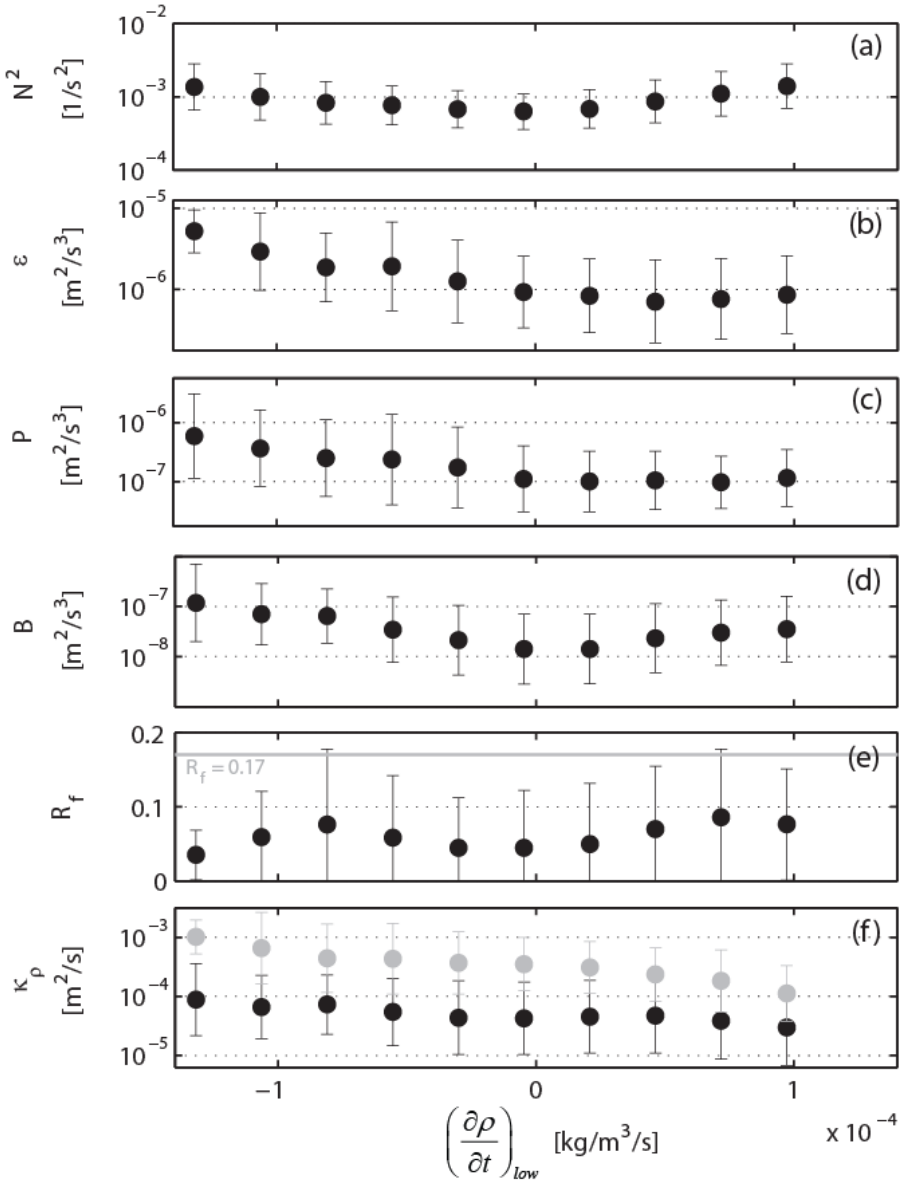

Figure 4.9: (a) Buoyancy frequency squared (N^2), (b) dissipation of TKE (ε), (c) production (P) of TKE, (d), buoyancy flux (B), (e) flux Richardson number (R_f), and (f) vertical turbulent diffusivity calculated using the measured R_f, $\kappa_\rho = \frac{B}{N^2} = \frac{R_f}{1-R_f}\frac{\varepsilon}{N^2}$ (black circles), and a constant R_f = 0.17 [grey line, panel (e)], $\kappa_\rho = 0.2\frac{\varepsilon}{N^2}$ (grey circles), all as a function of the low-pass filtered, time derivative of density. Black circles represent bin-averaged values using measurements at all instrument heights, while the error bars signify the standard deviation of the bin-averaged results. Calculations were restricted to regions of strong density gradients ($N^2 > 10^{-3.5}$ 1/s^2) to isolate the bore interface (see text for details).

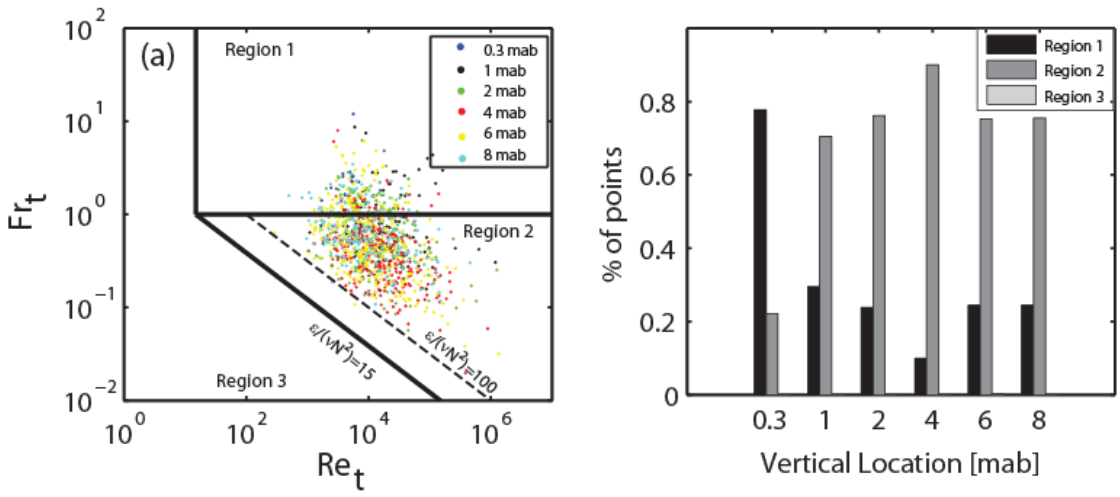

Figure 4.10: (a) Turbulent Froude number (Fr_t) vs turbulent Reynolds number (Re_t) diagrams for all measurements. The color circles represent measurements at the various vertical tower locations. The solid black lines denote the three regions identified by *Ivey and Imberger* [1991] (see text for details). The dashed black line indicates $\varepsilon/\nu N^2 = 100$. (b) Histogram indicating the percentage of points in each of the three regions in (a) for each vertical location. Note that Region 3 was largely absent from the dataset.

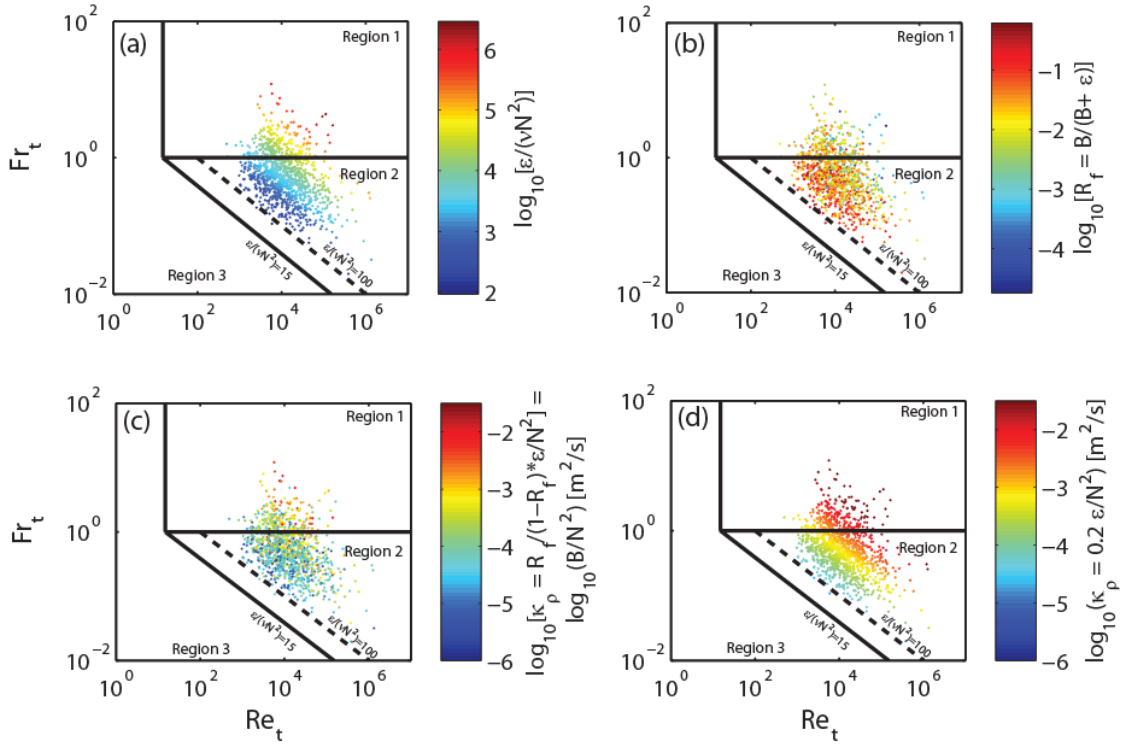

Figure 4.11: Turbulent Froude number (Fr_t) vs turbulent Reynolds number (Re_t) diagrams for all measurements. The color scale represents the (a) turbulence activity number ($\varepsilon/\nu N^2$), (b) the flux Richardson number (R_f), (c) the vertical turbulent diffusivity calculated using the measured R_f, $\kappa_\rho = \frac{B}{N^2} = \frac{R_f}{1-R_f}\frac{\varepsilon}{N^2}$, and (d) the vertical turbulent diffusivity calculated using a constant R_f = 0.17, $\kappa_\rho = 0.2\frac{\varepsilon}{N^2}$. The solid black lines denote the three regions identified by *Ivey and Imberger* [1991] (see text for details). The dashed black line indicates $\varepsilon/\nu N^2 = 100$.

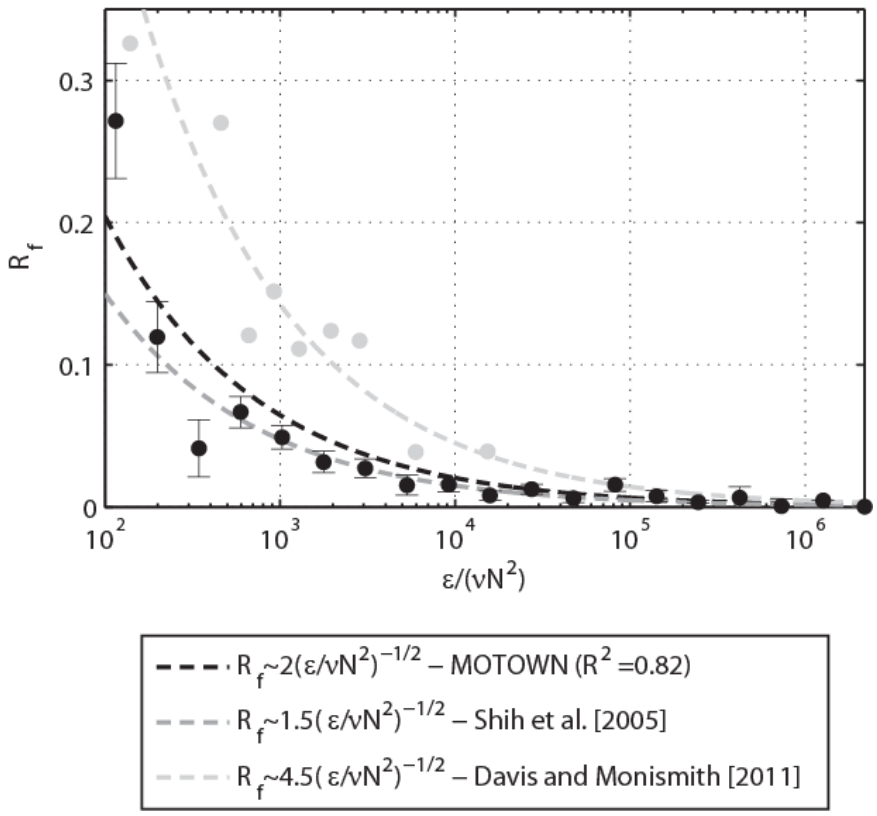

Figure 4.12: The flux Richardson number (R_f) as a function of the turbulence activity number ($\varepsilon/\nu N^2$). The black dots represent binned median values, while the error bars signify the standard error for the current data set. The dashed black line is the least squares power law fit to the current data set (see text for details). Also shown are the power law fits from the DNS simulations of *Shih et al*. [2005] (dashed dark grey line) and the field observations of *Davis and Monismith* [2011] (dashed light grey line and light grey dots) for comparison.

Chapter 5: Nonlinear internal waves and turbulent mixing at a coastal upwelling front

This chapter is prepared as a manuscript for future submittal. As the main author of the work, I made the major contributions to the research and writing. Co-authors include C. Brock Woodson[2], Marek Stastna[3], Leif N. Thomas[4], and Stephen G. Monismith[1].

[1]Environmental Fluid Mechanics Laboratory, Stanford University, Stanford, CA, USA

[2]COBIA Lab, College of Engineering, University of Georgia, Athens, GA, USA

[3]Department of Applied Mathematics, University of Waterloo, Waterloo, Ontario, Canada

[4]Department of Environmental Earth System Science, Stanford University, Stanford, CA, USA

5.1: Abstract

We present high resolution observations of a rank-ordered packet of nonlinear internal waves (NLIWs) at a persistent upwelling front in the nearshore environment (~20 m) of northern Monterey Bay, CA. These waves represent some of the largest nonlinear waves ever observed on the continental shelf, based on a comparison of the wave amplitude (~10 m for the largest waves) to the total water depth (~20 m). The observed waves are described by the fully nonlinear Dubreil-Jacotin-Long equation and are shown to be unstable to shear instabilities. Thorpe scale analysis reveals large (~3 m) overturns and turbulent diffusivities in excess of 10^{-2} m^2/s in the stratified interior during the passage of the waves. We surmise that the modulation of the buoyant plume front by the diurnal winds is linked to the formation of the NLIWs, a phenomenon that is likely prevalent in other coastal upwelling systems.

5.2: Introduction

Nonlinear internal waves (NLIWs) are a widespread feature of the coastal ocean, [e.g., *Pingree and Mardell*, 1985; *Stanton and Ostrovsky*, 1998; *Klymak and Moum*, 2003; *Moum et al*., 2003; *Hosegood and van Haren*, 2004; *Scotti and Pineda*, 2004; *Nash and Moum*, 2005; *Woodson et al*., 2011; *Alford et al*., 2012; *Jackson et al*., 2012; *van Haren et al*., 2012; *Walter et al*., 2012) and often play a key role in cross-shelf exchange of nutrients, sediments, and contaminants [*Wolanski and Pickard*, 1983; *Leichter et al*., 1996; *Boehm et al*., 2002; *Hosegood and van Haren*, 2004]; larval transport [*Pineda* 1991, 1994, 1995, 1999]; and turbulent dissipation and diapycnal mixing [*Moum et al*., 2003; *Hosegood and van Haren*, 2004; *Venayagamoorthy and Fringer*, 2007, 2012; *Woodson et al*., 2011; *van Haren et al*., 2012; *Walter et al*., 2012]. NLIWs in the coastal ocean thus represent an important problem from a fundamental and practical standpoint with significant implications for many physical and biological processes.

Despite their importance, many questions still remain with respect to the evolution, fate, and impact of NLIWs in the nearshore environment. Specifically, previous studies have focused mainly on deeper shelf waters (50+ m depths; see Table 1 of *Alford et al*., [2012]), while the impact of NLIWs in shallower regions (~20 m) has been mainly speculative. There is a dearth of high resolution observations of NLIWs in shallow, nearshore waters [cf. *van Haren et al*., 2012; *Walter et al*., 2012], an environment that is often more energetic than further offshore, is subject to quickly changing environmental conditions, and can be thought of as the “swash zone” for larger-scale internal wave fields on the shelf [e.g., *Walter et al*., 2012]. It is thus clear

that further observations are needed to better understand the effect of NLIWs in the nearshore coastal ocean region, which is generally taken to be one of the most productive and ecologically important parts of the ocean.

During the summer upwelling season, a persistent front forms in northern Monterey Bay, CA. Regional winds create a strong upwelling jet at Point Año Nuevo that flows southward across the mouth of the bay [*Rosenfeld et al*., 1994], while the Santa Cruz mountains shield waters within the bay so that a sharp front forms between the warm waters within the bay and cooler waters offshore [*Woodson et al*., 2009] (Figure 5.1a). On a local scale, diurnal sea breezes modulate the daily propagation of this front (up to 5 km a day) up and down the coast [*Woodson et al*., 2009]. During the evening and early morning when the local winds are weak, the front is able to propagate along-shore poleward due to baroclinic and barotropic pressure gradients. However, as the diurnal winds strengthen, the front decelerates and reverses back into the bay (see *Woodson et al*., [2009] for a discussion of regional and local forcing mechanisms of the front). As the winds weaken in the early evening, amplitude-ordered packets of NLIWs are consistently observed near the location of the front and propagate back into the bay oriented in the along-shore direction [*Woodson et al*., 2011]. Previous observations of the waves have shown that they may be prone to shear instabilities and lead to enhanced turbulent mixing [*Woodson et al*., 2011]. Yet, these observations lacked sufficient vertical and temporal resolution to adequately resolve the dynamics. Here, we take advantage of detailed measurements of NLIWs in this region to better understand their characteristics and potential effects on the nearshore environment.

In Section 5.3, we describe the experimental setup consisting of a dense array of high temporal and vertical resolution measurements. General features over the entire study period are discussed, followed by a detailed examination of the events prior to the arrival of a rank-ordered packet of NLIWs on 17 July 2011, in Section 5.4. These waves represent some of the largest nonlinear waves ever observed on the continental shelf, based on a comparison of the wave amplitude to the total water depth (cf. Table 1 of *Alford et al*. [2012]). Section 5.5 examines the wave features in detail using fully nonlinear theory (i.e., the Dubreil-Jacotin-Long equation). After this, the effect of the waves on local turbulent mixing, and the potential for the waves to transport biological scalars large distances, is explored using a Thorpe scale analysis and wave energetics in Section 5.6. In Section 5.7 we speculate on possible generation mechanisms. Finally, we summarize the findings and highlight potential ecological implications in Section 5.8.

5.3: Experiment

Moored instrument arrays were deployed from 8 to 21 July 2011 in order to capture frontal dynamics and internal wave activity. Two moorings were deployed on the 21 m isobath roughly 220 m apart in the along-shore direction offshore of Sandhill Bluff, CA located in northern Monterey Bay (Figure 5.1b-c). This is the location of frequent front crossings and along-shore propagating (equatorward) internal waves [*Woodson et al*., 2009, 2011]. The northernmost mooring (FDN) was equipped with a dense vertical arrangement of SBE39 and SBE56 temperature loggers (n = 17), with increased resolution (0.5 m vertical spacing) near the pycnocline (Figure 5.1c). In

order to capture the propagation of internal waves and the front, the southernmost mooring (FDS) was also equipped with thermistors, but with lower spatial resolution (n = 5). Both moorings had SBE37 conductivity-temperature-depth (CTD) loggers bracketing the water column [1 and 18 meters above the bottom (mab)], as well as RDI 1200 kHz Workhorse acoustic Doppler current profilers (ADCPs). FDN sampled in fast-ping mode 12 (1 s) with 0.5 m vertical bin spacing, while FDS sampled at 5 s with 0.5 m bins. We note that the NLIWs examined are much longer than the ADCP beam spacing so that the velocity measurements in the presence of the waves are valid [cf. *Scotti et al*., 2005]. During the summer upwelling season, salinity variations in Monterey Bay are sufficiently small so that density is largely controlled by temperature [e.g., *Woodson et al*., 2009, 2011; *Walter et al*., 2012]. Hence, we calculated density at all thermistor locations using the average of the top and bottom salinity measurements derived from the CTDs; the maximum error using this method is 0.01 kg/m^3. Local winds were obtained at five-minute intervals from Long Marine Laboratory (LML, Figure 5.1b), and regional offshore winds were collected at ten-minute intervals from the National Data Buoy Data Center (NDBC) buoy 46042 (36.785 N, 122.469 W). Wind stresses were calculated using the method of *Large and Pond* [1981]. All times referenced in the text and figures are in Pacific Daylight Time, unless otherwise noted.

In this contribution, we focus on a single, well-defined, packet of NLIWs during the evening of 17 July 2011. First, we describe the sequence of events and development prior to propagation of the NLIWs past the mooring array. Next, we focus our discussion on the wave characteristics and potential for turbulent mixing

during the passage of these waves. We note that the entire record is marked by a number of frontal crossings at the moorings followed by packets of internal waves that occur in the late evening (Figure 5.2b). Understanding what factors influence the wave characteristics observed in different wave packets is the subject of future research and will be reported elsewhere. Nonetheless, long term observations, albeit with less temporal and vertical resolution than the current study, indicate that these results may be representative of the ~7 month long upwelling season where 68% of the total days in the season contained NLIW signatures [*Woodson et al.*, 2011].

5.4: Observations

5.4.1: General Features Over the Entire Study Period

Throughout the study period, regional offshore winds remained upwelling favorable, though they varied in magnitude (Figure 5.2a). Likewise, the local wind forcing was particularly strong and showed a distinct diurnal signal (Figure 5.2a and Figure 5.3b). The temperature structure is marked by episodic frontal crossings delineated by sharp transitions from cool (~10 °C) recently upwelled waters to warm (~12-15 °C) upwelling shadow waters (Figure 5.2b). The middle of the record (13 to 15 July) is highlighted by large regional upwelling favorable winds, in addition to strong local winds, so that the front is pushed back into the Bay (i.e., equatorward of the moorings) by the strong upwelling plume. This can be seen in the temperature field, where the influence of the upwelling jet is expressed as well-mixed waters near 10° C lasting several days. This is consistent with long-term observations made by

Woodson et al. [2009]. Also evident throughout the temperature record, and in particular after frontal crossings, is the presence of strong internal wave activity.

5.4.2: Events Prior to the Arrival of a Packet of NLIWs on 17 July 2011

Prior to the arrival of the front, the water column is well mixed (~10 °C), indicative of recently upwelled waters from Point Año Nuevo [*Rosenfeld et al*., 1994] (Figure 5.4b). It is important to note that the well-mixed waters ahead (poleward) of the front do not provide a propagation pathway for internal waves in this direction; however, internal waves are allowed to propagate into the stratified medium behind the nose of the front (equatorward). From hereafter, this study will refer to ahead of the front to mean poleward of the front's nose (well-mixed waters), while behind the front will denote equatorward of the nose (stratified waters). These definitions will apply regardless of the front propagation direction (e.g., once the front has reversed, as discussed below, these descriptions will still be used to maintain consistency).

In the early morning, while the local along-shore winds are still weak, a sharp jump in temperature (ΔT ~ 3-4° C, Fig. 4b) occurs throughout the water column as the front propagates northward on a slight preexisting northward barotropic current (see *Woodson et al*. [2009] for regional and local forcing mechanisms of the front). Coincident with the front crossing is a rapid increase in along-shore velocities (Δv ~ 0.20-0.25 m/s, Figure 5.4c). Convergence in the along-shore velocities near the frontal region gives rise to significant downwelling. Cross-shore velocities were generally weak, when compared to the along-shore currents, and followed the same circulation at the front described by *Woodson et al*., [2009] (Figure 5.4d). The passage of the front ("Frontal Passage" period, Figure 5.4) stratifies the water column locally and drives

large vertical velocities that impart vertical displacements to the pycnocline behind the front. These displacements aid in converting the kinetic energy of the front into potential energy and internal waves.

After the frontal crossing, the local diurnal winds begin to increase in what we refer to as the "Wind Modulation" period (Figure 5.4a). During this period, we hypothesize that the along-shore equatorward winds arrest the poleward advection of the front and reverse the currents in the along-shore direction to flow equatorward (Figure 5.4c). This is in accord with long-term observations made by *Woodson et al*. [2009], which indicate that the local diurnal winds are responsible for the flow reversal of the front. This is highlighted by the fact that during extended regional and local wind relaxation events when the local winds essentially shut down for several days, the along-shore currents remained poleward and did not reverse back into the bay on a diurnal time scale (Figure 7 in *Woodson et al*., [2009]). The reversal of the currents by a local wind stress is analyzed by considering the depth-integrated momentum equation over the "Wind Modulation" period (8:45 – 18:00, Figure 5.4), where brackets denote a temporal average over this period. This analysis reveals that the poleward deceleration (i.e., equatorward acceleration) of the currents,

$$\left\langle \int_{-H}^{0} \frac{\partial v}{\partial t} dz \right\rangle = -1.0x10^{-4} \frac{m^2}{s^2}, \tag{5.1}$$

is consistent with the observed wind stress,

$$\left\langle \frac{\tau_{wind}}{\rho_o} \right\rangle = -9.5x10^{-5} \frac{m^2}{s^2} \approx -10^{-4} \frac{m^2}{s^2}, \tag{5.2}$$

over the "Wind Modulation" period.

In the above analysis, tidal effects were neglected. Several different tidal models of the Monterey Bay region indicate that near the study site 1) both the barotropic and baroclinic tides are dominated by the M_2 (12.42 hr period) tidal component with a slight contribution from the K_1 (23.93 hr period) component, 2) depth-averaged and surface tidal current ellipses are on the order of 5 cm/s and ~2-3 cm/s for the M_2 and K_1 tidal components, respectively, and 3) baroclinic tides are generally negligible away from the canyon (i.e., on the shelf and the location of this study) [*Rosenfeld et al*., 2009; *Wang et al*., 2009; *Carter*, 2010; etc.]. *Rosenfeld et al*., [1999] note that near the study site the observed K_1 surface currents, derived from high-frequency (HF) radar, are significantly stronger than those produced by the tidal model and postulate that this is due to strong diurnal wind forcing. In the current study, analysis of both the depth-averaged and surface along-shore velocity spectra reveals a dominant peak at the diurnal frequency with a smaller peak at the semi-diurnal frequency (Figure 5.3a). Additionally, the peak of the surface velocity spectra at the diurnal frequency is much larger than that of the depth-averaged flow, suggesting a surface-intensification of the currents at this frequency likely driven by the local diurnal winds (Figure 5.3a). This is supported by a statistically significant coherence between the local winds and the surface (depth-averaged) velocities at the diurnal frequency (not shown).

To further validate the claim that the currents are predominantly wind driven and not significantly influenced by the tides, tidal harmonic analysis was performed on the velocity observations over the entire study period (8 to 21 July 2011) using the T_TIDE package [*Pawlowicz et al*., 2002]. The K_1 and M_2 components were dominant

for the depth-averaged velocity, with amplitudes of 7.0 cm/s and 4.7 cm/s, respectively. Also, the T_TIDE results for the surface velocity did not contain a significant M_2 tidal component (i.e., low signal to noise ratio as determined by T_TIDE), while the K_1 constituent had an amplitude of 11.2 cm/s. The large K_1 amplitudes computed by T_TIDE are likely due to signal contamination of the diurnal band by strong local winds, given that the tidal models in this region show tidal ellipses on the order of 2-3 cm/s for this component. In a region where the M_2 tides should be larger than the K_1 tides (Figure 5.3c) [e.g., *Rosenfeld et al*., 2009; *Wang et al*., 2009; *Carter*, 2010; *Suanda et al*., 2011], the above points corroborate the idea that the local diurnal winds are responsible for the flow reversal of the front, whereas tidal effects are small.

At this point, the front is poleward of the moorings, but is moving in the equatorward direction along-shore due to the winds. At the end of the "Wind Modulation" period, the local winds are slackening, so that the equatorward advection of the buoyant plume front begins to decrease slightly due to barotropic and baroclinic pressure gradient forces that attempt to drive the front poleward [cf. *Woodson et al*., 2009]. This is an important point since the front is accelerated equatorward during the "Wind Modulation" period; however, as the winds slacken at the end of the "Wind Modulation" period the front begins to slow down, although still moving in the equatorward direction (see Section 5.7). After this, a rank-ordered packet of large amplitude internal waves (Figure 5.4, "NLIWs" period) is observed propagating back into the bay (along-shore equatorward direction, see Section 5.5).

5.5: Wave Features

5.5.1: Field Observations

The rank-ordered train of NLIWs observed on 17 July 2011 is characterized by upper and lower mixed layers with a thick (~2-5 m) pycnocline (Figure 5.5a), as well as a strongly sheared baroclinic flow in the along-shore direction (Figure 5.5b). We again note that the waves examined are much longer than the ADCP beam spacing so that the measured velocities are valid [cf. *Scotti et al*., 2005]. The observed, nonlinear propagation velocity (c_{obs}) of individual waves in the presence of an ambient current is calculated using the difference in arrival time of wave troughs between the moorings. This formulation takes into account the effect of finite amplitudes (i.e., nonlinearity) on the wave propagation speeds. As noted previously, this method reveals that the observed waves are propagating in the negative along-shore direction (equatorward), consistent with the idea that the waves were generated at and radiated behind the nose (i.e., equatorward) of the equatorward propagating front (see Section 5.7). The leading large amplitude wave (e.g., the initial wave has an amplitude of ~10 m with a total water depth of ~20 m and a top layer depth of ~5 m) takes the form of a broad, blunt trough with isopycnals that are depressed from their upstream height (i.e., an internal wave of depression) and propagates at a speed of 0.3 m/s in the negative along-shore direction (i.e., c_{obs} = -0.3 m/s). Based on a comparison of the wave amplitude (~ 10 m) to the total water depth (~ 20 m), the initial 2-3 waves in the rank-ordered packet are among the largest nonlinear waves ever reported on the continental shelf (Figure 5.5a) (cf. Table 1 of *Alford et al*. [2012]).

Examination of the vertical velocity field reveals that convergence (divergence) zones in the leading (trailing) edges of the waves drive large downwelling (upwelling) events (Figure 5.5c). As the current speed in the upper layer of the water column decreases, the waves become smaller, likely due to the sustained weakening of the buoyant front [*Nash and Moum*, 2005]. This is due to the fact that the front is continually losing kinetic energy to the potential energy of the internal waves, in which case the amplitude of each subsequent wave is decreased. This leads to a rank-ordered train of waves [cf. *Nash and Moum*, 2005], with the largest, fastest (i.e., most nonlinear) waves seen propagating past the mooring array first. While the leading wave is clearly a depression wave, the trailing waves (~22:00) appear to undergo a polarity reversal and morph into waves of elevation as the pycnocline shoals towards the surface (Figure 5.5a). Thus, it is possible that depression waves experience a change of environmental conditions in which waves of depression can no longer exist so that they form large amplitude undular bores.

The mean background density (ρ_b) and along-shore velocity (v_b) profiles for the period before the arrival of the wave train (18:25 – 19:15), along with the standard deviation of the profiles over the same period, were computed and are shown in Figure 5.6a and Figure 5.6b, respectively. The period of time was chosen by first computing a running, windowed standard deviation of the density profile and horizontal (i.e., along-shore) current. Subsequently, we chose a period over which the standard deviation was minimized. While the flow never achieves an exact steady state, the standard deviation of both the background current and density profile, both shown as grey-filled regions, can be seen to be quite small. This illustrates the existence of a

quasi-steady background state prior to the wave train, and confirms that the initial wave is a depression wave.

The velocity profiles of the leading waves of the NLIW train are examined in Figure 5.7a. The bottom panels show along-shore velocity profiles of the background (v_b, black), total at the wave trough (v, blue), and wave-induced ($v_w = v - v_b$, grey) velocities as a function of depth at the wave-trough locations indicated by vertical lines in Figure 5.7a. It can be seen that both waves induced similar horizontal currents. In particular, the wave-induced currents exhibit an inflection point near the mid-depth, or pycnocline, region. A similar inflection point was found for wave-induced profiles at the next five troughs in the NLIW train (not shown). The location of the inflection point was not sensitive, and remained nearly constant, using different background currents within the grey shaded region of Figure 5.7b.

5.5.2: Fully Nonlinear Theory

The wave train can be described by a variety of theoretical models. Linear theory, through the Taylor-Goldstein (TG) equation, can yield estimates of the wave propagation speed in the presence of an ambient current. The intrinsic phase velocity (c_{linear}, includes the effects of the ambient currents in its formulation, and therefore represents the phase velocity relative to the ground and not the water) of a linear wave prior to the release of the waves (e.g., mean background period discussed above) is calculated using the TG equation [*Nash and Moum*, 2005]. The TG equation considers normal mode perturbations to a stratified, parallel shear flow, and its eigenvalues and

eigenfunctions provide the linear phase velocity (c_{linear}) and vertical structure function ($\hat{\psi}$), respectively, of a linear disturbance,

$$\frac{d^2\hat{\psi}}{dz^2}+\left[\frac{N^2}{(V-c_{linear})^2}-\frac{V_{zz}}{(V-c_{linear})}-k^2\right]\hat{\psi}=0, \tag{5.3}$$

where $N^2(z)=-\frac{g}{\rho_o}\frac{\partial\rho}{\partial z}$ is the buoyancy frequency squared and $V(z)$ is the time-averaged along-shore velocity, both calculated using the mean background density (ρ_b) and along-shore velocity (v_b) profiles prior to the initial wave, respectively; k represents the horizontal (i.e., along-shore) wavenumber; and the stream function is given by $\psi=\hat{\psi}(z)e^{ik(x-c_{linear}t)}$. Imposing rigid lid boundary conditions at the surface and bottom [$\hat{\psi}(z=0)=\hat{\psi}(z=H)=0$], the TG equation was solved numerically in the longwave limit following the numerical scheme described by *Smyth et al*. [2011] to obtain the linear phase velocity of the first vertical internal mode (c_{linear}) in the negative along-shore direction (i.e., same direction as the observed waves). We note that the solution in the longwave limit (i.e., $k\to 0$) was nearly identical to the solution using a horizontal wavenumber based on the observed waves ($k=\frac{2\pi}{\lambda}\approx 1.3$ x 10^{-2} 1/m, where the leading wave has an approximate wavelength of $\lambda\approx 470$ m) given that the observed waves were very long (i.e., $kH_1 << 1$, where $H_1\approx 5$ m is the top layer depth). Using this approach, we obtain a linear phase velocity of $c_{linear}\approx$ - 0.23 m/s (oriented in the negative along-shore direction), which is much smaller than the observed nonlinear phase velocity of c_{obs} = - 0.3 m/s indicating the importance of nonlinearity. Additionally, linear theory (TG equation) only yields qualitative

information about the vertical structure of the wave-induced currents and no information about the wave shape or amplitude can be extracted.

Weakly nonlinear theories, leading to the Korteweg-de Vries (KdV) or Gardner equations for the horizontal structure of the waves can give more information about the possible wave shapes, along with estimates of the increase in propagation speed due to finite amplitude effects. We refer the reader to *Helfrich and Melville* [2006] for a detailed review of weakly nonlinear theories. Since the undisturbed density profile upstream of the wave train has a main pycnocline near the mid-depth region, the second order nonlinear term (α_2 in *Helfrich and Melville* [2006]), leading to the Gardner equation, may be expected to play a significant role [*Helfrich and Melville,* 2006]. This would suggest that the largest amplitude waves can be expected to be flat-troughed waves, as is evident in the shape of the leading wave (Figure 5.5a). However, the need to include the second order nonlinearity makes the application of the dnoidal wave solution of the KdV equation difficult [*Apel,* 2003]. Weakly nonlinear theory can be used to quantify the importance of the background shear current. Computation of the first order coefficient of nonlinearity (α_1 in *Helfrich and Melville* [2006]) suggests that the value of this parameter is roughly four times more sensitive to the shear currents with a geometric shape computed from the data, as discussed above, oriented in the direction of wave propagation. This indicates that the observed waves are strongly affected by shear. Despite their utility in reaching qualitative conclusions, weakly nonlinear theories are well known to have difficulty in quantitatively representing vertical profiles of wave-induced currents [*Lamb and Yan*,

1996; *Lamb*, 1999; *Stastna and Peltier*, 2005] when the wave amplitude is large, as is clearly the case for the observed waves (Figure 5.5a).

Therefore, we attempted to extract information about the wave train in Figure 5.5 using the exact (fully nonlinear) theory, or in other words, the Dubreil-Jacotin-Long (DJL) equation. The DJL equation describes internal solitary waves (ISW) and is equivalent to the full set of stratified Euler equations. In a frame of reference moving with the ISW, the flow is steady and the governing stratified Euler equations reduce to the DJL equation, which has been extended to include a background shear current, $V(z)$ [e.g., *Stastna and Lamb*, 2002]:

$$\nabla^2\eta + \frac{V'(z-\eta)}{c-V(z-\eta)}\left[\eta_x^2 + (1-\eta_z)^2 - 1\right] + \frac{N^2(z-\eta)}{[c-V(z-\eta)]^2}\eta = 0, \tag{5.4}$$

where $\eta(x,z)$ is the isopycnal displacement, subject to the boundary conditions,

$$\eta(x,0) = \eta(x,H) = 0 \text{ and } \lim_{x\to\pm\infty}\eta(x,z) = 0. \tag{5.5}$$

Solutions of the DJL equation have been successfully used to match vertical profiles of wave-induced velocities in simulations of resonantly generated waves [*Stastna and Peltier* 2004, 2005]. Using a variational formulation [*Turkington et al*., 1991] extended to include background shear currents [*Stastna and Lamb*, 2002], the DJL equation can be solved to obtain solitary waves of various amplitudes. *Dunphy et al*. [2011] discuss a publically available MATLAB implementation of the solver, which we have employed for the calculations presented below. In general, wave amplitudes can be computed up to a limiting wave amplitude, with the upper bound given by either the onset of breaking (i.e., overturning isopycnals), wave broadening to the so-called conjugate flow, or the onset of shear instability.

Using only the background density field (i.e., background current is initially zero), the solution to the DJL equation yields a solitary wave of depression with a broad central region (not shown). With its geometric profile fixed, the background current is progressively introduced by increasing the magnitude of the profile to match the observed velocity profile. Since the wave-induced baroclinic vorticity of the computed waves is of the same sign as the vorticity due to the background current (Figure 5.8b), an increase in the magnitude of the background current reduces the maximum possible wave amplitude. This is consistent with the results of *Stastna and Lamb* [2002], though this simple heuristic cannot be applied to the observed waves, due to the observed inflection point in the wave-induced profiles shown in Figure 5.7b-c. However, the upper bound of wave amplitude is difficult to identify in the present case, due to a gradual "wandering" of the numerical algorithm associated with a decreasing gradient Richardson number, $Ri = \frac{N^2}{S^2}$, where $S^2 = \left(\frac{\partial U}{\partial z}\right)^2 + \left(\frac{\partial V}{\partial z}\right)^2$, or physically, with a propensity for shear instability.

Figure 5.8b shows v_b (black), v (blue), and v_w (grey) as a function of depth for the largest wave amplitude-current strength combination with which it was possible to compute waves. Figure 5.8c shows the vertical profile of the gradient Richardson number at the wave trough, indicating a region of possible shear instability near the trough of the wave (Ri < 0.25, blue curve). While it is likely that shear instabilities precluded a full amplitude solution to the DJL equation (see Figure 5.5a and Figure 5.8a for the observed and computed amplitude, respectively), this criterion (i.e., Ri < 0.25) does not guarantee the onset of shear instability in progressive internal waves. It

is well known that gradient Richardson number must fall well below the canonical critical value of 0.25 for long enough time periods in order to induce instability [cf. *Troy and Koseff*, 2005; *Barad and Fringer*, 2010; *Lamb and Farmer*, 2011]. Likewise, the presence of the waves creates a region of minimal stratification near the surface causing the gradient Richardson number to drop significantly. Given this, the gradient Richardson number might not be the best predictor of the onset of shear instability in this region. While we hypothesize that the waves enhance the shear enough to induce instability and preclude full amplitude solutions to the DJL equation, we cannot say this with certainty. This will be explored further below in Section 5.6.

The general structure of the wave-induced currents is similar to those shown in Figure 5.7b and Figure 5.7c, though the inflection point in the wave-induced profile is largely absent. It is interesting to note that increasing the strength of the background shear current further, and allowing the variational algorithm to take one unstable step, leads to wave-induced profiles that exhibit the inflection point shown in the data. It is thus possible that the algorithm attempts to take a step toward a wave that is realizable in nature, but is not a true minimum of the mathematically constrained optimization problem [*Turkington et al*., 1991].

5.6: Turbulent Mixing

5.6.1: Thorpe Scale Analysis

It is necessary to further validate the claim that shear instabilities precluded a full amplitude solution to the DJL equation, and that these instabilities are indeed physical. Consistent with the numerical results, we observed regions of potential shear

instability (*Ri* < 0.25, Figure 5.9c) in the pycnocline during the passage of the wave packet, particularly in the initial large-amplitude waves. It is important to note that regions with *Ri* < 0.25 were observed in the regions with the strongest stratification (i.e., the pycnocline; Figure 5.9a). Also interesting is the development of large shear near the bottom of the water column as the wave train propagates past the mooring array, although not as large as the shear values within the pycnocline (Figure 5.9b).

The assertion that the waves are unstable to shear instabilities is further supported by performing a Thorpe scale analysis in the pycnocline. Turbulent mixing in the pycnocline (12 to 17 mab), due to the passage of the waves (~19:45 to 23:00), was estimated using the 0.5 m spaced thermistors. Thorpe length scales were calculated by first identifying unstable overturns greater than the instrument resolution in instantaneous density profiles and then calculating the root mean square of the Thorpe displacement [e.g., *Thorpe*, 1977]. Average turbulent kinetic energy (TKE) dissipation rates ($\bar{\varepsilon}$) in the pycnocline were then estimated as $\bar{\varepsilon} = \overline{L_{t,i}{}^2 \langle N \rangle_i^3}$, where a subscript *i* refers to the *i*th overturn, $\langle N \rangle_i$ is the mean buoyancy frequency in the reordered (statically stable) region of the *i*th overturn, an overbar represents the average of all *i* events in the pycnocline, and we have assumed that the Ozmidov length scale (L_o) equals the Thorpe length scale (L_t). From the above calculation for the dissipation rate, average diapycnal diffusivities in the pycnocline were quantified following the *Osborn* [1980] formulation, $\kappa_\rho = \Gamma \bar{\varepsilon} / N^2$, where N^2 is calculated from the average background profile in the pycnocline (no reordering since turbulent diffusion acts on the background density gradient) and the mixing efficiency is taken

to be a constant, $\Gamma = 0.2$. While the mixing efficiency has been shown to be a function of the turbulence activity number, age of the turbulent patch, and origin of the turbulence [e.g., *Smyth et al*. 2001; *Shih et al*. 2005; *Davis and Monismith*, 2011], we use $\Gamma = 0.2$ with the caveat that diffusivity estimates may be sensitive to the choice of mixing efficiency used [cf. *Dunckley et al*., 2012].

Deriving TKE dissipation rates using a Thorpe scale analysis in a time-variable basic state requires that the available potential energy (APE) contained in a particular overturning event has time to convectively overturn and completely dissipate in a temporally evolving flow field (e.g., due to the waves). Thus, the time scale for convective overturning (T_{over}) is estimated and compared to the time it takes for the background flow to evolve (T_{back}). If the former is much shorter than the latter, then the assumption of an instantaneous APE release is justified. From the Thorpe scale analysis, the average overturning height ($\overline{L_t}$) and buoyancy anomaly ($\bar{b}$) within the pycnocline are derived. The average buoyancy anomaly, $\bar{b} = -g\dfrac{\overline{rms_i\left(\rho - \rho_{sort}\right)}}{\rho_o}$, is calculated using the root mean square deviation of the measured density profile (ρ) from the sorted profile (ρ_{sort}) within the *i*th overturn and an average value of all *i* events in the pycnocline is estimated in the same manner as the average TKE dissipation rates ($\bar{\varepsilon}$). It follows that the scaling for the overturning time is $T_{over} \sim \left(\dfrac{\overline{L_T}}{\bar{b}}\right)^{1/2}$. We compare the overturning time scales to the time it takes for the background flow to evolve using a wave period of twenty minutes (i.e., T_{back} = 20 min, typical of the waves during the "NLIWs" period, especially for the leading two or

three large amplitude waves) since the waves represent the major modulator of the quasi-steady state background flow. The background flow evolves slower than the time it takes for convective overturning to occur (i.e., $T_{over} << T_{back}$), thereby justifying the dissipation estimates (Figure 5.10).

The leading waves (~20:00 to 21:00) contained large turbulent overturns (3 m) and elevated dissipation rates (up to ~10^{-5} m^2/s^3), likely due to local shear instabilities ($Ri < 0.25$). These enhanced rates of TKE dissipation in the pycnocline are consistent with previous estimates by *Woodson et al*. [2011] found using isopycnal slope spectra. Vertical turbulent diffusivities in excess of 10^{-2} m^2/s were also detected in the pycnocline during the passage of the leading waves (Figure 5.5d), while the average diffusivity during the passage of the NLIW train was of order 10^{-3} m^2/s, both of which are well above the canonical value of ~10^{-5} m^2/s for the ocean interior [*Gregg* 1989]. This suggests that shear-produced by the wave train leads to short length scale instabilities, and a significant increase in TKE, and thus drives active mixing in the stratified interior. Consequently, this affects diapycnal mixing that is critical for many ecologically important processes. On a larger scale, the turbulence stress divergence in the vicinity of these NLIW trains, such as the one described above, may play a critical role in the along-shore momentum balance and further deceleration of the front [*Kilcher et al*., 2012]. The generation of internal waves at frontal interfaces may thus provide an important mechanism for the cascade of energy from the kinetic energy of the large-scale front to the gravitational potential energy of the internal waves to small-scale turbulence as the waves become unstable.

5.6.2: Energetics and Dissipation

We hypothesize that these waves are able to transport biological scalars, such as larvae, back into the Bay, providing a mechanism for nearshore retention and larval connectivity [*Lamb*, 1997; *Pineda*, 1991]. Following the approach of *Klymak and Moum* [2003], the total wave energy of the initial large-amplitude wave is estimated and compared to the estimated dissipation rate to derive a time-scale associated with the decay of the wave due solely to turbulent dissipation. The total wave energy (E_w) is calculated using the perturbation kinetic energy (KE_w) and the available potential energy (APE_w) densities. The perturbation kinetic energy density is defined as,

$$KE_w = \frac{1}{2}\rho_o(u'^2 + v'^2 + w'^2), \tag{5.6}$$

where (u', v', w') are the wave perturbation velocities found by subtracting the quasi-steady background velocity (u_b, v_b, 0) from the measured velocities during the passage of the initial wave. The available potential energy density, or the portion of the potential energy that can be converted into kinetic energy, is defined using the positive-definite expression that is commonly used for nonlinear internal waves [*Scotti et al*., 2006; *Lamb and Nguyen*, 2009; *Kang and Fringer*, 2010]:

$$APE_w = \int_{z^*}^{z} g[\rho(z) - \rho_b(z')]dz', \tag{5.7}$$

where $z^*(y, z, t)$ is the height of the fluid parcel at (y, z) in the reference (i.e., background) stratification. Finally, the total wave energy is calculated by integrating the available potential and kinetic energy densities over the area of the wave,

$$E_w = \iint \left(APE_w + KW_w \right) dzdy, \tag{5.8}$$

where $dy = c_{obs}dt$ is calculated using the observed phase speed of the initial wave (c_{obs} = 0.30 m/s). The total calculated wave energy for the initial wave is 5.9 kJ/m, which is in line with previous estimates made by *Woodson et al*. [2011] for nonlinear internal waves in this region.

Next, it is assumed that the total wave energy is dissipated solely due to turbulence following the analysis of *Klymak and Moum* [2003]. The rate of decay is estimated by integrating the turbulent dissipation rate found using the Thorpe scale analysis over the area of the wave, $\iint \rho_o \varepsilon dzdy$. The dissipation rates found using the Thorpe scale analysis are only valid in the pycnocline. Thus, the near-bed, bottom-generated turbulence is estimated using the law of the wall scaling, $\varepsilon \sim \frac{u_*^3}{\kappa z}$, where u_* is the friction velocity, $\kappa = 0.41$ is the Von Kármán constant, and z is the height above the bed [*Pope*, 2000]. The friction velocity squared is approximated using a drag-law near the bed, $u_*^2 = C_d u_b^2$, where C_d = 2.5 x 10^{-3} is the drag coefficient for a sandy bottom [cf. *Gross and Nowell*, 1983] , and $u_b = \sqrt{u^2 + v^2}$ is the near-bed velocity taken to be at the first ADCP bin height of z = 1.3 m. Hence, the near-bed turbulent dissipation rate can be approximated by $\varepsilon \sim \frac{(C_d)^{3/2} u_b^3}{\kappa z}$. The mean near-bed dissipation rate during the passage of the initial wave was approximately 10^{-7} m^2/s^3, which is comparable to the dissipation rates found using the Thorpe scale analysis in pycnocline during the passage of the initial wave. Therefore, a constant value of ε =

10^{-7} m^2/s^3 is used throughout the water column [cf. *Klymak and Moum*, 2003], and a time scale for the dissipation of the initial wave is defined as $E_w / \iint \rho_o \varepsilon dzdy$.

This results in a wave dissipation time scale of 0.84 days, and with a phase speed of c_{obs} = 0.30 m/s, this implies that the initial wave will propagate just over 21 km before being dissipated due to turbulence. We note that the above estimate might be slightly over dissipative since there is a stratified, and presumably less dissipative region, between the active pycnocline and near-bed region. Using a dissipation rate of 10^{-8} m^2/s^3 (one order of magnitude lower), yields a wave propagation distance of 210 km. Thus, dissipative losses due to turbulence cannot control the distance that these waves can propagate before they reach the nearshore. Moreover, it is likely that changing environmental conditions influence the propagation and dissipation of these waves. Likewise, since the near-surface current near the wave trough (Fig. 5b) is comparable to the wave's observed phase speed (c_{obs} = 0.30 m/s), along with the fact that passive particles may encounter several waves in the NLIW train, significant particle transport is expected to occur [cf. *Lamb* 1997]. These waves thus have the potential to transport scalars into the Bay, in addition to reaching the nearshore region where the waves can form nearshore internal bores [e.g., *Walter et al.*, 2012].

5.7: Possible Generation Mechanisms

Woodson et al. [2011] documented the presence of rank-ordered packets of NLIWs near the location of the front across multiple upwelling seasons and hypothesized that variations in the flow field and diurnal wind-modulation of the front may be the generation mechanism. The following observations from *Woodson et al*.

[2011] were drawn from a multiple-year time series from long-term moorings, as well as ten years of synthetic aperture radar (SAR) images: the NLIWs were consistently observed in the late evening (20:00 – 23:00 local time, same as this study), there was an increased prevalence of the waves along the frontal boundary during periods of strong diurnal wind forcing, the waves were oriented in the along-shore direction, and the waves were absent poleward and outside of the upwelling front. The aforementioned observations, in addition to the lack of any significant topographic features near the study site, suggest that internal tide propagation and/or tide-topography interactions are not the generation mechanism.

Expanding on the work of *Woodson et al*. [2011], we propose several mechanisms by which the internal waves may be generated by the front. While the proposed dynamic scenarios cannot be verified exactly with the moored instrument array, they support further examination of the phenomena and offer insight into the potential source of the large amplitude train of NLIWs. We focus specifically on the rank-ordered packet of NLIWs ("NLIWs" period) travelling along-shore equatorward. The NLIWs observed prior to this period (e.g., "Wind Modulation" period) are the subject of ongoing research and will be reported elsewhere. The first mechanism we explore is a transcritical Froude number mechanism.

During the "Wind Modulation" period, the local winds arrest the poleward propagation of the front and reverse the currents to flow equatorward. At this point, a Froude number ($Fr = u_f/c$) can be defined based on the velocity at the nose of the front (u_f) and the intrinsic phase velocity of the first vertical internal mode (c) behind the front and traveling in the same direction as the front (equatorward). The intrinsic

phase velocity includes the effects of the ambient currents in its formulation, and therefore represents the phase velocity relative to the ground and not the water (e.g., TG equation, see *Nash and Moum*, [2005]). It is important to point out that this situation is more complicated than the traditional transcritical generation by flow over topography scenario (see *Stastna* [2011] and the references therein). This is because in the current study, the front reverses its propagation direction. This implies that while the frontal velocity is defined at the nose of the front, the intrinsic phase velocity is defined behind (equatorward) the nose of the front, the medium into which the waves propagate. Thus, small-amplitude perturbations at the nose of the front are unable to radiate behind (equatorward) the front as waves when the currents at the nose of the front exceed the first mode intrinsic internal wave speed behind the front ($Fr > 1$). On the other hand, if the velocity at the nose of the front decreases enough relative to the intrinsic internal wave speed behind the front, a transition to a subcritical ($Fr < 1$) state will occur so that waves are able to overcome the velocities behind the front and radiate behind it into the stratified medium as freely propagating waves. We note that internal waves are dynamically unable to radiate ahead (poleward) of the front since the water column is well-mixed in this region and hence there is no waveguide.

Thus, it is hypothesized that during the "Wind Modulation" period, the front is accelerated equatorward (i.e., poleward deceleration) and able to reach a supercritical state (~19:00). At the end of the "Wind Modulation" period, the local winds are slackening, so that the equatorward advection of the buoyant plume front begins to decrease slightly due to barotropic and baroclinic pressure gradient forces that attempt to drive the front poleward (~20:00) [cf. *Woodson et al*. 2009]. We surmise that as the

front begins to slow down, although still moving in the equatorward direction, it reaches a subcritical state. This would then allow the release of freely propagating waves in the same direction as the current and front. This dynamic situation, as well as the precise time and location of wave fission, cannot be verified using the moored instruments since we are not tracking the front directly. Further observations and in-situ measurements are required to verify the proposed transcritical mechanism. However, it is worth noting that this would not be the first evidence of internal waves propagating behind the nose of a buoyant plume front [cf. *Luketina and Imberger*, 1987, Figure 13; *Nash and Moum*, 2005, Figure 1; *White and Helfrich*, 2008].

An alternative mechanism for the generation of the large amplitude NLIW train is that the front itself has disintegrated into an undular bore, which manifests itself as the initial blunt wave of depression and trailing internal waves. The water column stability is examined on 17 July using the gradient Richardson number. Figure 5.4e highlights that following the potentially unstable event ($Ri < 0.25$) associated with the initial frontal passage, the water column remains stable (i.e., $Ri > 0.25$) until the end of the "Wind Modulation" period. At this time, the along-shore velocities reach their near surface maximum in the negative direction. Shortly following this, a potentially unstable region ($Ri < 0.25$) develops near the surface and penetrates into the pycnocline during the passage of the rank-ordered packet of NLIWs ("NLIWs" period). We note that the gradient Richardson number may not be meaningful in regions of minimal stratification (i.e., near the surface). Thus, it may be that the flow goes unstable to shear instabilities and the front develops into an undular bore and rank-ordered NLIW train.

This dynamic situation whereby the front disintegrates into the train of NLIWs is closely connected with, and in some ways similar to, the proposed Froude number mechanism. Notably, both descriptions offer an explanation for the existence of a rank-ordered packet in that the kinetic energy of the front is converted into potential energy and internal waves (i.e., the undular bore is simply a breaking wave that removes potential energy from the front). As the front weakens and/or disintegrates, the amplitude of the released waves is successively decreased leading to a rank-ordered train. Additionally, both mechanisms require the modulation of the front and flow by strong diurnal winds, in line with previous long-term observations that consistently observed the waves in the late evening following strong diurnal wind forcing [*Woodson et al*., 2011]. Further in-situ observations, and direct tracking of the front, are warranted to better elucidate the generation mechanisms proposed above.

5.8: Summary and Implications

Discussion of the role of NLIWs in the shallow (~20 m), nearshore environment has been mainly speculative, and many questions still remain with respect to the evolution, fate and impact of NLIWs in this biologically productive region. We present high resolution observations of a rank-ordered packet of NLIWs in the nearshore environment of northern Monterey Bay, CA. These waves represent some of the largest nonlinear waves ever observed on the continental shelf, when comparing the wave amplitude (~10 m) to the total water depth (~20 m) (cf. Table 1 of *Alford et al*. [2012]). The NLIWs are observed at a persistent front that forms between the recently upwelled waters from Point Año Nuevo and warmer waters within the

bay. The front propagates up and down the coast in the along-shore direction as a buoyant plume front due to modulation by strong diurnal wind forcing.

The sequence of events leading to the eventual formation of NLIWs near the front is demonstrated in Figure 5.4. During the "Frontal Passage" period, the poleward propagating front stratifies the water column providing a propagation pathway for internal waves back into the bay. After this, local diurnal winds arrest the poleward advection of the front ("Wind Modulation" period) and reverse the currents so that the front moves along-shore equatorward due to the winds. Finally, a rank-ordered packet of large amplitude NLIWs is observed at the mooring array during the "NLIWs" period. We hypothesize that the release of these waves is controlled by a transcritical Froude number criterion and may be linked to the disintegration of the front into the NLIW train; however, further observations and in-situ measurements are required to verify the proposed mechanisms.

The observed waves demonstrate the intriguing possibility that waves that start out as waves of depression morph into waves of elevation. Field observations documenting the reversal of wave polarity are rare [*Shroyer et al.*, 2009], with important implications for the formation of internal bores that can dramatically alter the physics and biology of coastal environments [*Walter et al.*, 2012]. The leading waves in the NLIW train were likely unstable to shear instabilities ($Ri < 0.25$), contained large turbulent overturns (3 m), and exhibited elevated turbulent diffusivities (10^{-2} m^2/s) well above the canonical value for the ocean interior. Consequently, local shear-produced TKE induced by these waves dominates mixing in the stratified interior and affects diapycnal mixing that is critical for many ecologically

important processes. These processes include nutrient cycling, benthic grazing, benthic grazing, and the mixing of tracers such as pollutants from sewage outfalls [e.g., *Wolanski and Pickard*, 1983; *Leichter et al*., 1996; *Boehm et al*., 2002]. Since upwelling fronts are regions of high biological activity due to increased primary production and the aggregation of phytoplankton due to localized convergence [*Graham et al*., 1992; *Ryan et al*., 2008; *Ryan et al*., 2010], the internal wave packets described above can provide a transport mechanism for moving biological material aggregated at the front, such as planktonic larvae, back into the Bay. We validate this claim by deriving a time-scale associated with the decay of the wave due to turbulent dissipation and show that the waves are able to travel an estimated distance of ~20 – 200 km before being completely dissipated. Hence, these waves can affect the recruitment, settlement, and connectivity of larvae [*Woodson et al*., 2011]. Likewise, the strong shear that develops during the passage of the waves near the bottom of the water column may have implications for larval settlement and recruitment [e.g., *Crimaldi et al*., 2002; *Koehl and Hadfield*, 2010].

The shape of the coastline is likely important for both the oceanic and atmospheric dynamics that contribute to the NLIW formation. The upwelling point north of the bay drives a cold water jet across the warm upwelling shadow within the bay, while the coastline within the bay drives the strong diurnal wind forcing due to daily heating and cooling of the adjacent land surfaces. The coastline orientation is a necessary factor for the modulation of the buoyant plume front by diurnal winds and potentially the release of internal waves. This dynamic situation exists all along the California Current Large Marine Ecosystem (CCLME), but is by no means

geographically unique, being present in other eastern boundary currents and "upwelling shadow" systems (e.g., Peru-Chile Current System, Benguela Current System, see *Graham and Largier* [1997]). Thus, the modulation of coastal upwelling fronts by diurnal winds and the subsequent formation of NLIWs at the front may be realized in coastal upwelling systems around the world. These NLIWs are expected to dramatically alter the nearshore, physical environment with important ecological implications.

5.9: Acknowledgements

R. Walter was supported by the National Defense Science and Engineering Graduate (NDSEG) Fellowship through the Department of Defense and the Stanford Graduate Fellowship, C. B. Woodson by the Center for Ocean Solutions, M. Stastna by the Natural Sciences and Engineering Research Council of Canada, and S. Monismith by the National Science Foundation (NSF) Physical Oceanography program through grants OCE-0824972 and OCE-0926340. We acknowledge Bill Smyth for providing code and advice; John Ryan for SST satellite photos; and Ryan Moniz, Derek Fong, Oliver Fringer, and Jeffrey Koseff for helpful discussions. Bathymetry data used in this study were acquired, processed, archived, and distributed by the Seafloor Mapping Lab of California State University Monterey Bay.

5.10: Figures

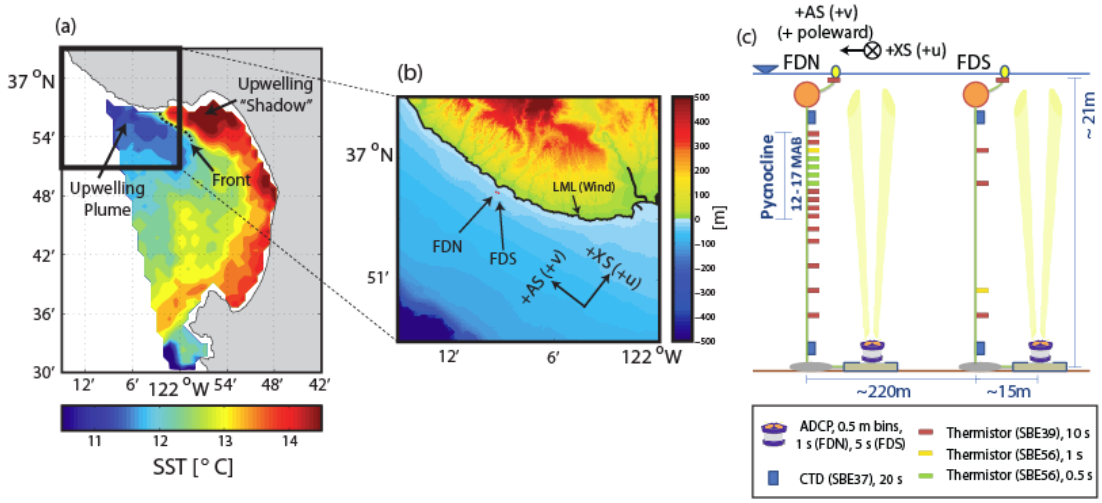

Figure 5.1: (a) AVHHR SST image from 14 July 2011, 04:56:00 GMT highlighting the upwelling plume, upwelling "shadow," front location (dashed line), and nearshore study site (black box). (b) Bathymetry and topography of the study site with mooring locations (red dots). (c) Experimental setup showing mooring and instrument configuration.

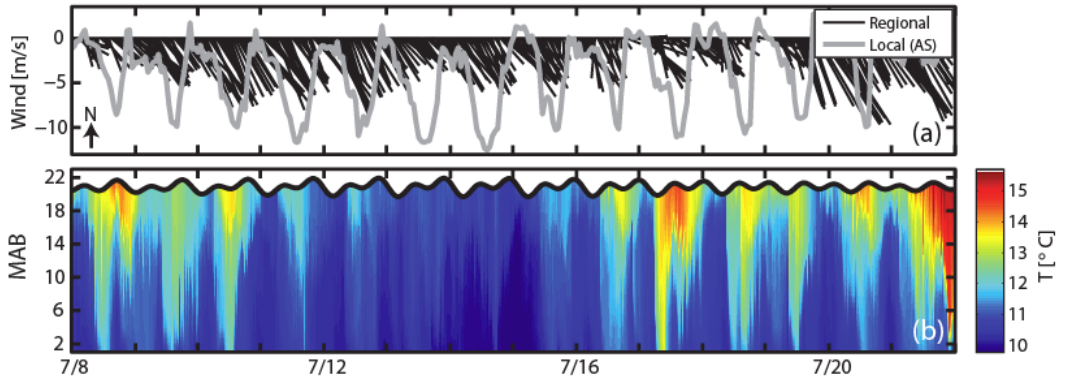

Figure 5.2: Time series during the entire study period of (a) regional (offshore buoy) wind vectors (black, positive to the north) and local along-shore wind speeds (gray, positive poleward), and (b) vertical temperature structure at FDN along with the location of the free surface (black).

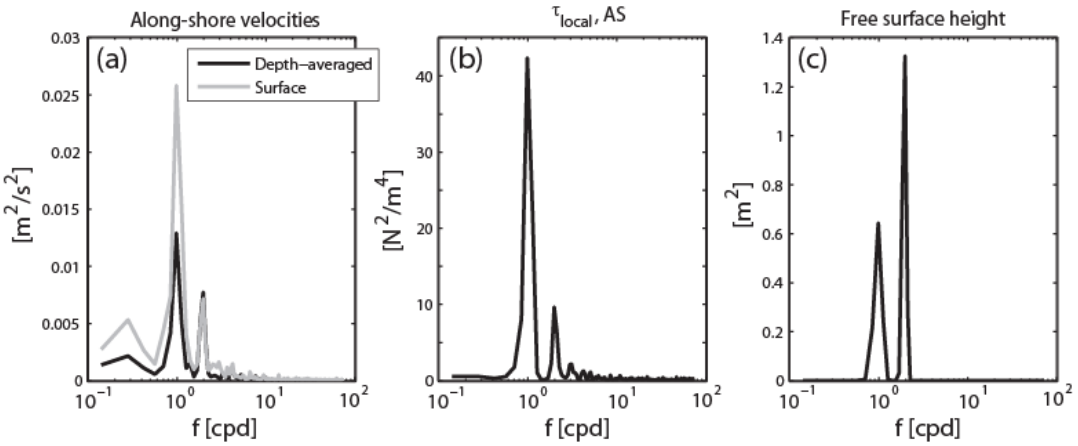

Figure 5.3: Variance-preserving power spectra over the entire record of (a) surface (gray) and depth-averaged (black) along-shore velocities, (b) local along-shore wind stress, and (c) free surface height.

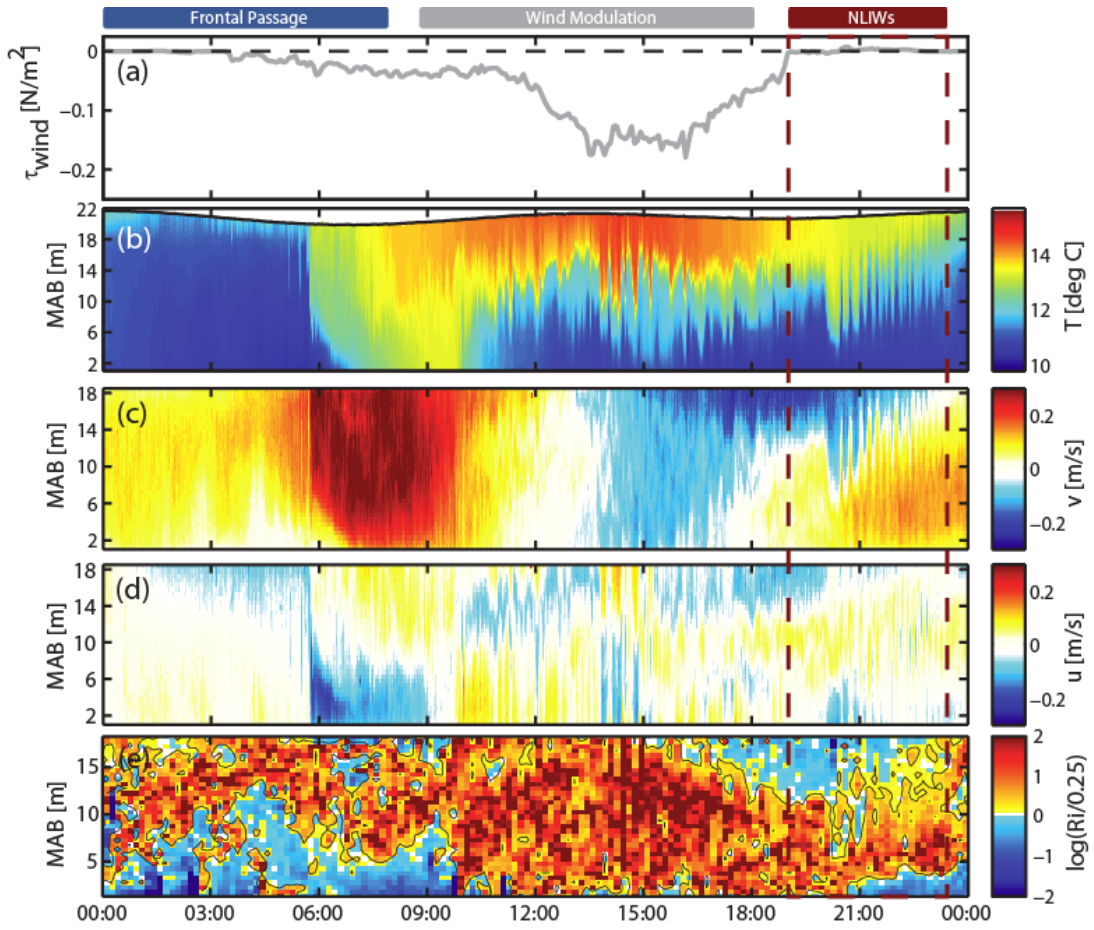

Figure 5.4: Sequence of events leading to the eventual formation of NLIWs near the front on 17 July 2011. (a) Time series of local along-shore wind stress (positive, poleward) from LML. (b) Temperature, (c) along-shore velocity (positive, poleward), and (d) cross-shore velocity (positive, onshore) contour plots from FDN. (e) Space-time variability of water column stability using the normalized, logarithmic gradient Richardson number [$\log(Ri/0.25) < 0$ is equivalent to $Ri < 0.25$]. Ten-minute averages were used for the buoyancy frequency and vertical shear in the calculation of the gradient Richardson number. The black contour denotes regions where $Ri = 0.25$. The free surface height (black) is also shown in panel (b). "NLIWs" period shown in detail in Figure 5.5 and Figure 5.9.

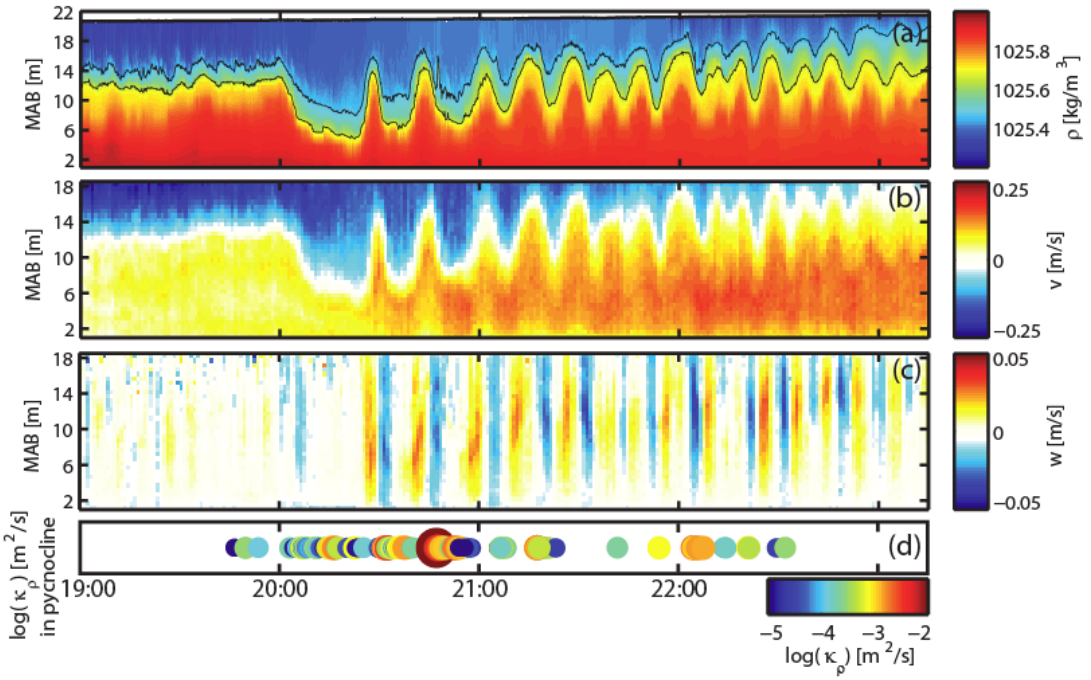

Figure 5.5: "NLIWs" period from Figure 5.4 at FDN. (a) Density contour plot highlighting the NLIW packet. The pycnocline region is highlighted by the 1025.48 kg/m^3 and 1025.68 kg/m^3 isopycnals (black lines). (b) Along-shore velocities (positive, poleward) showing sheared baroclinic flow and (c) vertical velocities. (d) Turbulent diffusivities in the pycnocline calculated from the Thorpe scale analysis are indicated by scaled circles (colorbar).

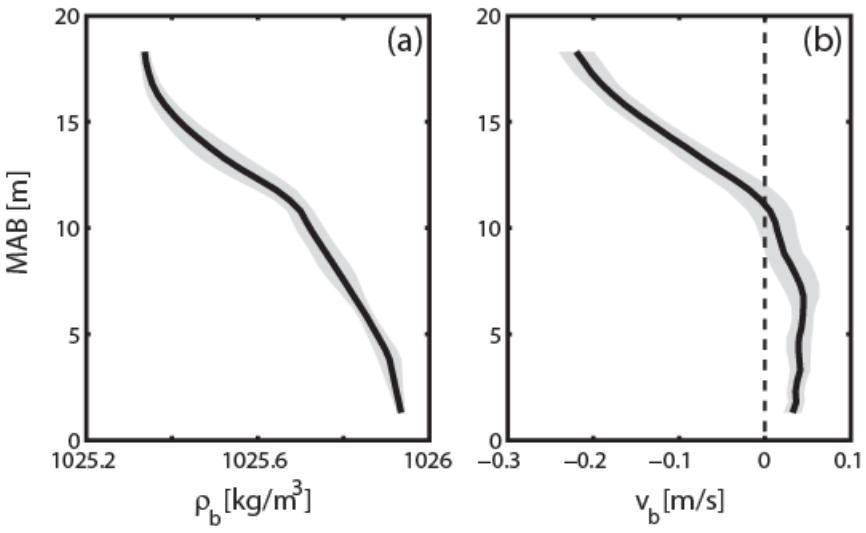

Figure 5.6: Vertical profiles of the mean (solid black) (a) density and (b) horizontal (i.e., along-shore, where positive is poleward) velocity for the period prior to the arrival of the NLIW train (18:25 – 19:15). The standard deviation (grey shading) of the profiles over the same period is also shown, highlighting the quasi-steady state of the background flow.

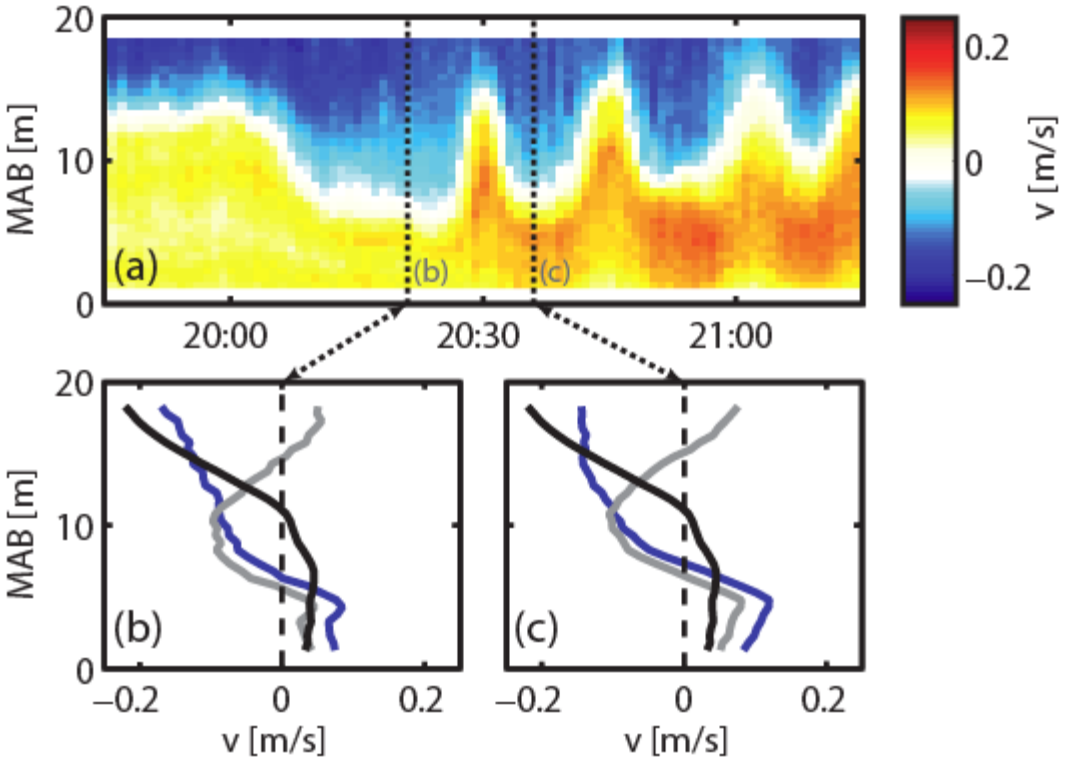

Figure 5.7: (a) Along-shore velocity (positive, poleward) contour plot of the leading waves in the NLIW train. The vertical lines (dotted, black) in panel (a) denote the times when the vertical velocity profiles plotted in panels (b) and (c) were taken (i.e., at the wave trough). The profiles correspond to the background (v_b, black), total at the wave trough (v, blue), and wave-induced ($v_w = v - v_b$, grey) components of the along-shore velocity.

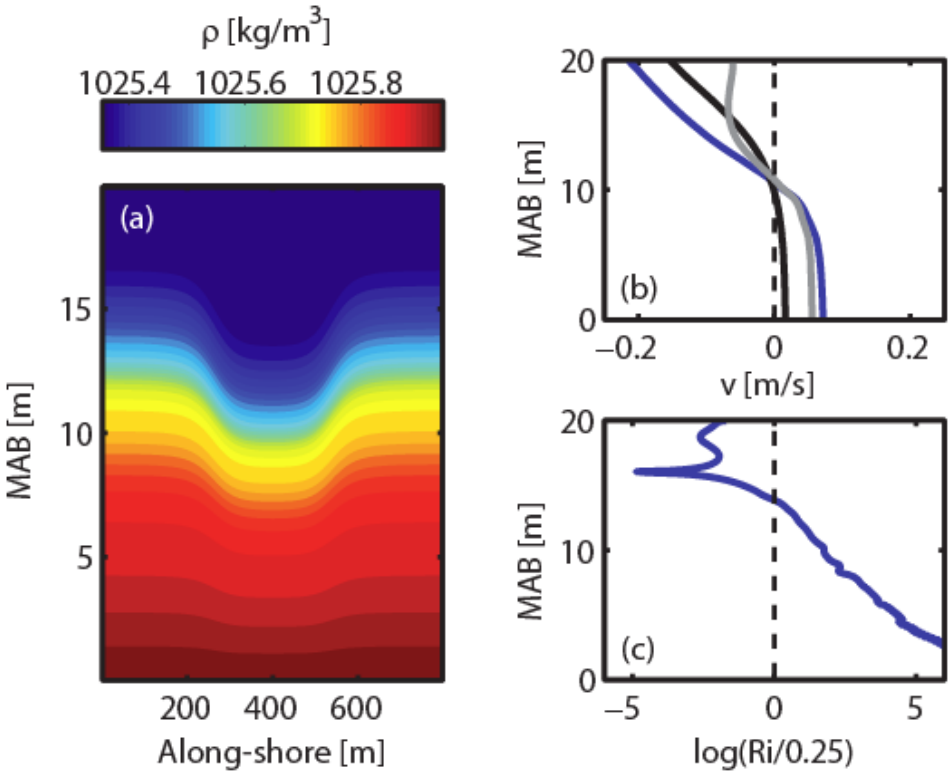

Figure 5.8: Solution to the DJL equation using the background density and largest background current strength with which it was possible to compute waves (see Waves Features section). Panel (a) shows a density contour plot, while panel (b) highlights the background (v_b, black), total at the wave trough (v, blue), and wave-induced ($v_w = v - v_b$, grey) along-shore velocity profiles as a function of depth at the wave trough. (c) Vertical profile of the normalized, logarithmic gradient Richardson number [$\log(Ri/0.25) < 0$ is equivalent to $Ri < 0.25$] at the wave trough (blue). The dashed black line in panel (c) indicates $Ri = 0.25$.

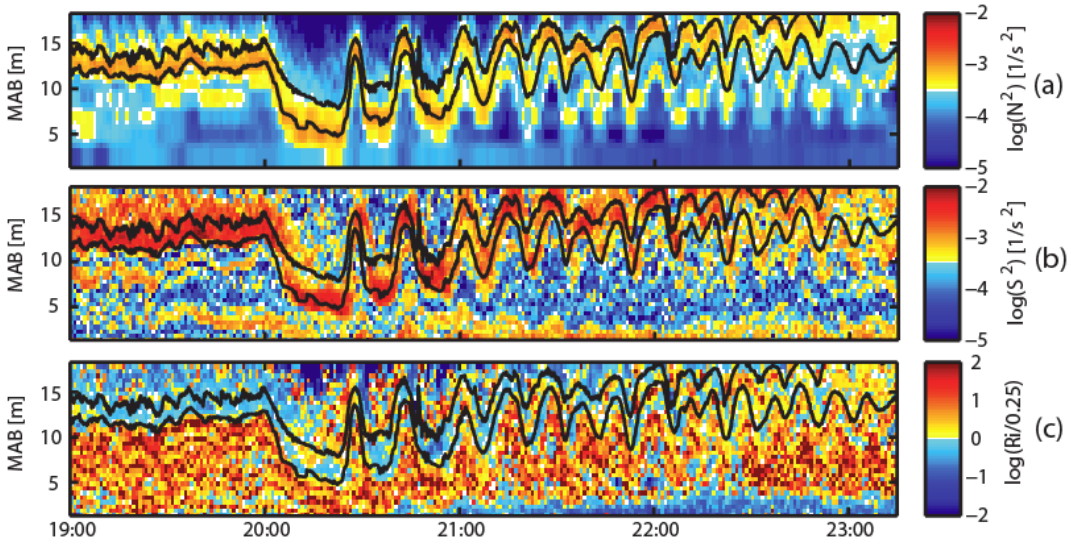

Figure 5.9: Space-time variability of the water column stability for the "NLIWs" period. The pycnocline region is highlighted by the 1025.48 kg/m^3 and 1025.68 kg/m^3 isopycnals (black lines), as in Figure 5.5. One-minute averages of the (a) buoyancy frequency squared (N^2), (b) vertical shear in the horizontal direction (S^2), and (c) the normalized, logarithmic gradient Richardson number [$\log(Ri/0.25) < 0$ is equivalent to $Ri < 0.25$].

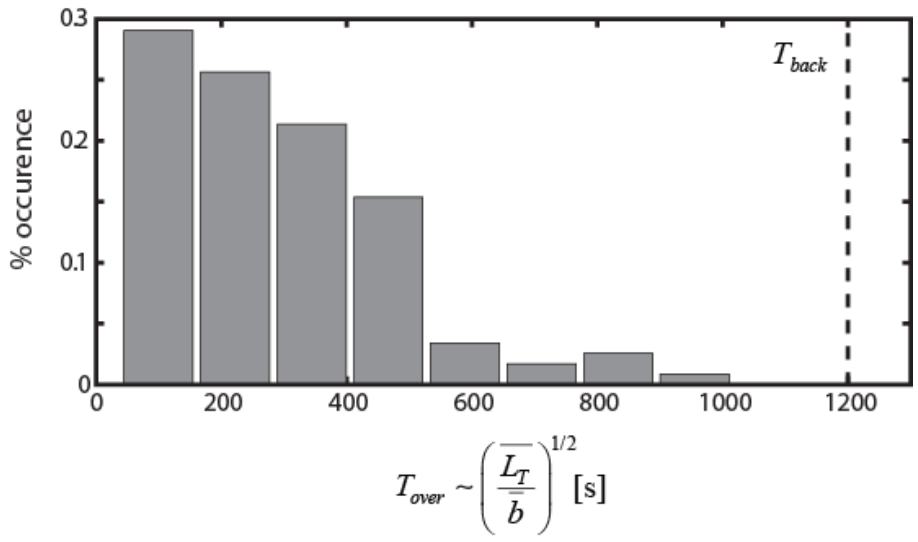

Figure 5.10: Histogram of convective overturning time scales (grey bars) derived from Thorpe scale analysis. The dashed black line represents the time scale for the evolution of the background flow. The time scale for convective overturning to occur is much shorter than the time it takes for the background flow to evolve, thereby justifying the dissipation estimates in Section 5.6.

Chapter 6: Conclusion

6.1: Summary of Findings

The primary objective of this dissertation was to better understand the evolution, fate, and impact of NLIWs and internal bores in the nearshore coastal environment. Observational field studies were conducted in Monterey Bay, CA, and major findings are highlighted below. Detailed summaries can be found in each respective chapter.

High resolution observations of transient stratification and mixing events, associated with nearshore internal bores, were observed in southern Monterey Bay using an array of oceanographic moorings. The transient stratification and mixing events generated by these bores alter the physical environment found in the nearshore and represent the dominant source of variability in this ecologically important region of the inner shelf. The internal bores control temperature and circulation dynamics, local mixing, cross-shelf transport, and dissolved oxygen (DO) variability in the nearshore. Notably, the turbulence in the presence of the nearshore internal bores is substantially different than would be expected from the standard conceptual model of a bottom mixed layer under a stratified interior, as these features lead to elevated levels of turbulence and mixing in the stratified interior.

This work also examined how upwelling wind cycles, offshore stratification, and bottom bathymetry influence the strength and structure of nearshore internal bores. The non-canonical nature of the nearshore bores was examined with a numerical model and explained by the dependence on the internal Iribarren number

(ratio of the local bathymetric slope to the internal wave slope). Furthermore, the observations suggest that suggest low-frequency upwelling wind forcing (i.e., upwelling/relaxation cycles) modulates the offshore (i.e., shelf-scale) stratification, thermocline depth, and internal wave field. This then alters the strength and structure of bores in the nearshore, as well as oxygen variability. A new nearshore bore index is proposed, which could prove useful in predicting and assessing how various physical and biological processes are affected by these features.

Additionally, this dissertation characterizes the fundamental dynamics of stratified turbulence in the nearshore coastal environment using high-frequency turbulence measurements collected with an underwater turbulence flux tower. The evolution of various turbulence quantities and direct measurements of the flux Richardson number (i.e., mixing efficiency) were examined in the near-bed region and the stratified interior. The results confirm that individual bores drive substantial changes to local turbulence and mixing dynamics, with considerable differences between the various phases of the bores. Furthermore, this work demonstrates that the commonly used assumption of a constant mixing efficiency for calculating turbulent diffusivities leads to significant overestimates compared to diffusivities computed using the directly measured mixing efficiency. A parameterization of the flux Richardson number as a function of the turbulence activity number is presented.

Finally, this work describes high resolution measurements of a rank-ordered packet of NLIWs at a persistent upwelling front in the nearshore environment of northern Monterey Bay. These waves represent some of the largest nonlinear internal waves ever observed on the continental shelf, based on a comparison of the wave

amplitude (~10 m for the largest waves) to the total water depth (~20 m). The observed waves are shown to be unstable to shear instabilities, leading to elevated mixing in the stratified interior.

From a broader perspective, understanding the physics that govern temperature dynamics and circulation in the coastal ocean is critical to protecting nearshore ecosystems. Indeed, the physics strongly influence ecologically and economically important fisheries (e.g., lobster, squid, etc.) and habitats (i.e., kelp forests, eelgrass beds, coral reefs). As the results of this work show, NLIWs and internal bores drive substantial fluctuations in temperature and circulation, and they need to be considered when evaluating nearshore physics. This is especially true for higher frequency processes (i.e., tidal and supertidal), as these bores represent the dominant mode of variability in this frequency range.

Internal bores are an important mechanism by which subthermocline waters are transported to the nearshore. While it is well known that upwelling acts to advect subthermocline waters onto the continental shelf, internal bores drive these subthermocline waters into the nearshore at higher frequencies than upwelling/relaxation cycles. This higher frequency variability drives shock-like changes to the coastal ecosystem with important implications for a variety of biogeochemical processes, as well as nearshore productivity. For instance, the nutrient fluxes provided by these features fuel the productivity of the nearshore. On the other hand, these subthermocline waters are low in DO/pH. An increased prevalence of inner shelf hypoxic intrusions has caused massive mortality, and other deleterious impacts, to fish and invertebrates in the California Current Large Marine Ecosystem.

Internal bore driven transport and exchange of subthermocline waters is important for assessing hypoxia risk and ocean acidification processes.

The delivery of pelagic larvae to adult habitats in the nearshore is critical for nearshore community structure and population dynamics. However, scientists are still not able to accurately predict the transport of marine larvae to their adult populations, partially due to the lack of understanding of the underlying physical mechanisms. While previous studies have focused on the cross-shelf exchange of scalars and larvae via wind- and surface wave-driven processes, internal bores are likely an important mechanism by which planktonic larvae are transported in the ocean interior from the inner shelf to the nearshore coastal ocean (e.g., 53% of cross-shelf velocity variance due to the bores in southern Monterey Bay in the late upwelling season of 2012). This work will help inform parameterization efforts of numerical models that attempt to predict larval connectivity, which will ultimately aid in the ability of coastal management agencies to engage in ecosystem based management.

Internal bores can also substantially alter local vertical mixing dynamics in the nearshore. The conventional model is that stratification suppresses vertical mixing, whereas internal bore events produce elevated levels of vertical mixing in the stratified interior. This vertical mixing allows nutrients at depth to mix vertically where they are utilized by phytoplankton in the photic zone. Additionally, the vertical mixing may drive reoxygenation of low DO bottom waters by mixing oxygenated waters down from the surface. Finally, the vertical mixing due to internal bores sets the vertical distribution of density, consequently affecting the local density-driven circulation.

Momentum deposition by the internal waves and bores may also affect local circulation dynamics.

The physics of internal bores are important for the development of a baseline understanding of coastal physics and ecosystem dynamics. It is well documented that human activities are changing the planet, resulting in fluctuations in atmospheric and oceanic processes. For instance, shifting wind patterns from climate variability have led to marked changes in oceanic processes, ranging from general circulation patterns to temperature dynamics to ocean acidification to hypoxia (low oxygen) development. These alterations have important ecological and economic consequences, and a more thorough understanding of how the ocean responds to climate variability is needed so that policy leaders, resource managers, and federal and state agencies are able to plan for and respond to these changes. However, before scientists can begin to model and predict the oceanic response to climatic changes, an understanding of the baseline system is needed. NLIWs and internal bores in the nearshore are a critical component of this baseline system.

As the results of this work show, NLIWs and internal bores need to be considered when evaluating nearshore water column dynamics and local mixing. The results may prove useful in informing future numerical modeling efforts, since internal bores and NLIWs are often not resolved, or accurately parameterized, in regional (e.g., ROMs) or global scale models. Implications for various biological and ecological processes such as larval connectivity, diapycnal mixing, and the cross-shelf transport of low DO/pH subthermocline waters are discussed. It is anticipated that the findings will benefit 1) ecosystem-based management plans for existing marine protected areas

(MPAs) in the Monterey Bay region and the CCLME, 2) planning for new MPAs under California's Marine Life Protection Act and similar initiatives in other systems worldwide, 3) initiatives to address and mitigate the emergence of hypoxia in the CCLME and other systems worldwide, 4) efforts to predict the effects of climate change on the coastal ocean worldwide, and 5) the ability of municipalities and governments to respond effectively to pollutant spills with transport modeling.

6.2: Future Areas of Research

Additional studies on the nearshore NLIW and internal bore climate would be useful in expanding and generalizing some of the results presented in this dissertation. Specifically, the results and conclusions in this work were drawn from observations in Monterey Bay, CA during the summer upwelling season. Longer time records are needed to validate some of the conclusions drawn from the shorter time records and also to understand how seasonal variability influences these features (i.e., upwelling versus non-upwelling conditions, early versus late upwelling season, etc.).

Further observations and comparisons of NLIWs and bores are also needed in other shallow regions to accurately assess their respective influence on the nearshore and to parameterize these features in numerical models. In particular, comparisons of bores and NLIWs at locations with different bathymetric slopes (i.e., internal Iribarren number) and offshore conditions (i.e., strong vs. weak upwelling systems, stratification, coastal trapped waves, etc.) are warranted. While it is well known that internal bores are a common feature on the shelf and in the nearshore, their respective influence on nearshore physics (i.e., temperature dynamics, cross-shelf exchange,

turbulent mixing, circulation, hypoxia development, etc.) in many systems is an active area of research [e.g., *Suanda*, 2014]. This also warrants measuring some of the biologically motivated variables (e.g., nitrogen, DO, pH) with higher spatial resolution.

Future research projects will aim to complement the nearshore observations with more comprehensive offshore measurements. These offshore measurements will be used to further validate existing hypotheses about how offshore characteristics and forcing affect the strength and structure of internal bores in the nearshore. Future work will look at the evolution of the internal bores as they shoal into the nearshore using a cross-shore array of moorings (e.g., MOTOWN, spring 2013 experiment). The influence of rocky reefs and kelp forests on the dynamics will also be explored. This will also complement ongoing work to understand factors influencing subthermocline transport by internal bores. While this dissertation shows that nearshore internal bores contribute to the majority of the variance in the cross-shelf velocity field, further work is needed to quantify subthermocline transport since waters below the thermocline are typically low in DO/pH and high in nutrients. An assessment of how offshore wave characteristics (i.e., polarity, shape, etc.), offshore environmental conditions (e.g., thermocline depth, stratification, ambient currents), and the strength and structure of nearshore internal bores affect subthermocline transport is needed. Additionally, testing whether or not the bore indices/proxies developed in Monterey Bay can effectively capture internal bore variability in other environments and locations is needed, which could ultimately aid in future parameterizations of NLIWs and bores in the nearshore.

Chapter 5 highlights how NLIWs may be modified (e.g., structure, stability, polarity, etc.) by the presence of a strong background shear current. Ongoing numerical work [*Stastna and Walter*, submitted] on the transcritical generation of NLIWs in the presence of a background shear flow suggests that a non-zero background shear can have rich implications for dynamics. Further examination of the effects of a background shear current on NLIWs in the field is warranted and will be explored with the existing data.

Finally, the data collected using the turbulence tower during the MOTOWN experiments represent two of the most comprehensive data sets on stratified turbulence ever collected. There are a number of analyses that can be performed on these data sets both with respect to the internal bores and the fundamental characteristics of stratified turbulence in the nearshore environment. This includes, but it not limited to, comparing the scalar and velocity cospectra to universal curves, looking at various parameterizations for mixing efficiency and the vertical diffusivity, analyzing the efficacy of wave-turbulence (both surface and internal) separation schemes, and parameterizing turbulent mixing by nearhsore internal bores.

Appendix A: Similarity scaling of turbulence spectra and cospectra in a shallow tidal flow

This chapter is a reproduction of the work published in the *Journal of Geophysical Research – Oceans*. As the main author of the work, I made the major contributions to the research and writing. Co-authors include Nicholas J. Nidzieko[1, 2], and Stephen G. Monismith[3].

DOI: 10.1029/2011JC007144

[1]Applied Ocean Physics and Engineering, Woods Hole Oceanographic Institution, Woods Hole, MA, USA

[2]Now at Horn Point Laboratory, University of Maryland Center for Environmental Science, Cambridge, MD, USA

[3]Environmental Fluid Mechanics Laboratory, Stanford University, Stanford, CA, USA

A.1: Abstract

Measured turbulence power spectra, cospectra, and ogive curves from a shallow tidal flow were scaled using Monin-Obukhov similarity theory to test the applicability to a generic tidal flow of universal curves found from a uniform, neutrally-stable atmospheric boundary layer (ABL). While curves from individual ten-minute data bursts deviate significantly from similarity theory, averages over large numbers of sufficiently energetic bursts follow the general shape. However, there are several differences: (1) Variance in the measured curves was shifted towards higher frequencies; (2) At low frequencies, velocity spectra were significantly more energetic than theory while cospectra were weaker; (3) Spectral ratios of momentum flux normalized by turbulent kinetic energy (TKE) indicate decreased fluxes and/or elevated TKE levels. Several features of the turbulence structure may explain these differences. First, turbulent dissipation exceeded production indicating non-equilibrium turbulence, possibly from advection of TKE. Indeed using the production rate rather than dissipation markedly improves agreement in the inertial subrange. Secondly, spectral lag of the largest eddies due to inhomogeneous boundary conditions and decaying turbulence could explain spectral deviations from theory at low frequencies. Finally, since the largest eddies dominate momentum transfer, the consequence of the cospectra difference is that calculated ogive curves produced smaller total momentum fluxes compared to theory, partly due to counter-gradient fluxes. While ABL similarity scaling applied to marine bottom boundary layers (MBBL) will produce curves with the general shape of the universal curves, care

should be taken in determining details of turbulent energy and stress estimates, particularly in shallow and inhomogeneous MBBL.

A.2: Introduction

Turbulence power spectra of the along-channel (*u'*) and vertical (*w'*) velocity fluctuations are often used to describe the range of scales in turbulence, in particular the dominant eddy sizes responsible for turbulent transfer, as well as the distribution of variance with frequency [*Roth et al.*, 1989]. Likewise, turbulence cospectra, or their integral versions, ogive curves, are used to describe the distribution of the covariance *(u'w'*) across the frequency domain, where *u'w'* represents a vertical flux of along-channel momentum due to turbulent fluctuations.

Monin-Obukhov similarity theory postulates that in a uniform, homogeneous atmospheric boundary layer (ABL), turbulence spectra, cospectra, and ogive curves will take universal forms when appropriately non-dimensionalized. In particular, for the neutrally stable case, one in which turbulent production is dominated by mechanical shear with negligible production by buoyancy, only three parameters are needed to collapse the curves to a universal form: the friction velocity (u_*), the average horizontal velocity magnitude (U_{hor}), and the height above the surface (z). Using Monin-Obukhov theory and data acquired in a flat, uniform ABL in Kansas, *Kaimal et al*. [1972] derived a set of non-dimensional curves for the power spectra of along-channel velocity fluctuations ($S_{u'u'}^{*}$), power spectra of the vertical velocity fluctuations ($S_{w'w'}^{*}$), and cospectra of along-channel and vertical velocity fluctuations ($Co_{u'w'}^{*}$). These are:

$$S_{u'u'}^{*}\left(f^{*}\right)=\frac{S_{u'u'}(f)\cdot U_{hor}}{z\cdot u_{*}^{2}}=\frac{105}{(1+33\cdot f^{*})^{5/3}}\ , \qquad \text{(A.1)}$$

$$S_{w'w'}{}^{*}\left(f^{*}\right)=\frac{S_{w'w'}(f)\cdot U_{hor}}{z\cdot u_{*}{}^{2}}=\frac{2}{[1+5.3\cdot(f^{*})^{5/3}]}\ , \tag{A.2}$$

$$Co_{u'w'}{}^{*}\left(f^{*}\right)=\frac{-Co_{u'w'}(f)\cdot U_{hor}}{z\cdot u_{*}{}^{2}}=\frac{14}{(1+9.6\cdot f^{*})^{2.4}}\ , \tag{A.3}$$

where a superscript asterisk represents a non-dimensional quantity, f is the frequency, and $f^{*} = fz/U_{hor}$ is a non-dimensional frequency [*Kaimal et al*., 1972]. The above empirical relationships were derived assuming that equilibrium turbulence exists, whereby production (P) of turbulent kinetic energy (k) is in balance with dissipation (ε) of turbulent kinetic energy.

Given this, measured spectra, cospectra, and ogive curves, when made non-dimensional appropriately, are generally supposed to exhibit the relations found by *Kaimal et al*. [1972], hereafter referred to as the Kaimal curves [e.g., *Kristensen and Fitzjarrald*, 1984; *Roth et al*., 1989; *Al-Jiboori et al*., 2001]. Since then, numerous studies performed in marine bottom boundary layers (MBBL), such as those found in coastal and/or estuarine environments, have used Kaimal curves derived from the ABL for calculating non-dimensional turbulence spectra, cospectra, and ogive curves [e.g., *Soulsby*, 1977; *Feddersen and Williams*, 2007]. Various investigators have used the Kaimal curves in the MBBL for various purposes including filtering waves from turbulence [*Shaw and Trowbridge*, 2001; *Feddersen and Williams*, 2007; *Kirincich et al*., 2010], comparing the general shape and form to the Kaimal curves [*Soulsby*, 1977; *Scully et al*., 2011], analyzing the vertical structure of Reynolds stresses [*Feddersen and Williams*, 2007], determining turbulent scales in the coastal ocean [*Trowbridge and Elgar*, 2003], and modeling vorticity flux spectra [*Lien and Sanford*, 2000]. In all of these cases, however, the Kaimal scaling was assumed to hold. Here, instead we

test the validity of the Kaimal scaling using data acquired in a fairly generic estuarine tidal flow. Turbulence spectra, cospectra, and ogive curves of a well-mixed, tidal flow will be scaled according to Monin-Obukhov similarity theory and compared to the Kaimal curves.

A.3: Site Description and Methods

A.3.1: Experimental Setup

Velocity data were collected over a spring-neap cycle from 12 to 28 October 2004 in the main channel of Elkhorn Slough, California, located in the center of Monterey Bay (Figure A.1). Elkhorn Slough is a shallow, tidally forced estuary that is protected from significant surface wave activity. The site is characterized by a maximum tidal range of ~2.5 m [*Nidzieko et al.*, 2006]. The bed in the main channel is a mix of mud and shell hash, with several intermittent patches of eel grass and deep scour holes. Vertical density data in the main channel of Elkhorn Slough were obtained from the Land/Ocean Biogeochemical Observatory (LOBO), which is part of the Monterey Bay Aquarium Research Institute (MBARI). The observations (not shown) depict approximately well-mixed conditions throughout the study period, except around 21 October where precipitation occurred and caused small density differences between surface waters and deeper waters. However, most events during this precipitation event did not fit the data quality criterion (likely because it was the first precipitation event of the season) and were discarded ($\overline{\Delta\rho} \approx 1.5\text{x}10^{-2}$ kg/m^3 for time periods analyzed excluding bracketed region around events that were discarded because of the precipitation event, where $\overline{\Delta\rho}$ is the average density difference between

measurements made at 2 m depth and the surface). Furthermore, including or excluding this small period of weak stratification did not affect any of the major results and/or conclusions of this paper (see Section A.5.1).

Instantaneous velocity measurements were made in the main channel at a height of 1 m above the bottom using a Nortek 6-MHz Vector acoustic Doppler velocimeter (ADV). Samples were collected in ten-minute bursts, every half hour, at a sampling frequency of 16 Hz, capturing both the spring and neap events over the 16 day sampling period. Co-located with the ADV was a Teledyne-RDI 1.2-MHz Workhorse acoustic Doppler current profiler (ADCP). The ADCP was deployed in Mode 12, sampling 16 subpings at 40 ms intervals for an actual recording rate of 1 Hz [*Nidzieko et al*., 2006]. The ADCP was programmed with 0.25 m bins, with the location of the center of the bin at 1 m coincident with the ADV sample volume. Both the ADV and ADCP were leveled by divers in order to minimize instrument tilt errors. A more detailed description of the experimental setup can be found in *Nidzieko et al*. [2006].

A.3.2: Data Analysis

A.3.2.1: Data Processing

We computed cospectra and spectra for all data bursts including all tidal phases. However, it was clear that near slack water ($|U|< 0.1$ m/s), the computed curves were too noisy to usefully examine turbulence behavior. On the other hand, outside this velocity range, and for all tidal phases, shapes and variations in the shape of spectra and cospectra appeared similar. Hence, we focused on maximum flood and ebb currents in further analysis, since these present the clearest picture of the behavior

of the turbulence field (ADV velocity range in m/s of $0.32 \leq |U| \leq 0.55$ and $0.30 \leq |U| \leq 0.73$ for the max flood and ebb currents, respectively). Velocity measurements for both the ADV and ADCP were converted into along-channel (u), cross-channel (v), and vertical velocities (w), using a principal axes analysis [*Emery and Thompson*, 2004]. The ADV and ADCP had very similar flow orientations so the same angle of rotation was used for both. Positive u velocities were defined as up-estuary, with v and w defined as across-channel and vertical, respectively. Average (U, V, W) and fluctuating (u', v', w') velocities were computed using ten minute windows, an average that represents a trade-off between capturing desired turbulent length scales and maintaining quasi-stationary statistics [*Soulsby*, 1980]. ADV data with correlations less than 0.85 and $|u'| > 0.35$ m s^{-1} were discarded and linearly interpolated back into the data set. Ten minute windows with more than 5% discarded data were not used for further analyses.

A.3.2.2: Spectral Calculations

Power spectra of the along-channel and vertical ADV velocities were calculated using the fluctuating components (u' and w'), while cross-spectra were calculated for the vertical covariance terms ($u'w'$ and $v'w'$), both using the fast Fourier technique over ten minute windows. Each ten minute window (n = 9600) was linearly de-trended and then split into four smaller segments (n = 2400), which were zero padded to achieve the next power of two for the fast Fourier transform and to increase frequency resolution (n = 4096). The choice of segment length represented a compromise between the increased number of degrees of freedom (DOF), decreased frequency resolution, and the ability to delineate the low frequency end of the

spectrum [*Emery and Thompson*, 2004]. A Hamming window with 50% overlap was applied to each segment in order to reduce spectral leakage, spectral densities were calculated using the fast Fourier technique, and segments were block averaged to smooth the spectra and cross-spectra [*Emery and Thomspon*, 2004]. Thus, each ten-minute window had spectral values (n = 2049) up to the Nyquist frequency with a frequency resolution of $\Delta f = 3.9\text{x}10^{-3}$ Hz. The "equivalent" number of DOF ($\nu = 23.6$) was determined by taking into account the type of window, percent overlap, and the size of the segments, and 95% confidence intervals were calculated using a chi-square variable analysis [*Emery and Thompson*, 2004]. The confidence limits for individual spectra indicate that the ratio of true spectrum to the measured spectrum at a particular frequency will be about 0.6 and 1.9 for the lower and upper 95% confidence limits, respectively [*Emery and Thompson*, 2004]. As is commonly done, ogive curves ($Og_{u'w'}$) were calculated by taking the cumulative integral of the cospectra, the real parts of the cross-spectra, and non-dimensionalized as,

$$Og_{u'w'}(f^*) = \frac{-\int_0^f Co_{u'w'}(\tilde{f})d\tilde{f}}{u_*^2}. \qquad \text{(A.4)}$$

After this, the spectra, cospectra, ogive curves, and frequency components were all made non-dimensional according to Equations (A.1) - (A.4). The average horizontal speed was calculated as, $U_{hor} = \sqrt{U^2 + V^2}$ using the ADV data, with V usually one to two orders of magnitude smaller than U, hence contributing negligibly to U_{hor}. The friction velocity squared is defined as $u_*^2 = \frac{\tau}{\rho}$, where τ is the bottom shear stress and ρ is the density. Friction velocities can be estimated by fitting mean velocity

profiles to a logarithmic profile, directly using Reynolds stress measurements near the bed, or with measurements of dissipation of turbulent kinetic energy and the assumption of equilibrium turbulence [e.g., *Sanford and Lien*, 1999]. The dissipation method is not valid in this study since equilibrium turbulence is not present (Section A.5.3). Likewise, previous studies in ocean and estuarine boundary layers have found deviations from a simple logarithmic dependence and the existence of multiple log layers [*Perlin et al*., 2005; *Sanford and Lien*, 1999]. Studies in the ABL commonly estimate bed stress at the particular measurement height assuming a constant stress layer over the ABL [e.g., *McNaughton and Laubach*, 2000; *Smeets et al*., 1998; *Zhang et al*., 2010], an assumption generally not valid over the entire MBBL. *Kaimal et al*. [1972] used a drag plate to estimate friction velocities in the ABL and found that stresses were constant with height to within 20 percent of the surface stress [*Haugen et al*., 1971]. In this study, vertical profiles of Reynolds stresses estimated from the ADCP indicate a small region of nearly constant stress in the bottom 1.5 m. Thus, we will approximate the friction velocity using the average vertical Reynolds stresses near the bed as,

$$u_*^2 = \sqrt{(-\overline{u'w'})^2 + (-\overline{v'w'})^2}\ , \tag{A.5}$$

where an over-bar represents a ten-minute average and the stresses are measured with the ADV at a height of 1 m above the bottom. However, the cross-channel, vertical Reynolds stress ($-\overline{v'w'}$) was consistently one to two orders of magnitude smaller than the along-channel, vertical Reynolds stress ($-\overline{u'w'}$), which makes $(-\overline{v'w'})^2$ negligible in the squared friction velocity calculation. Given this, the squared friction velocity

was estimated by integrating the $Co_{u'w'}$ determined from the ADV data over a ten-minute window:

$$u_*^2 = -\int_0^\infty Co_{u'w'}(f)df \,, \tag{A.6}$$

For spectral calculations of the max ebb events, *u* and *v* velocities were rotated 180 degrees, or multiplied by negative one, so that normalized cospectra and ogive curves would yield positive values.

Finally, the non-dimensional curves were all averaged together in frequency space over all max flood and ebb events, respectively. The same number of spectrally calculated frequency bins (n = 2049) was used in calculating the non-dimensional frequency bins. In order to capture all events in the non-dimensional frequency range, the maximum non-dimensional frequency range of all individual events was selected and split into n = 2049 non-dimensional frequency bins ($\Delta f^* = 1.2\text{x}10^{-2}$). After this, all non-dimensional curves ($\overline{n}$ = 50 for flood and $\overline{n}$ = 42 for ebb) within a particular non-dimensional frequency bin were ensemble averaged together to create the non-dimensional frequency-averaged curves. Frequency-averaged 95% confidence intervals were calculated similarly to individual ten-minute spectra using a chi-square variable analysis, but with an increased number of DOF depending on the number of spectra averaged in a particular non-dimensional frequency bin [*Emery and Thompson*, 2004]. All non-dimensional curves were plotted up to $f^* \approx 14$, where noise begins to dominate the signal, and averaged non-dimensional cospectra were smoothed at high frequencies ($f^* > 6$) using a moving average in f^* over 50 points, which comprises less than 2.5% of the entire record. This plotting range and smoothing does not affect any of the conclusions or analysis of the paper.

A.3.2.3: Turbulent Production and Dissipation

The turbulent kinetic energy (TKE) is defined as [*Pope*, 2000],

$$k = \frac{1}{2}\left[\overline{(u')^2} + \overline{(v')^2} + \overline{(w')^2}\right]. \tag{A.7}$$

In equilibrium, unstratified, homogeneous sheared turbulent flows [*Pope*, 2000], it is generally found that production of TKE by shear is balanced by its dissipation by small-scale strains. Thus, the extent to which this holds is often a measure of the extent to which a given shear flow resembles a canonical homogeneous shear.

The shear production (P) of TKE is given by,

$$P = -\overline{u'w'}\frac{\partial U}{\partial z} - \overline{v'w'}\frac{\partial V}{\partial z}, \tag{A.8}$$

In our case, the Reynolds stresses are measured directly from the ADV and vertical velocity gradients are calculated using the ADCP.

In contrast, dissipation of turbulent kinetic energy (ε) was estimated using spectra of the vertical velocity fluctuations assuming Taylor's frozen field turbulence hypothesis holds and using Kolmogorov's famous -5/3 law [e.g., *Shaw et al*., 2001],

$$S_{w'w'}(f) = \frac{12}{55}\alpha\varepsilon^{2/3}\left(\frac{U}{2\pi}\right)^{2/3} f^{-5/3}, \tag{A.9}$$

where $\alpha = 1.56$ is the empirical Kolmogorov constant for velocity. The spectrum of vertical velocity fluctuations was used since this velocity component is the least noisy [*Voulgaris and Trowbridge*, 1997]. Dissipation was estimated by fitting a power law in the inertial subrange using several hundred points between frequencies 1 and 2.5 Hz, encompassing the range where the inertial subrange exists in our data. Power law fits to the spectra in the inertial subrange had mean exponent values of -1.65 and -1.67

for all flood and ebb events, respectively, and never deviated significantly from -5/3, indicating the existence of an inertial subrange and adequate separation between the production and dissipation length scales [cf. *Gross and Nowell*, 1985]. Equation (A.9) was used to calculate dissipation by choosing values of $S_{w'w'}$ and f in the inertial subrange and subtracting off the ADV noise floor from $S_{w'w'}$.

A.4: Results

A.4.1: Velocity Power Spectra

Individual and ensemble averaged, non-dimensional power spectra of the along-channel velocity fluctuations are seen in Figure A.2 for both the max flood and ebb events. They are plotted against the Kaimal curves and the -5/3 power law in the inertial subrange predicted by turbulent theory [*Pope*, 2000]. While individual ten minute data bursts are scattered and often deviate significantly from similarity theory, the average spectra for both events follow the general trend and slope of the Kaimal curves and -5/3 power law, particularly in the inertial subrange. However, the calculated averages are shifted to the right of the Kaimal curves, indicating more energy at a given frequency compared to the Kaimal spectrum. Additionally, the low frequencies ($f^* < 0.1$) of the calculated spectra are somewhat more energetic than is the Kaimal spectrum. At the highest frequencies, our spectra become more uncertain due to instrument noise and begin to flatten out, possibly due to viscous dissipation.

Non-dimensional power spectra of the vertical velocity fluctuations are also presented and compared to the Kaimal curves and a -5/3 power law in Figure A.3. Similar to $S_{u'u'}{}^*$, the observed spectra ($S_{w'w'}{}^*$) are highly varied across individual bursts

and on average are more energetic at any given frequency than is the Kaimal spectrum. Like the horizontal velocity components, the low frequencies ($f^* < 0.1$) are more energetic than is the Kaimal spectrum. This is especially the case on the max flood events, while on the max ebb events, the lower confidence interval just captures the Kaimal spectrum.

A.4.2: Momentum Flux Cospectra

Calculated non-dimensional cospectra of the along-channel and vertical velocity fluctuations, i.e., the vertical fluxes of horizontal momentum, are plotted against the Kaimal curves for both the max flood and ebb events in Figure A.4. A -7/3 power law is also plotted since the cospectra should follow a -7/3 spectral slope in the inertial subrange [*Wyngaard and Cote*, 1972; *Kaimal et al*., 1972].

The calculated cospectra follow the general shape of the Kaimal curves and -7/3 power law. Yet, as with the spectra, the calculated cospectra have higher covariance values at any given frequency than does the Kaimal curve. However, unlike the spectra, at the low frequency end of the cospectra ($f^* < 0.1$), the observed values fall somewhat below the Kaimal curves.

In order to highlight negative covariance values, and hence counter-gradient momentum fluxes, an alternative non-dimensional form of the cospectra is plotted in Figure A.5. The cospectra are extremely erratic and highly unpredictable across individual ten-minute data bursts. Frequent sign reversals are also seen across all frequencies.

A.4.3: Total Momentum Flux Ogive Curves

Non-dimensional ogive curves, which represent the cumulative flux of horizontal momentum in the vertical direction at a particular frequency, are compared to the Kaimal curves, in Figure A.6. It is important to note that many individual spectra deviate significantly from the Kaimal forms, particularly at low frequencies where large counter-gradient fluxes are common. Indeed at an early point in our study, an examination of data bursts from one tidal cycle showed that only approximately half of the bursts exhibited cospectra and/or ogive curves that in any way resembled the Kaimal curves.

The observed ogive curves are shifted to the right of the universal curves indicating that the largest streamwise scale motions near the bottom in our estuarine channel contribute less to the overall transfer of momentum than was observed by *Kaimal et al*. [1972] in the ABL. Given that these large eddies are thought to be important contributors to the overall momentum fluxes [*Lien and Sanford*, 2000; *Stacey et al*., 1999], this may indicate that the overall momentum transfer from the bed to the overlying flow may be reduced relative to that which would be expected for a canonical channel flow.

A.4.4: Turbulent Kinetic Energy, Production, and Dissipation

In canonical, homogeneous shear flows, the ratio of the principal Reynolds shear stress to the TKE is found to be a constant, i.e., $-\overline{u'w'}/k \approx 0.3$ [*Pope*, 2000]. We can examine the extent to which this behavior appears in our data by examining the spectral variation of this ratio which is plotted for the max flood and ebb periods in Figure A.7 and again compared to the canonical value.

Data from both periods exhibit ratios much smaller than the canonical value of 0.3 across all frequencies, especially at higher frequencies. This indicates that the efficiency of creation of momentum fluxes by turbulence is lower than in a canonical, homogeneous shear flow, an effect seen, for example, in density stratified flows (see e.g., *Holt et al*. [1992]). *Scully et al*. [2011] argue that this behavior may be the result of the advection of turbulent kinetic energy generated elsewhere, i.e., lack of a local equilibrium.

An easy check of local equilibrium is to compare production and dissipation of turbulent kinetic energy to each other (Figure A.8), noting that local buoyancy flux effects have been ignored because of insignificant stratification. In our case, we find that dissipation values are more than triple those of production for both periods, confirming that the turbulence we observed was not in local equilibrium. Note that the larger values of ε on the ebb than on the flood reflect the ebb dominance of Elkhorn Slough [*Nidzieko et al*., 2009].

A.5: Discussion

A.5.1: Low-Frequency Behavior of Spectra

Both velocity power spectra were more energetic at low frequencies than are shown by the Kaimal curves, an effect that was particularly evident in the vertical velocity spectra, especially during periods of max flood tide. This same behavior has been observed in the MBBL [e.g., *Scully et al*., 2011; *Soulsby*, 1977] and in many studies in the ABL over various terrains and containing inhomogeneous boundary conditions [e.g., *Al-Jiboori et al*., 2001; *Andreas*, 1987; *Högström et al*., 1982; *Li et*

al., 2007; *McNaughton and Laubach*, 2000; *Roth et al*., 1989; *Smeets et al*., 1998; *Zhang et al*., 2010]. Taken collectively, these results suggest that something affects the large-scale turbulent structures in many natural flows.

Previous studies attribute stratification and internal waves to differing energetics at low frequencies [*Lien and Sanford*, 2004; *Zhang et al*., 2010]. Yet, in the absence of significant internal waves, stratification would act to suppress turbulence and limit the largest eddy length scales. As mentioned previously, vertical density measurements indicated approximately well-mixed conditions throughout the study period except for a small precipitation event. All calculated curves were reanalyzed, excluding the small time period of weak stratification from the precipitation, and all these curves were nearly indistinguishable from the curves over the entire study period (not shown). Hence, stratification and internal waves were likely not contributing to low frequency deviations.

Another factor affecting the turbulence we observed could have been the rough, inhomogeneous bathymetry of the study site, with nearby irregular eelgrass patches up to two meters depth and deep scour holes (see Figure A.1), typical of the bottom variability found in estuaries. One study of the ABL over rough, urban terrain found deviations from the Kaimal curves at low frequencies similar to those we observe and suggested that internal boundary layers may affect turbulent dynamics [*Högström et al*., 1982]. These internal boundary layers may form in transitions from rough to smooth boundaries, such is the case in this study due to eelgrass patches upstream of the measurement site on both the flood and ebb periods (see Figure A.1). While turbulent transfer may occur between the “inner” and “outer” boundary layers,

it is more likely that internal boundary layers would constrain the largest length scales at low frequencies (much like the free surface constrains the largest length scales). This would then result in less energy at low frequencies, which is not the case in this study.

On the other hand, studies in the ABL over inhomogeneous terrain suggest that spectral lag may cause more energetic values at low frequencies in rough to smooth transitions [*Al-Jiboori*, 2001; *Högström et al*., 1982; *Li et al*., 2007; *Panofsky et al*. 1982], a consequence of the fact that the largest (low frequencies) eddies take longer to adjust than do smaller scales (higher frequencies) in decaying turbulence [see *Batchelor*, 1953]. Hence, irregularities and increased turbulence in the bathymetry upstream of the sample site (e.g., eelgrass patches and channel shoals especially seen upstream of the flood tide, Figure A.1) will locally input relatively large amounts of energy into the flow due to shear production. For example, *Lacy and Wyllie-Echeverria* [2011] found increased turbulence and friction velocities at sites containing eelgrass canopies compared to unvegetated, sandy sites. As the energy input from shear production is reduced near the measurement site and the turbulence decays, the spectra are not in equilibrium. While the small scales at high frequencies adjust rapidly to the new conditions and local momentum flux, the large scales at low frequencies lag significantly (spectral lag) and tend to preserve their shape and energy from upstream conditions. Thus, irregularities of the MBBL could have caused the observed deviations from the Kaimal curves at low frequencies.

Another phenomenon that may be contributing to the low frequency energy of the calculated curves are very long meandering “superstructures” that have been

observed in the ABL [*Hutchins and Marusic*, 2007; *Drobinski et al*., 2004]. While the exact mechanism of formation is still unknown, the "superstructures" often exceed twenty times the boundary layer thickness in length; are typically smaller than the boundary layer thickness in the span-wise direction; meander substantially along their length, possibly explaining the variability of low frequency energy in the along-channel velocity spectra observed in this study; and are hypothesized to affect the low frequency energy of all velocity components ($S_{v',v'}^{*}$ were also more energetic than the Kaimal curves at low frequencies in this study, but are not shown for brevity) [*Hutchins and Marusic*, 2007]. While the measurements in this study lack the temporal and spatial resolution necessary for detection of these "superstructures," they may be an important mechanism affecting the turbulent dynamics at low frequencies.

A.5.2: Cospectra Erratic Behavior and Countergradient Momentum Fluxes

The cospectra curves show the most erratic and unpredictable behavior across individual events, partially due to the fact that there are both positive and negative values. These negative values, which are seen across all frequencies, might represent counter-gradient momentum fluxes. Likewise, the cospectra were less energetic at low frequencies relative to the Kaimal curves. Erratic variability of the cospectra and/or frequent sign reversals has been observed in the MBBL [e.g., *Gross and Nowell*, 1985; *Lien and Sanford*, 2000; *Scully et al*., 2011; *Soulsby*, 1977] and under various conditions in the ABL [e.g., *Andreas*, 1987; *Chimonas*, 1984; *Foken*, 2008; *Gal-Chen et al*., 1992; *Prabha et al*., 2006; *Roth et al*., 1988; *Sakai et al*., 2001; *Smeets et al*., 1988; *Zhang et al*., 2010].

While Figure A.5 depicts that on average the momentum flux is down gradient (positive values across all frequencies for frequency averaged curve), it is important to determine whether the counter-gradient fluxes (negative values) seen in individual cospectra are physical or due to uncertainty. In order to assess the uncertainty associated with the individual cospectra in Figure A.5, non-dimensional standard deviations from the mean curve at a particular frequency were calculated across different frequency ranges. For low frequencies ($f^* < 10^{-1}$), the average standard deviation at a particular frequency for the flood and ebb events was 0.18 and 0.14, respectively. At intermediate frequencies ($10^{-1} < f^* < 10^0$), the average standard deviation from the mean at a particular frequency for flood and ebb events, respectively, was 0.23 and 0.21. Finally, at high frequencies ($f^* > 10^0$), the standard deviations were 0.07 for both events. Given the values above, it is conceivable that some of the counter-gradient fluxes may be due to uncertainties; however, given the large deviation from the mean of many of the individual events seen in Figure A.5 (especially several events in the low frequency range and many of the events at high frequencies), it is likely that many of the negative cospectral values are physical.

Direct numerical simulations (DNS) and large eddy simulations (LES) of stratified turbulence frequently show counter-gradient fluxes when stratification effects are pronounced [*Holt et al.*, 1992]. Similar to the effect of stratification, it seems conceivable that in our case counter-gradient momentum fluxes may reflect the effects of the free surface and limited depth on the largest scales of motion. In the case of the atmospheric flow studied by *Kaimal et al.* [1972], the measurements were made close to the boundary relative to the overall depth of the planetary boundary layer.

Examining $Co_{u',w'}^{*}$ from Figure A.4, the deviation from the Kaimal curves typically occurs around $f^{*} = fz/U_{hor} = 10^{-1}$. Invoking Taylor's frozen turbulence hypothesis ($k_{wave} = \frac{2\pi f}{U_{hor}}$, where k_{wave} is a wavenumber), this corresponds to a streamwise length scale of 10 m. Given that the average depth in the estuary was 6 m during the max flood and ebb periods, the free surface may act to squash the largest eddies thereby causing the deviation of the cospectra at low frequencies. This is supported by field observations where eddies were seen at the surface and by calculations of the average integral length scale, which was found to be around 5.4 m and 5.7 m for the flood and ebb events, respectively. The average integral length scale was found by integrating the autocorrelation function over time for each burst and converting to a length scale by invoking Taylor's frozen field turbulence hypothesis. *Gross and Nowell*, [1985] observed that the largest eddies in well-mixed tidal channel had been flattened out due to the free water surface so that the cospectra may not have been representing the low frequency scales correctly; however, they also found that vertical velocity spectra were reduced at low frequencies, which is not the case in this study. The fact that the observed momentum flux cospectra fall significantly below the Kaimal curves at low frequencies supports the view that the limited depth is acting to alter the turbulence, but this is in contrast to what is observed with the turbulence spectra where it is expected that the limited depth would enhance the along-channel velocity spectra and diminish the vertical velocity spectra with respect to the Kaimal curves. Additionally, spectral ratios of vertical to horizontal velocity variances (not shown) depict a value just over the canonical value of 4/3 expected in the inertial subrange for isotropic

turbulence and fall below this value at lower frequencies similar to *Kaimal et al*.,[1972]. Thus, there is likely another mechanism besides the limited depth contributing to low frequency deviations of the cospectra from the Kaimal curves and counter-gradient fluxes that is still unknown.

Counter-gradient momentum fluxes have been ubiquitously observed in turbulent boundary layers under various conditions. Previous studies in the ABL found frequent sign reversal of the cospectra (counter-gradient momentum fluxes) due to unstable stratification and convective motions [*Andreas et al*., 1987; *Gerz and Shumann*, 1995; *Roth et al*., 1989; *Sakai et al*., 2001; *Zhang et al*., 2010], influences of irregular topography and vortical motions [*Andreas*, 1987; *Foken*, 2008; *Smeets et al*., 1998], and atmospheric waves [*Chimonas* 1984; *Gal-chen et al*., 1992]. Given that the current study took place under well mixed conditions and that there were no significant surface waves present, these mechanisms are unlikely. The long meandering "superstructures" may contribute to the observed stresses [e.g., *Hutchins and Marusic*, 2007]; however, this cannot be confirmed with the measurements taken. Other mechanisms that remain to be identified are partially responsible for the erratic and highly unpredictable nature of the cospectra.

A.5.3: Non-equilibrium Turbulence

Velocity spectra and cospectra curves were consistently shifted towards higher frequencies, indicating that observed spectral values fell above the Kaimal curves at any given frequency. Although never addressed in the respective studies, this same feature has been observed in the ocean and estuarine boundary layers [*Soulsby*, 1977; *Scully et al*., 2011] and over urban terrain in the atmosphere [*Al-Jiboori et al*., 2001].

Observed ratios of momentum flux to turbulent kinetic energy suggest that turbulent kinetic energy was advected into the measurement volume [*Scully et al*., 2011; *Gross and Nowell,* 1983]. The absence of equilibrium was confirmed by our observation that dissipation rates were more than triple production rates. Since the Kaimal curves were derived on the basis of equilibrium ($P = \varepsilon$), it seems likely that the spectral shift we observe is a result of this lack of equilibrium.

As seen in Equation (A.9), spectral energy density is proportional to $\varepsilon^{2/3}$ in the inertial subrange. Thus, advection of turbulent kinetic energy into the region that causes an increase in ε will result in spectral energy densities that are larger than the equilibrium values intrinsic to the Kaimal curves. In light of this, $S_{u'u'}^{*}$, $S_{w'w'}^{*}$, and $Co_{u'w'}^{*}$ were all recalculated and scaled to equilibrium turbulence values by multiplying by $\gamma = (\varepsilon_{equilibrium} / \varepsilon_{non-equilibrium})^{2/3}$ where $\varepsilon_{equilibrium}$ is the equilibrium dissipation value determined from production and $\varepsilon_{non\text{-}equilibrium}$ is the non-equilibrium value of dissipation originally calculated ($\overline{\gamma}$ = 0.36 and 0.43 for max flood and ebb events, respectively). Figure A.9 illustrates the effect of this scaling on the power spectra of the vertical velocity fluctuations.

Both the average max flood and ebb events follow the Kaimal curves much more closely in the inertial subrange. Equation (A.9), which was used to derive the scaling is only valid in the inertial subrange, indicating that the effect of scaling in the low frequency range ($f^{*} < 0.1$) cannot be determined and the discussion above concerning turbulence alteration is unaffected. The scaled along-channel velocity spectra and cospectra yield a similar match in the inertial subrange (not shown). This suggests that the spectral shift in the inertial subrange portion of the curves towards

higher frequencies further supports the hypothesis that the turbulence we observed was not in equilibrium.

A further check on our revised dissipation scaling can be had by considering the law of the wall values of turbulence dissipation $\varepsilon \approx u_*^3 / (\kappa z)$, where $\kappa = 0.41$ is the Von Kármán constant [*Pope*, 2000]. Figure A.10 shows a plot of the dissipation against the law of the wall scaling expected in an equilibrium boundary layer flow, where the dissipation ($\varepsilon = \varepsilon_{equilibrium} + \varepsilon_{excess}$) has been decomposed into two components. The equilibrium dissipation ($\varepsilon_{equilibrium} = P$) is equal to the turbulent production calculated using Equation (A.8), while the excess dissipation ($\varepsilon_{excess} = \varepsilon - P$) represents the remaining dissipation after subtraction of the equilibrium dissipation. While the observed dissipation rates (ε) do not match the law of the wall scaling, the equilibrium dissipation ($\varepsilon_{equilibrium}$) values follow the scaling.

Likewise, the excess dissipation (ε_{excess}) was proportional to $u_*^{2.6}$ (not shown), implying that the local friction velocity is smaller than the friction velocity in the region where the excess dissipation was generated. Differences in the friction velocity can be attributed to irregularities in bathymetry and bottom roughness in the MBBL.

A.5.4: Total Momentum Flux Estimates

The calculated ogive curves were shifted towards higher frequencies than what is seen in the Kaimal curves and often showed large regions of counter-gradient momentum fluxes, particularly at low frequencies. One application of the Kaimal curves is to use them to filter out wave effects on turbulent fluxes or to assess the quality of wave-turbulence separations [*Shaw and Trowbridge*, 2001; *Feddersen and Williams*, 2007; *Davis*, 2008; *Kirincich et al.*, 2010]. Often times screening criteria

based on the wave orbital velocities and wavelengths will result in the elimination of many measurements. For instance, one study in the coastal ocean had to eliminate 40% of the data and stress measurements based on the initial screening criteria of the wave properties [*Kirincich et al.*, 2010]. Given that these methods rely on the comparison of the non-dimensional ogive curves with respect to the Kaimal curves, and that the methods already allow for limited measurements due to the presence of waves, estimates on the uncertainty of the ogive curves and total momentum flux estimates need to be addressed.

In much of our data, deviation of the calculated ogive curves from the Kaimal curve was the result of counter-gradient momentum fluxes, as discussed in Section A.5.2. Table 1 displays the percent occurrence of these fluxes across all events in the low frequency range. In order to quantify the counter-gradient fluxes and estimate deviations of the ogive curves from the Kaimal curves, the non-dimensional frequency range, $df^* = f_2^* - f_1^*$ where f_1^* and f_2^* are the beginning and end frequencies of the counter-gradient fluxes in the low frequency range, was calculated; the results are displayed in Table 1. Also shown is the median of the maximum negative and maximum positive values of the ogive curves that displayed counter-gradient fluxes at low frequencies. Taking the ratio of these two values (last row of Table 1) yields a percentage that represents an approximate assessment of the magnitude of the counter-gradient fluxes.

Both ebbs and floods show similar ranges of counter-gradient fluxes in the low frequencies. While 37.8% (37.6%) of the max ebb (all ebb) events had counter-gradient fluxes in the low frequency range, this resulted in only a 4.0% (5.0 %) change

in the normalized amplitude. On the other hand, 27.4% (28.1%) of the max flood (all flood) events resulted in a normalized amplitude change of 11.3% (8.3%). There was little difference between the max flood/ebb events and all flood/ebb events, indicating that deviations in the ogive curves due to counter-gradient fluxes occur independently of flow strength. Another study [*Feddersen and Williams*, 2007] rejected Reynolds stress estimates based on heuristically selected limits to the ogive curves and found between 23% and 35% of events failed the ogive curve test using one method [*Feddersen and Williams*, 2007] and between 40% and 60% using another method [*Shaw and Trowbridge*, 2001]. While removing some of the uncertainties of the individual curves by averaging over longer time periods and/or shorter windowed segments may improve agreement of individual curves to the Kaimal curves, there are still counter-gradient fluxes due to physical phenomena as well as uncertainties from non-equilibrium turbulence due to inhomogeneous streamwise turbulence. Hence, the frequency of occurrence of these large counter-gradient fluxes and deviations of the ogive curves from the Kaimal curves may need to be taken into account when considering using ogive curves to estimate momentum fluxes and removing wave effects from turbulent flux signals.

A.6: Conclusions

Turbulence power spectra, cospectra, and ogive curves calculated from ADV data taken in a shallow estuarine tidal flow were scaled according to Monin-Obukhov similarity theory to determine whether universal curves derived from a uniform, neutrally-stable ABL are applicable in this case. All of the calculated curves followed

the general shape of the Kaimal curves and turbulent power laws; however, the curves were all shifted towards higher frequencies. Spectral ratios of momentum flux to turbulent kinetic energy suggested that non-equilibrium turbulence was present, likely the effect of advection from upstream. Analysis of the production and dissipation of turbulent kinetic energy confirmed the presence of non-equilibrium turbulence with dissipation always exceeding production. This may have been the result of inhomogeneous bathymetry and bottom roughness. Scaling the spectra and cospectra so that the energy was equal to that expected for equilibrium conditions resulted in the curves matching up much closer to the Kaimal curves in the inertial subrange.

Additionally, the along-channel and vertical velocity spectra were more energetic than the Kaimal curves at low frequencies ($f^* < 0.1$). This was likely due to rougher conditions upstream of the measurement site and the phenomenon of spectral lag in decaying turbulence, whereby the largest eddies (low frequencies) take longer to adjust to changes in bottom conditions. Internal boundary layers and long meandering "superstructures" may have also contributed to the low frequency deviations. Additionally, momentum flux cospectra underestimated stresses at low frequencies ($f^* < 0.1$). Consideration of the turbulence length scales involved suggests that the largest eddy length scales might have been altered by the presence of the water surface, or equivalently the limited depth. This suggests that the results from *Kaimal et al*. [1972] may only be directly applicable when the measurement height is much less than the depth of the flow, or thickness of the boundary layer. Likewise, the underestimation of the cospectra at low frequencies resulted in the ogive curves being shifted towards higher frequencies compared to the Kaimal curves. This produced lower estimates of

total momentum fluxes than with the Kaimal curves. Calculated cospectra were also extremely variable and highly erratic with counter-gradient momentum fluxes seen across all frequencies. These counter-gradient momentum fluxes, especially at low frequencies, resulted in uncertainties in the ogive curves, which has implications for methods that use ogive curves for removal of wave effects from turbulent flux signals.

One consequence of our results is that it shows that there are limits to the applicability of ABL similarity scaling to ocean and estuarine flows. While the general shapes and slopes of the universal curves match our data, spectral energy densities and momentum fluxes were different, possibly reflecting the behavior of non-equilibrium turbulence that might characterize the irregular and inhomogeneous bottom boundary layers likely to be found in the ocean and in estuaries. Finally, use of the Kaimal curves to remove waves from turbulent signals, should be done with care given the significant deviations from those curves that are possible.

A.7: Acknowledgements

The data was collected with support from NSF Grant ECCS-0308070 to SGM as part of the LOBO program (Ken Johnson, P.I.). The analysis presented here was supported by the Department of Defense (DoD) through the National Defense Science & Engineering Graduate Fellowship (NDSEG) Program and through ONR grant N00014-10-1-0236 (Scientific officers: Dr. Thomas Drake, Dr. C. Linwood Vincent, and Dr. Terri Paluszkiewicz). Additional support was provided by the Stanford Graduate Fellowship (SGF). Special thanks to Derek Fong and Jim Hench for the original data collection and experimental design.

A.8: Figures and Tables

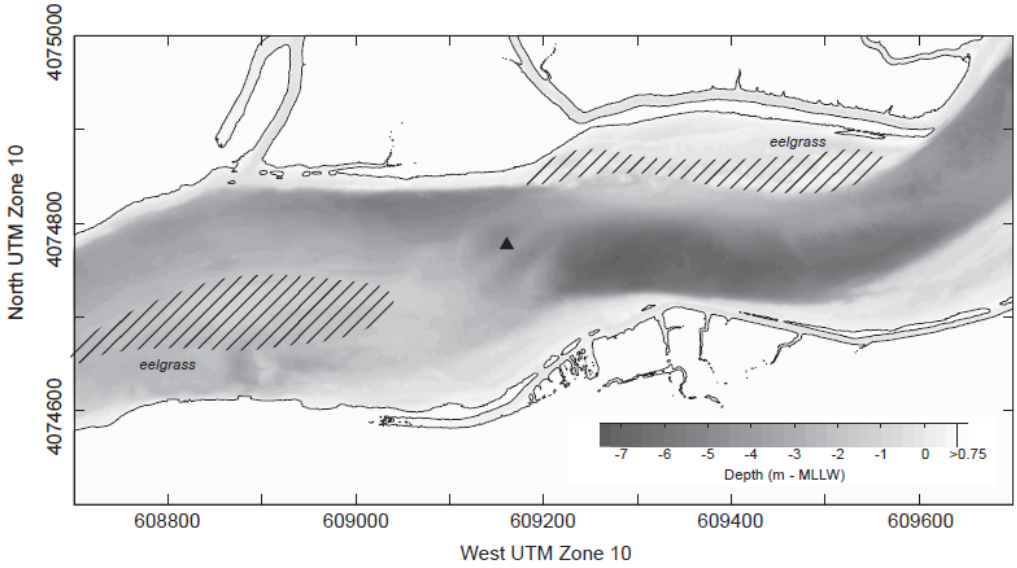

Figure A.1: The experimental site showing the main channel of Elkhorn Slough, CA with the ocean located about 1 km west of the study site. The location of the co-located ADV and ADCP is indicated with a black triangle. Depths are in meters below mean lower low water and white shading depicts land greater than 0.75 m elevation. Black dashed lines indicate the approximate extent of eelgrass coverage obtained from aerial photos. Figure modified from *Nidzieko et al*. [2006], © American Meteorological Society. Reprinted with permission.

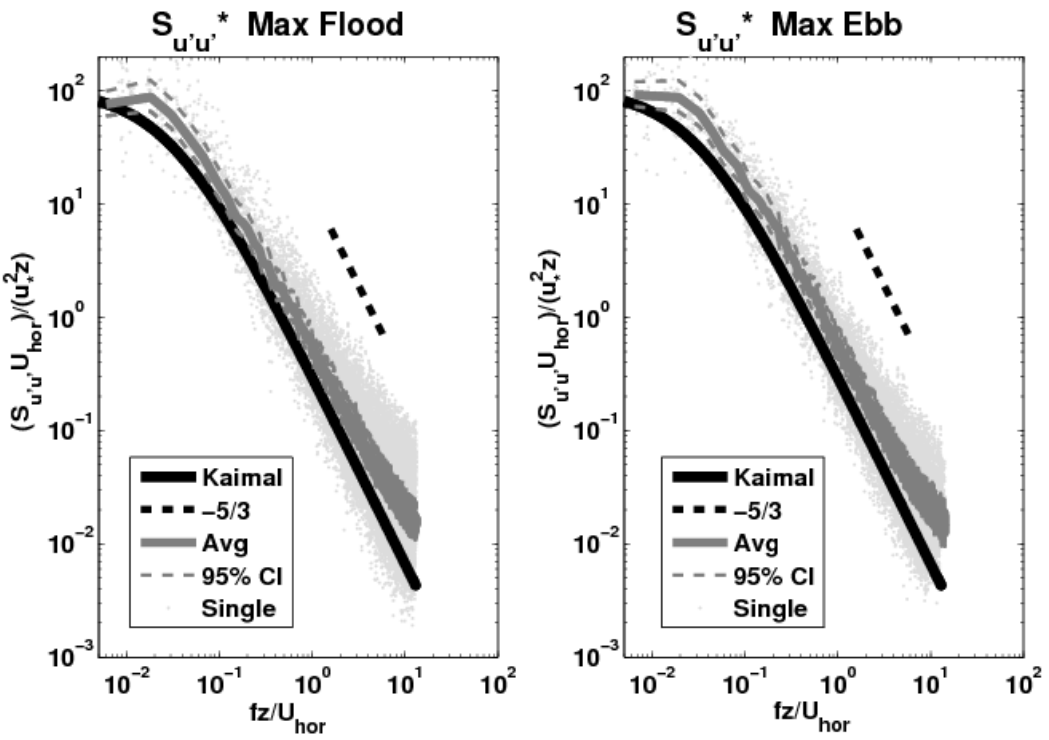

Figure A.2: Non-dimensional power spectra of along-channel velocity fluctuations for the max flood (left) and ebb (right) events. The individual spectra are denoted by light gray dots, the frequency averaged spectrum by a solid dark gray line, 95% confidence intervals for the frequency averaged spectrum by dashed gray lines, the *Kaimal et al*. [1972] universal curve by a solid black line, and the -5/3 power law in the inertial subrange by a dashed black line.

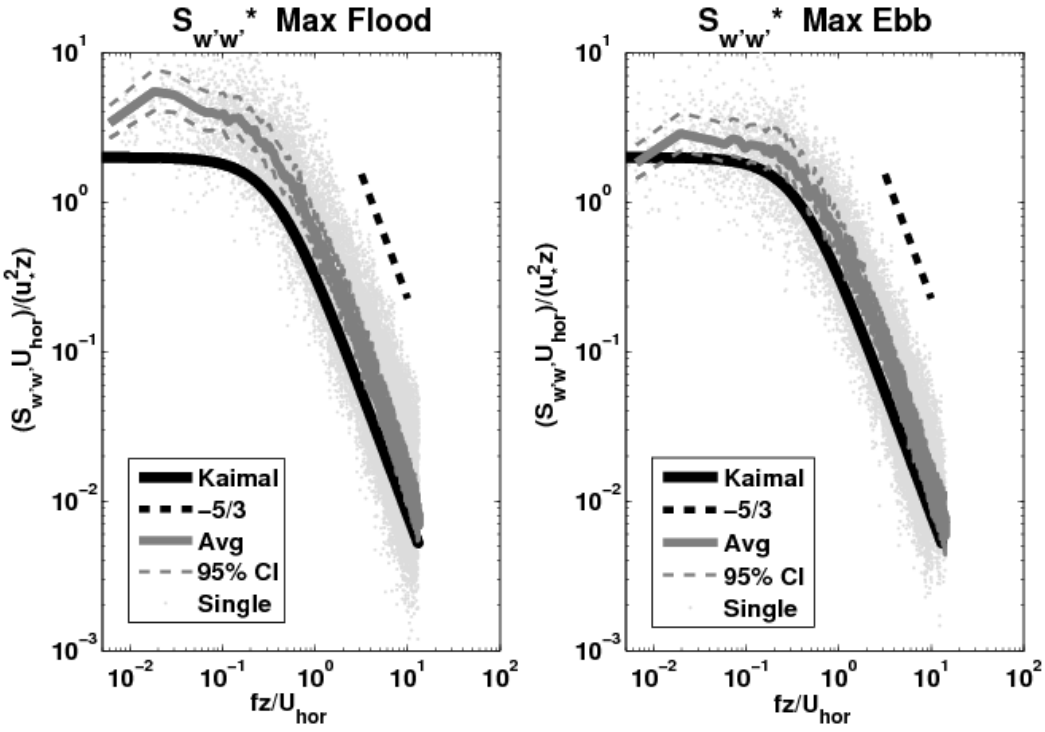

Figure A.3: Non-dimensional power spectra of vertical velocity fluctuations for the max flood (left) and ebb (right) events. The individual spectra are denoted by light gray dots, the frequency averaged spectrum by a solid dark gray line, 95% confidence intervals for the frequency averaged spectrum by dashed gray lines, the *Kaimal et al*. [1972] universal curve by a solid black line, and the -5/3 power law in the inertial subrange by a dashed black line.

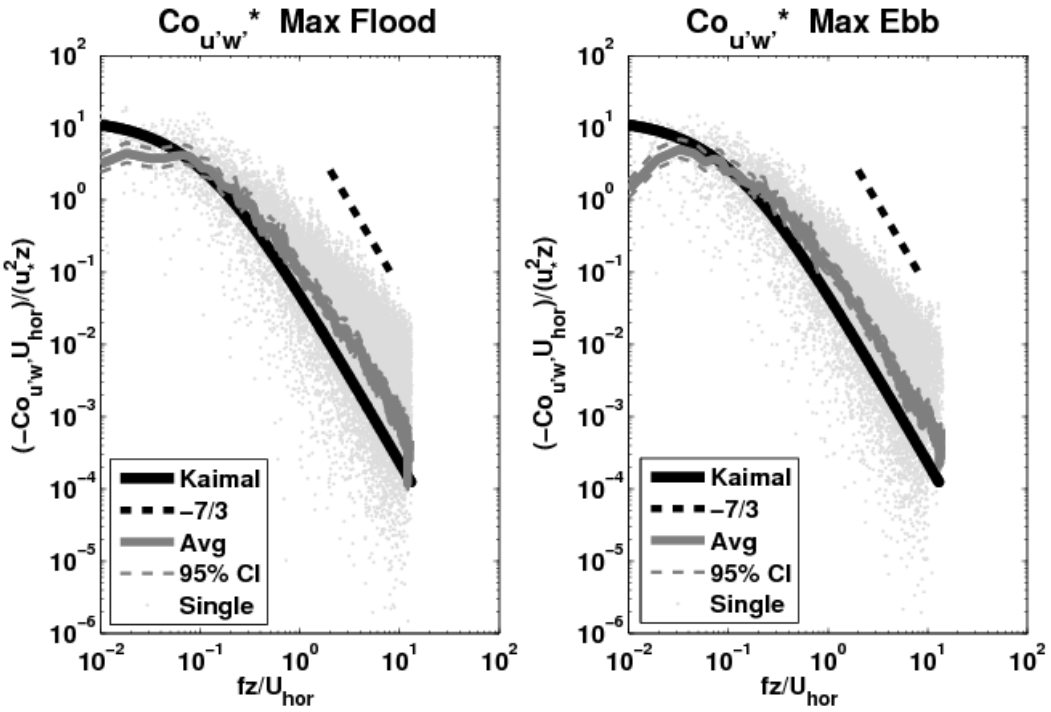

Figure A.4: Non-dimensional cospectra of along-channel and vertical velocity fluctuations for the max flood (left) and ebb (right) events. The individual cospectra are denoted by light gray dots, the frequency averaged cospectrum by a solid dark gray line, 95% confidence intervals for the frequency averaged cospectrum by dashed gray lines, the *Kaimal et al*. [1972] universal curve by a solid black line, and the -7/3 power law in the inertial subrange by a dashed black line.

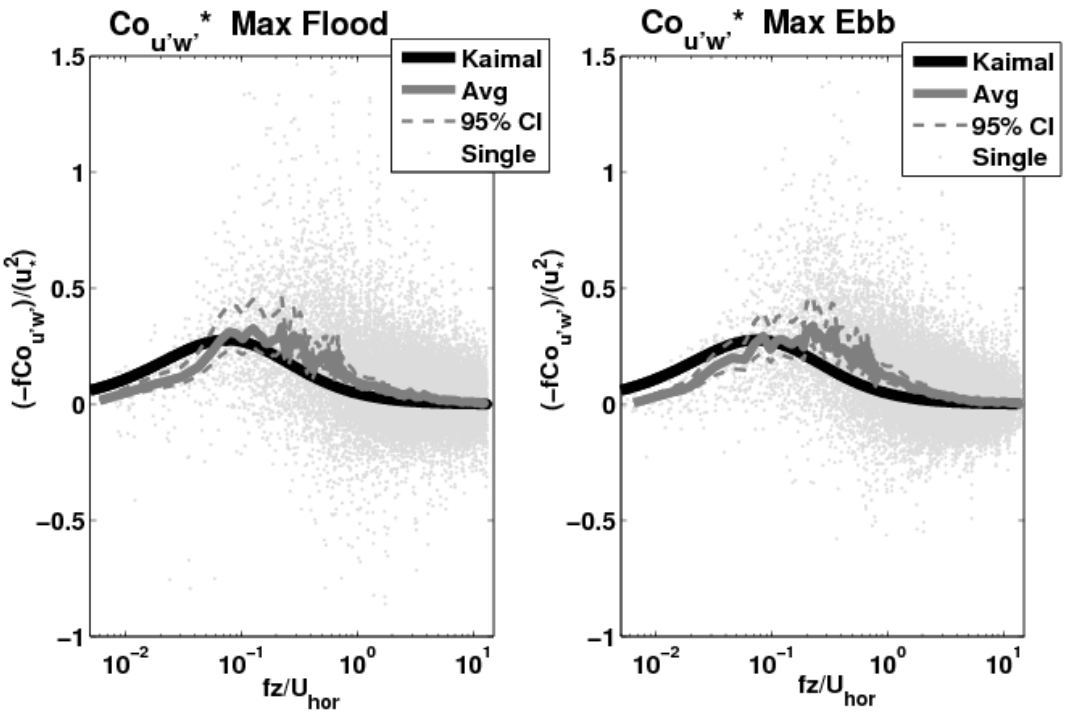

Figure A.5: Non-dimensional cospectra of along-channel and vertical velocity fluctuations for the max flood (left) and ebb (right) events in alternative non-dimensional form and on a semi-log plot. The individual cospectra are denoted by light gray dots, the frequency averaged cospectrum by a solid dark gray line, 95% confidence intervals for the frequency averaged cospectrum by dashed gray lines, and the universal curve by a solid black line.

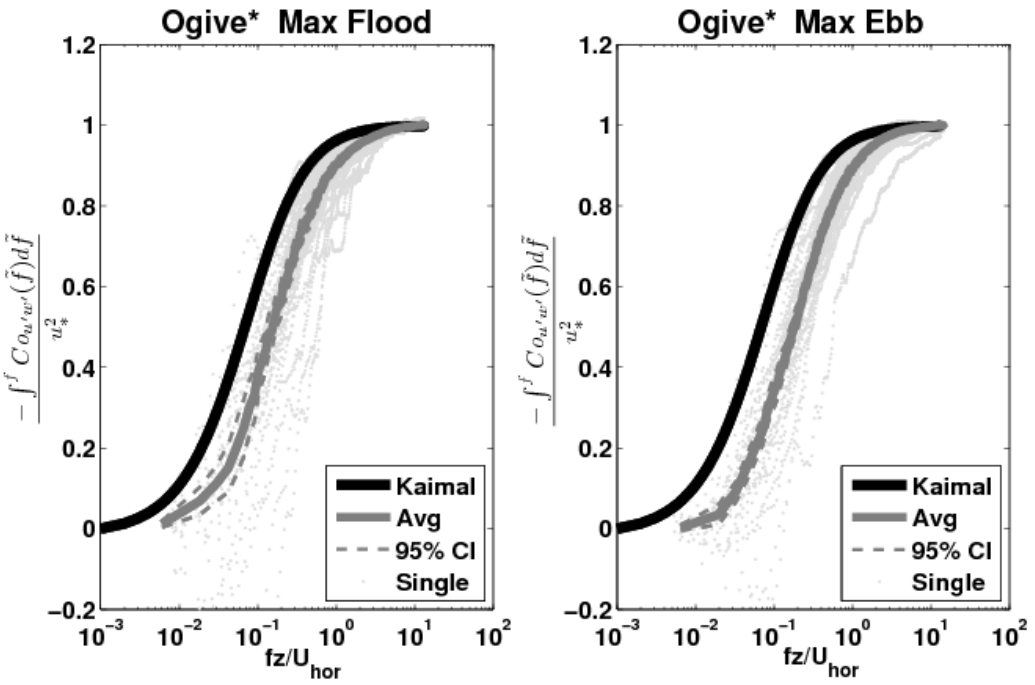

Figure A.6: Non-dimensional ogive curves of along-channel and vertical velocity covariances for the max flood (left) and ebb (right) events. The individual curves are denoted by light gray dots, the frequency averaged curve by a solid dark gray line, 95% confidence intervals for the frequency averaged curve by dashed gray lines, and the *Kaimal et al*. [1972] universal curve by a solid black line.

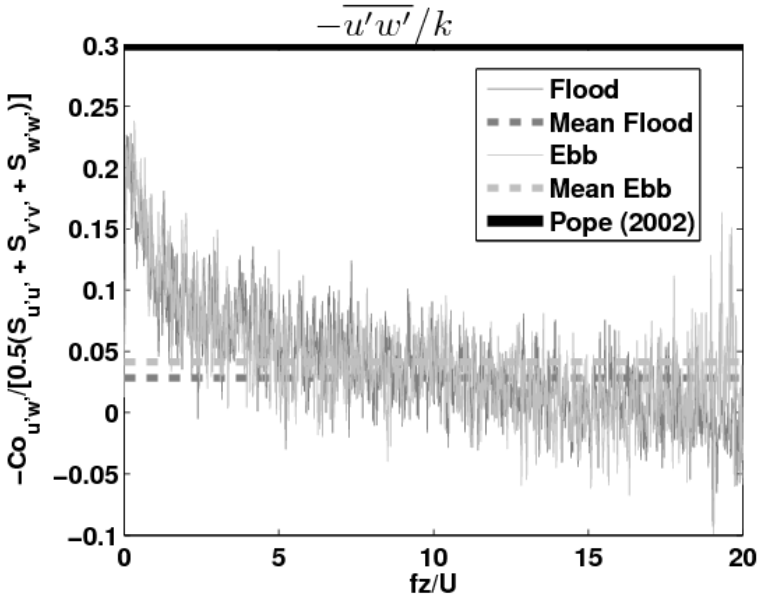

Figure A.7: Spectral representation of the ratio of momentum flux to turbulent kinetic energy for both the max flood and ebb events. The canonical equlibrium turbulence value of 0.3 is indicated with a solid black line [*Pope*, 2000], the average flood event with a dark gray line, the average ebb event with a light gray line, and the mean of the frequency averaged flood/ebb events with dahsed dark/light gray lines.

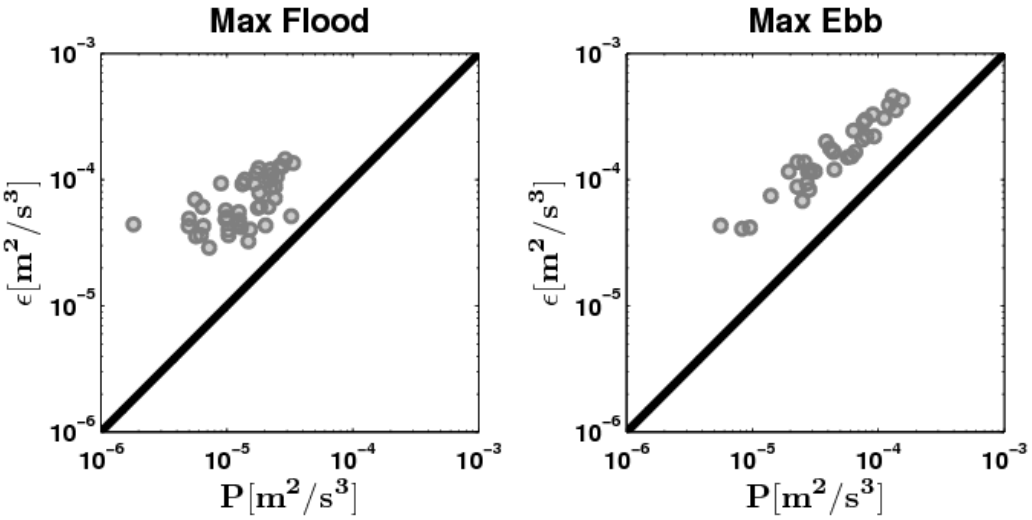

Figure A.8: Production (P) and dissipation (ε) of turbulent kinetic energy for both the max flood (left) and ebb (right) events. Production was calculated using Equation (A.8) and dissipation with Equation (A.9). Individual events are indicated with gray circles, while the solid black line represents equilibrium turbulence ($P = \varepsilon$).

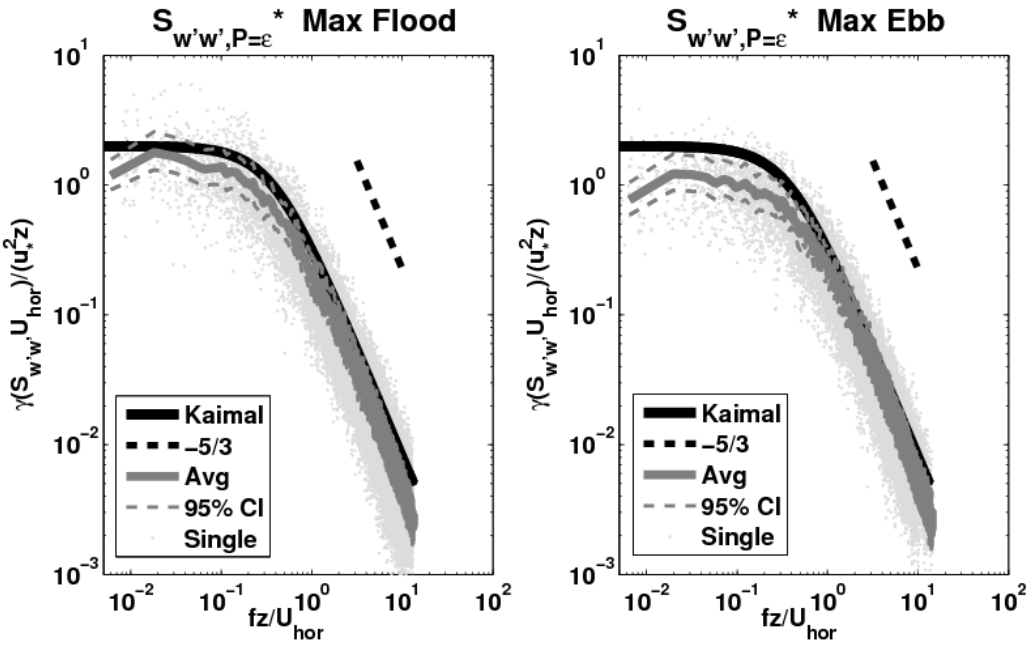

Figure A.9: Non-dimensional power spectra of vertical velocity fluctuations for the max flood (left) and ebb (right) events. Calculated spectra are scaled so that dissipation (ε) equals production (*P*) of turbulent kinetic energy in the inertial subrange. The scaled individual spectra are denoted by light gray dots, the scaled and frequency averaged spectrum by a solid dark gray line, 95% confidence intervals for the scaled and frequency averaged spectrum by dashed gray lines, the *Kaimal et al*. [1972] universal curve by a solid black line, and the -5/3 power law in the inertial subrange by a dashed black line.

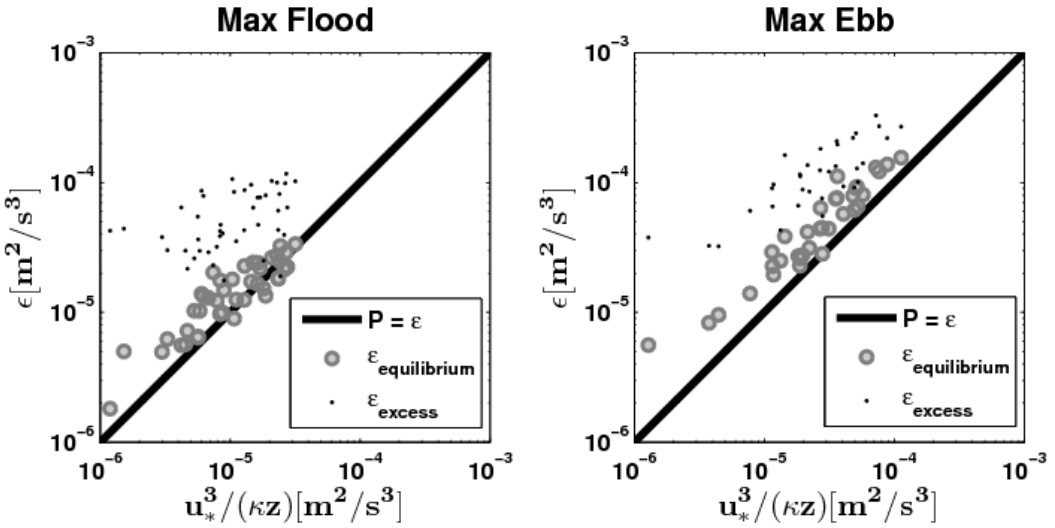

Figure A.10: Dissipation (ε) of turbulent kinetic energy against the scaling of dissipation expected in an equilibrium boundary layer flow, $\varepsilon_{equilibrium} \sim u_*^3/(\kappa z)$. The solid black line represents equilibrium turbulence ($P = \varepsilon$); the gray circles are the production values calculated using Equation (A.8), which represent the equilibrium dissipation values ($\varepsilon_{equilibrium} = P$); and the black dots represent the excess dissipation ($\varepsilon_{excess} = \varepsilon - P$) found by subtracting the production ($\varepsilon_{equilibrium} = P$) from the non-equilibrium value of dissipation (ε) originally calculated using Equation (A.9).

Table A.1: Uncertainty analysis of the non-dimensional ogive curves with respect to counter-gradient fluxes in the low frequency range on the max flood and ebb events, respectively, compared to all flood and ebb events.

Quantity	Max Flood	All Flood	Max Ebb	All Ebb
% Occurrence	27.4%	28.1%	37.8%	37.6%
Mean f_1*	1.1E-02	2.1E-02	8.5E-03	1.8E-02
Mean f_2*	2.9E-02	4.5E-02	2.6E-02	3.9E-02
Mean *df**	1.8E-02	2.4E-02	1.7E-02	2.1E-02
Median Min Ogive*	-0.11	-0.08	-0.04	-0.05
Median Max Ogive*	1.00	1.00	0.99	1.00
Median |Min/Max| %, Ogive *	11.3%	8.3%	4.0%	5.0%

Appendix B: Monterey Tower Node (MOTOWN) Experiment

This section contains additional details about the Monterey Tower Node (MOTOWN) experiments during the fall of 2012 and spring of 2013 at Hopkins Marine Station of Stanford University in southern Monterey Bay, CA. The objective of the MOTOWN studies was to understand how nearshore internal bores affect circulation dynamics and turbulent mixing in the nearshore coastal environment.

B.1: Tables and Figures

Table B.1: Data inventory for the fall 2012 MOTOWN experiment (3 August 2012 to 22 August 2012).

Mooring ID	Location		Water Depth (m)	Instrument Depth (mab)	Sampling Interval (s)	Serial Numbers
	Latitude (°N)	Longitude (°W)				
Thermistors (SBE39 and SBE56*)						
MN (Main/Tower)	36.6212	121.9005	15	0-9 in 0.5 m intervals*, 10*, 11*, 12*, surf	0.5*, 12	533-539, 540, 542, 544, 545, 547, 549, 550-554, 612, 614-616, 5028
OS (Offshore)	36.6221	121.8988	23	2, 4, 6, 8, 10, 12, 14, 16, 18, surf (39s)	12	1992, 524, 3442, 5174, 579, 572, 1376, 1440, 1439, 1882
NS (Nearshore)	36.6208	121.9013	10	1, 2, 3, 4, 5, 6, surf (39s)	12	5173, 5030, 577, 3735, 525, 3445, 3352
ASB (Alongshore Bayside)	36.6207	121.8999	15	1, 2, 4, 6, 8, 10, surf (39s)	12	5176, 5026, 575, 5172, 526, 3441, 5029
ASO (Alongshore Oceanside)	36.622	121.9009	15	1, 2, 4, 6, 8, 10, surf (39s)	12	5175, 4712, 847, 3388, 574, 3444, 3349
CTDs (SBE37 and 16+*)						
MN (Main/Tower)	36.6212	121.9005	15	0, 2, 4, 6, 8	24, 6, 6, 6, 24	7686, 9232, 9233, 9234, 7685
OS (Offshore)	36.6221	121.8988	23	0* (16+ w/ DO), 20	24, 24	4782, 4733
NS (Nearshore)	36.6208	121.9013	10	0, 7	24, 24	6345, 4688
ASB (Alongshore Bayside)	36.6207	121.8999	15	0, 12	24, 24	6346, 5563
ASO (Alongshore Oceanside)	36.622	121.9009	15	0, 12	24, 24	5562, 4734
ADCPs (RDI)						
MN (Main/Tower)	36.6212	121.9005	15	0, 0.5 m bins, 1200 kHz	1 s (Mode 12)	6462
OS (Offshore)	36.6221	121.8988	25	0, 1 m bins, 600 kHz	1 s	473
NS (Nearshore)	36.6208	121.9013	10	0, 0.5 m bins, 1200 kHz	1 s (Mode 12)	5959
ASB (Alongshore Bayside)	36.6207	121.8999	15	0, 0.5 m bins, 1200 kHz	1 s (Mode 12)	6023
ASO (Alongshore Oceanside)	36.622	121.9009	15	0, 0.5 m bins, 1200 kHz	1 s (Mode 12)	6024
ADVs (Nortek Vector)						
MN (Main/Tower)	36.6212	121.9005	15	0.3, 1, 2, 4, 6, 8	1/64	4371, 4390, 4611, 4620, 4629, 4587
Fast CTs (PME Inc.)						
MN (Main/Tower)	36.6212	121.9005	15	0.3, 1, 2, 4, 6, 8	1/64	18, 6, 7, 17, 35, 16

Table B.2: Data inventory for the spring 2013 MOTOWN experiment (19 April 2013 to 21 May 2013).

Mooring ID	Latitude (°N)	Longitude (°W)	Depth (m)	Instrument Depth (mab)	Sampling Interval (s)	Serial Numbers
Thermistors (SBE39 and SBE56*)						
MN (Main/Tower)	36.6212	121.9004	15	0-12 in 0.5 m intervals, surf (all*)	1*	533-540, 542, 544, 545, 1887, 547, 550-553, 1886, 1862-1864, 1866-1869, 1872
OS (Offshore)	36.6222	121.8989	23	1, 3, 5, 7, 9, 11, 13, 15, 17, 19, 21, surf (all*)	1*	2257-2258, 2260-2268, 2270
DOS (Deep OS)	36.6232	121.8949	40	1, 4, 7, 10, 13, 16, 19, 22, 25, 28, 31, 34, 37, surf (all*)	1*	1885-1873, 543, 1882
NS (Nearshore)	36.6206	121.9008	12	1*, 2.5*, 4*, 5.5*, 7*, 8.5*, surf*	1*	2275-2281
SNS (Shallow NS)	36.6202	121.9018	8	1*, 2.5*, 4*, surf*	1*	2271-2274
ASB (Along-shore Bayside)	36.6207	121.8995	15	1*, 2, 3, 4, 5, 6, 7*, 9, 11, 13, surf	20 (1*)	613, 1882, 1992, 5026, 5028, 5029, 33, 5030, 5172-5174
ASO (Along-shore Oceanside)	36.622	121.9009	15	1*, 2, 3, 4, 5, 6, 7*, 9, 11, 13, surf	20 (1*)	546, 3349, 3352, 3388, 3441-3442, 25, 3444-3445, 3735, 4712
KNS (Kelp NS)	36.6216	121.90176	10	0, 1*, 2, 3, 4, 5*, 6, 7, 8, surf, bottom_10m, bottom_20m	20 (1*)	1441, 1870, 579, 577, 575, 2283, 574, 572, 526, 573, 1376, 5175
KSNS (Kelp SNS)	36.6213	121.90195	9	1*, 2, 3, 4*, surf	20 (1*)	1871, 847, 1439, 2282, 1440
CTDs (SBE37)						
MN	36.6212	121.9004	15	0, 2, 4, 6, 8	60, 10, 10, 10, 60	4734, 9232-9234, 7685
OS	36.6222	121.8989	23	0* (16+ w/ DO), 20	60, 60	4733, 4688
DOS	36.6232	121.8949	40	3, 37	60, 60	4733, 7686
NS	36.6206	121.9008	12	0	60	5562
SNS	36.6202	121.9018	8	0	60	6345
ASB	36.6207	121.8995	15	0	60	5563
ASO	36.622	121.9009	15	0	60	6346
ADCP (RDI)						
MN (Main/KFA)	36.6212	121.9004	15	0, 0.5 m bins, 1200 kHz	1 (Mode 1)	KFA ADCP
MN (Main/Tower)	36.6212	121.9004	15	8 (top of tower), 0.25 m bins, 1200 kHz	1 (Mode 12, 4 subpings, 5 m waves)	6462
OS	36.6222	121.8989	23	0, 1 m bins, 600 kHz	2 (Mode 1, 2 pings)	473
DOS	36.6232	121.8949	40	0, 2 m bins, 300 kHz	2 (Mode 1, 1 ping)	1601 (Berkeley ADCP)
NS	36.6206	121.9008	12	0, 0.5 m bins, 1200 kHz	2 (Mode 12, 5 subpings)	5959
SNS	36.6202	121.9018	8	0, 0.5 m bins, 1200 kHz	2 (Mode 12, 5 subpings)	4867
ASB	36.6207	121.8995	15	0, 0.5 m bins, 1200 kHz	2 (Mode 12, 5 subpings)	6023
ASO	36.622	121.9009	15	0, 0.5 m bins, 1200 kHz	2 (Mode 12, 5 subpings)	6024
ADVs (Nortek Vector)						
MN (Tower)	36.6212	121.9004	15	0.3, 1, 2, 4, 6, 8	1/64	4919, 4390, 4611, 4620, 4629, 4587
Fast CTs (PME Inc.)						
MN (Tower)	36.6212	121.9004	15	0.3, 1, 2, 4, 6, 8	1/64	18, 6, 7, 17, 35, 16

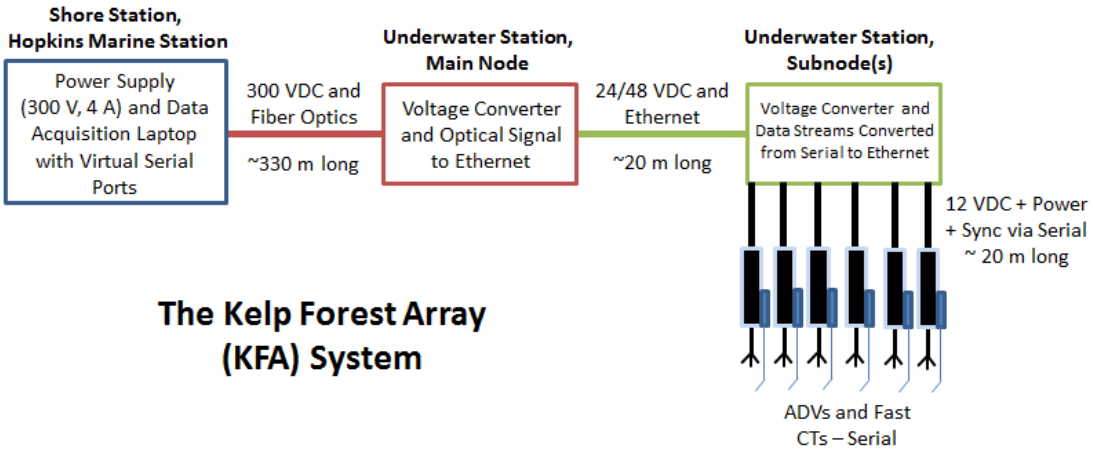

Figure B.1: Schematic of the Kelp Forest Array (KFA) cabled observatory system at Hopkins Marine Station in southern Monterey Bay, CA. The KFA system was used to power and interface with oceanographic instruments (ADVs, fast CTs) on the tower during the fall 2012 and spring 2013 MOTOWN experiments.

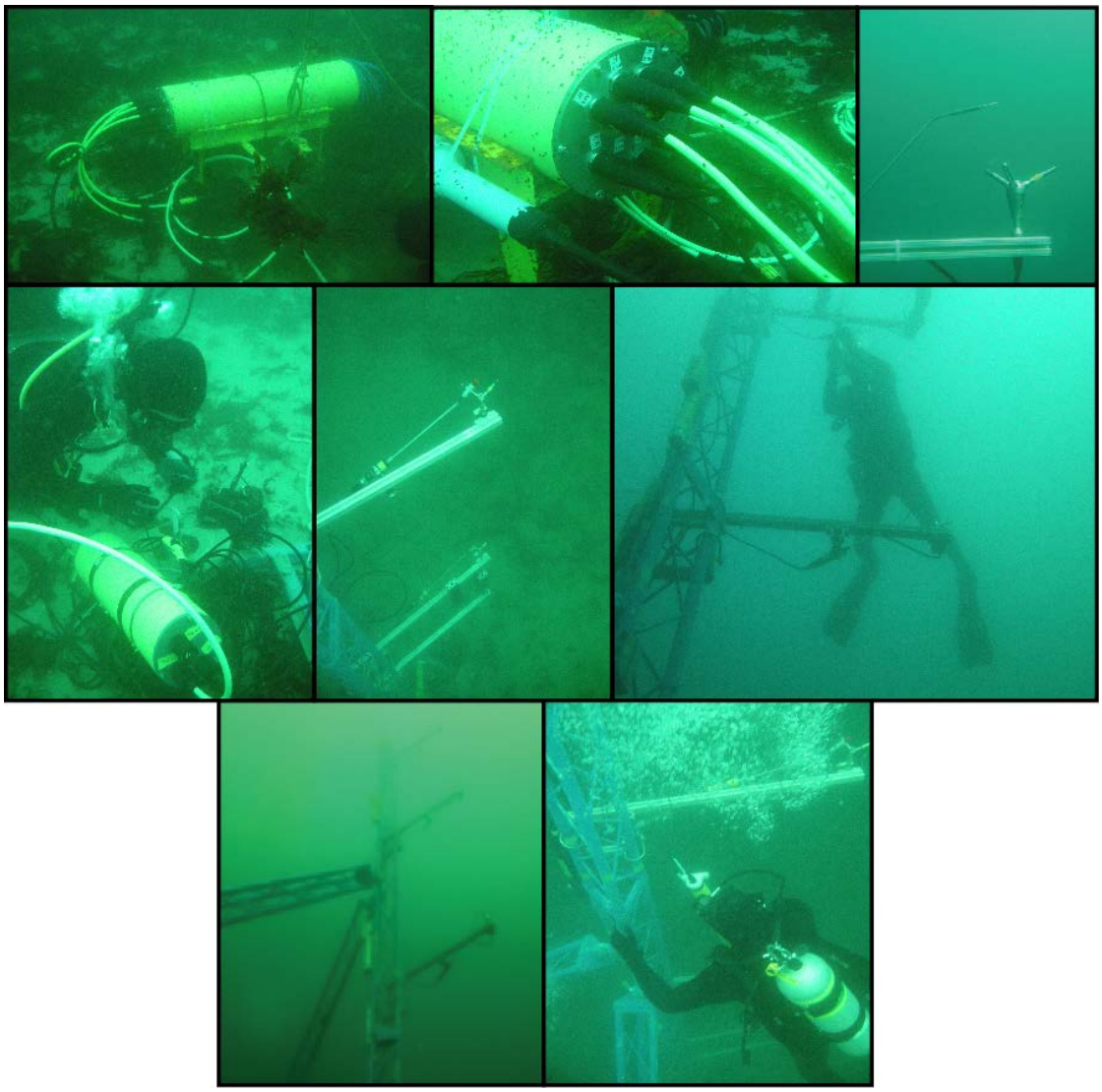

Figure B.2: Field photographs of the fall 2012 and spring 2013 MOTOWN experiments highlighting the turbulence tower and the Kelp Forest Array (KFA) system.

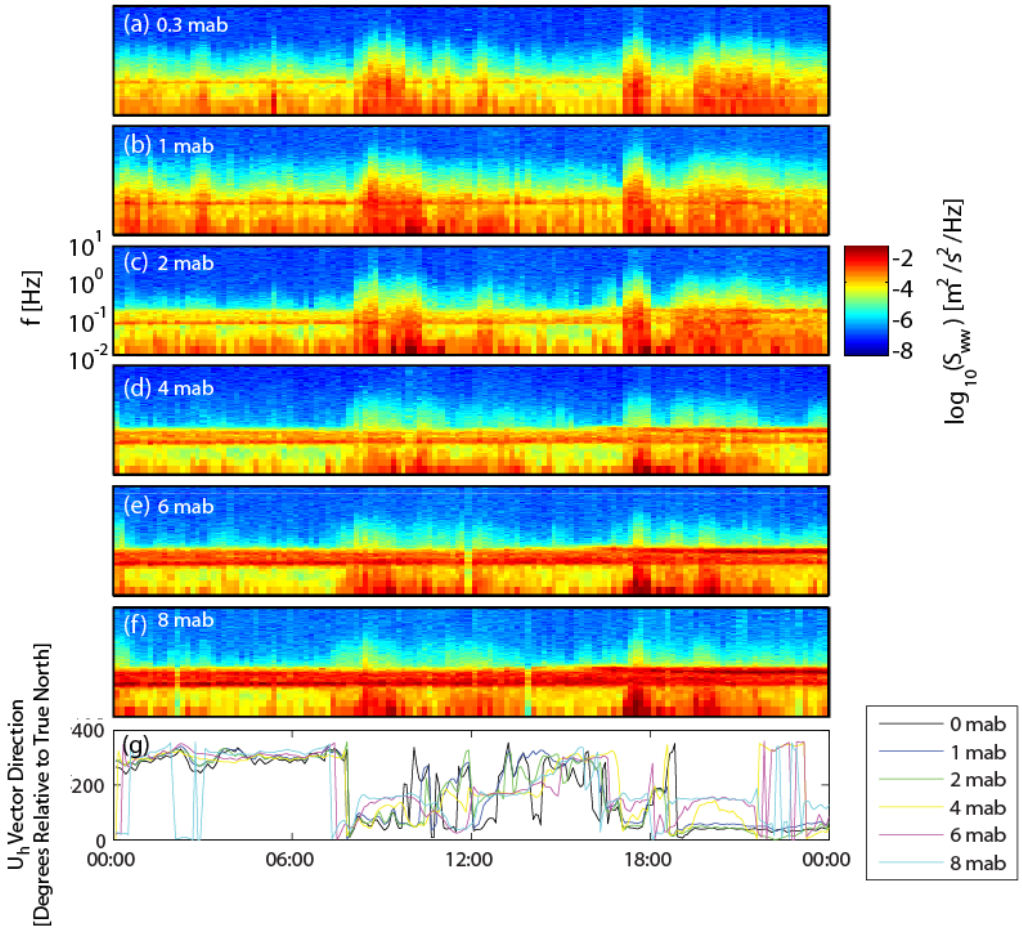

Figure B.3: Vertical velocity spectrograms over a one day period (16 August) during the MOTOWN 2012 experiment. Each panel (a-f) represents the time evolution of the vertical velocity spectra at the various instrument heights denoted in the figure. Spectra were calculated using ten-minute windows using standard methods [cf. *Walter et al.*, 2011]. (g) Mean horizontal current direction relative to true north at the various instrument heights. Panels (a, b, e, f) have the same frequency axis and colorbar as panel (c).

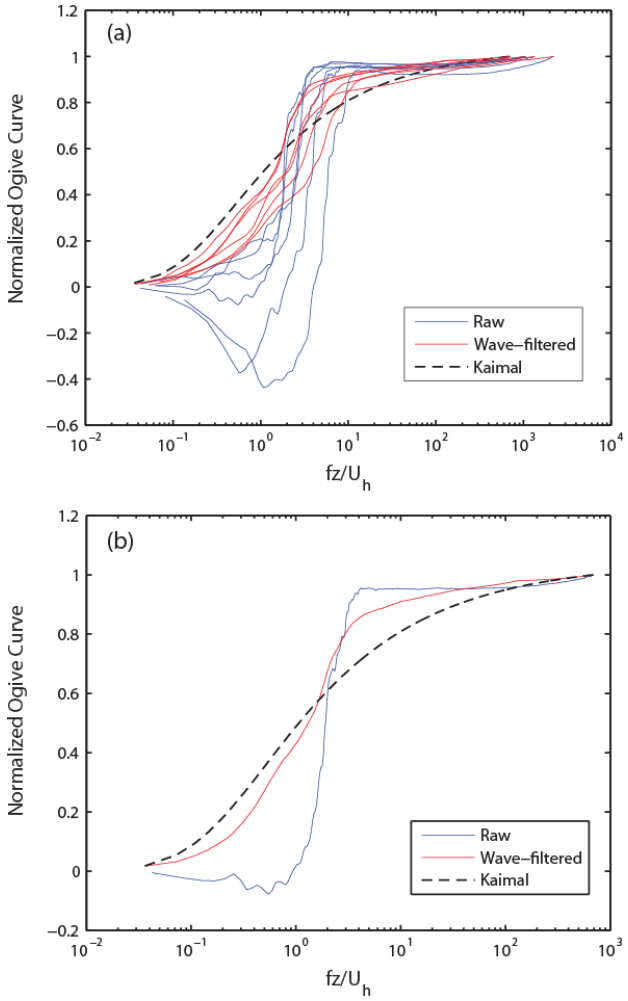

Figure B.4: Example (1 mab ADV, MOTOWN 2012) of the cumulative integral of the velocity cospectra (*u'w'* component, ogive curves) normalized by the integral of the velocity cospectra as a function of the non-dimensional frequency, highlighting the effectiveness of the wave-filtering method. (a) Raw (blue) and wave-filtered (red) normalized ogive curves calculated using six individual ten-minute bursts over an hour and (b) a single ten-minute burst. The *Kaimal et al.* [1972] empirical curve (black dashed) is shown for reference.

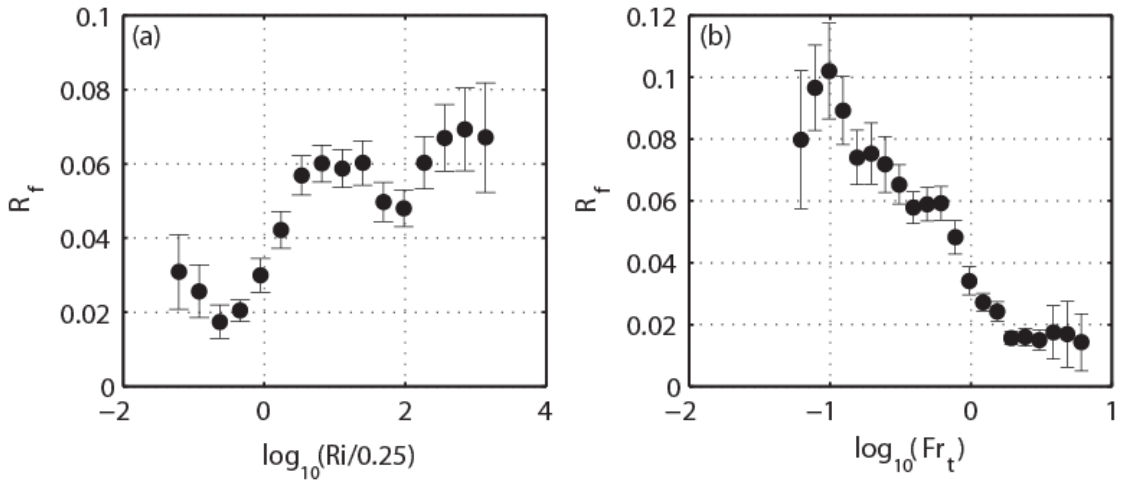

Figure B.5: The flux Richardson number (R_f) as a function of the (a) normalized gradient Richardson number (Ri) and (b) the turbulent Froude number (Fr_t) during MOTOWN 2012. The black dots represent binned-averaged values, while the error bars signify the standard error.

Bibliography

Alford, M.H., J.B. Mickett, S. Zhang, P. MacCready, Z. Zhao, and J. Newton (2012), Internal waves on the Washington continental shelf, *Oceanography* 25(2), 66–79, http://dx.doi.org/10.5670/oceanog.2012.43.

Al-Jiboori, M. H., Y. Xu, and Y. Qian (2001), Velocity spectra over different terrains, *Atmospheric Science Letters*, *2*, 32-38, doi: 10.1006/asle.2001.0042.

Andreas, E. L. (1987), Spectral measurements in a disturbed boundary layer over snow, *J. Atmos. Sci., 44*, 1912-1939.

Apel, J. R. (2003), A new analytical model for internal solitons in the ocean, *J. Phys. Oceanogr*., *33*, 2247-2269.

Apel, J. R., J. R. Holbrook, A. K. Liu, and J. J. Tsai (1985), The Sulu Sea internal soliton experiment, *J. Phys. Oceanogr., 15*, 1625-1651.

Bakun, A. (1990), Global climate change and intensification of coastal ocean upwelling, *Science, 247*(4939), 198–201, doi:10.1126/science.247.4939.198.

Barad, M. F., and O. B. Fringer (2010), Simulations of shear instabilities in interfacial gravity waves, *J. Fluid Mech., 644*, 61-95, doi:10.1017/S0022112009992035

Barry, M. E., G. N. Ivey, K. B. Winters, and J. Imberger (2001), Measurements of diapycnal diffusivities in stratified fluids, *J. Fluid. Mech*., *442*, 267-291.

Batchelor, G. K. (1953), The Theory of Homogeneous Turbulence, Cambridge University Press, New York, NY.

Beardsley, R. C., C. E. Dorman, C. A. Friehe, L. K. Rosenfeld, and C. D. Winant (1987), Local atmospheric forcing during the coastal ocean dynamics experiment 1. A description of the marine boundary layer and atmospheric conditions over a northern California upwelling region, *J. Geophys. Res., 92*, 1467-1488.

Bluteau, C. E., N. L. Jones, G. N. Ivey (2011), Estimating turbulent kinetic energy dissipation using the inertial subrange method in environmental flows, *Limnol. Oceanogr. Methods, 9*, 302-321.

Boegman, L., G. N. Ivey, and J. Imberger (2005), The degeneration of internal waves in lakes with sloping topography, *Limnol. Oceanogr*., 50, 1620-1637, doi:10.4319/lo.2005.50.5.1620.

Boehm, A. B., B. F. Sanders, and C. D. Winant (2002), Cross-Shelf transport at Huntington Beach. Implications for the fate of sewage discharged through an offshore ocean outfall, *Environ. Sci. Technol., 36*, 1899-1906.

Bograd, S. J., C. G. Castro, E. Di Lorenzo, D. M. Palacios, H. Bailey, W. Gilly, and F. P. Chavez (2008), Oxygen declines and the shoaling of the hypoxic boundary in the California Current, *Geophysical Research Letters*, *35*(12), 1–6, doi:10.1029/2008GL034185.

Booth, J. A. T. et al. (2012), Natural intrusions of hypoxic, low pH water into nearshore marine environments on the California coast, *Cont. Shelf Res.,* 45, 108-115.

Bouffard, D. and L. Boegman (2013), A diapycnal diffusivity model for stratified environmental flows, *Dynamics of Atmospheres and Oceans, 61-62*, 14-34.

Brady, D. C., and T. E. Targett (2010), Characterizing the escape response of juvenile summer flounder Paralichthys dentatus to diel-cycling hypoxia, *Journal of fish biology*, *77*(1), 137–52, doi:10.1111/j.1095-8649.2010.02663.x.

Breaker, L. C. and W. W. Broenkow (1994), The circulation of Monterey Bay and related processes, *Oceanography and Marine Biology, An Annual Review, 32*, 1-64.

Breitburg, D. L., D. W. Hondorp, L. A. Davias, and R. J. Diaz (2009), Hypoxia, nitrogen, and fisheries: Integrating effects across local and global landscapes, *Annual Review of Marine Science, 1*, doi:http://dx.doi.org/10.1146/annurev.marine.010908.163754.

Bricker, J. D. and S. G. Monismith (2007), Spectral wave-turbulence decomposition, *J. Atmos. Ocean. Technol., 24*, 1479-1487.

Burton, D. T., L. B. Richardson, and C. J. Moore (1980), Effect of oxygen reduction rate and constant low dissolved oxygen concentrations on two estuarine Fish, *Transactions of the American Fisheries Society*, *559*, 552–557.

Carter, G. S. (2010), Barotropic and baroclinic M_2 tides in the Monterey Bay region, *J. Phys. Oceanogr., 40*, 1766-1783.

Carter, G. S., M. C. Gregg, and R. Lien (2005), Internal waves, solitary-like waves, and mixing on the Monterey Bay shelf, *Cont. Shelf Res., 25*, 1499-1520.

Chan, F., J. A. Barth, J. Lubchenco, A. Kirincich, H. Weeks, W. T. Peterson, and B. A. Menge (2008), Emergence of anoxia in the California Current large marine ecosystem, *Science, 319*, 920-920.

Checkley Jr., D. M. and J. A. Barth (2009), Patterns and processes in the California Current System, *Prog. Oceanogr., 83*, 49-64.

Chimonas, G. (1985), Apparent counter-gradient heat fluxes generated by atmospheric waves, *Boundary-Layer Meteorology, 31*, 1-12.

Colosi, J. A., R. C. Beardsley, J. F. Lynch, G. Gawarkiewicz, C. Chiu, and A. Scotti (2001), Observations of nonlinear internal waves on the outer New England continental shelf during the summer Shelfbreak Primer study, *J. Geophys. Res., 106*, 9587-9601.

Craig, J. K. (2012), Aggregation on the edge: effects of hypoxia avoidance on the spatial distribution of brown shrimp and demersal fishes in the Northern Gulf of Mexico, *Marine Ecology Progress Series, 445*, 75–95, doi:10.3354/meps09437.

Crimaldi, J. P., J. K. Thompson, J. H. Rosman, R. J. Lowe, and J. R. Koseff (2002), Hydrodynamics of larval settlement: The influence of turbulent stress events at potential recruitment sites, *Limnol. Oceanogr., 47*(4), 1137-1151

Davis, K. A. (2008), Dynamics of Internal Waves on the Southeastern Florida Shelf: Implications for Cross-Shelf Exchange and Turbulent Mixing on a Barrier Reef System, PhD, Department of Civil and Environmental Engineering thesis, Stanford University, Stanford, CA.

Davis, K. A. and S. G. Monismith (2011), The modification of bottom boundary layer turbulence and mixing by internal waves shoaling on a barrier reef, *J. Phys. Oceanogr., 41*, 2223-2241.

Drobinski, P., P. Carlotti, R. K. Newsom, R. M. Banta, R. C. Foster, and J. Redelsperger (2004), The structure of the near-neutral atmospheric surface layer, *J. Atmos. Sci., 61*, 699-714.

Dunckley, J. F., J. R. Koseff, J. V. Steinbuck, S. G. Monismith, and A. Genin (2012), Comparison of mixing efficiency and vertical diffusivity models from temperature microstructure, *J. Geophys. Res., 117*, C10008, doi: 10.1029/2012JC007967,

Dunphy, M., C. Subich, and M. Stastna (2011), Spectral methods for internal waves: indistinguishable density profiles and double-humped solitary waves, *Nonlin. Processes Geophys., 18*, 351-358.

Eby, L. A., and L. B. Crowder (2002), Hypoxia-based habitat compression in the Neuse River Estuary: context-dependent shifts in behavorial avoidance thresholds, *Canadian Journal of Fisheries and Aquatic Sciences, 59*, 952–965.

Ekau, W., H. Auel, H.-O. Pörtner, and D. Gilbert (2010), Impacts of hypoxia on the structure and processes in pelagic communities (zooplankton, macro-invertebrates and fish), *Biogeosciences, 7*(5), 1669–1699, doi:10.5194/bg-7-1669-2010.

Emery, W. J. and R. E. Thomson (2004), *Data Analysis Methods in Physical Oceanography*, Second and Revised Edition ed., 638 pp., Elsevier, Amsterdam, The Netherlands.

Farmer, D. and L. Armi (1999), The generation and trapping of solitary waves over topography, *Science, 283*, 188-190.

Feddersen, F. and A. J. Williams (2007), Direct estimation of the Reynolds stress vertical structure in the nearshore, *J. Atmos. Ocean. Technol., 24*, 102-116.

Feddersen, F., J. H. Trowbridge, and A. J. Williams (2007), Vertical structure of dissipation in the nearshore, *J. Phys. Oceanogr., 37*, 1764-1777.

Foken, T. (2008), The energy balance closure problem: An overview, *Ecol. Appl., 18*, pp. 351-1367.

Frieder, C. A., S. H. Nam, T. R. Martz, and L. A. Levin (2012), High temporal and spatial variability of dissolved oxygen and pH in a nearshore California kelp forest, *Biogeosciences, 9*(10), 3917–3930, doi:10.5194/bg-9-3917-2012.

Fringer, O. B., M. Gerritsen, and R. L. Street (2006), An unstructured-grid, finite-volume, nonhydrostatic, parallel coastal ocean simulator, *Ocean Modelling, 14*, 139-173.

Gal-Chen, T., M. Xu, and W. L. Eberhard (1992), Estimations of atmospheric boundary layer fluxes and other turbulence parameters from Doppler lidar data, *J. Geophys. Res., 97*, 18409-18423.

García-Reyes, M. and J. L. Largier (2012), Seasonality of coastal upwelling off central and northern California: New insights, including temporal and spatial variability, *J. Geophys. Res., 117*, C03028, doi:10.1029/2011JC007629.

Gargett, A. E., T. R. Osborn, and P. W. Nasmyth (1984), Local isotropy and the decay of turbulence in a stratified fluid, *J. Fluid Mech., 144*, 231-280.

Gerbi, G. P., J. H. Trowbridge, J. B. Edson, A. J. Plueddemann, E. A. Terray, and J. J. Fredericks (2008), Measurements of momentum and heat flux across the air-sea interface, *J. Phys. Oceanogr., 38*, 1054-1072.

Gerz, T. and U. Schumann (1996), A possible explanation of countergradient fluxes in homogeneous turbulence, *Theoretical and Computational Fluid Dynamics, 8*, 169-181.

Goring, D. G. and V. I. Nikora (2002), Despiking acoustic Doppler velocimeter data, *J. Hyd. Eng., 128(*1*)*, 117-126.

Graham, W. M. and J. L. Largier (1997), Upwelling shadows as nearshore retention sites: the example of northern Monterey Bay, *Cont. Shelf Res., 17*, 509-532.

Graham, W. M., J. G. Field, and D. C. Potts (1992), Persistent “upwelling shadows” and their influence on zooplankton distributions, *Marine Biology, 114*, 561-570.

Grantham, B. A., F. Chan, K. J. Nielsen, D. S. Fox, J. A. Barth, A. Huyer, J. Lubchencho, B. A. Menge (2004), Upwelling-driven nearshore hypoxia signals

ecosystem and oceanographic changes, *Nature*, *429*, 749–754, doi:10.1038/nature02612.1.

Gregg, M. C. (1989), Scaling turbulent dissipation in the thermocline, *J. Geophys. Res.*, *94*, 9686-9698.

Grimshaw, R., E. Pelinovsky, and T. Talipova (1999), Solitary wave transformation in a medium with sign-variable quadratic nonlinearity and cubic nonlinearity, *Physica D*, *132*, 40-62.

Gross, T. F., and A. R. M. Nowell (1983), Mean flow and turbulence scaling in a tidal boundary layer, *Cont. Shelf Res.*, 2, 109–126, doi:10.1016/0278-4343(83)90011-0.

Hansen, J. C. R. and M. A. Reidenbach (2012), Wave and tidally driven flows in eelgrass beds and their effect on sediment suspension, *Mar. Ecol. Prog. Ser.*, *448*, 271-287.

Haugen, D. A., J. C. Kaimal, and E. F. Bradley (1971), An experimental study of Reynolds stress and heat flux in the atmospheric surface layer, *Q. J. R. Meteorol. Soc.*, *97*, 168-180.

Helfrich, K. R. and W. K. Melville (2006), Long nonlinear internal waves, *Annu. Rev. Fluid Mech.*, *38*, 395-425, doi: 10.1146/annurev.fluid.38.050304.092129.

Helly, J. J. and L. A. Levin (2004), Global distribution of naturally occurring marine hypoxia on continental margins, *Deep Sea Research Part I: Oceanographic Research Papers*, *51*(9), 1159–1168, doi:10.1016/j.dsr.2004.03.009.

Hofmann, A. F., E. T. Peltzer, P. M. Walz, and P. G. Brewer (2011), Hypoxia by degrees: Establishing definitions for a changing ocean, *Deep Sea Research Part I: Oceanographic Research Papers*, *58*(12), 1212–1226.

Hogstrom, U., H. Bergstrom, and H. Alexandersson (1982), Turbulence characteristics in a near neutrally stratified urban atmosphere, *Bound.-Layer Meteorol.*, *23*, 449-472; 472, doi: 10.1007/BF00116272.

Holloway, P. E. (1987), Internal hydraulic jumps and solitons at a shelf break region on the Austrialian NorthWest Shelf, *J. Geophys. Res.*, *92*, C5, 5405-5416.

Holt, S. E., J. R. Koseff, and J. H. Ferziger (1992), A numerical study of the evolution and structure of homogeneous stably stratified sheared turbulence, *J. Fluid Mech., 237*, 499.

Holt, S. E., J. R. Koseff, and J. H. Ferziger (1992), A numerical study of the evolution and structure of homogeneous stably stratified sheared turbulence, *J. Fluid. Mech., 237*, 499-539.

Hosegood, P. and H. van Haren (2004), Near-bed solibores over the continental slope in the Faeroe-Shetland Channel, *Deep Sea Research Part II: Topical Studies in Oceanography, 51*, 2943-2971.

Hult, E. L., C. D. Troy, and J. R. Koseff (2011a), The mixing efficiency of interfacial waves breaking at a ridge: 1. Overall mixing efficiency, *J. Geophys. Res., 116*, C02003.

Hult, E. L., C. D. Troy, and J. R. Koseff (2011b), The mixing efficiency of interfacial waves breaking at a ridge: 2. Local mixing processes, *J. Geophys. Res., 116*, C02004.

Hutchins, N. and I. Marusic (2007), Evidence of very long meandering features in the logarithmic region of turbulent boundary layers, *J. Fluid Mech., 579*, 1.

Itsweire, E. C., K. N. Helland, and C. W. Van Atta (1986), The evolution of grid-generated turbulence in a stably stratified fluid, *J. Fluid Mech., 162*, 299-338.

Ivey, G. N. and J. Imberger (1991), On the nature of turbulence in a stratified fluid. Part I: The energetics of mixing, *J. Phys. Oceanogr., 21*, 650-658.

Ivey, G. N., K. B. Winters, and J. R. Koseff (2008), Density stratification, turbulence, but how much mixing?, *Annu. Rev. Fluid. Mech., 40*, 168-184.

Jackson, C.R., J.C.B. da Silva, and G. Jeans (2012), The generation of nonlinear internal waves, *Oceanography*, *25*(2), 108–123.

Kaimal, J. C., J. C. Wyngaard, Y. Izumi, and O. R. Coté (1972), Spectral characteristics of surface-layer turbulence, *Q. J. R. Meteorol. Soc., 98*, 563-589.

Kamykowski, D. and S. Zentara (1990), Hypoxia in the world ocean as recorded in the historical data set, *Deep Sea Research*, *37*(12), 1861–1874.

Kang, D. and O. B. Fringer (2010), On the calculation of available potential energy in internal wave fields, *J. Phys. Oceanogr., 40*, 2539-2545.

Keeling, R. F. and H. E. Garcia (2002), The change in oceanic O_2 inventory associated with recent global warming. *Proceedings of the National Academy of Sciences of the United States of America*, *99*(12), 7848–53. doi:10.1073/pnas.122154899

Kelly, S. M. and J. D. Nash (2010), Internal-tide generation and destruction by shoaling internal tides, *Geophys. Res. Lett., 37*, L23611.

Kilcher, L. F., J. D. Nash, and J. N. Moum (2012), The role of turbulence stress divergence in decelerating a river plume, *J. Geophys. Res., 117*, C05032.

Kildow, J. and C. S. Colgan (2005), California's Ocean Economy, *National Ocean Economics Program Report to the Resources Agency, State of California*, 1-156.

Kirincich, A. R., S. J. Lentz, and G. P. Gerbi (2010), Calculating Reynolds stresses from ADCP measurements in the presence of surface gravity waves using the cospectra-fit method, *J. Atmos. Ocean. Technol., 27*, 889-907.

Klymak, J. M. and J. N. Moum (2003), Internal solitary waves of elevation advancing on a shoaling shelf, *Geophys. Res. Lett., 30*, 2045.

Klymak, J. M. and J. N. Moum (2007a), Oceanic isopycnal slope spectra. Part I: Internal waves, *J. Phys. Oceanogr., 37*, 1215-1231.

Klymak, J. M. and J. N. Moum (2007b), Oceanic isopycnal slope spectra. Part II: Turbulence, *J. Phys. Oceanogr., 37*, 1232-1245.

Koehl, M. A. and M. G. Hadfield (2010), Hydrodynamics of larval settlement from a larva's point of view, *Integr. Comp. Biol.*, *50*(4), 539-551.

Kristensen, L. and D. R. Fitzjarrald (1984), The effect of line averaging on scalar flux measurements with a sonic anemometer near the surface, *J. Atmos. Ocean. Technol., 1*, 138-146.

Kunze, E., L. K. Rosenfeld, G. S. Carter, and M. C. Gregg (2002), Internal waves in Monterey Submarine Canyon, *J. Phys. Oceanogr., 32*, 1890-1913.

Lacy, J. R. and S. Wyllie-Echeverria (2011), The influence of current speed and vegetation density on flow structure in two macrotidal eelegrass canopies, *Limnology and Oceanography: Fluids and Environments*, *1*, 38-55, doi: 10.1215/21573698-1152489.

Lamb, K. G. (1994), Numerical experiments of internal wave generation by strong tidal flow across a finite amplitude bank edge, *J. Geophys. Res.*, 843, doi: 10.1029/93JC02514.

Lamb, K. G. (1997), Particle transport by nonbreaking, solitary internal waves, *J. Geophys. Res.*, 102, C8, doi: 10.1029/97JC00441.

Lamb, K. G. (1999), Theoretical descriptions of shallow-water solitary internal waves: Comparisons with fully-nonlinear waves, *The 1998 WHOI\IOS\ONR Internal Solitary Wave Workshop: Contributed Papers*, Tech. Rep. WHOI-99-07, edited by T. F. Duda and D. M. Farmer, WHOI-99-07, Woods Hole Oceanogr. Inst., Woods Hole, Mass.

Lamb, K. G. and D. Farmer (2011), Instabilities in an internal solitary-like wave on the Oregon shelf, *J. Phys. Oceanogr.*, *41*, 67-87.

Lamb, K. G. and L. Yan (1996), The evolution of internal wave undular bores: Comparisons of a fully nonlinear numerical model with weakly nonlinear theory, *J. Phys. Oceanogr., 26*, 2712-2734.

Lamb, K. G., and V. T. Nguyen (2009), Calculating energy flux in internal solitary waves with an application to reflectance, *J. Phys. Oceanogr.*, *39*, 559-580. doi: http://dx.doi.org/10.1175/2008JPO3882.1.

Lamb, K.G. (2013), Internal wave breaking and dissipation mechanisms on the continental slope/shelf, *Ann. Rev. Fluid Mech.*, In Press

Large, W. G. and S. Pond (1981), Open ocean momentum flux measurements in moderate to strong winds, *J. Phys. Oceanogr., 11*, 324-336.

Lee, O. S. (1961), Observations on internal waves in shallow water, *Limnol. Oceanogr., 6*, pp. 312-321.

Leichter, J. J., S. R. Wing, S. L. Miller, and M. W. Denny (1996), Pulsed delivery of subthermocline water to Conch Reef (Florida Keys) by internal tidal bores, *Limnol. Oceanogr., 41*, pp. 1490-1501.

Lentz, S. J. and M. R. Fewings (2012), The wind- and wave- driven inner-shelf circulation, *Annual Review of Marine Science, 4*, 317-343.

Lentz, S. J., M. R. Fewings, P. Howd, J. Fredericks, and K. Hathaway (2008), Observations and a model of undertow over the inner continental shelf, *J. Phys. Oceanogr., 38*, 2341-2357.

Lerczak, J. A., C. D. Winant, and M. C. Hendershott (2003), Observations of the semidiurnal internal tide on the southern California slope and shelf, *J. Geophys. Res., 108*, C3, 3068.

Li, W., T. Hiyama, and N. Kobayashi (2007), Turbulence spectra in the near-neutral surface layer over the Loess Plateau in China, *Bound.-Layer Meteorol., 124*, 449-463; 463, doi: 10.1007/s10546-007-9180-y.

Lien, R. and T. B. Sanford (2000), Spectral characteristics of velocity and vorticity fluxes in an unstratified turbulent boundary layer, *J. Geophys. Res., 105*, 8659-8672.

Lien, R. and T. B. Sanford (2004), Turbulence spectra and local similarity scaling in a strongly stratified oceanic bottom boundary layer, *Cont. Shelf Res., 24*, 375-392.

Lucas, A. J., P. J. S. Franks, and C. L. Dupont (2011), Horizontal internal-tide fluxes support elevated phytoplankton productivity over the inner continental shelf, *Limnology & Oceanography: Fluids & Environments, 1*, 56-74

Luketina, D. A. and J. Imberger (1987), Characteristics of a surface buoyant jet, *J. Geophys. Res., 92*, C5, doi: 10.1029/JC092iC05p05435.

Lumley, J. L. and E. A. Terray (1983), Kinematics of turbulence convected by a random wave field, *J. Phys. Oceanogr., 13*, 2000-2007.

MacVean, L. J. and J. R. Lacy (2014), Interactions between waves, sediment, and turbulence on a shallow estuarine mudflat, *J. Geophys. Res. Oceans, 119*, 1534-1553.

Mann, K. H. (2000), *Ecology of Coastal Waters, with Implications for Management*, 406 pp., Blackwell Science, Oxford, UK.

McClatchie, S., R. Goericke, R. Cosgrove, G. Auad, and R. Vetter (2010), Oxygen in the Southern California Bight: Multidecadal trends and implications for demersal fisheries, *Geophysical Research Letters*, *37*(19), 1–5, doi:10.1029/2010GL044497.

McNaughton, K. G. and J. Laubach (2000), Power spectra and cospectra for wind and scalars in a disturbed surface layer at the base of an advective inversion, *Bound.-Layer Meteorology*, *93*, 143-185.

McPhee-Shaw, E., D. A. Siegel, L. Washburn, M. A. Brzezinski, J. L. Jones, A. Leydecker, and J. Melack (2007), Mechanisms for nutrient delivery to the inner shelf: Observations from the Santa Barbara Channel, *Limnol. Oceanogr.*, *52*, 1748-1766.

Monismith, S. G. and D. A. Fong (1996), A simple model of mixing in stratified tidal flows, *J. Geophys. Res.*, *101*, 28583-28595.

Moum, J. N. and T. P. Rippeth (2009), Do observations adequately resolve the natural variability of oceanic turbulence?, *J. Mar. Syst.*, *77*, 409-417.

Moum, J. N., D. M. Farmer, W. D. Smyth, L. Armi, and S. Vagle (2003), Structure and generation of turbulence at interfaces strained by internal solitary waves propagating shoreward over the continental shelf, *J. Phys. Oceanogr.*, *33*, 2093-2112.

Munk, W. and C. Wunsch (1998), Abyssal recipes II: energetics of tidal and wind mixing, *Deep Sea Research Part I: Oceanographic Research Papers*, *45*, 1977-2010.

Nam, S. and U. Send (2011), Direct evidence of deep water intrusions onto the continental shelf via surging internal tides, *J. Geophys. Res.*, *116*, C05004.

Nash, J. D. and J. N. Moum (2005), River plumes as a source of large-amplitude internal waves in the coastal ocean, *Nature*, *437*, 400-403.

Nash, J. D., E.L. Shroyer, S. M. Kelly, M. E. Inall, T. F. Duda, M. D. Levine, N. L. Jones, and R. C. Musgrave (2012), Are any coastal internal tides predictable?, *Oceanogr.*, 25(2), 80-95.

Nash, J. D., M. H. Alford, and E. Kunze (2005), Estimating internal wave energy fluxes in the ocean, *J. Atmos. Oceanic Technol.*, 22, 1551–1570.

Nidzieko, N. J., D. A. Fong, and J. L. Hench (2006), Comparison of Reynolds stress estimates derived from standard and fast-ping ADCPs, *J. Atmos. Ocean. Technol., 23*, 854-861.

Nidzieko, N. J., J. L. Hench, and S. G. Monismith (2009), Lateral circulation in well-mixed and stratified estuarine flows with curvature, *J. Phys. Oceanogr., 39*, 831-851.

Noble, M., B. Jones, P. Hamilton, J. Xu, G. Robertson, L. Rosenfeld, and J. Largier (2009), Cross-shelf transport into nearshore waters due to shoaling internal tides in San Pedro Bay, CA, *Cont. Shelf Res., 29*, 1768-1785.

Osborn, T. R. (1980), Estimates of the local rate of vertical diffusion from dissipation measurements, *J. Phys. Oceanogr., 10*, 83-89.

Panofsky, H. A., D. Larko, R. Lipschutz, G. Stone, E. F. Bradley, A. J. Bowen, and J. Højstrup (1982), Spectra of velocity components over complex terrain, *Q. J. R. Meteorol. Soc., 108*, 215-230.

Pauly, D. and V. Christensen (1995), Primary production required to sustain global fisheries, *Nature, 374*, 255-257.

Pawlowicz, R., B. Beardsley, and S. Lentz (2002), Classical tidal harmonic analysis including error estimates in MATLAB using T_TIDE, *Comput. Geosci.*, 28, 929 – 937, doi:10.1016/S0098-3004(02)00013-4.

Peltier, W. R. and C. P. Caulfield (2003), Mixing efficiency in stratified shear flows, *Annu. Rev. Fluid Mech., 35*, 135-167, doi: 10.1146/annurev.fluid.35.101101.161144.

Perlin, A., J. N. Moum, J. M. Klymak, M. D. Levine, T. Boyd, and P. M. Kosro (2005), A modified law-of-the-wall applied to oceanic bottom boundary layers, *J. Geophys. Res., 110*, C10S10.

Petruncio, E. T., L. K. Rosenfeld, and J. D. Paduan (1998), Observations of the internal tide in Monterey Canyon, *J. Phys. Oceanogr., 28*, 1873-1903.

Pineda, J. (1991), Predictable upwelling and the shoreward transport of planktonic larvae by internal tidal bores, *Science, 253*, 548-549.

Pineda, J. (1994), Internal tidal bores in the nearshore: Warm-water fronts, seaward gravity currents and the onshore transport of neustonic larvae, *J. Mar. Res., 52*, 427-458.

Pineda, J. (1995), An internal tidal bore regime at nearshore stations along western USA: Predictable upwelling within the lunar cycle, *Cont. Shelf Res., 15*.

Pineda, J. (1999), Circulation and larval distribution in internal tidal bore warm fronts, *Limnol. Oceanogr., 44*, 1400-1414.

Pineda, J. and M. Lopez (2002), Temperature, stratification, and barnacle larval settlement in two Californian sites, *Cont. Shelf Res., 22*, 1183-1198.

Pingree, R. D. and G. T. Mardell (1985), Solitary internal waves in the Celtic Sea, *Progress in Oceanography, 14*, 431–441, http://dx.doi.org/10.1016/0079-6611(85)90021-7.

Pope, S. B. (2000), *Turbulent Flows*, 771 pp., Cambridge University Press, Cambridge, UK.

Prabha, T. V., M. Y. Leclerc, A. Karipot, and D. Y. Hollinger (2007), Low-frequency effects on eddy covariance fluxes under the influence of a low-level jet, *J. Appl. Meteor. Climatol., 46*, 338-352.

Raheem, N., S. Colt, E. Fleishman, J. Talberth, P. Swedeen, K. J. Boyle, M. Rudd, R. D. Lopez, D. Crocker, D. Bohan, T. O'Higgins, C. Willer, and R. M. Boumans (2012), Application of non-market valuation to California's coastal policy decisions, *Marine Policy, 36*, 1-6.

Rehmann, C. R. (2004), Scaling for the mixing efficiency of stratified grid turbulence, *Journal of Hydraulic Research, 42*:1, 35-42.

Rehmann, C. R. and J. R. Koseff (2004), Mean potential energy change in stratified grid turbulence, *Dynamics of Atmospheres and Oceans, 37*, 271-294.

Reidenbach, M. A., S. G. Monismith, J. R. Koseff, G. Yahel, and A. Genin (2006), Boundary layer turbulence and flow structure over a fringing coral reef, *Limnol. Oceanogr., 51*, 1956-1968.

Reynolds, W. C. and A. K. M. F. Hussain (1972), The mechanics of an organized wave in turbulent shear flow. Part 3. Theoretical models and comparisons with experiments, *J. Fluid Mech., 54*, 263.

Rohr, J. J., E. C. Itsweire, and C. W. Van Atta (1984), Mixing efficiency in stably-stratified decaying turbulence, *Geophysical & Astrophysical Fluid Dynamics*, *29*:1-4, 221-236.

Rosenfeld, L. K., F. B. Schwing, N. Garfield, and D. E. Tracy (1994), Bifurcated flow from an upwelling center: a cold water source for Monterey Bay, *Cont. Shelf Res., 14*, 931-964.

Rosenfeld, L. K., I. Shulman, M. Cook, J. D. Paduan, and L. Shulman (2009), Methodology for regional tidal model evaluation, with application to Central California, *Deep-Sea Res. II*, 56, 199–218.

Rosman, J. H., J. L. Hench, J. R. Koseff, and S. G. Monismith (2008), Extracting Reynolds stresses from acoustic Doppler current profiler measurements in wave-dominated environments, *J. Atmos. Oceanic Technol., 25*, 286-306.

Roth, M., T. R. Oke, and D. G. Steyn (1989), Velocity and temperature spectra and cospectra in an unstable suburban atmosphere, *Bound.-Layer Meteorol., 47*, 309-320; 320, doi: 10.1007/BF00122336.

Ryan, J. P., A. M. Fischer, R. M. Kudela, M. A. McManus, J. S. Myers, J. D. Paduan, C. M. Ruhsam, C. B. Woodson, and Y. Zhang (2010), Recurrent frontal slicks of a coastal ocean upwelling shadow, *J. Geophys. Res., 115*, C12070.

Ryan, J. P., M. A. McManus, J. D. Paduan, and F. P. Chavez (2008), Phytoplankton thin layers caused by shear in frontal zones of a coastal upwelling system, *Mar Ecol Prog Ser, 354*, 21-34.

Sakai, R. K., D. R. Fitzjarrald, and K. E. Moore (2001), Importance of low-frequency contributions to eddy fluxes observed over rough surfaces, *J. Appl. Meteorol., 40*, 2178-2192.

Sandstrom, H. and J. A. Ellitot (1984), Internal tide and solitons on the Scotian Shelf: A nutrient pump at work, *J. Geophys. Res, 89*, C4, 6415-6426.

Sanford, T. B. and R. Lien (1999), Turbulent properties in a homogeneous tidal bottom boundary layer, *J. Geophys. Res., 104*, 1245-1257.

Scotti, A. and J. Pineda (2004), Observation of very large and steep internal waves of elevation near the Massachusetts coast, *Geophys. Res. Lett., 31*, L22307.

Scotti, A., B. Butman, R. C. Beardsley, P. Soupy-Alexander, and S. Anderson (2005), A modified beam-to-earth transformation to measure short-wavelength internal waves with an acoustic Doppler current profiler. *J. Atmos. Oceanic Technol.*, 22, 583–591.

Scotti, A., R. C. Beardsley, and B. Butman (2006), On the interpretation of energy and energy fluxes of nonlinear internal waves: An example from Massachusetts Bay, *J. Fluid Mech.*, 561, 103-112.

Scully, M. E., W. R. Geyer, and J. H. Trowbridge (2011), The influence of stratification and nonlocal turbulent production on estuarine turbulence: An assessment of turbulence closure with field observations, *J. Phys. Oceanogr., 41*, 166-185.

Shaw, W. J. and J. H. Trowbridge (2001), The direct estimation of near-bottom fluxes in the presence of energetic wave motions, *J. Atmos. Ocean. Technol., 18*, 1540-1557.

Shaw, W. J., J. H. Trowbridge, and A. J. Williams III, (2001), Budgets of turbulent kinetic energy and scalar variance in the continental shelf bottom boundary layer, *J. Geophys. Res., 106*, 9551-9564.

Shea, R. E. and W. W. Broenkow (1982), The role of internal tides in the nutrient enrichment of Monterey Bay, California, *Estuar. Coast. Shelf Sci., 15*, 57-66.

Shih, L. H., J. R. Koseff, G. N. Ivey, and J. H. Ferziger (2005), Parameterization of turbulent fluxes and scales using homogeneous sheared stably stratified turbulence simulations, *J. Fluid Mech., 525*, 193.

Shroyer, E. L., J. N. Moum, and J. D. Nash (2009), Observations of polarity reversal in shoaling nonlinear internal waves. *J. Phys. Oceanogr., 39*, 691–701.

Simpson, J. H., C. M. Allen, and N. C. G. Morris (1978), Fronts on the continental shelf, *J. Geophys. Res.*, *83*, C9, doi: 10.1029/JC083iC09p04607.

Smeets C. J. P. P., P. G. Duynkerke, and H. F. Vugts (1998), Turbulence characteristics of the stable boundary layer over a mid-latitude glacier. Part I: A combination of katabatic and large-scale forcing, *Boundary-Layer Meteorology, 87*, 117-145.

Smyth, W. D., J. N. Moum, and D. R. Caldwell (2001), The efficiency of mixing in turbulent patches: Inferences from direct simulations and microstructure observations, *J. Phys. Oceanogr., 31*, 1969-1992.

Smyth, W. D., J. N. Moum, and J. D. Nash (2011), Narrowband oscillations in the upper Equatorial ocean. Part II: properties of shear instabilities, *J. Phys. Oceanogr., 41*, 412-428.

Soulsby, R. L. (1980), Selecting record length and digitization rate for near-bed turbulence measurements, *J. Phys. Oceanogr., 10*, 208-219.

Stacey, M. T., S. G. Monismith, and J. R. Burau (1999), Measurements of Reynolds stress profiles in unstratified tidal flow, *J. Geophys. Res., 104*, 10933-10949.

Stanton, T. P. and L. A. Ostrovsky (1998), Observations of highly nonlinear internal solitons over the continental shelf, *Geophys. Res. Lett., 25*, 2695-2698.

Stastna, M. (2011), Resonant generation of internal waves by short length scale topography, *Phys. Fluids*, *23*, 116601, http://dx.doi.org/10.1063/1.3658773.

Stastna, M. and R. K. Walter (submitted), Transcritical generation of nonlinear internal waves in the presence of background shear flow, *Phys. Fluids*.

Stastna, M. and W. R. Peltier (2004), Upstream propagating solitary waves and breaking internal waves in flow over the sill in Knight Inlet, *Proc. R. Soc. London*, *460A*, 3159-3190.

Stastna, M. and W. R. Peltier (2005), On the resonant generation of large-amplitude internal solitary and solitary-like waves, *J. Fluid Mech.*, *543*, 267-292, doi: 10.1017/S002211200500652X.

Stastna, M., and K. G. Lamb (2002), Large fully nonlinear internal solitary waves: the effect of background current, *Phys. Fluids, 14*, 2897-2999.

Stoker, J. J. (1948), The formation of breakers and bores: the theory of nonlinear wave propagation in shallow water and open channels, *Communications on Pure and Applied Mathematics,* 1, 1-87.

Storlazzi, C. D., M. A. McManus, and J. D. Figurski (2003), Long-term, high-frequency current and temperature measurements along central California: insights into upwelling/relaxation and internal waves on the inner shelf, *Cont. Shelf Res., 23,* 901-918.

Stramma, L., G. C. Johnson, J. Sprintall, and V. Mohrholz (2008), Expanding oxygen-minimum zones in the tropical oceans, *Science*, *320*(5876), 655–8, doi:10.1126/science.1153847.

Stramma, L., S. Schmidtko, L. A. Levin, and G. C. Johnson (2010), Ocean oxygen minima expansions and their biological impacts, *Deep Sea Research Part I: Oceanographic Research Papers*, *57*(4), 587–595, doi:10.1016/j.dsr.2010.01.005.

Stretch, D. D., J. W. Rottman, S. K. Venayagamoorthy, K. K. Nomura, and C. R. Rehmann (2010), Mixing efficiency in decaying stably stratified turbulence, *Dynamics of Atmospheres and Oceans, 49*, 25-36.

Suanda, S. H. (2014), Tidal-band variability and high-frequency internal variability on the central Oregon inner shelf, PhD, College of Earth, Ocean, and Atmospheric Sciences thesis, Oregon State University, Corvallis, OR.

Suanda, S. H., J. A. Barth, R. A. Holman, and J. Stanley (2014), Shore-based observations of nonlinear internal waves across the inner shelf, J. *Atmos. Oceanic Technol., 31*, 714-728, doi: http://dx.doi.org/10.1175/JTECH-D-13-00098.1.

Suanda, S. H., J. A. Barth, and C. B. Woodson (2011), Diurnal heat balance for the northern Monterey Bay inner shelf, *J. Geophys. Res., 116*, C09030.

Tennekes, H. and J. L. Lumley (1972), *A First Course in Turbulence*, The MIT Press, Cambridge, Massachusetts.

Thorpe, S. A. (1977), Turbulence and mixing in a Scottish loch, *Philos. Trans. Roy. Soc. London, 286*, 125-181.

Trowbridge, J. and S. Elgar (2003), Spatial scales of stress-carrying nearshore turbulence, *J. Phys. Oceanogr., 33*, 1122-1128.

Trowbridge, J. H. (1998), On a technique for measurement of turbulent shear stress in the presence of surface waves, *J. Atmos. Ocean. Technol., 15*, 290-298.

Trowbridge, J. H., W. R. Geyer, M. M. Bowen, and A. J. Williams (1999), Near-bottom turbulence measurements in a partially mixed estuary: Turbulent energy balance, velocity structure, and along-channel momentum balance*, *J. Phys. Oceanogr., 29*, 3056-3072.

Troy, C. D. and J. R. Koseff (2005), The instability and breaking of long internal waves, *J. Fluid Mech., 543*, 107-136, doi: 10.1017/S0022112005006798.

Turkington, B., A. Eydeland, S. Wang (1991), A computational method for solitary internal waves in a continuously stratified fluid, *Stud. Appl. Maths, 85*, 93-127.

van Haren, H., L. Gostiaux, M. Laan, M. van Haren, E. van Haren, L. J. A. Gerringa (2012), Internal Wave Turbulence Near a Texel Beach, *PLoS ONE, 7*(*3*), e32535, doi:10.1371/journal.pone.0032535.

Vaquer-Sunyer, R. and C. M. Duarte (2008), Thresholds of hypoxia for marine biodiversity. *Proceedings of the National Academy of Sciences of the United States of America, 105*, 15452-15457.

Venayagamoorthy, S. K. and O. B. Fringer (2007), On the formation and propagation of nonlinear internal boluses across a shelf break, *J. Fluid Mech., 577*, 137.

Venayagamoorthy, S.K. and O.B. Fringer (2012), Examining breaking internal waves on a shelf slope using numerical simulations, *Oceanography* 25(22), 132–139, http://dx.doi.org/10.5670/oceanog.2012.48.

Vojkovich, M. (1998), The California fishery for market squid (Loligo opalescens), *California Cooperative Oceanic Fishery Investigations Reports, 39,* 55-60.

Voulgaris, G. and J. H. Trowbridge (1998), Evaluation of the acoustic Doppler velocimeter (ADV) for turbulence measurements, *J. Atmos. Ocean. Technol., 15*, 272-289.

Walter, R. K., C. B. Woodson, P. R. Leary, and S. G. Monismith (2014), Connecting wind-driven upwelling and offshore stratification to nearshore internal bores and oxygen variability, *J. Geophys. Res. Oceans*, *119*, doi:10.1002/2014JC009998.

Walter, R. K., C. B. Woodson, R. S. Arthur, O. B. Fringer, and S. G. Monismith (2012), Nearshore internal bores and turbulent mixing in southern Monterey Bay, *J. Geophys. Res.*, *177*, C07017, doi:10.1029/2012JC008115.

Walter, R. K., N. J. Nidieko, and S. G. Monismith (2011), Similarity scaling of turbulence spectra and cospectra in a shallow tidal flow, *J. Geophys. Res.*, *116*, C10019, doi:10.1029/2011JC007144.

Wang, X., Y. Chao, C. Dong, J. Farrara, Z. Li, J. C. McWilliams, J. D. Paduan, and L. K. Rosenfeld (2009), Modeling tides in Monterey Bay, California, *Deep-Sea Res. II*, 56, 219–231.

Wannamaker, C. and J. Rice (2000), Effects of hypoxia on movements and behavior of selected estuarine organisms from the southeastern United States, *Journal of Experimental Marine Biology and Ecology*, *249*(2), 145–163.

White, B. L. and K. R. Helfrich (2008), Gravity currents and internal waves in a stratified fluid, *J. Fluid Mech.*, *616*, 327-356.

Wilson, M. L., D. R. Webster, and M. J. Weissburg (2013), Spatial and temporal variation in the hydrodynamic landscape in intertidal salt marsh systems, *Limnol. Oceanogr.*: *Fluids and Environments, 3*, 156-172.

Wolanski, E. and G. Pickard (1983), Upwelling by internal tides and kelvin waves at the continental shelf break on the Great Barrier Reef, *Marine and Freshwater Research, 34*, 65-80.

Wong, S. H. C., A. E. Santoro, N. J. Nidzieko, J. L. Hench, and A. B. Boehm (2012), Coupled physical, chemical, and microbiological measurements suggest a connection between internal waves and surf zone water quality in the Southern California Bight, *Cont. Shelf Res.*, *34*, 64-78.

Woodson, C. B. (2013), Spatiotemporal variation in cross-shelf exchange across the inner shelf of Monterey Bay, CA, *J. Phys. Oceanogr.*, *43*, 1648-1665.

Woodson, C. B. et al. (2011), Observations of internal wave packets propagating along-shelf in northern Monterey Bay, *Geophys. Res. Lett., 38*, L01605.

Woodson, C. B., L. Washburn, J. A. Barth, D. J. Hoover, A. R. Kirincich, M. A. McManus, J. P. Ryan, and J. Tyburczy (2009), Northern Monterey Bay upwelling shadow front: Observations of a coastally and surface-trapped buoyant plume, *J. Geophys. Res., 114*, C12013.

Wyngaard, J. C. and O. R. Coté (1972), Cospectral similarity in the atmospheric surface layer, *Quarterly Journal of the Royal Meteorological Society, 98*, 590-603, doi: 10.1002/qj.49709841708.

Wyrtki, K. (1962), The oxygen minima in relation to ocean circulation, *Deep Sea Research, 9*(1-2), 11–23, doi:10.1016/0011-7471(62)90243-7.

Young, M. A., R. G. Kvitek, P. J. Iampietro, C. D. Garza, R. Maillet, and R. T. Hanlon (2011), Sea floor mapping and landscape ecology analyses used to monitor variations in spawning site preference and benthic egg mop abundance for the California market squid (Doryteuthis opalescens), *Journal of Experimental Marine Biology and Ecology, 407*(2), 226–233, doi:10.1016/j.jembe.2011.06.017.

Zeidberg, L. D., J. L. Butler, D. Ramon, A. Cossio, K. L. Stierhoff, and A. Henry (2012), Estimation of spawning habitats of market squid (Doryteuthis opalescens) from field surveys of eggs off Central and Southern California, *Marine Ecology, 33*(3), 326–336. doi:10.1111/j.1439-0485.2011.00498.x

Zeidberg, L. D., W. M. Hamner, N. Nezlin, and A. Henry (2006), The fishery for California market squid (Loligo opalescens) (Cephalopoda: Myopsida), from 1981 through 2003, *Fishery Bulletin, 104*(1), 46–59.

Zhang, Y., H. Liu, T. Foken, Q. L. Williams, S. Liu, M. Mauder, and C. Liebethal (2010), Turbulence spectra and cospectra under the influence of large eddies in the Energy Balance EXperiment (EBEX), *Boundary-Layer Meteorology, 136*, 235-251.